## Bitlis Eren Üniversitesi
# Fen Bilimleri Dergisi

## Bitlis Eren University
## Journal of Science

ISSN : 2147-3129
e-ISSN : 2147-3188

Cilt / *Volume*: 13 Sayı / *Number*: 2 Yıl / *Year*: 2024

**Yazışma Adresi**

Bitlis Eren Üniversitesi
Lisansüstü Eğitim Enstitüsü
13000, Merkez, Bitlis/TÜRKİYE
Tel: 0 (434) 2220071

https://dergipark.org.tr/tr/pub/bitlisfen

# BEU FBD

## Bitlis Eren Üniversitesi Fen Bilimler Dergisi

*Bitlis Eren University Journal of Science*

Yıl/*Year:* 2024 - Cilt/*Volume:* 13 - Sayı/*Number:* 2

**Sahibi / *Owner***
Prof. Dr. Necmettin ELMASTAŞ

**Sorumlu Müdür** / *Director*
Doç. Dr. Mehmet Bakır ŞENGÜL

**Baş Editör** / *Editor in Chief*
Doç.Dr.Engin YILMAZ

**Editörler** / *Editors*
Doç.Dr. Kesran AKIN
Doç.Dr. Erdal BAŞARAN
Doç.Dr. Fatih AVCIL
Dr. Öğr. Üyesi Ufuk KAYA
Dr. Öğr. Üyesi Yunus SAYAN
Dr.Öğr. Üyesi Ömer KARABEY
Arş. Gör. Dr. Mehmet Akif YERLİKAYA

**Dil Editörleri** / *Language Editors*
Öğr. Gör. Murat ÇAN (İngilizce)

**Dizgi / *Typographic***
Doç. Dr. Engin YILMAZ

**Dergi Sekreteri** / *Journal Secretary*
Ahmet UĞUR

## **Editör (Yayın) Kurulu /** *Editorial Board*

| | |
|---|---|
| Prof. Dr. Zekeriya YERLİKAYA | Kastamonu Üniversitesi |
| Doç. Dr. Ali ÇAKMAK | Bitlis Eren Üniversitesi |
| Doç. Dr. Yunus Levent EKİNCİ | Bitlis Eren Üniversitesi |
| Doç. Dr. Engin YILMAZ | Bitlis Eren Üniversitesi |
| Doç. Dr. Kesran AKIN | Bitlis Eren Üniversitesi |
| Doç. Dr. Tuncay TUNÇ | Mersin Üniversitesi |
| Doç. Dr. Ayşegül Demir YETİŞ | Bitlis Eren Üniversitesi |
| Doç. Dr. Ramazan KATIRCI | Sivas Bilim ve Teknoloji Üniversitesi |
| Dr. Sajad KHORSANDROO | North Carolina Agricultural and Technical State University |
| Dr. Öğr. Üyesi Zehra Nur KULUÖZTÜRK | Bitlis Eren Üniversitesi |
| Dr. Öğr. Üyesi Halil YETGİN | Bitlis Eren Üniversitesi |
| Dr. Öğr. Üyesi Erdal AKIN | Bitlis Eren Üniversitesi |
| Dr. Öğr. Üyesi Faruk ORAL | Bitlis Eren Üniversitesi |
| Dr. Öğr. Üyesi Necla ÖZDEMİR | Bitlis Eren Üniversitesi |
| Dr. Nadjet LAOUET | Constantine 1 University |
| Arş. Gör. Dr. İsmet SÖYLEMEZ | Abdullah Gül Üniversitesi |

## **Danışma Kurulu** / *Advisory Board*

| | |
|---|---|
| Prof. Dr. Atilla ARSLAN | Selçuk Üniversitesi |
| Prof. Dr. Nurtaç ÖZ | Sakarya Üniversitesi |
| Prof. Dr. Saim ÖZDEMİR | Sakarya Üniversitesi |
| Prof. Dr. Soner ÖZGEN | Fırat Üniversitesi |
| Prof. Dr. Hasan SEVGİLİ | Ordu Üniversitesi |
| Prof. Dr. Mahmut BÖYÜKATA | Kırıkkale Üniversitesi |
| Prof. Dr. Esvet AKBAŞ | Van Yüzüncü Yıl Üniversitesi |
| Prof. Dr. Mikail ET | Fırat Üniversitesi |
| Prof. Dr. Özdemir ADIZEL | Van Yüzüncü Yıl Üniversitesi |
| Prof. Dr. Orhan Taner CAN | Bursa Teknik Üniversitesi |
| Doç. Dr. Bayram GÜNDÜZ | Malatya Turgut Özal Üniversitesi |
| Doç. Dr. Sait İZGİ | Siirt Üniversitesi |
| Doç. Dr. Murat ÇELTEK | Trakya Üniversitesi |
| Doç. Dr. Cem KOŞAR | Gaziantep Üniversitesi |
| Doç. Dr. Tarkan YORULMAZ | Çankırı Karatekin Üniversitesi |
| Dr. Öğr. Üyesi Serhat Berat EFE | Bandırma Onyedi Eylül Üniversitesi |
| Dr. Öğr. Üyesi Mehmet Can BALCI | Batman Üniversitesi |

## **Dergi Hakkında** / *About Journal*

Bitlis Eren Üniversitesi Fen Bilimleri Dergisi, mühendislik ve temel bilimler alanlarındaki gelişmeleri ve yenilikleri takip etmek, meslek kuruluşlarının, araştırmacıların ve bireylerin ulusal ve uluslararası gelişimlerine katkıda bulunmak ve bu alanlarda elektronik bir kaynak oluşturmak amacıyla yayımlanmaktadır. Derginin yazım dili Türkçe veya İngilizcedir. Fen Bilimleri Dergisi, Bitlis Eren Üniversitesi Lisansüstü Eğitim Enstitüsü yayını olup, 2012 yılından bu yana ücretsiz ve açık erişimli olarak yayın hayatına devam etmektedir. Mühendislik ve temel bilimlerin bilgi tabanına ve teknolojik gelişmelere ışık tutması amacıyla bu alanlarda yapılmış deneysel ve teorik ilerlemeleri konu alan özgün araştırma makalelerine yer verilmektedir. Dergiye gönderilen çalışmaların benzerlik oranı %25'i geçmemelidir. Yazım kurallarına uymayan makaleler, hakemlere gönderilmeden önce düzeltilmek üzere yazara geri gönderilir. Bu nedenle, derginin yazım kuralları dikkate alınmalıdır. Ayrıca, editörlerden yazarlara iletilen düzeltmelere veya taleplere 30 gün içerisinde cevap verilmediği takdirde ilgili makaleler reddedilir. Makaleler şekiller ve tablolar dâhil 20 sayfayı geçmemelidir. Dergiye yayın için gönderilen makaleler en az iki hakem tarafından değerlendirilir. Yazarlardan hakem önerisi talep edilmemektedir. Makalelerin dergide yayımlanabilmesi için hakemler tarafından olumlu görüş bildirilmesi gerekmektedir. Dergi Editör Kurulu, hakem raporlarını (*en aziki hakemin değerlendirmeleri geldikten sonra*) dikkate alarak makalelerin yayımlanmak üzere kabul edilip edilmemesine karar verir. Fen Bilimleri Dergisi, yılda dört defa (*Mart*, *Haziran, Eylül, Aralık*) yayımlanmaktadır. **Dergimiz Tübitak-Ulakbim Mühendislik ve Temel Bilimler Veri Tabanı Dergi Listesinde taranmaktadır.**

# **B.E.Ü. Fen Bilimleri Dergisi 13(2), 2024 /** *B.E.U. Journal of Science 13(2), 2024*
# **İÇİNDEKİLER /** *CONTENTS*

Bitlis Eren Üniversitesi Fen Bilimleri Dergisi
BİTLİS EREN UNIVERSITY JOURNAL OF SCIENCE
ISSN: 2147-3129/e-ISSN: 2147-3188
VOLUME: 13 NO: 2 PAGE: 366-375 YEAR: 2024
DOI:10.17798/bitlisfen.1186130

# Comparative Genome Analysis of *Lactiplantibacillus paraplantarum*

Ruveyda BENK[1], Fatih ORTAKCI[2*]

*[1]Department of Biomedical Engineering, Faculty of Engineering, Erciyes University, Kayseri, TR*
*[2]Department of Food Engineering, Faculty of Chemical and Metallurgical Engineering,*

*Istanbul Technical University, Istanbul, TR*

*(ORCID: 0000-0002-5831-9431) (ORCID: 0000-0003-1319-0854)*

**Keywords:** *Lactiplantibacillus paraplantarum*, comparative genomics, bacteriocin, prophage, carbohydrate, adaptation.

## Abstract

*Lactiplantibacillus paraplantarum* is a lactic acid bacteria species that is associated with food microbiomes and has been found to be either detrimental or beneficial to specific food processes. In this study, an *in-silico* genomic approach was applied using JGI's IMG/MER and PATRIC to compare the genomes of the *L. paraplantarum* DSM10667, L-ZS9, and AS-7 strains to uncover metabolic differences and lifestyle adaptations between these isolates, and better utilizing these species in food bioprocesses. Bacteriocin and prophage screenings were performed using Bagel4 and PHASTER software, respectively. BRIG was used to identify alignments of strains with each other for visual inspection of each genome. KEGG was used to predict putative carbohydrate, pyruvate, and aminoacid metabolisms. Genome sizes of DSM10667, L-ZS9, and AS-7 were 3.36, 3.14, and 3.01 Mbp, respectively. Unique genes were found to predict the evolutionary adaptation of strains against their corresponding microniche. For example, the gene encoding arginase was only found in sausage isolate L-ZS9, while the dextran-sucrase-encoding gene was unique to beer contaminant DSM10667. Three strains were predicted to carry the plnAEFJ operon for plantaricin biosynthesis, and the AS-7 genome contains leucocin K. Although DSM 10667 harbors four intact prophages, both L-ZS9 and AS-7 carried one prophage region, still showing the plasticity of the genome. Genome analysis predicted that isolation sources might potentially affect the metabolic capabilities of strains as part of the adaptation of the strains to their habitats.

## 1. Introduction

The genus Lactobacilli is a primary comprehensive group of lactic acid bacteria that was isolated from various ecological niches [1]. Before the re-taxonomic structuring of the *Lactobacillus* genus into 23 new genera, *Lactiplantibacillus* species were considered part of the *L. plantarum* group [2]. The *Lactiplantibacillus* genus is composed of 17 species: *Lactiplantibacillus argentoratensis*, *Lactiplantibacillus songbeiensis*, *Lactiplantibacillus dongliensis*, *Lactiplantibacillus daowaiensis*, *Lactiplantibacillus nangangensis*, *Lactiplantibacillus daoliensis*, *Lactiplantibacillus pingfangensis*, *Lactiplantibacillus garii*, *Lactiplantibacillus modestisalitolerans*, *Lactiplantibacillus plajomi*, *Lactiplantibacillus mudanjiangensis*, *Lactiplantibacillus xiangfangensis*, *Lactiplantibacillus herbarum*, *Lactiplantibacillus fabifermentans*, *Lactiplantibacillus pentosus*, *Lactiplantibacillus plantarum*, and *Lactiplantibacillus paraplantarum*.

*L. paraplantarum* strains have been isolated from a variety of different fermented foods, such as sourdough [3], Awa-bancha fermented tea [1], cheese [4], Rice Bran Pickles [5], kimchi [6], Tulum cheese [7], breast milk [8], gundruk (i.e., a fermented leafy

---

[*] Corresponding author: ortakci@itu.edu.tr

*Received: 08.10.2022, Accepted: 09.11.2023*

vegetable) [9], sliced ham [10], fermented sausage [11], fruit and vegetables [12], and beer [13]. Given that *L. paraplantarum* strains have been isolated from a variety of different food matrices, only four different strains of *Lactiplantibacillus paraplantarum* complete whole genome sequences are available in the Joint Genome Institute public database as of September 5, 2022, which limits our understanding of niche-specific adaptation strategies that those organisms developed. Those *L. paraplantarum* strains are: i) DSM 10667, isolated from beer as a contaminant; ii) L-ZS9, isolated from fermented sausage, and iii) AS-7, isolated from fruit and vegetables [14].

To avoid confusion between *L. plantarum* and *L. paraplantarum* species, Curk [19] reported that the G+C content of the *L. paraplantarum* DNA is around 44-45% while *L. plantarum* has a G+C content of 41% [19]. *Lactiplantibacillus paraplantarum* is a rod-shaped bacterium that exists in short chains or pairs. *L. paraplantarum* is phenotypically remarkably close to *L. plantarum*, which was initially characterized at the Pasteur Institute by French scientist Curk [19]. *L. paraplantarum* is a facultatively anaerobic, gram-positive, and catalase-negative species that forms creamy-colored, dome-shaped colonies on the MRS agar between pH 5 and pH 7 at 30-37°C. Besides, *L. paraplantarum* strains have been shown to have potential for use in food protection and preservation [15].

Looking into the literature, comparative genome analysis within several different *lactobacillus* species at strain level has been conducted to better elucidate their lifestyle adaptation to the microenvironments they inhabit, and strain level differences have been put forth [16–18]. However, to our knowledge, no comparative genomic studies were performed to understand strain level differences within *L. paraplantarum* strains. Thus, the present study fills an important gap in the literature by performing comparative genome analysis of three different strains of *L. paraplantarum* that were isolated from sausage, beer, or fruits and vegetables. An *in-silico* approach using bioinformatic tools was utilized to predict metabolic and functional characteristics of *L. paraplantarum* DSM 10667, L-ZS9, and AS-7 for unravelling lifestyle adaptations and strain-level genomic differences [19].

## 2. Material and Method

We performed a comparative genome analysis of three *L. paraplantarum* strains that were isolated from diverse ecosystems such as beer, sausage, fruit, and vegetables. The genome sequence data for *L. paraplantarum* DSM 10667, L-ZS9, and AS-7 were downloaded from the Joint Genome Institute as shown in Table 1 with IMG genome IDs [14] and IMG/MER [20]. The average Nucleotide Identity of *L. paraplantarum* strains was calculated using the JGI IMG/MER Pairwise ANI tool [20]. The unique genes that are specific to each strain being evaluated were extracted using homologous and non-homologous functions of IMG/MER under the phylogenetic profilers' platform. Genome alignments were conducted on PATRIC services using the MAUVE genome alignment tool.

Visualization of genome alignments was conducted using the BLAST Ring Image Generator (BRIG) [21], including a ring for each genome and a ring for GC content and GC skew. A BLAST type of BLASTn [22] was used with the following options: a lower identity threshold of 70% and an upper identity threshold of 90% with a ring size of 30. Genomic features with low BLAST identity were inspected through visual genomic evaluation. The similarity of the three strains that were compared against each other and other closely related genomes was performed using the orthoANI algorithm in IMG/MER. A phylogenetic tree was built using the Type Strain Genome Server [36] for taxonomic analysis based on highly conserved 16s rRNA sequences and complete whole genomes.

Prediction of metabolic pathways of *L. paraplantarum* DSM10667, LZS-9, and AS-7 was conducted using the PATRIC KEGG database [23]. Putative glycolysis, pentose phosphate, galactose, fructose, rhamnose, maltose, pyruvate, nitrogen, histidine, and arginine pathways were elucidated and further compared across all three strains. Genome analysis for the presence of putative bacteriocin biosynthesis-responsible gene cluster(s) was performed using the web tool BAGEL 4 [24]. Each putative bacteriocin-encoding protein sequence was further confirmed using BLASTp against a non-redundant protein sequence database [25]. The prophage regions on each genome were identified and annotated using the PHASTER-Phage Search Tool Enhanced Release [26].

To better understand the evolutionary relationships across *L. paraplantarum* DSM10667, LZS-9, and AS-7, the MAUVE alignment tool, and IMG/MER's Dot Plot were performed. The latter employs the Mummer alignment tool to generate dot plot diagrams between two genomes [27] [28].

The presence of Clustered Regularly Interspaced Short Palindromic Repeat (CRISPR) regions and Cas genes was screened using

CRPISPRviz and CRISPR Cas Finder [29]. Carbohydrate active enzymes (CAZyme)-related genes were identified using the CAZy database (v10) on the dbCAN server [30] by HMMER version 3.1b2 according to the suggested protocol of dbCAN. Results of the CAZYme analysis were classified based on a suggested threshold minimum of 0.35 coverage and a cut-off E-value of 1e-15.

**Table 1.** JGI /IMG-MER Genome ID accession numbers and isolation sources of three *L. paraplantarum* strains

| Strains | IMG Genome ID | Isolation Source |
|---|---|---|
| *Lactiplantibacillus paraplantarum* DSM10667 | 2896850075 | Fruit and vegetables |
| *Lactiplantibacillus paraplantarum* LZS-9 | 2609460312 | Fermented Sausage |
| *Lactiplantibacillus paraplantarum* AS-7 | 2922794270 | Beer |

## 3. Results and Discussion

### 3.1. Genomic Analysis

Genetic distances among *L. paraplantarum* strains were determined via the Type Strain Genome server at https://tygs.dsmz.de/ with default settings [31]. Strains were compared based on whole genome sequences (Figure 1). Among the 10 *L. paraplantarum* strains being analyzed, only DSM 10667, L-ZS9, and AS-7 possess complete genome sequence data that is publicly available in the Joint Genome Institute IMG/Genome Database [14]. According to Figure 1, *L. paraplantarum* DSM 10667 and AS-7 were closely related to each other and were isolated from beer and plant material. However, *L. paraplantarum* L-ZS9 was closely related to the *L. paraplantarum* KMB-599 strain, and the former was being isolated from sausage, though the isolation source for the *L. paraplantarum* KMB-599 strain is not described [32].

**Table 2.** Genomic characteristics of *Lactiplantibacillus paraplantarum* DSM 10667, L-ZS9 and AS-7.

| Feature | DSM 10667 | L-ZS9 | AS-7 |
|---|---|---|---|
| **Size (bp)** | 3.36853 | 3.13973 | 3.00744 |
| **GC content (%)** | 43.89 | 44.0 | 44.1 |
| **Genes (total)** | 3399 | 2974 | 2905 |
| **Protein coding sequences** | 3063 | 2812 | 2689 |
| **tRNA** | 68 | 66 | 59 |
| **rRNA** | 16 | 6 | None |
| **Crispr Count** | 1 | 4 | 1 |
| **Pseudogenes** | 64 | 78 | 62 |
| **Plasmid** | 2 | None | None |

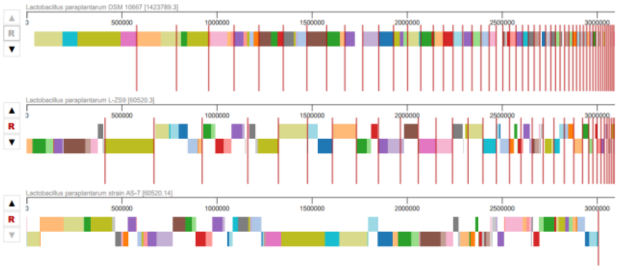

**Figure 1**. Whole genome comparisons. Mauve alignment of all complete *L. paraplantarum* genomes

### 3.1.1 Phylogenetic analysis

The phylogenetic tree was structured in Patric [23] to reveal the evolutionary relationships between ten *L. paraplantarum* strains. It was shown that *L. paraplantarum* AS-7 and DSM 10667 are closely related strains, while *L. paraplantarum* L-ZS9 is positioned far from these two strains. We speculate that since *L. paraplantarum* L-ZS9 has a quite different isolation source than AS-7 and DSM 10667 strains, the phylogenetic distance might be a result of this fact. Indeed, AS-7 and DSM 10667 do not have the exact same isolation source, but their environmental conditions are perhaps more closely related (i.e., plant-based) than the L-ZS9 (i.e., meat-based).

The genomic features of *L. paraplantarum* DSM10667, L-ZS9, and AS-7 are given in Table 2. The sizes of genomes are as follows: DSM 10667>L-ZS9>AS-7, which is in alignment with the total genes and protein-coding sequences of each strain. It was interesting to note that although L-ZS9 and AS-7 did not carry any plasmids in their cytoplasm, DSM10667 contains 2 plasmids. The L-ZS9 strain carried four CRISPR loci, whereas DSM 10667 and AS-7 carried one CRISPR loci.

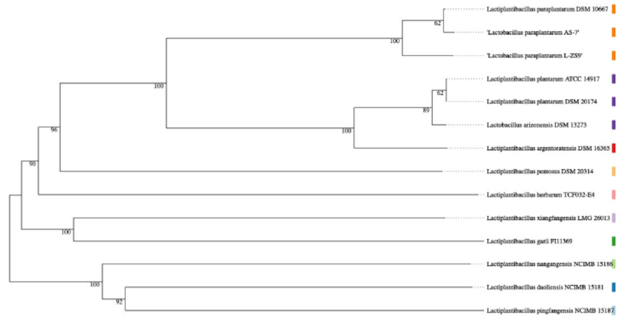

**Figure 2.** Phylogenetic distance tree of *L. paraplantarum* strains based on whole genome sequence alignment

### 3.1.2. Comparative Genome Analysis

Functional comparisons of DSM 10667, L-ZS9, and AS-7 based on whole genomes were summarized in Supplementary Table 1, Table 2, and Table 3. It was revealed that DSM 10667 harbors 438 unique genes that do not exist in L-ZS9 and AS-7. Although some of those genes were being annotated as hypothetical proteins, the DSM10667 excelled with 4 prophages and 3 bacteriocin-encoding genes. On the other hand, both L-ZS9 and AS-7 carried a single intact prophage in their genomes.

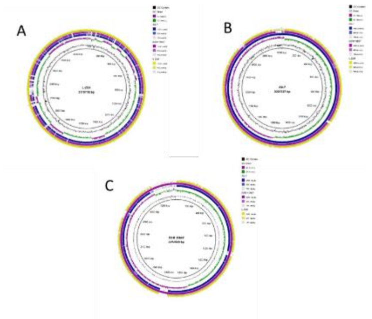

**Figure 3**. Genome wide BLAST comparison of all strains against reference strain: A)DSM10667 and AS-7 against L-ZS9 B)DSM 10667 and L-ZS9

against AS-7 C)L-ZS9 and AS-7 against DSM 10667 references

### 3.1.3 Unique genes

*L. paraplantarum* AS-7 contains 35 strain-specific genes (i.e., unique genes) composed of 13 hypothetical protein-encoding genes, which are not found in either *L. paraplantarum* DSM 10667 or L-ZS9. Likewise, L-ZS9 harbors 248 unique genes, including 89 hypothetical protein-encoding genes. Across all three genomes, *L. paraplantarum* DSM 10667 harbors the highest number of unique genes (438), more than half of which contain hypothetical protein-encoding genes (Tables S1, S2, and S3).

### 3.1.4. Bacteriocins

The Bagel4 tool predicted that *L. paraplantarum* DSM 10667 encodes plantaricin A, E, F, J, and leucocin K [24]. On the other hand, both L-ZS9 and AS-7 contain class I bacteriocins of plantaricin A, E, F, J and K (Figure 4A, 4B, 4C). Evidence of putative bacteriocin biosynthesis-associated genes might imply that the potential antimicrobial activity of *L. paraplantarum* against competitive microorganisms (i.e., including pathogens) coexists in a similar environmental ecosystem that *L. paraplantarum* strains inhabit [33].

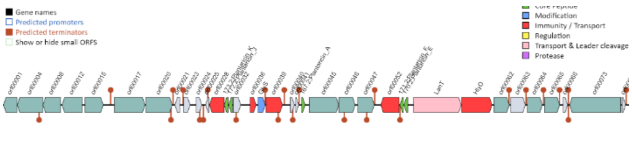

**Figure 4**. The predicted gene cluster of L-ZS9 responsible for the biosynthesis of Plantaricins by using the BAGEL4 webserver

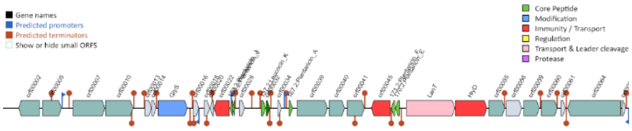

**Figure 5.** The predicted gene cluster of AS-7 responsible for the biosynthesis of Plantaricins by using the BAGEL4 webserver

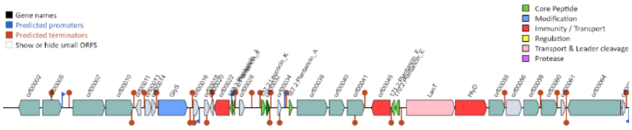

**Figure 6.** The predicted gene cluster of DSM 10667 responsible for the biosynthesis of Plantaricins and Leucocin K by using the BAGEL4 webserver

### 3.1.5. Prophages

In *L. paraplantarum* DSM10667, six prophage regions were predicted. Four of those were complete, one of which was incomplete and questionable (Figure 2). The sizes of the regions were 48.3 Kb, 24.9 Kb, 41.9 Kb, 59.2 Kb, 15 Kb, and 8.1 Kb. One of these phages could be Lactob_Sha1, which is commonly present in various microorganisms [34]. *L. paraplantarum* L-ZS9 contains one intact and one questionable region with a size of 15.9 Kb and 39.6 Kb, respectively. Hovewer, *L. paraplantarum* AS-7 harbors only one intact prophage region at a size of 50.9 Kb. Other prophages predicted were Lactob_KC5a, Lactoc_bIL309, Oenoco_phiS1, Paenib_Tripp, Strept_315.2, and Oenoco_phiS13. This perhaps indicates the plasticity of all three strains, of which DSM 10667 ranks the highest. The high plasticity of the DSM 10667 genome could be due to the liquid matrices of the beer system from which this strain was isolated. We speculate that both L-ZS9 and AS-7 isolation sources were closer to solid matrices, which perhaps reduces the infectivity of the (pro)phages to resident organisms in that environment. We'd anticipate a different trend of phage infectivity between dairy and meat starter cultures, where dairy cultures are more prone to phage attacks and perhaps prophage attachments due to the liquid structure of milk, whereas meat matrices provide protection to bacterial strains.

OrthoANI (Orthologous Average Nucleotide Identity) represents the similarity ratios of orthologous regions between multiple genomes. According to OrthaANI results, the most closely related strains are *L. paraplantarum* AS-7 and DSM 10667, with a similarity percentage of 99.749% achieved. This close similarity could perhaps be linked to the origin of those strains, which is a plant-based environment. L-ZS9 was segregated from the other two strains based on a remarkably lower similarity rate of 97.49% and 97.86% against AS-7 and DSM 10667, respectively. In a parallel manner, synteny plots achieved across three strains revealed that DSM 10667 and AS-7 have better synteny compared to DSM 10667 vs. L-ZS9 or AS-7 vs. L-ZS9. (Supplementary Figures 1, 2, and 3).

**Table 3.** The predicted prophage regions of *Lactiplantibacillus paraplantarum* strains

| Strain name | Region Length | Region Position | Completeness | Most Common Phage | Total Protein | G-C % Content |
|---|---|---|---|---|---|---|
| DSM 10667 | 48.3Kb | 966930-1015283 | Intact | Lactob_Sha1 | 64 | 41.22% |
| | 24.9Kb | 1773553-1798540 | Intact | Lactob_KC5a | 31 | 43.89% |
| | 41.9Kb | 1801471-1843386 | Intact | Lactob_KC5a | 54 | 42.15% |
| | 59.2Kb | 2119916-2179148 | Intact | Oenoco_phiS1 | 69 | 41.45% |
| | 8.1Kb | 2315784-2323924 | Questionable | Paenib_Tripp_ | 8 | 41.09% |
| | 15Kb | 1840319-1855322 | Incomplete | Lactoc_bIL30 | 23 | 39.97% |
| AS-7 | 50.9Kb | 530636-581617 | Intact | Oenoco_phiS13 | 57 | 41.68% |
| L-ZS9 | 39.6Kb | 2210312-2250005 | Intact | Oenoco_phiS13 | 48 | 41.90% |
| | 15.9Kb | 36418-52364 | Questionable | Strept_315.2 | 21 | 41.83% |

**Table 4**. OrthoANI percentage of *Lactiplantibacillus paraplantarum* DSM 10667, L-ZS9 and AS-7.

| Genome 1 Name | Genome 2 Name | ANI 1->2 | ANI2->1 | AF1->2 | AF2->1 |
|---|---|---|---|---|---|
| AS-7 | L-ZS9 | 97.4951 | 97.4954 | 90.053 | 86.975 |
| DSM 10667 | L-ZS9 | 97.8628 | 97.8615 | 79.231 | 85.603 |
| AS-7 | DSM 10667 | 99.749 | 99.7495 | 95.219 | 85.229 |

The CRISPRviz and CRISPRcas finder results did not identify any confirmed CRISPR or cas regions. However, all three strains are predicted to carry three questionable CRISPR genes.

## 3.2. Carbohydrate Metabolism

### 3.2.1. Glycolysis Pathway

The extracellular D-Glucose molecule has been transported into the cytoplasm through the phosphotransferase system, and this glucose is phosphorylated to D-Glucose 6-phosphate in only DSM 10667, which is further converted to Fructose 6-phosphate by glucose-6-phosphate isomerase [EC 5.3.1.9], Fructose 1,6-phosphate by phosphohexokinase [EC 2.7.1.11], Glyceraldehyde 3-phosphate by fructose-bisphosphate aldolase [EC 4.1.2.13], and Glycerone-phosphate by triose-phosphate isomerase [EC 5.3.1.1] in all three strains. The glyceraldehyde-3 phosphate is converted to Pyruvate, Acetyl CoA, and Lactate. The latter is also being utilized in propanoate metabolism. Arbutin and Salicin sugars are also being imported into the cell through specific PTS [EC2.7.1.69] by which can either feed into glycolysis or the pentose phosphate pathway. However, sausage isolate L-ZS9 and plant isolate AS-7 strains did not carry the [E.C. 2.7.1.69] enzyme, thus extracellular arbutin and salicin cannot be imported as arbutin-6P and salicin-6P into the cytoplasm. We speculate that, most likely, these sugars are being utilized through the EMP pathway (Figures S8, S9, and S10).

### 3.2.2. Pentose Phosphate Pathway

Five carbon sugars, such as D-Ribose, have been utilized by the pentose phosphate pathway for DSM 10667, part of its heterofermentative utilization of pentoses. Unlike other sugars discussed above, D-Ribose has been phosphorylated by the ribokinase [E.C. 2.7.1.15] enzyme to form D-Ribose 5-P, which can go to purine, pyrimidine, or histidine metabolism by ribose-phosphate diphosphokinase [EC 2.7.6.1], Ribose-5P by spermine oxidase [EC 1.5.3.16], or D-Glycrealdehyde3-P by nicotinamide N-methyltransferase [EC 2.1.1.1], which is later converted to lactate. L-ZS9 is the only strain that has the transaldolase enzyme; therefore, it can convert D-glyceraldehyde-3-phosphate to beta-D-fructose 6-phosphate (Figures S11, S12, and S13).

### 3.2.3. Putative Sugar Utilizations

In galactose metabolism, there are slight differences between the 3 strains. For example, *L. paraplantarum* AS-7 and L-ZS9 are predicted to convert Galactitol-1P to D-Tagatose-6P by the Galactitol-1-phosphate 5-dehydrogenase enzyme. Although *L. paraplantarum* DSM10667 cannot produce D-Tagatose-6P, all 3 strains can synthesize D-Tagatose-6P from D-Tagatose 1,6 P2 by removing one phosphate group and producing 1 mol ATP molecule. They can also produce raffinose from stachyose oligosaccharides, as shown in Figures S14, S15, and S16 in supplementary.

Genome analysis of *L. paraplantarum* revealed that only DSM10667 could ferment rhamnose sugar, while L-ZS9 and AS-7 cannot. Different from the other two strains, the DSM 10667 strain can make the conversion between L-rhamnose and L-rhamnulose sugars with the help of L-rhamnose isomerase. Only DSM 10667 produces sorbitol and sorbose pathways in fructose metabolism (Figures S17, S18, and S19).

*L. paraplantarum* DSM 10667 could be converted from extracellular maltose to Maltose-6P by N-phosphohistidine-D-mannose phosphotransferase. Also, it could perform the conversion of isomaltose to D-Glucose to maltose by oligo-1,6-glucosidase. When sucrose is present in fermentation, DSM 10667 could convert sucrose into dextran and fructose by dextransucrase [EC 2.4.1.5]. Dextran is an exopolysaccharide with a chemical structure of complex branched glucan with dextran chains of varying lengths from 3-2000 kDA [35]. The beer contaminant DSM 10667 strain has genes encoding the dextran-sucrase enzyme, which might cause a slimy structure in beer, which is called a structural defect and could be one of the reasons why this strain is being considered a beer contaminant. Therefore, DSM 10667, an unwanted adventitious lactic acid bacterium, could potentially cause quality defects and economic losses to beer processors (Figures S20, S21, and S22).

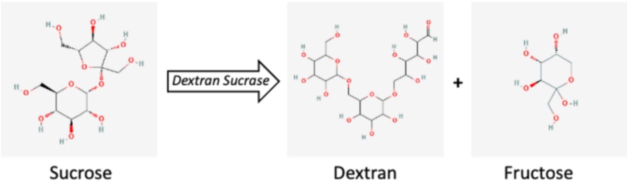

**Figure 7**. Activity of dextran-sucrase enzyme which can convert sucrose to dextran and fructose.

### 3.3. Nitrogen Metabolism

The putative nitrogen metabolism pathway indicated that L-Glutamine and L-Glutamate amino acids can be biosynthesized from ammonia in all three strains. They are also capable of converting L-Aspartate via aspartate ammonia-lyase [EC 4.3.1.1] or L-Asparagine via aspartate ammonia-ligase [EC 6.3.1.1]. The ammonia formation from aspartate can be a stress mechanism for combating the acidic condition of the cytoplasm to maintain a relatively neutral pH value within the cell matrix. Moreover, only L-ZS9 can convert nitrate to nitrite by the nitrate reductase [EC 1.7.99.4] enzyme, which is one of the technological attributes that is highly desirable in meat starter cultures (Figures S28, S29, and S30).

### 3.3.1. Histidine and Arginine

The putative histidine metabolism of all three strains predicted that L-Histidine can be biosynthesized from PRPP after a series of conversions. Since no histidine decarboxylase enzyme-encoding gene was found in the genome of strains, L-Histidine cannot be converted to the histamine molecule, which is detrimental to health. However, it was interesting to note that histamine can be converted to 4-Imidazole only by DSM 10667 (Figures S32, S33, and S34).

*L. paraplantarum* L-ZS9 has quite different in arginine metabolisms compared to the other two strains. For instance, DSM 10667 and AS-7 cannot complete the urea cycle due to the absence of arginase, while *L. paraplantarum* L-ZS9 could convert arginine to urea, also known as arginine decarboxylation, which further increases the pH, a potential acid stress response mechanism for bacteria, by neutralizing the cytoplasm. Interestingly, only DSM 10667 has the capability to produce p-coumaroyl putrescine and feruloyl putrescine in arginine metabolism.

## 3.4. Pyruvate Metabolism

Pyruvate is an intermediate molecule that is formed upon the cleavage of sugars through glycolysis or the pentose phosphate pathway. DSM 10667 can convert pyruvate to L-lactate by L-lactate dehydrogenase [EC 1.1.1.27] and D-Lactate by D-lactate dehydrogenase [EC 1.1.1.28]. The L-ZS9 strain also has these enzymes and can convert pyruvate to lactate molecules. All three strains can also convert pyruvate to Oxaloacetate by Pyruvate carboxylase [EC 6.4.1.1] or L-Malate by malate dehydrogenase [EC 1.1.1.40], Formate by formate C-acetyltransferase [EC 2.3.1.54], Acetyl Co-A, Acetaldehyde by acetaldehyde dehydrogenase [EC 1.2.1.10], and Acetyl phosphate by pyruvate oxidase [EC 1.2.3.3]. It is interesting to note that there is interconversion in DSM 10667 and AS-7 strains between D-Lactaldehyde and methylglyoxal glyoxylate reductase [EC 1.1.1.79], which is a brown color agent in fermented foods that is not a desirable attribute in most dairy products. Unlike DSM 10667, L-ZS9 does not convert methylglyoxal to D-Lactaldehyde. For example, methylglyoxal formation in cheese is causing a serious economic loss for dairy products in the USA. In a similar manner, the occurrence of these metabolites in beer can also be detrimental to the appearance of the product and might reduce its quality. There is another interconversion between acetyl Co-A intermediate and acetaldehyde by acetaldehyde dehydrogenase [EC 1.2.1.10], resulting in an aroma compound in some of the fermented dairy products, and this conversion also occurred in the L-ZS9 strain [EC1.2.1.10]. Another avenue from pyruvate is the conversion of Acetyl Co-A to Malonyl Co-A by acetyl-CoA carboxylase [EC 6.4.1.2], which is predicted to be a precursor for fatty acid biosynthesis (Figures S22, S23, and S24). *L. paraplantarum* DSM10667 can be distinguished from L-ZS9 and AS-7 by citric acid metabolism. DSM10667 can synthesize malate from oxaloacetate by the malate dehydrogenase enzyme and the conversion of 1 mol $NADH_2$ to NAD, then fumarate by the fumarate hydratase enzyme, and finally succinate by the succinate dehydrogenase enzyme, unlike L-ZS9 and AS-7 strains. During succinate production, $NADH_2$ turns into NAD molecules. L-ZS9 and AS-7 cannot produce succinate because of the absence of the succinate dehydrogenase enzyme, as shown in Figures S23, S24, and S25.

# 4. Conclusion

We performed a comparative genome analysis of three *L. paraplantarum* strains that were isolated from diverse ecosystems such as beer, sausage, fruit, and vegetables. The total genome sizes achieved were DSM 10667>L-ZS9>AS-7. Phylogenetic analysis based on whole-genome sequence and average nucleotide identity revealed that DSM 10667 and AS-7 were closely related, whereas L-ZS9 differed from both strains. This perhaps relates to the fact that the origins of strains DSM 10667 and AS-7 were relatively similar (i.e., plant-related material) compared to L-ZS9, which has a quite different origin (i.e., fermented sausage). These differences based on the origin of isolation are also evident in the unique genes found in each genome. For example, DSM 10667 harbors 438 unique genes, L-ZS9 harbors 248 unique genes, and AS-7 harbors 35 unique genes. Arginine, which is an abundant amino acid in sausage composition, can be converted to urea only by L-ZS9. Neither of the other two strains has that capability, perhaps because plant materials are not reliable sources of arginine. Another example is the dextran biosynthesis potential of DSM 10667, which has already been identified as an undesirable strain in beer manufacturing technology. These findings provide a better understanding of the genomic characteristics of *L. paraplantarum* strains for commercial and scientific interest.

## Acknowledgment

The authors would like to thank Mr. Ismail Gumustop for valuable support in manuscript formatting.

## Funding

There is no funding for this project.

## Conflict of Interest

The authors declare no competing interest.

## Author Contribution Statement

Conceptualization: FO
Method: FO, RB
Manuscript writing reviewing editing: FO, RB
Supervision: FO

## References

[1]. H. Nishioka, T. Ohno, H. Iwahashi, and M. Horie, "Diversity of Lactic Acid Bacteria Involved in the Fermentation of Awa-bancha," *Microbes Environ*, vol. 36, 2021. [Online]. Available: https://doi.org/10.1264/jsme2.ME21029.

[2]. J. Zheng, S. Wittouck, E. Salvetti, et al., "A taxonomic note on the genus Lactobacillus: Description of 23 novel genera, emended description of the genus Lactobacillus Beijerinck 1901, and union of Lactobacillaceae and Leuconostocaceae," *Int. J. Syst. Evol. Microbiol*., vol. 70, 2020. [Online]. Available: https://doi.org/10.1099/ijsem.0.004107.

[3]. Reale, T. Zotta, R. G. Ianniello, et al., "Selection criteria of lactic acid bacteria to be used as starter for sweet and salty leavened baked products," *LWT*, vol. 133, p. 110092, 2020. [Online]. Available: https://doi.org/10.1016/j.lwt.2020.110092.

[4]. S. Akbulut, M. O. Baltaci, G. Adiguzel, and A. Adiguzel, "Identification and biotechnological characterization of Lactic Acid Bacteria Isolated from White Cheese Samples," Research Square, 2021.

[5]. S. Nishida, M. Ishii, Y. Nishiyama, et al., "Lactobacillus paraplantarum 11-1 Isolated from Rice Bran Pickles Activated Innate Immunity and Improved Survival in a Silkworm Bacterial Infection Model," *Front. Microbiol*., vol. 8, 2017.

[6]. W. J. Park, K. H. Lee, J. M. Lee, et al., "Characterization of pC7 from Lactobacillus paraplantarum C7 derived from Kimchi and development of lactic acid bacteria--Escherichia coli shuttle vector," *Plasmid*, vol. 52, pp. 84–88, 2004. [Online]. Available: https://doi.org/10.1016/j.plasmid.2004.05.001.

[7]. W. E. Hussein, E. Huang, I. Ozturk, and A. E. Yousef, "Draft Genome Sequence of Lactobacillus paraplantarum OSY-TC318, a Producer of the Novel Lantibiotic Paraplantaracin TC318," *Microbiol. Resour. Announc*., vol. 8, p. e00274-19, 2019. [Online]. Available: https://doi.org/10.1128/MRA.00274-19.

[8]. K. Sharma, N. Sharma, S. Handa, and S. Pathania, "Purification and characterization of novel exopolysaccharides produced from Lactobacillus paraplantarum KM1 isolated from human milk and its cytotoxicity," *J. Genet. Eng. Biotechnol*., vol. 18, p. 56, 2020. [Online]. Available: https://doi.org/10.1186/s43141-020-00063-5.

[9]. S. M. Devi, N. K. Kurrey, and P. M. Halami, "In vitro anti-inflammatory activity among probiotic Lactobacillus species isolated from fermented foods," *J. Funct. Foods*, vol. 47, pp. 19–27, 2018. [Online]. Available: https://doi.org/10.1016/j.jff.2018.05.036.

[10]. R. J. da Costa, F. L. S. Voloski, R. G. Mondadori, et al., "Preservation of Meat Products with Bacteriocins Produced by Lactic Acid Bacteria Isolated from Meat," *J. Food Qual*., vol. 2019, p. e4726510, 2019. [Online]. Available: https://doi.org/10.1155/2019/4726510.

[11]. L. Liu and P. Li, "Complete genome sequence of Lactobacillus paraplantarum L-ZS9, a probiotic starter producing class II bacteriocins," *J. Biotechnol*., vol. 222, pp. 15–16, 2016. [Online]. Available: https://doi.org/10.1016/j.jbiotec.2016.02.003.

[12]. "IMG," [Online]. Available: https://img.jgi.doe.gov/cgi-bin/m/main.cgi?section=TaxonDetail&page=taxonDetail&taxon_oid=2922794270. Accessed: Sep. 4, 2023.

[13]. L. C. Reimer, A. Vetcininova, J. S. Carbasse, et al., "Bac Dive in 2019: bacterial phenotypic data for High-throughput biodiversity analysis," *Nucleic Acids Res.*, vol. 47, pp. D631–D636, 2019. [Online]. Available: https://doi.org/10.1093/nar/gky879.

[14]. H. Nordberg, M. Cantor, S. Dusheyko, et al., "The genome portal of the Department of Energy Joint Genome Institute: 2014 updates," *Nucleic Acids Res.*, vol. 42, pp. D26-31, 2014. [Online]. Available: https://doi.org/10.1093/nar/gkt1069.

[15]. J.-Y. Chun, W.-J. Jeong, J.-S. Kim, et al., "Hydrolysis of Isoflavone Glucosides in Soymilk Fermented with Single or Mixed Cultures of Lactobacillus paraplantarum KM, Weissella sp. 33, and Enterococcus faecium 35 Isolated from Humans," *J. Microbiol. Biotechnol.*, vol. 18, pp. 573–578, 2008.

[16]. R. Kant, J. Blom, A. Palva, et al., "Comparative genomics of Lactobacillus," *Microb. Biotechnol.*, vol. 4, pp. 323–332, 2011. [Online]. Available: https://doi.org/10.1111/j.1751-7915.2010.00215.

[17]. M. Schmid, J. Muri, D. Melidis, et al., "Comparative Genomics of Completely Sequenced Lactobacillus helveticus Genomes Provides Insights into Strain-Specific Genes and Resolves Metagenomics Data Down to the Strain Level," *Front. Microbiol.*, vol. 9, p. 63, 2018. [Online]. Available: https://doi.org/10.3389/fmicb.2018.00063.

[18]. S. Wuyts, C. N. Allonsius, S. Wittouck, et al., "Comparative genome analysis of Lactobacillus mudanjiangensis, an understudied member of the Lactobacillus plantarum group," *Microb. Genomics*, vol. 5, p. e000286, 2019. [Online]. Available: https://doi.org/10.1099/mgen.0.000286.

[19]. M. C. Curk, J. C. Hubert, and F. Bringel, "Lactobacillus paraplantarum sp. nov., a new species related to Lactobacillus plantarum," *Int. J. Syst. Bacteriol.*, vol. 46, pp. 595–598, 1996. [Online]. Available: https://doi.org/10.1099/00207713-46-2-595.

[20]. S. Mukherjee, D. Stamatis, J. Bertsch, et al., "Genomes OnLine Database (GOLD) v.8: overview and updates," *Nucleic Acids Res.*, vol. 49, pp. D723–D733, 2021. [Online]. Available: https://doi.org/10.1093/nar/gkaa983.

[21]. N.-F. Alikhan, N. Petty, N. Ben Zakour, and S. Beatson, "BLAST Ring Image Generator (BRIG): simple prokaryote genome comparisons," *BMC Genomics*, vol. 12, p. 402, 2011. [Online]. Available: https://doi.org/10.1186/1471-2164-12-402.

[22]. Z. Zhang, S. Schwartz, L. Wagner, and W. Miller, "A greedy algorithm for aligning DNA sequences," *J. Comput. Biol. J. Comput. Mol. Cell Biol.*, vol. 7, pp. 203–214, 2000. [Online]. Available: https://doi.org/10.1089/10665270050081478.

[23]. R. Wattam, D. Abraham, O. Dalay, et al., "PATRIC, the bacterial bioinformatics database and analysis resource," *Nucleic Acids Res.*, vol. 42, pp. D581–D591, 2014.

[24]. de Jong, S. A. F. T. van Hijum, J. J. E. Bijlsma, et al., "BAGEL: a web-based bacteriocin genome mining tool," *Nucleic Acids Res.*, vol. 34, pp. W273–W279, 2006. [Online]. Available: https://doi.org/10.1093/nar/gkl237.

[25]. J. Zhang and T. L. Madden, "PowerBLAST: a new network BLAST application for interactive or automated sequence analysis and annotation," *Genome Res.*, vol. 7, pp. 649–656, 1997. [Online]. Available: https://doi.org/10.1101/gr.7.6.649.

[26]. D. Arndt, J. R. Grant, A. Marcu, et al., "PHASTER: a better, faster version of the PHAST phage search tool," *Nucleic Acids Res.*, vol. 44, pp. W16-21, 2016. [Online]. Available: https://doi.org/10.1093/nar/gkw387.

[27]. G. Marçais, A. L. Delcher, A. M. Phillippy, et al., "MUMmer4: A fast and versatile genome alignment system," *PLOS Comput. Biol.*, vol. 14, p. e1005944, 2018. [Online]. Available: https://doi.org/10.1371/journal.pcbi.1005944.

[28]. I.-M. A. Chen, K. Chu, K. Palaniappan, et al., "The IMG/M data management and analysis system v.6.0: new tools and advanced capabilities," *Nucleic Acids Res.*, vol. 49, pp. D751–D763, 2021. [Online]. Available: https://doi.org/10.1093/nar/gkaa939.

[29]. D. Couvin, A. Bernheim, C. Toffano-Nioche, et al., "CRISPRCasFinder, an update of CRISRFinder, includes a portable version, enhanced performance and integrates search for Cas proteins," N*ucleic Acids Res.*, vol. 46, pp. W246–W251, 2018. [Online]. Available: https://doi.org/10.1093/nar/gky425.

[30]. H. Zhang, T. Yohe, L. Huang, et al., "dbCAN2: a meta server for automated carbohydrate-active enzyme annotation," *Nucleic Acids Res.*, vol. 46, pp. W95–W101, 2018. [Online]. Available: https://doi.org/10.1093/nar/gky418.

[31]. S. Mukherjee, R. Seshadri, N. J. Varghese, et al., "1,003 reference genomes of bacterial and archaeal isolates expand coverage of the tree of life," *Nat. Biotechnol.*, vol. 35, pp. 676–683, 2017. [Online]. Available: https://doi.org/10.1038/nbt.3886.

[32]. W. E. Hussein, E. Huang, I. Ozturk, et al., "Genome-Guided Mass Spectrometry Expedited the Discovery of Paraplantaricin TC318, a Lantibiotic Produced by Lactobacillus paraplantarum Strain Isolated From Cheese," *Front. Microbiol.*, vol. 11, p. 1381, 2020. [Online]. Available: https://doi.org/10.3389/fmicb.2020.01381.

[33]. S.-C. Yang, C.-H. Lin, C. T. Sung, and J.-Y. Fang, "Antibacterial activities of bacteriocins: application in foods and pharmaceuticals," *Front. Microbiol.*, vol. 5, 2014.

[34]. E. Evanovich, P. J. de Souza Mendonça Mattos, and J. F. Guerreiro, "Comparative Genomic Analysis of Lactobacillus plantarum: An Overview," *Int. J. Genomics*, vol. 2019, p. e4973214, 2019. [Online].

[35]. Al-Farga A, Abed S. Production of dextrans and their applications in human health and nutrition–Review. Eur Acad Res 29. (2016)

[36]. “Type Strain Genome Server,” *Dsmz.de*, 2019. https://tygs.dsmz.de/ (accessed Aug. 07, 2023).

**Bitlis Eren Üniversitesi Fen Bilimleri Dergisi**
BİTLİS EREN UNIVERSITY JOURNAL OF SCIENCE
ISSN: 2147-3129/e-ISSN: 2147-3188
VOLUME: 13 NO: 2 PAGE: 376-383 YEAR: 2024
DOI:10.17798/bitlisfen.1276212

# Lambda Scan for T- Channel Fermion Dark Matter

Emine GÜRPINAR GÜLER[1*]

*[1]Konya Technical University, Faculty of Engineering and Natural Sciences, Department of Engineering Basic Sciences, Konya, Turkey*
*(ORCID: 0000-0002-6172-0285)*

**Keywords:** Simplified Models, Large Hadron Collider, Dark Matter, Coupling Constant, t-channel Fermion Portal.

**Abstract**

The development of collider machines revealed a lot about matter in particle physics. The Large Hadron Collider (LHC) at CERN has made a great contribution to this field. Theorists proposed new models while comparing the LHC experimental data with the Standard Model (SM). Various parameters of many phenomenological studies have been tested for high-energy collisions. In this study, a simplified dark matter model, namely the t-channel Fermion Portal model, was examined with the lambda parameter scan at 14 TeV. Signal generation was performed using the Madgraph5 generator to scan the mediator and dark matter mass. The impact of the change in the lambda constant on the dark matter production mechanism of the model was investigated.

## 1. Introduction

One of the most exciting areas of particle physics is the study of dark matter. The link between dark matter (DM) and the Standard Model (SM) is the subject of the most investigations. Numerous cosmological and astrophysical observations provide strong support for the idea that dark matter exists. These are gravitational interactions. According to current measurements, the majority of dark matter acts like non-relativistic particles during structure development; they are commonly referred to as cold dark matter. These particles are stable throughout cosmic time scales, have no electrical charge, and are colorless. It should be noted, however, that certain models allow for the presence of hot, dark matter made up of relativistic particles. Today, dark matter makes up about 80% of the total density of matter in the universe. DM is investigated in three classes of search: (i) direct detection, which detects interactions of DM particles in terrestrial detectors [1-4], (ii) indirect detection, which detects DM-DM interactions in the cosmos, that is, DM-DM interactions at the center of the galaxy [4-8], and (iii) colliders, which produce DM and DM mediators in the Lab. The LHC at CERN is a distinguishedly proper machine to look for DM particles. Those found through direct and indirect searches are supplemented by the most current constraints that were obtained from the CMS and ATLAS experiments conducted at the LHC. [9].

At a hadron collider, the signature of DM generation is an overabundance of events in which a single final-state particle X recoils against huge quantities of missing transverse momentum or energy (MET). Different "mono-X" signatures, where "X" might represent hadron or gauge boson jets, the Higgs boson, top or bottom quarks in the final state, etc., have been studied by the ATLAS and CMS teams at the LHC.

DM analysis is interpreted with various models that have been discussed at the LHC Dark Matter Working Group (LHC DM WG), which brings together theorists and experimentalists to define guidelines and recommendations for the benchmark models, interpretation, and characterization necessary for broad and systematic searches for dark matter at the LHC. One possible line that could shed light on this discussion is the use of simplified models [10]. Assuming a particle genesis for DM, it could be possible for it to interact with SM processes and common matter. The DM is

---

[*] Corresponding author: egguler@ktun.edu.tr

*Received: 06.04.2023, Accepted: 21.03.2024*

treated as a massive particle in simplified models, and its interactions with the SM are mediated by a particle called the mediator. The mediator is a color singlet that links to two particles of dark matter, or a standard model in the so-called s-channel model [11]. In contrast, the so-called t-channel simplified model postulates that the mediator only interacts with a single SM state and dark matter [12].

Here, we take a simplified version of the t-channel model into account, one in which dark matter fermions play a role. [13-15]. A detailed discussion of this model and its relevance for the monojet phase space can be found in Ref. [13]. This model was interpreted in monojet analysis with data collected between 2016 and 2018 in proton-proton collisions at 13 TeV in the CMS experiment and corresponds to an integrated luminosity of 35.9 [17] and 137 $\text{fb}^{-1}$ [18], respectively. In the case of the fermion portal model, the findings of the analysis were presented in the form of exclusion limits at a confidence level of 95% in the plane of the DM candidate mass $M_\chi$ and the mediator mass $M_\phi$. It is assumed that the value of the coupling between the mediator, the right-handed up quark, and the DM candidate will remain unchanged and will be equal to $\lambda_u = 1$, and this is the default setting. In this study, we will show the result of the fermion portal model for 14 TeV at the parton level. First of all, we will determine the relationship between the lambda and the mediator, DM mass. Then we will show the signal cross-section expected for different signal hypotheses in the $M_\chi - M_\phi$ plane.

The following outline constitutes the structure of the current paper. In the next part, we will provide a concise definition of the framework for t-channel DM models, and then in the following section, the signal generation of our study will be discussed. In the fourth part, we present the findings and conclude.

## 2. T- channel Fermion Dark Matter Model

As stated in the previous section, the fermion portal DM model was compared with the proton-proton collision data obtained in the CMS experiment, and its limits were determined. For this reason, it is the most well-known of the t-channel models. Within the confines of this DM model [13], an SM singlet DM particle is responsible for mediating the interaction between quarks and the DM through a novel QCD color triplet state. As for the Lorentz properties of the DM model, there are several classifications of such models. One of these is the Dirac fermion. Others are sorted as complex scalars, real scalars, Majorana fermions, or vectors. In this paper, our primary emphasis is placed on the scenario in which the DM is a spin-1/2 particle considered a Dirac fermion. Depending on the kind of quarks that the dark matter couples to, one may specify the dark matter in a variety of different ways. We assumed that Dirac fermion DM couples universally to righthanded quarks via a color-triplet scalar mediator. The mediator primarily couples with gluons because of its SU(3) color representation. The Lagrangian that describes the coupling of a color-triplet scalar to quarks is given as follows:

$$\mathcal{L}_\chi = \lambda_{u_i}\phi_{u_i}\bar{\chi}_L u_R^i + \lambda_{d_i}\phi_{d_i}\bar{\chi}_L d_R^i + \text{h.c.} \qquad (1)$$

where $u_i$ = u, c, t ( $d_i$= d, s, b) are different SM quarks, where $\phi$ is the DM mediator, where $\chi$ is the DM candidate, and where $\lambda$ is coupling. The mediator's coupling with gluons can be represented by an effective Lagrangian term:

$$\mathcal{L}_{gluon} = \frac{\alpha_s}{\Lambda}\phi^\dagger T^a \phi G^a_{\mu\nu}\tilde{G}^{a\mu\nu} \qquad (2)$$

where $\phi$ is the DM mediator, $T^a$ are the Gell-Mann matrices, $G^a_{\mu\nu}$ is the gluon field strength tensor, $\alpha_s$ is the strong coupling constant, $\tilde{G}^{a\mu\nu}$ is the dual of the gluon field strength tensor and $\Lambda$ is a cutoff scale.

For this analysis, we will presume that the branching ratio of the decay $\phi_{u_i} \to \chi^{\bar{u}^i}$ is equal to 100 percent. The steps of the model's formation and degradation are depicted in Figure 1. For this investigation, we will only focus on the u quark; hence, our investigation of the three production methods in this study in the context of coupling to up quarks is depicted in Figure 1.

The generation of scalar mediator pairs is a task that is of the utmost significance to Hadron colliders. These scalar mediators eventually decay into Dark Matter (DM) particles and quarks as a result of their breakdown. As seen in Figure 1, this unique decay pattern has the potential to be a distinguishable experimental signature of FP DM models (a). The process for diagram (a) is denoted by the notation $pp \to \phi\ \phi \to \chi j\ \chi j$, and as a result, this phenomenon can be specifically defined by something that is referred to as the Two-phi mediator state. It is important to note that the final state of diagram (a) comprises two jets, which provides a unique signature. In addition to that, there is an additional fascinating process for the manufacturing of the substance. Co-production between the DM candidate and the scalar mediator is possible, but only under certain circumstances. This mode of production leads to what is known as the One-phi mediator state, and the corresponding processes for Figure b are $pp \to \phi \to \chi\chi j$. This state has a mono-jet-like signature, as can be seen in diagram (b), which is one of the characteristics that sets it apart from diagrams (a) and (b).

The creation of paired DM candidates represents yet another potential route that could be taken with the production. This generation is accomplished by the utilization of a t-channel exchange that incorporates the scalar mediator. It is not an easy task to implement this strategy with colliders. It is essential that parton radiation take place immediately from the ISR state, which is an abbreviation for the beginning state. Figure 1 illustrates this significant part of the manufacturing mechanism that is essential to its operation (c). The process that corresponds to Figure (c) is denoted by $pp \to \chi\chi j$. Because of the unique qualities that it possesses, this particular condition has been given the moniker of the mediator state of no-phi. This is an interesting fact. A mono-jet-like signature can also be seen in diagram (c), which is the same as diagram (b).

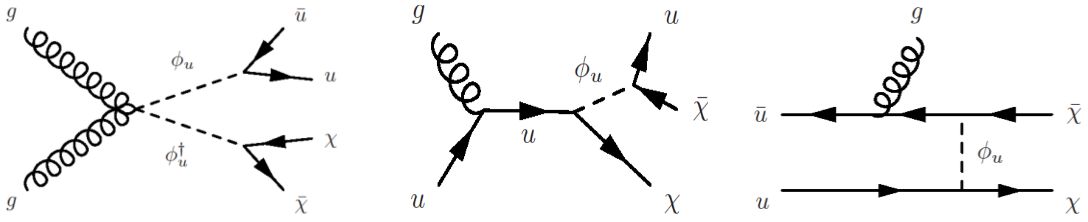

a) b) c)

**Figure 1.** Feynman diagrams describe the creation procedures of Dirac fermions by DM particles in the FP model when they are produced at the LHC in combination with a single quark or gluon. The ultimate state of the diagram represented by (a) contains two jets. The process for diagram (a) is pp → ϕ ϕ → χj χj. The diagrams represented by (b) and (c) only have one jet each. The processes for diagram (b) and (c) are pp → ϕ → χχj and pp → χχj respectively [13]

## 3. Signal Sample Production

In this paper, we show the result of the FP Dirac DM model at the parton level. The FP signal is generated using the MadGraph5 generator [16] at 14 TeV. For each mass point were generated 10k events. For the sample generations, the couplings of the mediator with the SM and the DM particle have been considered for u quarks. In this model, a set of distinct parameters can be scanned to search for dark matter:

- Dark matter mass ($M_\chi$)
- Mediator masses ($M_\phi$)
- Coupling to SM particles ($\lambda_u$)

Benchmarks points are a set of ($M_\chi$, $M_\phi$) combinations with different couplings $\lambda_u$. The benchmarks consist of representative points to cover the most interesting kinematic features in phase space. To determine the cross sections for the model, the event rates for the collider production of the quark partners were calculated at parton level at leading order using MadGraph5 v2.6.6.

The MadGraph files were generated using Fermion portal model FeynRules. Figure 2 shows signal cross-section expressed in pb, in the $M_\phi$ - $M_\chi$ plane for $\lambda_u$ =0.5, 1, and 2 a, b, and c, respectively, incorporating all processes seen in Fig. 1.( $pp \to \phi\, \phi \to \chi j\, \chi j$, $pp \to \phi \to \chi\chi j$ and $pp \to \chi\chi j$). It is clear seen that as the lambda increases, the cross section increases in the $M_\phi$ - $M_\chi$ plane.

For the Dirac case, the decay width of the $\phi_u$ particle is determined as follows using the up quark operator [13].

$$\Gamma(\phi \to \chi + \bar{u}) = \frac{\lambda_u^2}{16\pi} \frac{(M_\phi^2 - M_\chi^2)^2}{(M_\phi^3)} \tag{3}$$

Figure 3 depicts the overall width in GeV as a function of $M_\phi$ and $M_\chi$ for coupling strength parameters $\lambda_u$ 0.5, 1, and 2, respectively, incorporating all processes shown in Fig. 1.( $pp \to \phi\, \phi \to \chi j\, \chi j$, $pp \to \phi \to \chi\chi j$ and $pp \to \chi\chi j$). As can be seen clearly in equation 1, as the lambda increases, the width will increase proportionally to the square of the lambda.

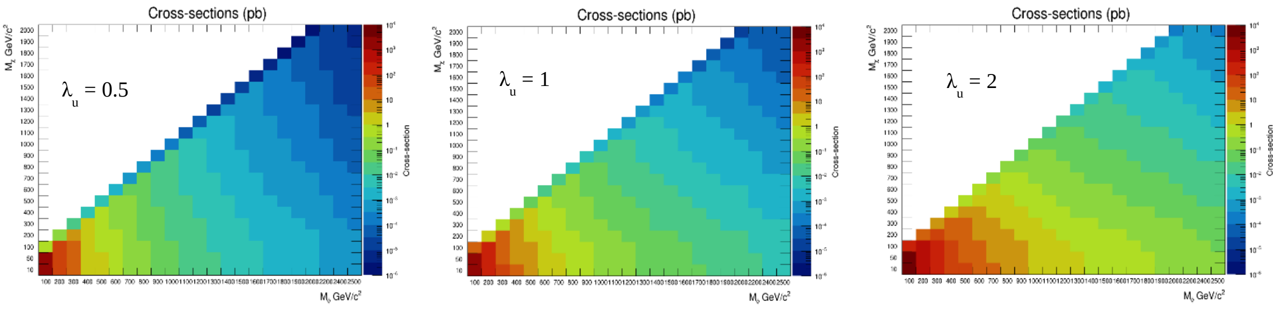

a) b) c)

**Figure 2**. Signal cross-section expressed in pb, expected different signal hypothesis in the $M_\phi$ - $M_\chi$ plane including all processes in Fig. 1.( $pp \rightarrow \phi\ \phi \rightarrow \chi j\ \chi j, pp \rightarrow \phi \rightarrow \chi\chi j$ *and* $pp \rightarrow \chi\chi j$) for $\lambda_u$ =0.5, 1 and 2 a, b and c respectively

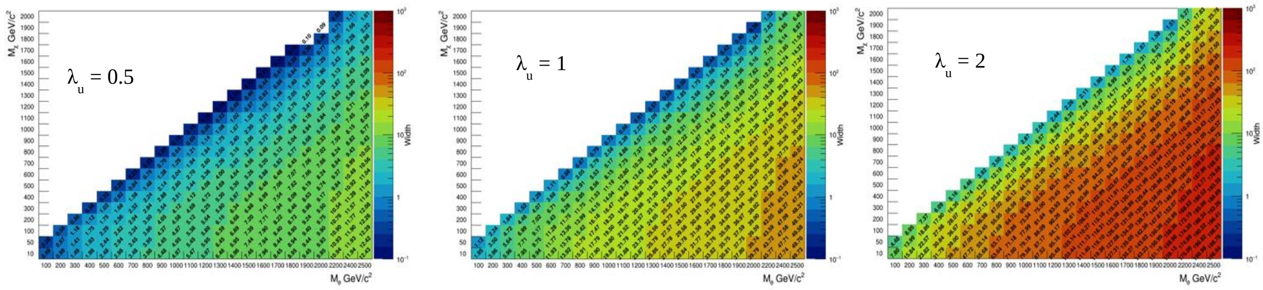

a) b) c)

**Figure 3**. Total mediator width ($\phi$) measured in GeV as a function of $M_\phi$ and $M_\chi$ including all processes in Fig. 1.( $pp \rightarrow \phi\ \phi \rightarrow \chi j\ \chi j, pp \rightarrow \phi \rightarrow \chi\chi j$ and $pp \rightarrow \chi\chi j$) for a) $\lambda_u$=0.5, b) $\lambda_u$=1 and c) $\lambda_u$=2

The cross section for production is identical to that of a single squark when $\lambda_u$ is close to 0 in the Minimal Superymmetric Standard Model (MSSM), and the meaningful diagram that can produce it is (a) in Figure 1. In the scenario in which $\lambda_u$ is not equal to zero, there are additional contributions from the t-channel dark matter exchange, and for the parton level process $u + \bar{u} \rightarrow \phi + \phi^*$, the cross-section is given by the following equation [13]:

$$\sigma = -\frac{1}{1728\pi s^3}\{2\sqrt{s\left(s-4m_\phi^2\right)}\left[4g_s^4\left(4m_\phi^2-s\right)+12g_s^2\lambda_u^2\left(s+2m_\chi^2-2m_\phi^2\right)+27\lambda_u^4 s\right]+3\lambda_u^2\left[16g_s^2\left(m_\chi^2 s+\left(m_\phi^2-m_\chi^2\right)^2\right)+9\lambda_u^2 s(s+2m_\chi^2-2m_\phi^2)\right]\log\left[\frac{s-\sqrt{s\left(s-4m_\phi^2\right)}+2m_\chi^2-2m_\phi^2}{s+\sqrt{s\left(s-4m_\phi^2\right)}+2m_\chi^2-2m_\phi^2}\right]\} \quad (4)$$

Process (b) in Figure 1 is the most important contributor to the formation of monojets when $u$ is set to a low value. The equation that describes the resulting cross section at LO for $u + g \rightarrow \phi + \chi$ is as follows[13]:

$$\sigma(u+g\rightarrow\phi+\chi) = \frac{\lambda_u^2 g_s^2}{768\pi s^3}\left(3s+2m_\chi^2-2m_\phi^2\right)\sqrt{\left(s+m_\chi^2-m_\phi^2\right)^2-4m_\chi^2 s} \quad (5)$$

where $\sqrt{s}$ is the center-of-mass energy.

## 4. Results and Discussions

This study was carried out to adjust the lambda constant to the most efficient monojet production of the signal to be produced for model interpretation of the data collected in proton-proton collisions with a center of mass energy of 14 TeV.

If $\lambda_u \approx 0$, jets plus missing transverse energy on pair production on a mediator that is in the diagram (Figure 1-a) gives the dominant contribution. This can be seen in Figures 4c and 5c, where the production cross-section is bigger than Figures 4-a and 4-b or Figures 5a and 5b at $\lambda_u \approx 0$. It is the same as the search that is performed in the instance of supersymmetric (SUSY) models looking for squarks. In the event that the gluinos are separated into individual particles, Squark interactions revolve around weak interactions in terms of their coupling. As a result, the significance of this contribution is minimal. The coupling, on the other hand, is a free parameter in the t-channel model, and it has the potential to be rather substantial

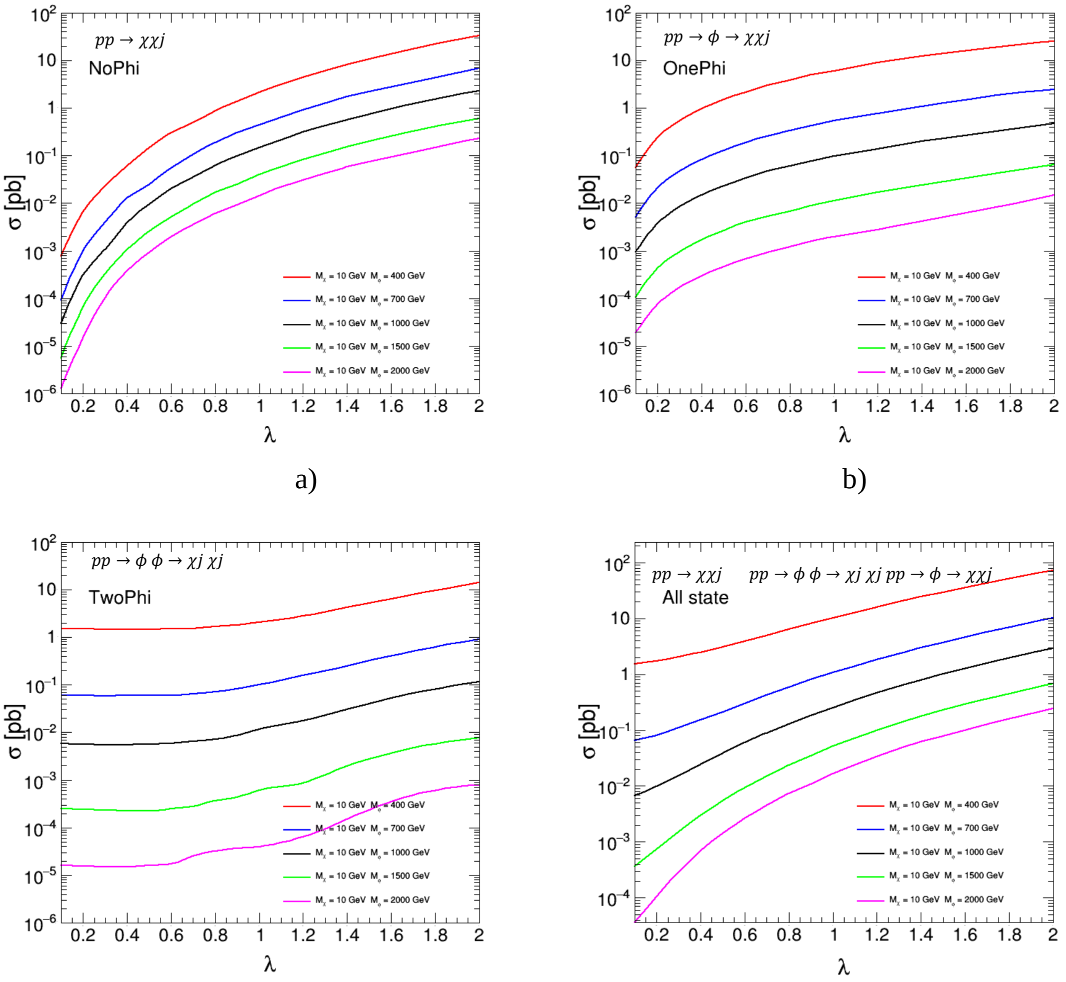

a) b)

c) d)

**Figure 4**. Production cross-section $\sigma$ as a function of coupling $\lambda_u$ for various mediator mass $M_\phi$ at fixed $M_\chi = 10$ GeV for no-phi mediator state ($pp \to \chi\chi j$) (a) one-phi mediator state ($pp \to \phi \to \chi\chi j$) (b) two-phi mediator state ( $pp \to \phi\,\phi \to \chi j\,\chi j$) (c) and including all state ($pp \to \chi\chi j$ & $pp \to \phi \to \chi\chi j$ & $pp \to \phi\,\phi \to \chi j\,\chi j$) (d).

As expected, the t-channel DM exchange state and one mediator final state are dominant for $0.5 < \lambda_u < 2$, in a word, the monojet signature makes an important contribution to this search in this coupling range. The combination of production cross-section is reported in Figure 5, where the expected cross-section rate in pb is reported for several signal mass points in the $M_\phi$-$M_\chi$ plane.

We observed that events with one phi state do not contribute to the cross-section when phi is much larger than chi. This phenomenon is illustrated in Figure 5-b. There is no cross-section of the one $\phi$ state (Figure 1-a) when $\lambda_u$ is greater than 2. Mediator pair production and t-channel production become the dominant contributors to the total cross-section state in this range. Since the production cross section decreases with decreasing coupling constants, the results, interpreted in terms of exclusion limit constraints, will be weaker for small coupling constants. Future searches, particularly at colliders, need to cover a considerable allowable proportion of the parameter space for small couplings, even for the mediator masses that are lower than a few hundred GeV. It has also come to our attention that there is a destructive interference for $\lambda_u$ in the range of 0.5 to 1.5 for two phi states, as is illustrated in Figure 4-c and Figure 5-c for high $M_\phi$ and low $M_\chi$. Consequently, we anticipate that the experimental limits from jets plus missing transverse energy on pair generation will weaken at some intermediate values of $\lambda_u$.

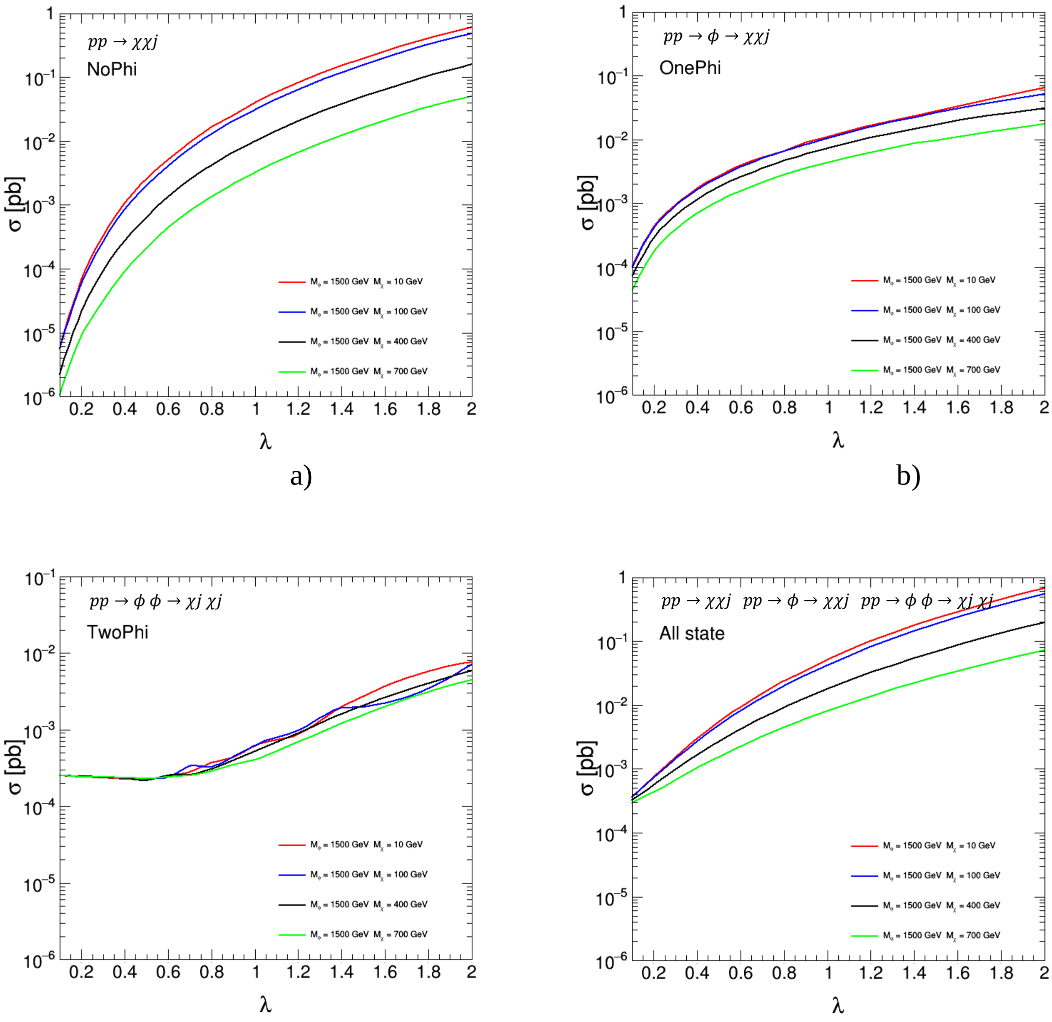

a)

b)

c)

d)

**Figure 5**. Production cross-section $\sigma$ as a function of coupling $\lambda_u$ for various mediator mass $M_\chi$ at fixed $M_\phi = 1500$ GeV for no-phi mediator state ($pp \to \chi\chi j$) (a), one-phi mediator state ($pp \to \phi \to \chi\chi j$) (b), two-phi mediator state ($pp \to \phi\,\phi \to \chi j\,\chi j$) (c), and including all state ($pp \to \chi\chi j$ & $pp \to \phi \to \chi\chi j$ & $pp \to \phi\,\phi \to \chi j\,\chi j$) (d)

## 5. Conclusion and Suggestions

Using a lambda parameter scan at 14 TeV, one of the simplified dark matter models, which is the t-channel Fermion Portal, is analyzed. The model's dark matter production mechanism was tested to see how it was affected by a change in the lambda constant. The T-channel Fermion Portal consists of three different interaction processes, and the lambda sensitivity of these processes was examined separately. Our study exclusively focuses on the u quark, and as such, our exploration of the three production methods is contextualized within the framework of coupling to up quarks. Initially, differences in the cross-section in the $M_\chi$ and $M_\phi$ plane for different $\lambda_u$ values, including all processes, were demonstrated. Then, the decay width for the same $\lambda_u$ in the $M_\phi$, and $M_\chi$ plane was demonstrated, highlighting the lambda sensitivity of the model. Lastly, based on this data, the cross-section variation for different $M_\phi$ masses for a fixed $M_\chi$ mass as a function of $\lambda_u$ values is separately shown for each process. Similarly, the lambda scan for each process is illustrated for different $M_\chi$ masses with a fixed $M_\phi$ mass. Based on the results presented in our paper, we can make the following observations: If $\lambda_u$ is close to zero, the dominant contribution will be jets plus the missing transverse energy from pair production on a mediator. It is the same as the search that is conducted when supersymmetric (SUSY) models are used to look for squarks. $\lambda_u$ Between a value of 0.5 and a value of 2, the t-channel DM exchange state and the one-mediator final state are the ones that clearly take the lead. However, when the value of phi is greater than that of chi, the contributions to the cross-section that come from events with a solitary phi state become substantially less important. When $\lambda_u$ values are greater than 2, both the production of the mediator pair and the production of the t-channel move into the foreground. Notably, the results of our research showed that there is a zone of destructive interference for $\lambda_u$ ranging between 0.5 and 1.5 at particular mass points. This indicates that there may be a reduction in the size of the experimental boundaries. In light of these new discoveries, future experiments, particularly those based on colliders, will need to investigate a broad parameter domain in search of more subtle couplings. This is true even for mediators whose masses are lower than a few hundred GeV. This research sheds light on the critical parameters that guide monojet production and highlights the necessity of recalibrating experimental strategies in accordance with the $\lambda_u$ spectrum.

## Statement of Research and Publication Ethics

The study is complied with research and publication ethics.

## References

[1] D. S. Akerib, S. Alsum, H. M. Araújo, X. Bai, A. J. Bailey, J. Balajthy et al., "Results from a search for dark matter in the complete LUX exposure," *Phys. Rev. Lett.*, vol. 118, no. 2, p. 021303, 2017. [Online]. Available: arXiv:1608.07648, doi: 10.1103/PhysRevLett.118.021303.

[2] E. Aprile et al., "First Dark Matter Search Results from the XENON1T Experiment," *Phys. Rev. Lett*., vol. 119, no. 181301, 2017. doi: 10.1103/PhysRevLett.119.181301. [Online]. Available: arXiv:1705.06655

[3] C. Amole, M. Ardid, I. J. Arnquist, D. M. Asner, D. Baxter, E. Behnke et al., "Dark Matter Search Results from the PICO-60 C3F8 Bubble Chamber," *Phys. Rev. Lett.*, vol. 118, no. 25, p. 251301, 2017, doi: 10.1103/PhysRevLett.118.251301. [Online]. Available: arXiv:1702.07666

[4] M. Klasen, M. Pohl, and G. Sigl, "Indirect and direct search for dark matter," 2015. [Online]. Available: arXiv:1507.03800v1 [hep-ph] Jul. 14, 2015.

[5] The Fermi-LAT, DES Collaborations, A. Albert, B. Anderson, K. Bechtol, A. Drlica-Wagner et al., "Searching for Dark Matter Annihilation in Recently Discovered Milky Way Satellites with Fermi-LAT," *Astrophys. J.*, vol. 834, no. 2, p. 110, 2017, doi: 10.3847/1538-4357/834/2/110. [Online]. Available: arXiv:1611.03184

[6] M. Aguilar, L. Ali Cavasonza, B. Alpat, G. Ambrosi, L. Arruda, N. Attig, et al., "Antiproton flux, antiproton-to-proton flux ratio, and properties of elementary particle fluxes in primary cosmic rays measured with the Alpha Magnetic Spectrometer on the International Space Station," *Phys. Rev. Lett.*, vol. 117, p. 091103, 2016. doi: 10.1103/PhysRevLett.117.091103.

[7] G. Ambrosi, Q. An, R. Asfandiyarov, P. Azzarello, P. Bernardini, B. Bertucci et al., "Direct detection of a break in the teraelectronvolt cosmic-ray spectrum of electrons and positrons," *Nature*, vol. 552, p. 63 EP, 2017. doi: 10.1038/nature24475.

[8] M. G. Aartsen, R. Abbasi, Y. Abdou, M. Ackermann, J. Adams, J. A. Aguilar, et al., "IceCube Search for Dark Matter Annihilation in nearby Galaxies and Galaxy Clusters," *Phys. Rev. D*, vol. 88, no. 122001, 2013. [Online]. Available: arXiv:1307.3473. doi: 10.1103/PhysRevD.88.122001.

[9] A. Albert, M. Backovic, A. Boveia, O. Buchmueller, G. Busoni, A. D. Roeck et al., "Recommendations of the LHC Dark Matter Working Group: Comparing LHC searches for heavy mediators of dark matter production in visible and invisible decay channels," 2017. [Online]. Available: arXiv:1703.05703.

[10] D. Alves, N. Arkani-Hamed, S. Arora, Y. Bai, M. Baumgart, J. Berger et al., "Simplified Models for LHC New Physics Searches," 2011. [Online]. Available: https://arxiv.org/abs/1105.2838

[11] A. Boveia, O. Buchmueller, G. Busoni, F. D'Eramo, A. D. Roeck, A. D. Simone, et al., "Recommendations on presenting LHC searches for missing transverse energy signals using simplified s-channel models of dark matter," 2019. doi: 10.1016/j.dark.2019.100365.

[12] C. Arina, B. Fuks, L. Mantani, "A universal framework for t-channel dark matter models," *Eur. Phys. J. C*, vol. 80, 2020, Article no. 409. [Online]. Available: arXiv:2001.05024.

[13] Y. Bai and J. Berger, "Fermion portal dark matter," *J. High Energy Phys.*, no. 11, Art. no. 171, 2013.

[14] H. An, L. Wang, H. Zhang, "Dark matter with t-channel mediator: a simple step beyond contact interaction," arXiv:1308.0592v2 [hep-ph], Mar. 6, 2014.

[15] C. Arina, B. Fuks, L. Mantani, H. Mies, L. Panizzi, J. Salko, "Closing in on t-channel simplified dark matter models," arXiv:2010.07559v2 [hep-ph], Dec. 31, 2020.

[16] J. Alwall, M. Herquet, F. Maltoni, O. Mattelaer, T. Stelzer, "MadGraph 5: Going Beyond," arXiv:1106.0522 [hep-ph], [Online]. Available: https://doi.org/10.48550/arXiv.1106.0522.

[17] The CMS Collaboration, A. Tumasyan, W. Adam, J. W. Andrejkovic, T. Bergauer, S. Chatterjee et al., "Search for new particles in events with energetic jets and large missing transverse momentum in proton-proton collisions at √s = 13 TeV," *J. High Energy Phys.*, vol. 2021, art. no. 153, 2021, doi: 10.1007/JHEP11(2021)153.

[18] The CMS Collaboration, A. M. Sirunyan, A. Tumasyan, W. Adam, F. Ambrogi, E. Asilar, T. Bergauer, et al., "Search for new physics in final states with an energetic jet or a hadronically decaying W or Z boson and transverse momentum imbalance at √s = 13 TeV," *Phys. Rev. D*, vol. 97, no. 092005, May 2018. doi: 10.1103/PhysRevD.97.092005.

Bitlis Eren Üniversitesi Fen Bilimleri Dergisi
BİTLİS EREN UNIVERSITY JOURNAL OF SCIENCE
ISSN: 2147-3129/e-ISSN: 2147-3188
VOLUME: 13 NO: 2 PAGE: 384-392 YEAR: 2024
DOI:10.17798/bitlisfen.1341929

# Layer Selection for Subtraction and Concatenation: A Method for Visual Velocity Estimation of a Mobile Robot

Mustafa Can BINGOL[1*]

[1] *Department of Electrical-Electronics Engineering, Burdur Mehmet Akif Ersoy University, Burdur 15100, Türkiye*

*(ORCID: 0000-0001-5448-8281)*

**Keywords:** Deep learning, Mobile robot, Velocity estimation.

**Abstract**

Kinematic information such as position, velocity, and acceleration is critical to determine the three-dimensional state of the robot in space. In this study, it is aimed at estimating, visually, the linear and angular velocity of a mobile robot. Additionally, another aim of this study is to determine the suitability of the concatenation or subtraction layer in the Convolutional Neural Network (CNN) that will make this estimate. For these purposes, first, a simulation environment was created. 9000 pairs of images and the necessary velocity information were collected from this simulation environment for training. Similarly, 1000 pairs of images and velocity information were gathered for validation. Four different CNN models were designed, and these models were trained and tested using these datasets. As a result of the test, the lowest average error for linear velocity estimation was calculated as 0.93e-3m/s, and the angular velocity estimation was measured as 4.37e-3rad/s. It was observed that the results were sufficient for linear and angular velocity prediction, according to the statistical analysis of errors. In addition, it was observed that the subtraction layer can be used instead of the concatenation layer in the CNN architectures for hardware-limited systems. As a result, visual velocity estimation of mobile robots has been achieved with this study, and the framework of CNN models has been drawn for this problem.

## 1. Introduction

Robotic systems must be able to measure their kinematic information, such as position, velocity, and acceleration. Also, these systems must be able to control this information according to the desired behavior in order to move autonomously in an environment. For example, Aydogmus and Boztas controlled the linear and angular velocities of a mobile robot by using the pure pursuit algorithm [1]. In another study, the design and analysis of a whole-body controller were realized for a velocity-controlled robot mobile manipulator [2]. The velocity of an omnidirectional wheeled mobile robot was controlled using computed voltage control with visual feedback [3]. In another study, a novel path-planning algorithm for Ackermann mobile robots was been developed. This algorithm is based on B-spline curves and the ant colony algorithm [4]. An omnidirectional mobile robot was real-time navigated in a dynamic environment by using a velocity obstacle and a hybrid A* algorithms [5].

Artificial intelligence is frequently used in many fields, from health to robotics. To illustrate, a liver tumor diagnosis was realized using deep learning techniques and CT - MR imaging [6]. In another study, an industrial robot was converted into a collaborative robot that did not harm people by utilizing deep learning techniques [7]. Artificial intelligence can be subdivided into two categories: deep learning and machine learning. In this study, Convolutional Neural Network (CNN) architectures,

---

[*] Corresponding author: *mcbingol@mehmetakif.edu.tr*

*Received: 12.08.2023, Accepted: 07.06.2024*

a sub-branch of deep learning, were used. CNN is a frequently used structure in robotic systems. For example, delamination was predicted using multimodal 1D CNN during the drilling process of carbon fiber-reinforced plastics [8]. Park et al. developed a novel vision-based autonomous pick and place method utilizing CNN [9]. A farm robot that formed fertilizing and cropping was developed using CNN [10].

In this study, a CNN-based estimation of the linear and angular velocity of a mobile robot is aimed at. There are few similar studies to the current study in the literature. For example, the velocity of omnidirectional mobile robots was estimated using an optical mouse [11]. In another study, state estimation of a mobile robot that was slip-velocity-aware was realized via invariant Kalman filtering and disturbance observer [12]. Arteaga–Pérez and Nuño designed a velocity observer for the consensus in delayed robot networks [13]. When the studies in the literature are examined, studies on velocity estimation of a mobile robot using artificial intelligence methods are limited.

From the past to the present, many researchers have worked on the control and positioning of mobile robots. In fact, the reason why these problems have not been solved is that the exact position of mobile robots is not known. In the current study, in addition to the methods in the literature, the velocity of a mobile robot was estimated by interpreting the images taken at different moments in a CNN-based architecture. In addition, different models have been tested for the selection of the layer to connect the input images in this CNN structure. In this way, it will contribute to the effective use of electronic hardware on a mobile robot.

The rest of the study consists of 3 sections. The first of these sections is Material and Method. In this section, the simulation environment, how the data is obtained, and the CNN models are discussed. Another section is findings. In this section, the training process of CNN models and statistical results according to the validation dataset are presented. The last section is the conclusion. This section presents the general conclusions of the study and future work.

## 2. Material and Method

### 2.1. Environment and Data Collection

One of the objectives of this study is to estimate the linear and angular velocity of a mobile robot based on visual data. For this purpose, one mobile robot and one camera that provides visual data are required. The linear velocity of a mobile robot is the linear displacement per unit time in the direction of its X-axis. The angular velocity of a mobile robot is the angular displacement per unit time in its Z axis. The linear ($v$) and angular ($\omega$) velocities of a mobile robot were presented in Equations 1 and 2. In these equations, $R$, $L$, $\omega_R$, and $\omega_L$ symbolise the wheel radius, the wheelbase of the robot, the angular velocity of the right wheel, and the angular velocity of the left wheel, respectively. In this study, the experimental environment presented in Figure 1 was formed. This experimental environment was designed using the Webots R2023 program, which is a robot simulator.

$$v = \frac{R}{2}(\omega_R + \omega_L) \tag{1}$$

$$\omega = \frac{R}{L}(\omega_R - \omega_L) \tag{2}$$

In Figure 1-a, the mobile robot and camera are symbolized by 1 and 2, respectively. In Figure 1-b, lamps are visualized with number 3. In this study, Turtlebot3 Burger was selected as the mobile robot. Turtlebot3 Burger mobile robot is 138mm x 178mm x 192mm in size and weighs 1 kg. In addition, its wheel diameter, linear velocity, and angular velocity are 66mm, 0.22m/s and 2.84 rad/s, respectively. The module in the simulator program was used as the camera. The camera's resolution, FOV (field of view), and exposure were selected as 224px x 224px, 0.785, and 1, respectively. In this study, the parquet pattern commonly used in indoor spaces such as a daily home was preferred as the ground. The simulation environment dimensions were chosen as 5m x 5m. Other parameters of the simulation were selected as default values and presented in Table 1.

**Table 1.** The simulation parameters.

| **Parameter Description** | **Value** |
|---|---|
| Gravity | 9.81 m/s^2 |
| Basic time step | 64 ms |
| 3D display frame per second | 60 |
| Physics disable linear velocity threshold | 0.01 |
| Physics disable angular velocity threshold | 0.01 |
| Drag force scale | 30 |
| Drag torque scale | 5 |

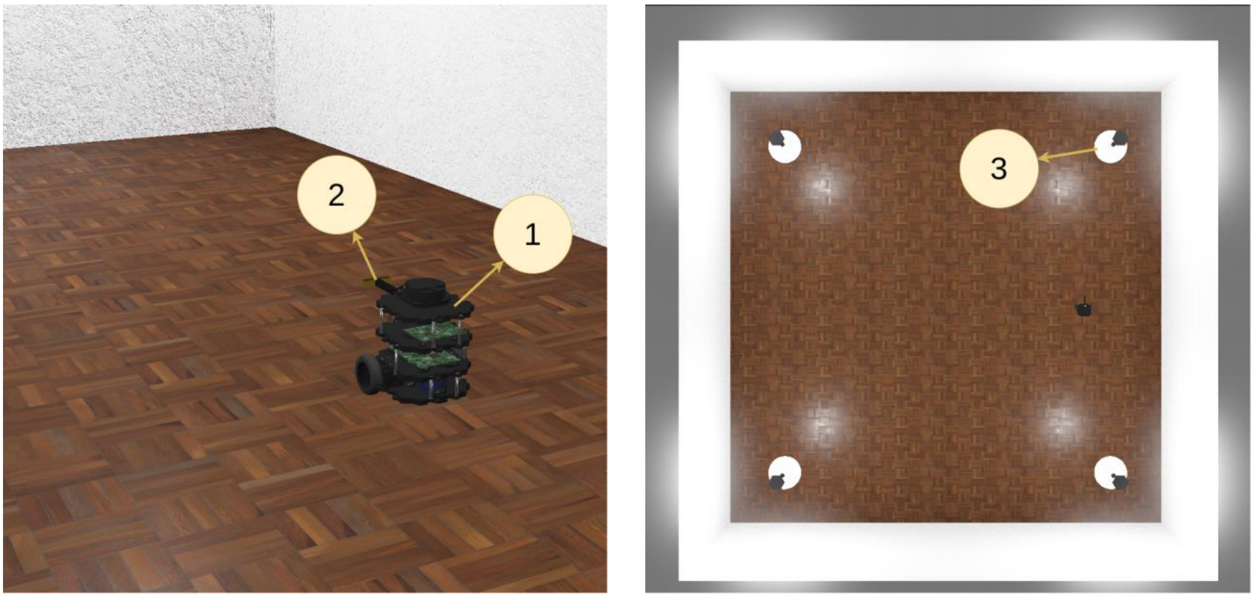

(a) (b)

**Figure 1.** The experimental environment; a- Isometric view, b- Top view.

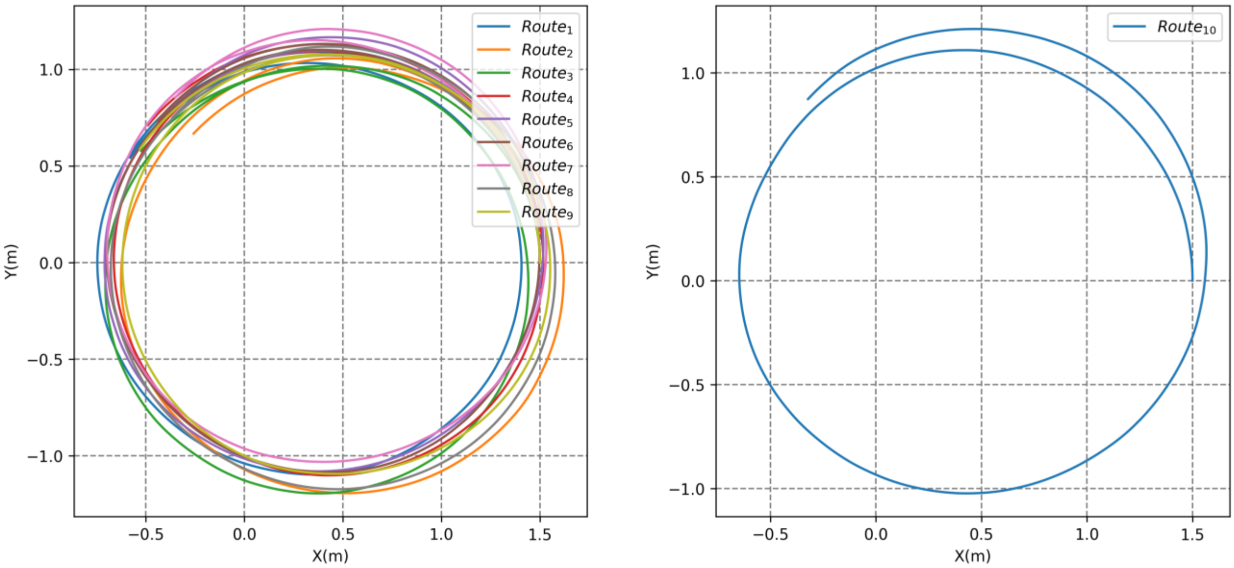

(a) (b)

**Figure 2.** Tracked routes by the robot; a- Training dataset routes, b- Validation dataset route.

After the simulation environment was designed, the 10 routes presented in Figure 2 were followed by the robot. These routes were created by randomly selecting linear and angular velocities between 0.1 and 0.2 (m/s-rad/s). Nine of these routes (Figure 2-a) were used for training, and one (Figure 2-b) was used for validating.

The robot followed each route for 1 minute and 4 seconds. During this tracking, it obtained images of the ground presented in Figure 3. There is one simulation time or 64 ms between the image on the left side of Figure 3 and the image on the right side. To express it discretely, the left image is at time t-1 while the right image is at time t.

Two datasets are created by recording the images presented in Figure 3 with linear and angular velocities when the routes in Figure 2 are followed by the robot. The training dataset, one of these two data sets, contains a total of 9000 images and their velocities. The validation dataset contains a total of 1000 images and their velocities.

**Figure 3.** Ground images at two different times.

After the datasets were created, the images went through a pre-processing stage. This pre-processing stage includes reducing the resolution of the images to 64px x 64px and converting their color from RGB to gray.

### 2.2. CNN Models

The purpose of this study is to reveal the difference between concatenation and subtraction layers in architectures that can predict the linear and angular velocities of a mobile robot visually. To this end, 4 different architectures presented in Figure 4 were trained with data obtained from simulation environments. Subtraction layers were used in Model 1 and Model 2. Concatenation layers were used in Model 3 and Model 4. Convolution and maximum pooling layers were added to the model after input layers were used to obtain the properties of the input layer in Model 1 and Model 3. In Model 2 and Model 4, input data was directly extracted or merged without a feature extraction process.

When the models presented in Figure 4 are analyzed, it is seen that the input layer sizes are 64 x 64 x 1. Also, the input of each model consists of two input layers. The inputs of these layers are images taken at different times. The convolution layer is the layer where intensive mathematical operations are performed, and the number of filters and kernel size are given in brackets, respectively. The stride size of this layer is 1 x 1, and the padding is selected as valid. In the maximum pooling layer, the pool size is given in brackets. In this layer, padding is selected as valid.

The subtraction layer applies the subtraction process to the incoming data. The concatenate layer combines the incoming data one after the other. A flatten layer is used to convert incoming matrices or tensors into vectors. A dropout layer is added to the models to solve the over-fitting problem. The hyper-parameters of the dropout layer are presented in brackets. The dense layer is the layer where the input data affects the entire output data. In these layers, the number of neurons is given in brackets. In addition, there are batch normalization and activation layers after the dense layer, except for the output layer. The batch normalization layer provides the statistical regulation necessary for the training process to proceed in a healthier way. The activation layer provides the learning process by passing the input data through a certain function. In this study, all activation functions except the output layer were chosen as rectified linear units (ReLU). In addition to these hyper-parameters, Model 1, Model 2, Model 3, and Model 4 structures consist of 7.3M, 7.3M, 7.7M and 7.3M learnable parameters, respectively.

## 3. Results and Discussion

Input data from datasets was pre-processed after the datasets were obtained from the simulation environment. After pre-processing, input and output data were generated to train. The input data were augmented by changing their brightness by 25% in the training phase. In this way, the system was able to produce more robust results for different brightness. In addition, the output data were normalized by subtracting the mean and dividing the result by its standard deviation. In this stage, the designed models were trained with the Adaptive Moment Estimation (Adam) algorithm for 50 steps.  In the first 5 steps of this training, the learning rate is 5e-4, and the learning rate between steps 6-19 is 1e-4. In the remaining training process, the learning rate was applied as 1e-5. The training times of the models are 19.687, 16.875, 22.500 and 16.875 minutes, respectively. Mean Squared Error (MSE) was used as the loss function during this training. Loss-Epoch plots during the training period are presented in Figure 5.

Figure 5 shows that the training and validation processes of the networks did not have any high bias or high variance problems. During this training, a mini-batch size of 8 was chosen, and the input data in one mini-batch of the validation dataset is presented in Figure 6.

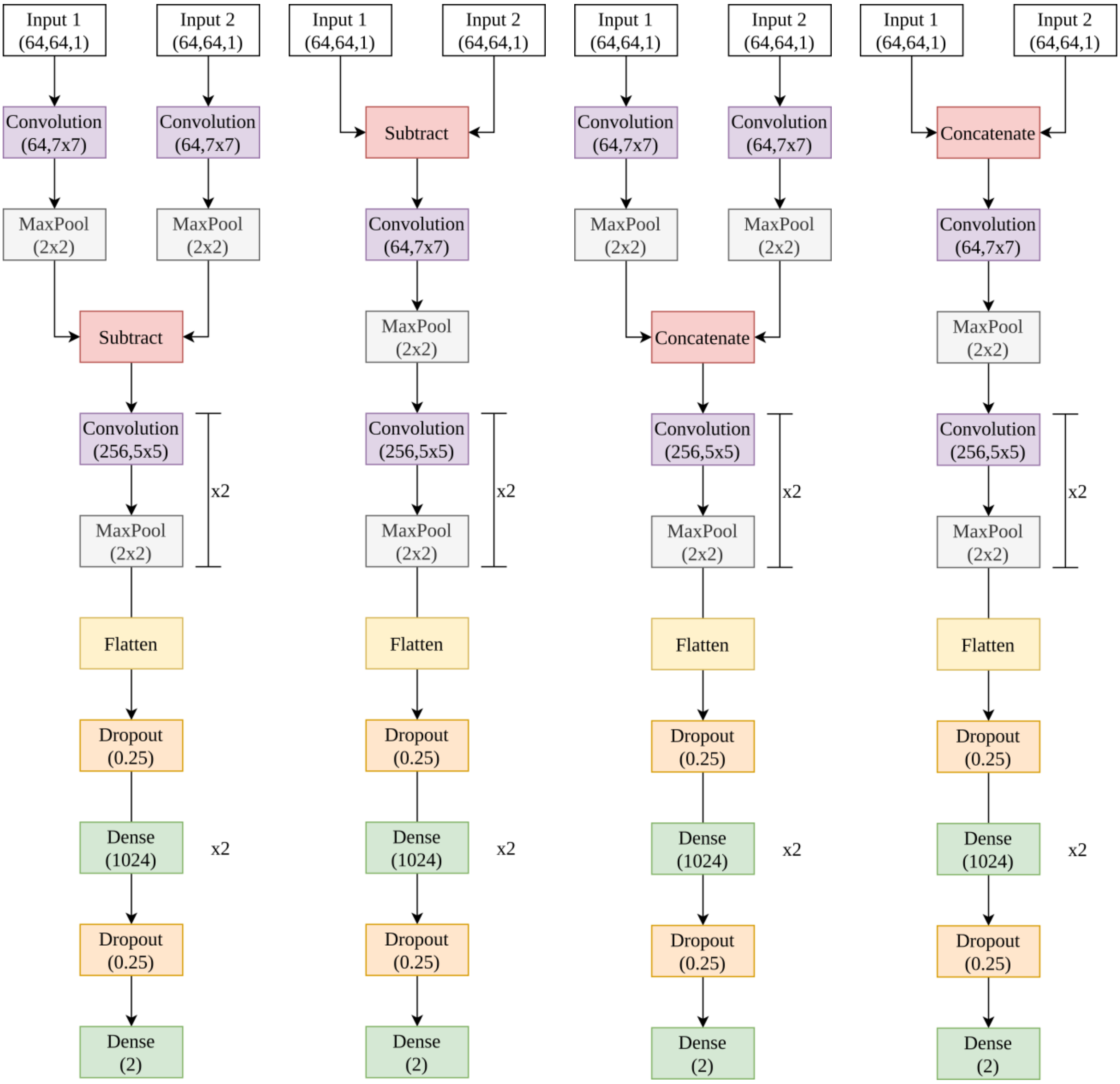

(a) (b) (c) (d)

**Figure 4.** CNN architectures; a-Model 1, b-Model 2, c-Model 3, d-Model 4.

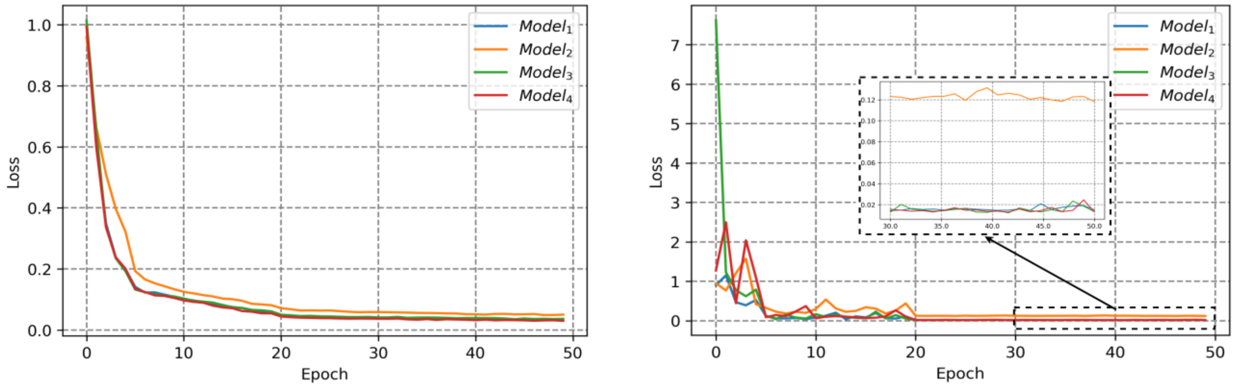

(a) (b)

**Figure 5.** Loss function graphs; a-Train loss, b-Validation loss.

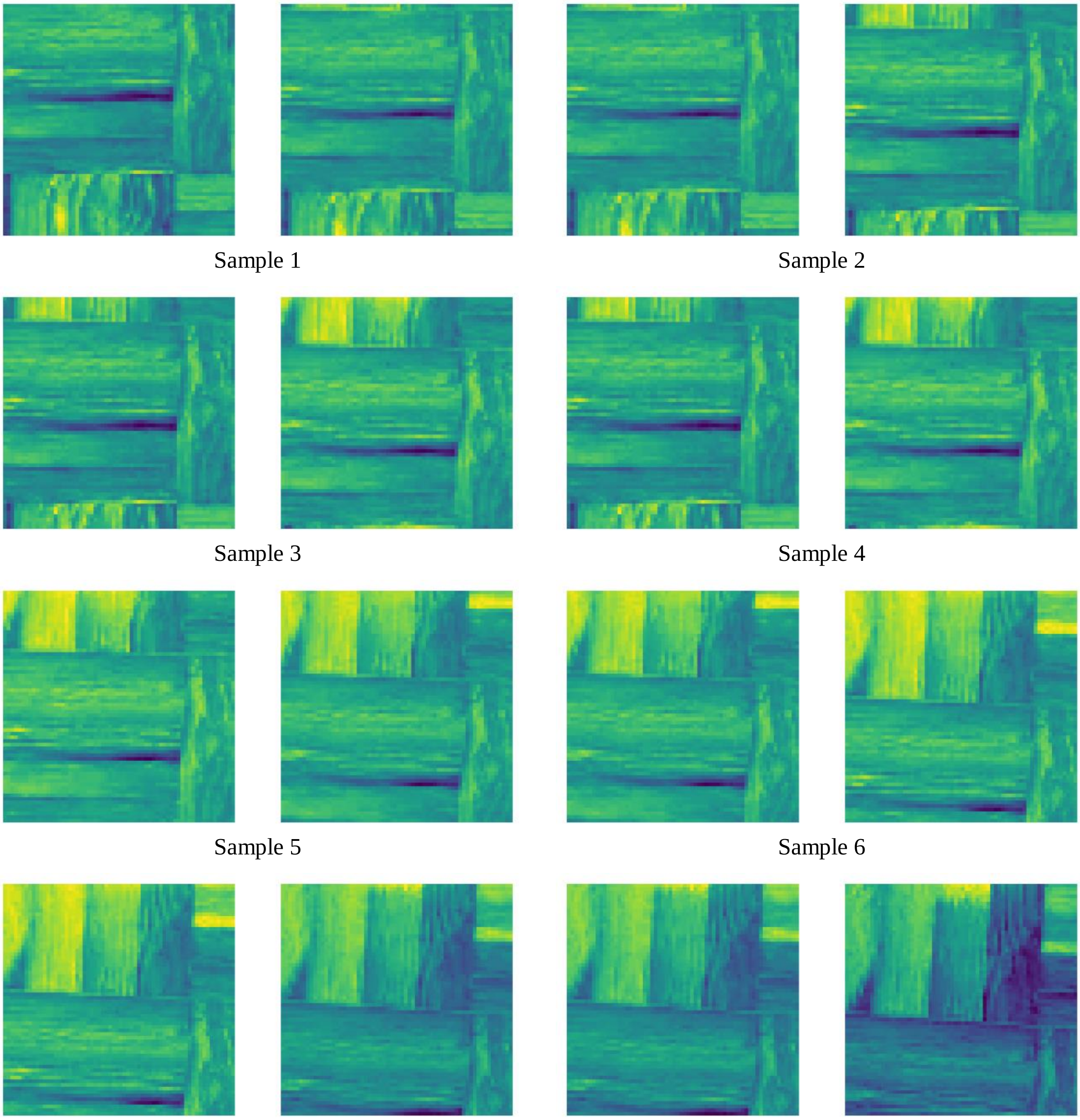

Sample 1

Sample 2

Sample 3

Sample 4

Sample 5

Sample 6

Sample 7

Sample 8

**Figure 6.** Mini-batch samples of the validation dataset.

The results generated against the inputs in Figure 6 are presented in Figure 7. The error amount of the data presented in Figure 7 is given in Figure 8. Figure 8 shows the measured error rates for a mini-batch. As this data is limited, it is insufficient for a comparison of model performance. For this reason, a descriptive analysis of the error between predicted and actual results for the 1000 data points in the validation dataset is presented in Table 2.

Table 2 shows the mean, standard deviation, standard error, and minimum and maximum values of the errors between the linear and angular velocity estimates and the actual value. The differences between linear (9.57e-3) and angular velocity (40.07e-3) errors are due to the units of both measurements. For example, if degrees/s were used instead of rad/s or km/h instead of m/s, the difference between linear and angular velocity would be different. It was investigated whether these calculated error values differed between the groups, and this result is presented in Tables 3 and 4.

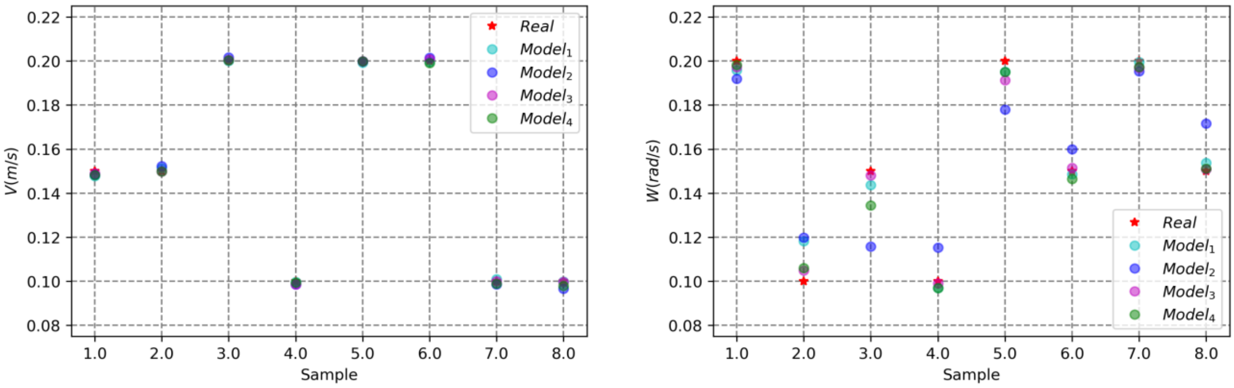

(a) (b)

**Figure 7.** Velocity predictions for mini-batch samples of the validation dataset; a- Linear velocities, b- Angular velocities.

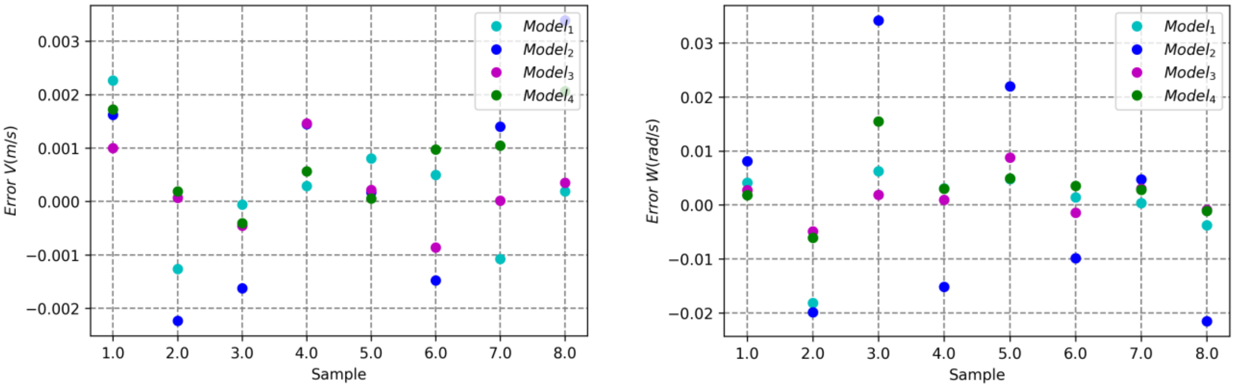

(a) (b)

**Figure 8.** Errors of velocity predictions for mini-batch samples of the validation dataset; a- Linear velocities, b- Angular velocities.

**Table 2.** Descriptive analysis of errors.

| | Model | N | Mean | Std. Deviation | Std. Error | Minimum | Maximum |
|---|---|---|---|---|---|---|---|
| **\|Error V\| (m/s)** | 1 | 1000 | 1.03e-3 | 0.81e-3 | 2.56e-5 | 1.04e-6 | 9.57e-3 |
| | 2 | 1000 | 1.95e-3 | 1.85e-3 | 5.86e-5 | 2.51e-6 | 21.87e-3 |
| | 3 | 1000 | 1.01e-3 | 1.00e-3 | 3.16e-5 | 1.25e-6 | 9.43e-3 |
| | 4 | 1000 | 0.93e-3 | 0.86e-3 | 2.72e-5 | 0.05e-6 | 7.56e-3 |
| **\|Error W\| (rad/s)** | 1 | 1000 | 4.66e-3 | 5.22e-3 | 16.52e-5 | 20.94e-6 | 40.07e-3 |
| | 2 | 1000 | 14.43e-3 | 13.53e-3 | 42.79e-5 | 4.05e-6 | 88.06e-3 |
| | 3 | 1000 | 4.37e-3 | 4.84e-3 | 15.53e-5 | 4.62e-6 | 40.50e-3 |
| | 4 | 1000 | 6.92e-3 | 4.96e-3 | 15.71e-5 | 0.61e-6 | 36.08e-3 |

**Table 3.** Model comparison according to the linear velocity error.

| Group 1 | Group 2 | p |
|---|---|---|
| Model 1 | Model 2 | **p<0.001** |
| | Model 3 | 0.99 |
| | Model 4 | 0.29 |
| Model 2 | Model 1 | **p<0.001** |
| | Model 3 | **p<0.001** |
| | Model 4 | **p<0.001** |
| Model 3 | Model 1 | 0.99 |
| | Model 2 | **p<0.001** |
| | Model 4 | 0.42 |
| Model 4 | Model 1 | 0.29 |
| | Model 2 | **p<0.001** |
| | Model 3 | 0.42 |

**Table 4.** Model comparison according to the angular velocity error.

| Group 1 | Group 2 | p |
|---|---|---|
| Model 1 | Model 2 | **p<0.001** |
| | Model 3 | 0.84 |
| | Model 4 | 0.60 |
| Model 2 | Model 1 | **p<0.001** |
| | Model 3 | **p<0.001** |
| | Model 4 | **p<0.001** |
| Model 3 | Model 1 | 0.84 |
| | Model 2 | **p<0.001** |
| | Model 4 | 0.97 |
| Model 4 | Model 1 | 0.60 |
| | Model 2 | **p<0.001** |
| | Model 3 | 0.97 |

According to Tables 3 and 4, a significant difference was observed between Model 2 and the other groups for both linear and angular velocity ($p<0.001$). There is no statistically significant difference between the other groups ($p>0.001$).

## 4. Conclusion and Suggestions

In this study, it is aimed at estimating the linear and angular velocity of a mobile robot as visualized by a CNN and to compare whether the concatenation or subtraction layer of different images at different times will be more effective in this CNN structure. For these purposes, firstly, a simulation environment was designed, and training and validation datasets were obtained from this environment. Then, 4 different CNN architectures were trained on the training dataset, and these models were tested on the validation dataset. The statistical results of the tests are presented in Tables 2, 3, and 4. Based on these data, the worst result was produced by Model 2. The results of other models are better than this model. In addition, no statistical difference was observed between the other models except Model 2. Based on this finding, each of the three models can be used. However, if structures similar to Model 1 using the subtraction layer are used, a few convolutional layers should be used first for feature extraction. In addition, the extraction layer used in Model 1 will be more suitable for designs made with limited capacity processors where the input and output data sizes are the same as the concatenating layer found in Model 3 and Model 4. If there is no hardware constraint in the designed system, Model 4, which can be more easily designed compared to other models, can be used. The other aim of this study is to estimate linear and angular velocity. When Tables 2, 3, and 4 are examined, it is clear that the system designed for linear and angular velocity estimation is quite useful.

In future studies, data will be obtained from real mobile robots for complex routes, and similar studies will be repeated. In addition, it will be tried to make the proposed algorithm usable not only for mobile robots but also for all robots in general.

### Conflict of Interest Statement

There is no conflict of interest between the authors.

### Statement of Research and Publication Ethics

The study is complied with research and publication ethics.

## References

[1] G. Boztaş and Ö. Aydoğmuş, "Implementation of Pure Pursuit Algorithm for Nonholonomic Mobile Robot using Robot Operating System," *Balkan Journal of Electrical and Computer Engineering*, vol. 9, no. 4, pp. 337–341, Oct. 2021, doi: 10.17694/bajece.983350.

[2] M. Li et al., "Design and analysis of a whole-body controller for a velocity controlled robot mobile manipulator," *Science China Information Sciences*, vol. 63, no. 7, Jul. 2020, doi: 10.1007/s11432-019-2741-6.

[3] A. Saenz, V. Santibañez, E. Bugarin, A. Dzul, H. Ríos, and J. Villalobos-Chin, "Velocity Control of an Omnidirectional Wheeled Mobile Robot Using Computed Voltage Control with Visual Feedback: Experimental Results," *Int J Control Autom Syst*, vol. 19, no. 2, pp. 1089–1102, Feb. 2021, doi: 10.1007/s12555-019-1057-6.

[4] F. Huo, S. Zhu, H. Dong, and W. Ren, "A new approach to smooth path planning of Ackerman mobile robot based on improved ACO algorithm and B-spline curve," *Rob Auton Syst*, vol. 175, May 2024, doi: 10.1016/j.robot.2024.104655.

[5] M. U. Shafiq et al., "Real-time navigation of mecanum wheel-based mobile robot in a dynamic environment," *Heliyon*, vol. 10, no. 5, Mar. 2024, doi: 10.1016/j.heliyon.2024.e26829.

[6] B. Lakshmipriya, B. Pottakkat, and G. Ramkumar, "Deep learning techniques in liver tumour diagnosis using CT and MR imaging - A systematic review," *Artificial Intelligence in Medicine*, vol. 141. Elsevier B.V., Jul. 01, 2023. doi: 10.1016/j.artmed.2023.102557.

[7] M. C. Bingol and O. Aydogmus, "Practical application of a safe human-robot interaction software," *Industrial Robot*, vol. 47, no. 3, pp. 359–368, May 2020, doi: 10.1108/IR-09-2019-0180.

[8] J. G. Choi, D. C. Kim, M. Chung, S. Lim, and H. W. Park, "Multimodal 1D CNN for delamination prediction in CFRP drilling process with industrial robots," *Comput Ind Eng*, vol. 190, Apr. 2024, doi: 10.1016/j.cie.2024.110074.

[9] J. Park, M. B. G. Jun, and H. Yun, "Development of robotic bin picking platform with cluttered objects using human guidance and convolutional neural network (CNN)," *J Manuf Syst*, vol. 63, pp. 539–549, Apr. 2022, doi: 10.1016/j.jmsy.2022.05.011.

[10] C. Cruz Ulloa, A. Krus, A. Barrientos, J. del Cerro, and C. Valero, "Robotic Fertilization in Strip Cropping using a CNN Vegetables Detection-Characterization Method," *Comput Electron Agric*, vol. 193, Feb. 2022, doi: 10.1016/j.compag.2022.106684.

[11] S. Kim and S. Lee, "Robustness analysis of mobile robot velocity estimation using a regular polygonal array of optical M," *in IFAC Proceedings Volumes (IFAC-PapersOnline)*, 2008. doi: 10.3182/20080706-5-KR-1001.0769.

[12] X. Yu et al., "Fully Proprioceptive Slip-Velocity-Aware State Estimation for Mobile Robots via Invariant Kalman Filtering and Disturbance Observer," Sep. 2022, [Online]. Available: http://arxiv.org/abs/2209.15140

[13] M. A. Arteaga-Pérez and E. Nuño, "Velocity observer design for the consensus in delayed robot networks," *J Franklin Inst*, vol. 355, no. 14, pp. 6810–6829, Sep. 2018, doi: 10.1016/j.jfranklin.2018.07.001.

**Bitlis Eren Üniversitesi Fen Bilimleri Dergisi**
BİTLİS EREN UNIVERSITY JOURNAL OF SCIENCE
ISSN: 2147-3129/e-ISSN: 2147-3188
VOLUME: 13 NO: 2 PAGE: 393-399 YEAR: 2024
DOI:10.17798/bitlisfen.1403830

# Investigation the Cytotoxic and Antimicrobial Effect of *Ranunculus poluninii*

İrem Nur MENEVŞE[1], Irmak İÇEN TAŞKIN[1*], Pelin YILMAZ SANCAR[2], Murat KÜRŞAT[3]

*[1] Inonu University, Faculty of Science and Arts, Department of Molecular Biology and Genetics, Malatya, Turkey*
*[2] Fırat University, Faculty of Science, Department of Biology, Elazığ, Turkey*
*[3] Bitlis Eren University, Faculty of Science and Arts, Department of Biology, Bitlis, Turkey*

*(ORCID: 0009-0004-3497-8397) (ORCID: 0000-0002-1612-0563)*
*(ORCID: 0000-0002-6134-622X) (ORCID: 0000-0002-0861-4213)*

**Keywords:** Antimicrobial, cytotoxic, MTT, MIC, *Ranunculus poluninii*.

**Abstract**
*Ranunculus* plant species, one of the endemic plants, are utilized to treat a number of illnesses such as febrile diseases, rheumatism and inflammatory rashes due to their pharmacological and toxicological activities. Considering these properties, it was aimed to investigate the cytotoxic effects of *Ranunculus poluninii* on A549 and HCT116 cancer cell lines, *Escherichia coli*, *Pseudomonas aeruginosa* and *Staphylococcus aureus* bacteria and *Candida albicans* and *Candida glabrata* yeasts. For this purpose, the extract of the plant was obtained by methanol extraction. Stocks were prepared from this plant at different concentrations of 200 µg/mL, 100 µg/mL, and 50 µg/mL for A549 cancer cell line and 400 µg/mL, 200 µg/mL, 100 µg/mL, and 50 µg/mL for HCT116 cancer cell line and applied to the cell lines. The 3- [4,5-dimethylthiazol-2 il]-2,5-diphenyl-tetrazolium bromide (MTT) assay was performed to evaluate the viability of the cells. In addition, plant extracts prepared at different concentrations of 800 µg/mL, 400 µg/mL, 200 µg/mL, 100 µg/mL, and 50 µg/mL were applied to *Escherichia coli, Pseudomonas aeruginosa and Staphylococcus aureus, Candida albicans* and *Candida glabrata* and minimum inhibitory concentration (MIC) values were determined. Our results showed that *Ranunculus poluninii* was reduced cell viability to 83.7% at 100 µg/mL and 79% at 200 µg/mL on A549 and HCT116 respectively. In addition, it decreased both *Candida albicans* and *Candida glabrata* growth to 91.5% at 800 µg/mL and 95.1% at 50 µg/mL respectively. Our results suggest that *Ranunculus poluninii* has anticancer effect and antifungal activity.

## 1. Introduction

One of the most prevalent and complicated illnesses that endanger people's health worldwide is cancer [1] and the burden of cancer mortality and incidence is increasing rapidly [2]. Various studies and research have been conducted to treat cancer and one of these studies is plant-based anticancer studies. Plants are essential to human life and are necessary for survival. Many countries utilize plants and extracts of plants for therapeutic purposes in order to prevent and treat diseases that affect humans. The importance of herbal-derived products continues to increase due to their low cost, less side effects and easy availability [3].

The *Ranunculaceae* family, popularly known as buttercup and consisting of plants such as small shrubs and woody vines, has nearly 60 genera and 2500 species in the world and 19 genera and 203 species in Turkey [4]. Plants of the *Ranunculaceae*

---

[*] Corresponding author: irmak.taskin@inonu.edu.tr

*Received:12.12.2023, Accepted: 20.03.2024*

family are distributed worldwide, mostly in temperate regions of the northern hemisphere. About 720 species of this plant family are distributed throughout China and have been used in traditional Chinese medicine for many years. Plants in this family contain a wide variety of chemical constituents such as benzylisoquinoline alkaloids, ranunculin, triterpenoid saponin and diterpene alkaloids [5]. The plant species *Ranunculus* has been used in traditional medicine for the treatment of various diseases such as febrile diseases, rheumatism and inflammatory rashes due to its pharmacological and toxicological activities. The family *Ranunculaceae,* which consists of herbaceous perennial or annual plants, also includes plant species with specific toxicological and pharmacological activities [6]. Studies using plant extracts of *Ranunculus* species have shown that they have antibacterial, antiviral and antiprotozoal effects, as well as antioxidant and anticarcinogenic properties [7]. In a study, the antimicrobial activity of a toxin called protoanemonin, which is found in all of the *Ranunculaceae* family, was investigated and showed that *Ranunculus bulbosus* has a significant inhibitory effect on fungi and yeast species [8]. *Ranunculus* plant species have also been used in anticancer studies. In a study with *Ranunculus repens* L., dichloromethane fraction of the plant was applied to gastric cancer AGS and chloroform fraction to colon and rectal tumors HCT116. As a result, the plant fractions inhibited the growth of cancer cells in a dose-dependent manner and were found to be active in reducing tumor cell migration [9]. In another study, ovarian cancer cell lines A2780 and SK-OV-3 were treated with *Ranunculus ternati* strain and the plant alone showed a remarkable cytotoxic effect on cell proliferation [10].

Based on previous studies, *Ranunculus poluninii* is expected to show antimicrobial, anticancer and antifungal properties like plant species in the *Ranunculaceae* family. This study focused on investigating the anticancer, antibacterial and antifungal properties of the plant by applying the plant extract to A549 and HCT116 cancer cell lines, as well as *Escherichia coli*, *Pseudomonas aeruginosa* and *Staphylococcus aureus* bacteria, and *Candida albicans* and *Candida glabrata* yeasts.

## 2. Material and Method

### 2.1. Methanol extraction

Root, stem, and leaf parts taken from the *Ranunculus poluninii* were pulverized and macerated in 80% methanol for 72 hours in a shaking incubator. Following a 72-hour period, filter paper was used to filter the solution and transferred to petri dishes left to dry for one day. After being weighed, the dry extract was dispersed in dimethyl sulfoxide (DMSO). Before usage, the mixture was kept at 4°C in a refrigerator [11].

### 2.2. Cell culture and incubation

Stocks of *Ranunculus poluninii* extract at different concentrations of 200 µg/mL, 100 µg/mL and 50 µg/mL for A549 cancer cell line and 400 µg/mL, 200 µg/mL, 100 µg/mL and 50 µg/mL for HCT116 cancer cell line were prepared and applied to cell lines. At 37°C and 5% $CO_2$, all cells were cultured in Dulbecco's Modified Eagle Media (DMEM). $1x10^4$ cells were seeded to 96 well plate. Lastly, to enable cell adhesion, dishes comprising cells were subjected to incubation for 24 hours at 37 °C in a 5% $CO_2$ environment.

### 2.3. MTT Assay

The 3- [4,5-dimethylthiazol-2 il]-2,5-diphenyl-tetrazolium bromide (MTT) assay was used to detect cellular viability of cells. Cells in the 96 well plate left to grow then transferred out of the incubator, and 1X PBS was used to clean each well. Each well was treated with *Ranunculus poluninii* solutions prepared at different concentrations and incubated for 24 hours. The wells were added with an amount of MTT reagent equal to 10% of the total volume of the wells and incubated again for 2-4 hours. After incubation DMSO was added and plates were incubated in incubator for 15 minutes. Absorbances were measured in a spectrophotometer [12].

### 2.4. Antimicrobial activity

*Candida albicans* (ATCC MYA-2876) and *Candida glabrata* (ATCC 2001) were used for antifungal tests, and *Escherichia coli* (ATCC 25922), *Staphylococcus aureus* (ATCC 29213) and *Pseudomonas aeruginosa* (ATCC 27853) were used for antimicrobial tests. BMD (Broth Microdilution) test was used for antifungal and antimicrobial MIC analyses. For the purposes of the antifungal and antimicrobial tests, *Ranunculus poluninii* stock solution was made using only DMSO. Next, multiple dilutions were prepared in 96-well plates by YPD (Yeast Peptone Dextrose) medium (2% glucose, 2% peptone, 1% yeast extract, pH 6.5) [13] for yeasts and LB (Luria-Bertani) broth medium (1% tryptone, 1% NaCl, 0.5% yeast extract, pH 7.0) [14] for bacteria. To achieve the necessary cell density and concentrations of the sample to be tested, cell solutions of bacteria ($1x10^6$ CFU/mL) and yeast ($1\text{-}5x10^5$ CFU/mL) were adjusted by sterile water. After incubation, the MIC was measured spectrophotometrically for yeasts at 530 nm and visually assessed for bacteria. For yeasts, plates were incubated for 24 hours at 37 °C, and for bacteria, for 16–18 hours at the same temperature. The lowest sample concentration that resulted in at least a 50% decrease in growth relative to the control (no sample) cell group was used to calculate the minimum inhibitory concentration (MIC) for yeasts, whereas the lowest sample concentration that resulted in no discernible growth was used to calculate the MIC for bacteria.

### 2.5. Statistical analysis

SPSS statistical programming was employed to conduct the statistical analysis. The data is shown as mean ± SD. The numerical data's mean and standard deviations were provided as a consequence of the analyses.

## 3. Results and Discussion

In numerous countries, cancer is one of the primary causes of death [15]. Researchers have carried out numerous experiments to prevent and treat cancer. Plants have an important place in studies on cancer and has been used in alternative medicine for many years [16]. Compounds from plants have been an important source of the anti-cancer agents [17]. The best known example of anticancer drug is Paclitaxel which is obtained from the bark of *Taxus brevifolia Nutt* [18]. Curcumin is also a another plant with anticancer activity [19].

Because of its pharmacological and toxicological properties, the *Ranunculus poluninii*, which is used in this study, is used to treat a variety of illnesses in, including rheumatism, inflammatory rashes, and febrile diseases. Although studies on anti-cancer activities of *Ranunculus* plant species are limited, studies using plant extracts of *Ranunculus* species have revealed that these extracts have antioxidant and anticarcinogenic properties [6,7]. Based to a study, an extract from the *Ranunculus ternatus*, which is a member of the *Ranunculaceae* family, dramatically and dose-dependently reduced the viability of Jurkat cells and induced death of the MCF-7 cells [20]. In study with *Ranunculus repens* L., Thymoquinone (TQ), a bioactive component of the plant with anti-cancer properties, was utilized. In the study, this bioactive substance obtained from the plant induced cell apoptosis at a higher rate in human gastric adenocarcinoma cell lines compared to the control and showed a decrease in cell proliferation [21]. In another study with *Ranunculus repens* L., the anticancer properties of *Ranunculus repens* L. were investigated and the dichloromethane fraction of the plant was applied to gastric cancer AGS and the chloroform fraction to colon and rectal tumor HCT116 cells. As a result, it was shown that the plant fractions were active in inhibiting cell growth and reducing tumor cell migration [9]. Another study used the *Ranunculus ternati* strain on the ovarian cancer cell lines A2780 and SK-OV-3. It revealed a notable cytotoxic effect on the proliferation of the cells [10].

In this study, anti-cancer effect of *Ranunculus poluninii* extract on cell viability against A549 and HCT116 cell line conducted at several concentrations between 50 and 200 µg/mL for A549 and 50 to 400 µg/mL for HCT116. Cells were treated with *Ranunculus poluninii* extract for 24 hours. There are significant decrease in cell viability was observed when the A549 and HCT116 cell lines were exposed to *Ranunculus poluninii*.

In the HCT116 cell, the decline in cell viability was slightly greater than A549 cell line. Cell viability for A549 cell line was 87.5% at 200 µg/mL, 83.7% at 100 µg/mL, and 91% at 50 µg/mL, while HCT116 cell line, cell viability was 87.2% at 400 µg/mL, 79% at 200 µg/mL, 80.5% at 100 µg/mL, and 80.1% at 50 µg/mL (Figure 1).

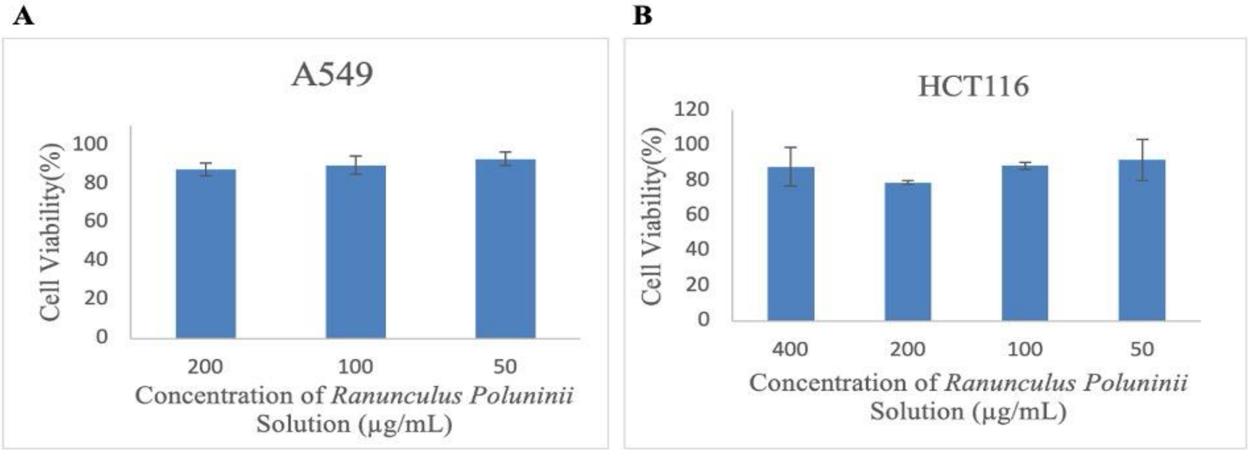

**Figure 1:** Effect of *Ranunculus poluninii*'s methanol extract on A549 (A) and HCT116 (B) cell lines.

In addition to the anticancer effect, *Ranunculaceae* family have antibacterial, antiviral and antiprotozoal effects [7]. Pathogenic yeast species *Candida albicans* and *Candida glabrata* were used for antifungal tests, and *Escherichia coli*, *Staphylococcus aureus* and *Pseudomonas aeruginosa* bacterial species were used for antimicrobial tests. *Ranunculus poluninii* was applied at different concentrations range from 50 to 800 µg/mL against bacterial and yeast species. MIC analyzes were performed with reference to EUCAST E.DEF 7.3.2 for yeasts [22] and were carried out utilizing the BMD (Broth Microdilution) test as described in CLSI M07 [23] for bacteria.

As a result of antibacterial experiments, *Ranunculus poluninii* extract did not show antibacterial effects on *Escherichia coli* (Figure 2A), *Pseudomonas aeruginosa* (Figure 2B) and *Staphylococcus aureus* (Figure 2C). All bacteria continued to grow despite application of *Ranunculus poluninii* extract.

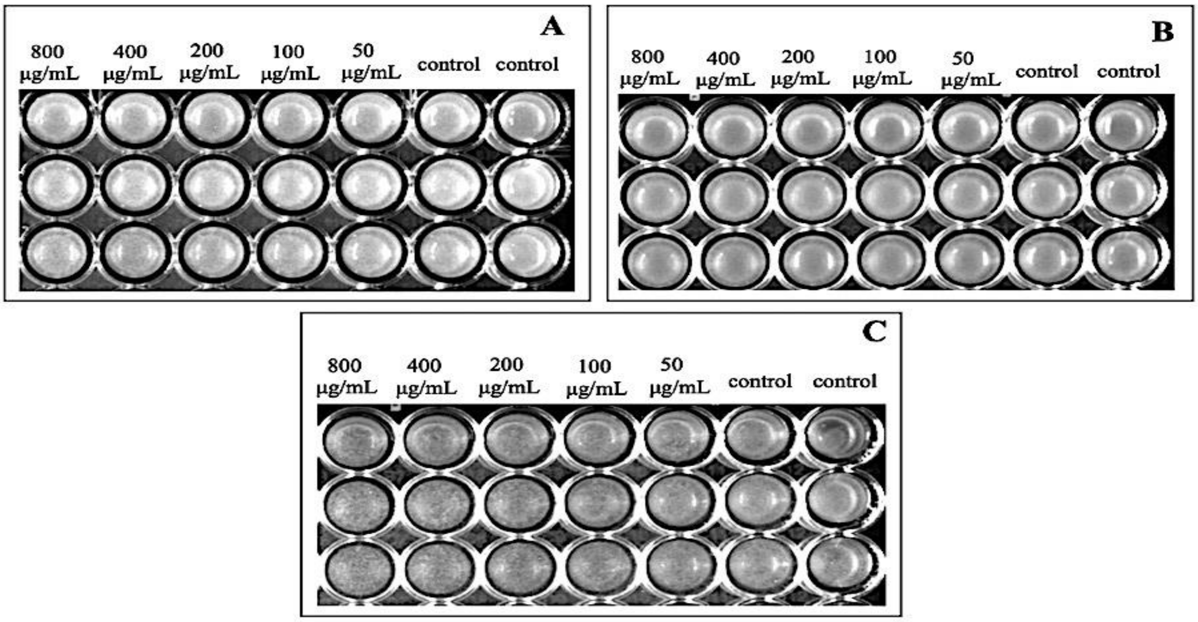

**Figure 2.** Antimicrobial activity of *Ranunculus poluninii's* methanol extract on *Escherichia coli* (A), *Pseudomonas aeruginosa* (B) and *Staphylococcus aureus* (C).

At the antifungal anaysis, cell viability for the *Candida albicans* was 91.5% at 800 µg/mL, 92.7% at 400 µg/mL, 95.2% at 200 µg/mL, 95.3% at 100 µg/mL, and 95.1% at 50 µg/mL, while the cell viability for *Candida glabrata* was 96.9% at 800 µg/mL, 97.2% at 400 µg/mL, and 96,3% at 200 µg/mL, 95.9% at 100 µg/mL, and 96.1% at 50 µg/mL (Figure 3).

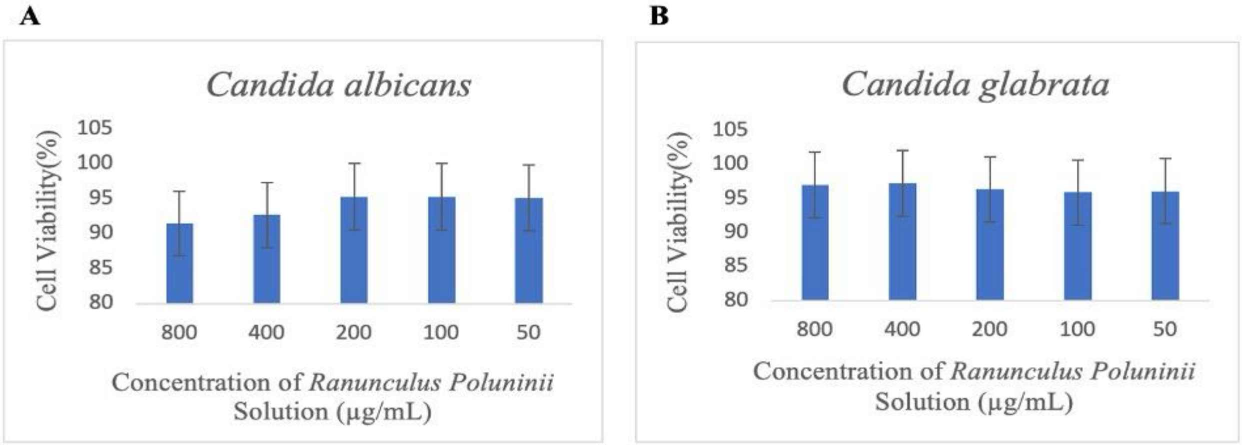

**Figure 3.** Effect of *Ranunculus poluninii's* methanol extract on *Candida albicans* (A) *and Candida glabrata* (B).

Previous studies have also demonstrated that a toxin called protoanemonin, which is found *Ranunculus bulbosus*, has been shown to have a significant inhibitory effect on fungi and yeast species. Among the tested strains, *Rhodotorula glutinis* was the most susceptible yeast and *Epidermophyton floccosum* was the most susceptible dermatophyte [8]. In a study investigating antimicrobial activity, nine test microorganisms including *Escherichia coli*, *Proteus sp.*, *Pseudomonas aeruginosa*, *Shigelladysenteria*, *Salmonella enteritidis*, *Salmonella typhi*, *Staphylococcus aureus*, *Streptococcus faecalis* and *Candida albicans* were investigated by single disk diffusion method. The methanol extract of the whole plant of *Ranunculus myosuroudes* was reported to be active against 88.8% of the tested microorganisms [24]. In another study, antibacterial and antifungal activities of four fractions (n-hexane, chloroform, ethyl acetate and ethanol) of *Ranunculus muricatus* were tested against *Staphylococcus aureus*, *Micrococcus luteus* and *Escherichia coli*, *Pseudomonas aeruginosa*, *Enterobactercloacae*, *Klebsiella Pneumoniae* strains. Almost all fractions exhibited antimicrobial activity. Among them, the ethyl acetate fraction showed maximum antimicrobial activity against *Staphylococcus aureus* [25].

Nevertheless, no inhibitory effect was observed by *Ranunculus poluninii* extracts on *Escherichia coli*, *Pseudomonas aeruginosa*, or *Staphylococcus aureus* in this investigation. However, unlike bacteria, the results of previous studies on yeast in the literature are similar to the present findings in this study. The application of *Ranunculus poluninii* methanol extract was found to reduce the cell viability of *Candida glabrata* and *Candida albicans*.

## 4. Conclusion and Suggestions

In conclusion, our findings indicate that *Ranunculus poluninii* exhibits anticancer properties on A549 and HCT116 cell lines, as well as antiyeast activity against *Candida albicans* and *Candida glabrata*. Nevertheless, additional investigation is required to precisely understand the impact of *Ranunculus poluninii* on cancer cell lines and yeast species.

## Acknowledgment

This study was supported by TUBITAK with 1919B012217255 project number.

## Conflict of Interest Statement

There is no conflict of interest between the authors.

## Statement of Research and Publication Ethics

The study is complied with research and publication ethics.

## References

[1] A. R. Amala Dev and J. Sonia Mol, “Citrus essential oils: A rational view on its chemical profiles, mode of action of anticancer effects/antiproliferative activity on various human cancer cell lines,” *Cell Biochem. Biophys.*, vol. 81, no. 2, pp. 189–203, 2023.

[2] H. Sung et al., “Global cancer statistics 2020: GLOBOCAN estimates of incidence and mortality worldwide for 36 cancers in 185 countries,” *CA Cancer J. Clin.*, vol. 71, no. 3, pp. 209–249, 2021.

[3] S. Z, “The natural products and healthy life,” *J. Tradit. Med. Clin. Naturop.*, vol. 07, no. 02, 2018.

[4] S. Almazov, P. Y. Sancar, M. Kürşat, O. Gedik, and Ş. Civelek, “Cytogenetic Investigation of Some Ranunculus L. Species Distributed in Bitlis and its Surroundings,” *Osmaniye Korkut Ata Üniversitesi Fen Bilimleri Enstitüsü Dergisi*, vol. 6, no. Ek Sayı, pp. 199–210, Dec. 2023, doi: 10.47495/okufbed.1149043.

[5] D.-C. Hao, P.-G. Xiao, H.-Y. Ma, Y. Peng, and C.-N. He, “Mining chemodiversity from biodiversity: pharmacophylogeny of medicinal plants of Ranunculaceae,” *Chin. J. Nat. Med.*, vol. 13, no. 7, pp. 507–520, 2015.

[6] H. Özçelik, “Endemik Ranunculus poluninii ve Ranunculus crateris Ranunculaceae Populasyonları Üzerinde Taksonomik ve Ekolojik Araştırmalar,” S*üleyman Demirel Üniv. Fen Dergisi*, vol. 11, no. 1, pp. 1–41, 2016.

[7] Y.-K. Goo, “Therapeutic potential of Ranunculus species (ranunculaceae): A literature review on traditional medicinal herbs,” *Plants*, vol. 11, no. 12, p. 1599, 2022.

[8] D. Mares, “Antimicrobial activity of protoanemonin, a lactone from ranunculaceous plants,” *Mycopathologia*, vol. 98, no. 3, pp. 133–140, 1987.

[9] T. Byambaa et al., “In vitro Study Results of the Ranunculus Repens L.’s Effect on Some Cancer Cells,” *In vitro*, vol. 29, no. 11, 2022.

[10] K. You, Y. Liu, L. Chen, H. Ye, and W. Lin, “Radix ranunculus temate saponins sensitizes ovarian cancer to Taxol via upregulation of miR let 7b,” *Exp. Ther. Med.*, vol. 23, no. 5, 2022.

[11] S. O. Udegbunam, R. I. Udegbunam, C. C. Muogbo, M. U. Anyanwu, and C. O. Nwaehujor, “Wound healing and antibacterial properties of methanolic extract of Pupalia lappacea Juss in rats,” *BMC Complement. Altern. Med.*, vol. 14, no. 1, 2014.

[12] N. Sharma, G. Arya, R. Kumari, N. Gupta, and S. Nimesh, “Evaluation of anticancer activity of silver nanoparticles on the A549 human lung carcinoma cell lines through Alamar blue assay,” *Bio Protoc.*, vol. 9, no. 1, 2019.

[13] F. M. Ausubel, R. Brent, R. Kingston, D. Moore, J. Smith, and K. Struhl, “Current Protocols in Molecular Biology,” *Current Protocols in Molecular Biology*, 1991.

[14] M. R. Green and J. Sambrook, Molecular cloning: a laboratory manual. V. 1. Cold Spring Harbor. N.Y.: *Cold Spring Harbor Laboratory Press*, 2012.

[15] F. Bray, M. Laversanne, E. Weiderpass, and I. Soerjomataram, “The ever-increasing importance of cancer as a leading cause of premature death worldwide,” *Cancer*, vol. 127, no. 16, pp. 3029–3030, 2021.

[16] W. Li, “Botanical drugs: The next new new thing?,” 2002. Available at: http://nrs.harvard.edu/urn-3:HUL.InstRepos:8965577 (accessed June 20, 2023).

[17] G. M. Cragg and D. J. Newman, “Plants as a source of anti-cancer agents,” *J. Ethnopharmacol.*, vol. 100, no. 1–2, pp. 72–79, 2005.

[18] M. C. Wani, H. L. Taylor, M. E. Wall, P. Coggon, and A. T. McPhail, “Plant antitumor agents. VI. Isolation and structure of taxol, a novel antileukemic and antitumor agent from Taxus brevifolia,” *J. Am. Chem. Soc*., vol. 93, no. 9, pp. 2325–2327, 1971.

[19] A. B. Kunnumakkara, P. Anand, and B. B. Aggarwal, “Curcumin inhibits proliferation, invasion, angiogenesis and metastasis of different cancers through interaction with multiple cell signaling proteins,” *Cancer Lett*., vol. 269, no. 2, pp. 199–225, 2008.

[20] M. Fang, T. Shinomiya, and Y. Nagahara, “Cell death induction by Ranunculus ternatus extract is independent of mitochondria and dependent on Caspase-7,” *3 Biotech*, vol. 10, no. 3, 2020.

[21] Narankhuu Ragchaasuren et al., “Antitumor Effects Of Phytochemicals Of Hot Three Plants On Gastric Adenocarcinoma,” *bioRxiv (Cold Spring Harbor Laboratory)*, Nov. 2021, doi: https://doi.org/10.1101/2021.11.21.469373.

[22] J. L. Rodriguez-Tudela et al., “EUCAST Definitive Document EDef 7.1: method for the determination of broth dilution MICs of antifungal agents for fermentative yeasts: Subcommittee on Antifungal Susceptibility Testing (AFST) of the ESCMID European Committee for Antimicrobial Susceptibility Testing (EUCAST),” *Clinical Microbiology and Infection*, vol. 14, no. 4, pp. 398–405, 2008.

[23] F. R. Cockerill and Clinical and Laboratory Standards Institute, Methods for dilution antimicrobial susceptibility tests for bacteria that grow aerobically: approved standard. Wayne, Pa: *Clinical and Laboratory Standards Institute*, 2012.

[24] E. K. Barbour, M. Al Sharif, V. K. Sagherian, A. N. Habre, R. S. Talhouk, and S. N. Talhouk, “Screening of selected indigenous plants of Lebanon for antimicrobial activity,” *Journal of Ethnopharmacology*, vol. 93, no. 1, pp. 1–7, Jul. 2004, doi: https://doi.org/10.1016/j.jep.2004.02.027.

[25] S. Nazir, “In vitro Screening of Ranunculus muricatus for Potential Cytotoxic and Antimicrobial Activities,” *Global Journal of Pharmacology*, 2014.

Bitlis Eren Üniversitesi Fen Bilimleri Dergisi
BİTLİS EREN UNIVERSITY JOURNAL OF SCIENCE
ISSN: 2147-3129/e-ISSN: 2147-3188
VOLUME: 13 NO: 2 PAGE: 400-407 YEAR: 2024
DOI:10.17798/bitlisfen.1404308

# Evaluation of the Contribution of Bayburt Tuffite (Bayburt Stone) Dust to the After Freeze-Thaw Strength Values of High Plasticity Clay Soils

Rıdvan KUL[1], Necmi YARBAŞI[2*]

[1] *Atatürk University, Graduate School of Sciences, Graduate student, Erzurum, Turkey*
[2] *Atatürk University, Faculty of Engineering, Civil Engineering Department, Erzurum, Turkey.*

*(ORCID: 0000-0003-1336-4471) (ORCID: 0000-0003-4259-1278)*

**Keywords:** Clay soil, Bayburt tuffite, strength, freeze-thaw

**Abstract**
In parallel with the increasing housing need in parallel with the population growth and the changing needs of the society depending on the continuous technological developments, the strength properties of the soils considered problematic such as high plasticity clay should be improved. In the last twenties when global climate changes started to be experienced, the improvement of the geotechnical properties of such soils that form the basis of engineering structures has become an important issue. Today, natural rocks are one step ahead of other additives in terms of being economical, sustainable and environmentally friendly. Based on this basic idea, in our study, Bayburt tuffite was added to the clay soil by powdering it at the rates of 5%, 10%, and 15% and the strength change after freezing-thawing was examined. The clay soil (CS) + Bayburt tuffite powder (BTP) mixture samples obtained at three different rates were cured in the laboratory environment for 7, 14 and 28 days. At the end of the curing period, the samples were subjected to +20ºC, -20ºC, 12 hours and 10 cycles in the freeze-thaw cabin and then the strength values were obtained with the Uniaxial pressure tester. The highest strength value after freezing-thawing was observed to increase by 29.55% in the CS + 5% BTP mixture cured for 28 days. As a result, in the light of the obtained data, it was concluded that this mixture ratio can be used as a foundation material in cold climate regions, shallow foundation depths and high plasticity clay soils.

## 1. Introduction

The strength properties of clayey soils that have not been sufficiently consolidated in the geological process and have weak geo-engineering properties can vary significantly under seasonal freeze-thaw cycles. Therefore, such clayey soils, which form the foundation or sub-base of engineering structures, have properties such as low bearing capacity, high plasticity, swelling, shrinkage, compressibility and low permeability due to the presence of the montmorillonite minera[1]. For this reason, the geotechnical properties of such high plasticity clay soils, which form the basis of engineering structures, need to be improved. In the last twenties, waste/residue materials, natural rocks and minerals, in addition to various chemicals and synthetic materials, have begun to be used significantly as additives in the improvement or strengthening of such soils.

In the modification of clay soils, waste/residue materials and natural rocks or minerals are widely used today as additives, both because they can reduce environmental pollution by reducing carbon dioxide emissions, which is a global problem, during production, and because they are economical and environmentally friendly [2-10].

In addition to natural, synthetic or various chemicals used within the scope of ground improvement, natural rocks and minerals are now frequently used in civil engineering because they are economical, sustainable, strength-increasing and environmentally friendly materials.

For this purpose, Tekin et al. (2012) in their study titled The Use of Bayburt Stone as an Improvement Material in Road Infrastructures,

---

[*] Corresponding author: nyarbasi@atuni.edu.tr

*Received:13.12.2023 Accepted:10.06.2024*

determined that Bayburt stone residue + Lime mixtures can be used as stabilization material in the sub-base layers of highways [11]. Yılmaz et al. (2015) used green Bayburt Stone mixtures to improve the usage properties of clay subbase layers [12], while Tekin (2016) created geopolymer composites using NaOH and marble, travertine, and volcanic tuff wastes as alkaline activators [13]. Additionally, Aykut (2017) used Bayburt Stone waste in the production of high-strength building bricks using the alkaline activator Sodium Hydroxide (NaOH) and geopolymerization method [14], while Taş et al. (2018) Bayburt tuffite obtained from fly ash and industrial wastes is used both as a material and to increase the strength of coarse or fine-grained materials with weak strength [15]. Tekin et al. (2018). In their study, it was determined that polynaphthalene sulfonate based superplasticizer can be used as a material in cements with white Bayburt stone addition [16].

The Bayburt Tuffite (Bayburt stone) powder used in this study is important in that it can be used to increase the strength of clayey soils, which are considered problematic soils, and to observe the change in strength values as a result of freezing and thawing.

It is of particular importance due to its contributions to today's world, especially where global climate changes have begun to take effect. The positive effect of the freeze-thaw effect on the strength (strengthening) of soils will make it possible to use it as both a building material and a shallow foundation material for engineering structures, especially in cold climate regions.

## 2. Material and Method

### 2.1. Clayey soil (CS)

CS materials were taken from the Oligocene aged unit of Oltu district of Erzurum province, northeastern Turkey. It is green in color and has the characteristics of a consolidated clayey rock [15].CS sample and granulometry graph in Figure 1, XRD and SEM images in Figure 2, and geotechnical properties are given in Table 1.

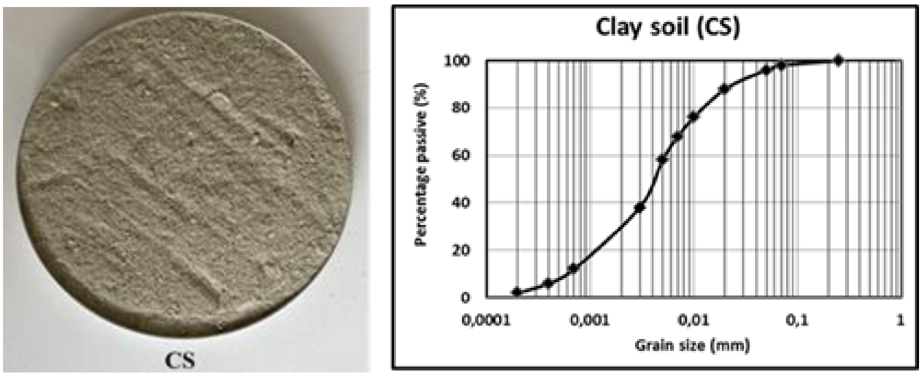

**Figure 1.** CS sample and granulometry

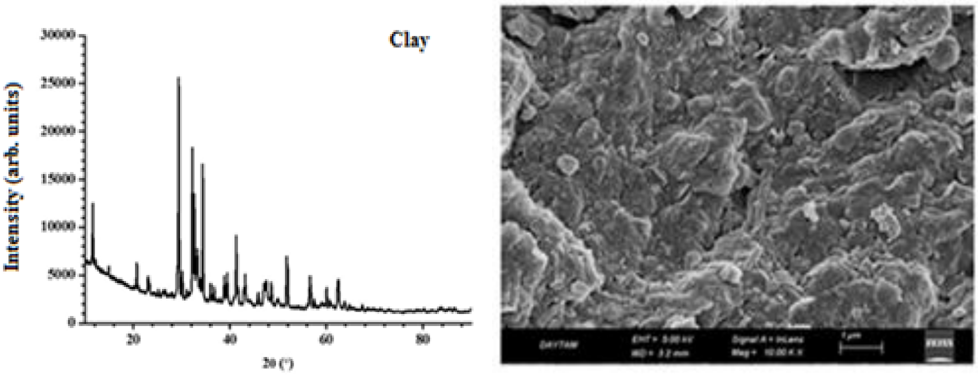

**Figure 2.** XRD graph and SEM image of CS

**Tablo 1.** Geotechnical properties of CS [17]

| Basic characteristics | Data |
|---|---|
| Specific weight | 2,64 |
| Sand (%) | 10,0 |
| Silt (%) | 58,0 |
| Clay (%) | 32,0 |
| WL (%) | 68 |
| PL (%) | 28 |
| PI (%) | 40 |
| [1]Optimum water amount, (%) | 25,8 |
| [1]Max. dry weight, (kN/m$^3$) | 14,1 |
| [2]Soil category | CH |

[1]Obtained from Standard Proctor Test.

[2]Soil class according to Unified Soil classification System (USCS)

## 2.2. Bayburt tuffite powder (BTP)

BTP is located as tuffite layers within the Yazyurdu Formation, which consists of Eocene-aged volcano-sedimentaries and carbonate units unconformably located on Jurassic-aged units cropping out in Bayburt province and its surroundings. It can be seen in yellowish, green spotted, yellow and green wavy colors. Bayburt stone has low hardness (2-3 on the Mohs scale) and chemically contains high amounts of silica ($Na_2(SiO_2)nO$) [11].

BTP sample and its granulometry are shown in Figure 3, XRD and SEM images are shown in Figure 4, and physico-chemical properties are shown in Table 2.

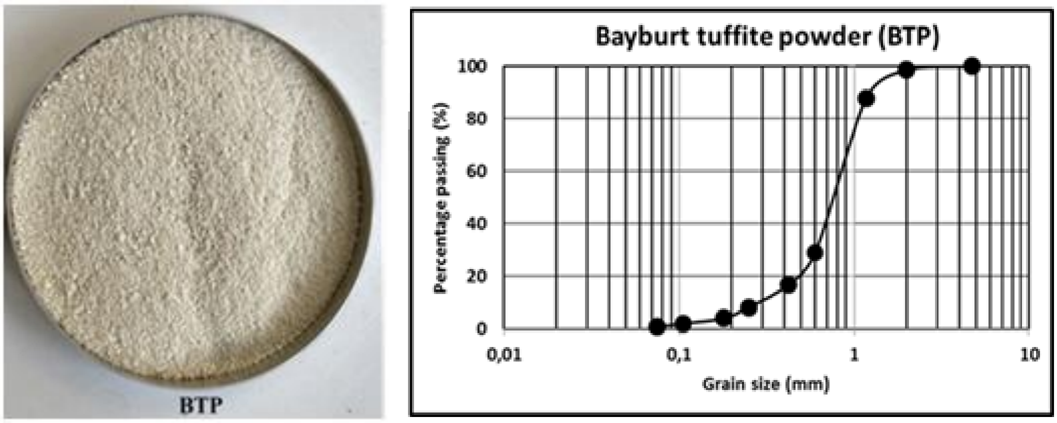

**Figure 3.** The BTP sample and granulometry

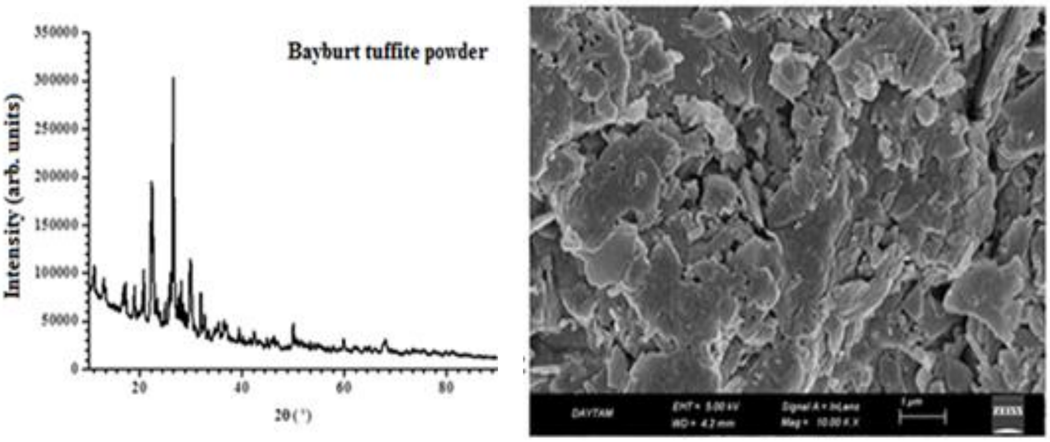

**Figure 4.** XRD and SEM images of BTP sample

**Tablo 2.** Physico-chemical properties of BTP [12]

| **Chemical properties** | **Data (%)** |
|---|---|
| Total $SiO_2$ | 69,96 |
| $Al_2O_3$ | 12,25 |
| $Fe_2O_3$ | 0,33 |
| CaO | 2,52 |
| MgO | 1,20 |
| $SO_3$ | 0,05 |
| $K_2O$ | 2,43 |
| $Na_2O$ | 0,57 |
| Cl | 0,0280 |
| **Physical properties** | **Data** |
| Specific weight (g/cm$^3$) | 2,31 |
| Surface area (cm$^2$/g) | 7193 |
| Activation | 8,8 |

## 2.3. Testing Procedures

The CS samples used in this study were obtained by excavating from the Oligocene-aged sedimentary unit in the west of the Oltu (Erzurum) district, from a depth of 0.75 m from the surface. The clay soil samples brought to the laboratory environment were dried in an oven at 105±5ºC for 24 hours, and then the hardened grains were ground in the Los Angeles machine at 6000 rpm.

Bayburt tuffite (Bayburt stone), which constitutes the second important element of this study, was obtained from rocks deposited in Eocene-aged lacustrine basins that crop out in large areas in Bayburt province and its immediate surroundings. After the yellow-white colored (yellowish) BTP was broken and disintegrated, it was ground into powder at 6000 rpm in the abrasion device.

CS and BTP mixture samples were obtained under dry environmental conditions by adding BTP at the rates of 5%, 10%, and 15% of the dry weight of the CS sample. Mixing proportions are shown in Table 3. The mixtures were mixed manually for at least 3 minutes with the necessary precision. Each mixture was compacted under standard proctor energy at the optimum water content determined by the compaction test. The compaction test results of the mixture samples are shown in Table 4.

**Table 3.** Mixing and ratios

| **Mixtures/Ratios** | **CS (%)** | **BTP (%)** |
|---|---|---|
| MIX0 (CS) | 100 | --- |
| MIX1 (CS+5% BTP) | 95 | 5 |
| MIX2 (CS+10% BTP) | 90 | 10 |
| MIX3 (CS+15% BTP) | 85 | 15 |

**Table 4.** Compaction test results of mixtures

| **Samples** | **Max. dry weight (g/cm$^3$)** | **Opt. water amount (%)** |
|---|---|---|
| MIX1 | 1,330 | 35,7 |
| MIX2 | 1,294 | 34,2 |
| MIX3 | 1,328 | 35,0 |

### 2.3.1. Compaction (Standard proctor) test

Standard proctor testing was performed according to ASTM D 698-12 (2021) [18] standards. In this test, optimum moisture content and maximum dry volume weight values are determined from the graph obtained from the relationship between dry unit volume weight and moisture content.

### 2.3.2. Uniaxial compressive strength (UCS) test

UCS values of BTP-doped CS samples were obtained according to ASTM D 2166-06 (2010) [19] standards. Determination of strength values was carried out in a uniaxial compression device on cylindrical samples (35 mm-70 mm) compressed at optimum moisture content.

### 2.3.3. Freezing and thawing (F-T) test

F-T tests were performed with a programmable freeze-thaw cabinet according to ASTM D 559-03 (2012) [20]. The samples were subjected to F-T tests at +20ºC, -20ºC, 12 hours, and 10 cycles.

### 2.3.4. Image analyzes

In order to see and evaluate the interaction between CS and BTP, XRD and SEM image analysis of natural CS and BTP reinforced mixture samples were performed using a scanning electron microscope D8 AXS XRD Spectrometer and Sigma 300 Zeiss Gemini FE-SEM instruments. These analyzes were carried out in the DAYTAM Laboratory established at Atatürk University.

### 2.3.5. Brunauer-Emmett-Teller (BET) analysis

The surface area and micropore size distribution of CS+BTP mixture samples were determined by BET analysis. These analyzes were performed with Micromeriti CS 3-Flex version 5.00 device in Atatürk University DAYTAM Laboratory.

## 3. Results and Discussion

### 3.1. Before-After F-T, UCS analysis

As shown in Table 3, UCS values were obtained after CS soil mixtures reinforced with three different ratios of BTP were cured in a +20°C laboratory environment for 7, 14 and 28 days and with a uniaxial compressive device. When the UCS values were compared with the material (witness) MIX0, it was seen that the highest strength was reached in the MIX1 mixture with a strength increase of 34.38% at the end of 28 days of curing. This mixture was followed by the MIX2 mixture with an increase of 18.75% and the MIX3 mixture with a 10.94% increase under the same conditions. The UCS graph of CS soil mixtures reinforced with BTP before freeze-thaw is shown in Figure 5 [21].

F-T tests were performed with a programmable freeze-thaw cabinet. CS soil mixtures reinforced with BTP at three different rates (5%, 10%, and 15%) were cured for 7, 14, and 28 days and then subjected to F-T test for 12 hours and 10 cycles at +20°C, -20°C. At the end of this test, UCS values were obtained with a uniaxial free pressure device. It was observed that the highest UCS strength value of BTP added CS samples after F-T was in the MIX1 mixture with an increase rate of 29.55%. This mixture is followed by the MIX2 mixture with 13.18% and the MIX3 mixture with 2.73%. The UCS distribution of CS + BTP mixture samples after F-T is Show in figure 5.

When the strength values before and after freeze-thaw were compared, it was seen that the lowest strength loss occurred in the MIX1 mixture with 4.83% after 28 days of curing. The other lowest strength losses following this mixture were 5.57% in the MIX2 mixture and 8.21% in the MIX3 mixture after 28 days of curing. In addition, the strength values obtained with a 28-day cure and 5% BTP mixture showed that the strength values both before and after F-T were the highest. It was seen in the data that increasing the BTP ratio (10%, 15%) in clayey soils caused a decrease in the strength of the mixtures.

Increases were observed in the strength values of the CS+BTP mixture both before and after freezing-thawing. In the graphical representations in Figure 5, it is seen that adding 5% BTP to CS significantly increases the strength of the sample, and the strength values in CS mixtures with 10% and 15% BTP addition decrease compared to CS. Mixture with 5% BTP addition. While the curing period had a positive effect on the development of this situation, the increase in the BTP rate caused strength decreases. However, when compared to the CS values, which is the main material, it is seen that the increase in strength values occurs at three different rates. As a result, the addition of 5% BTP material to CS material is the mixture in which the highest strength values are obtained before and after freezing-thawing.

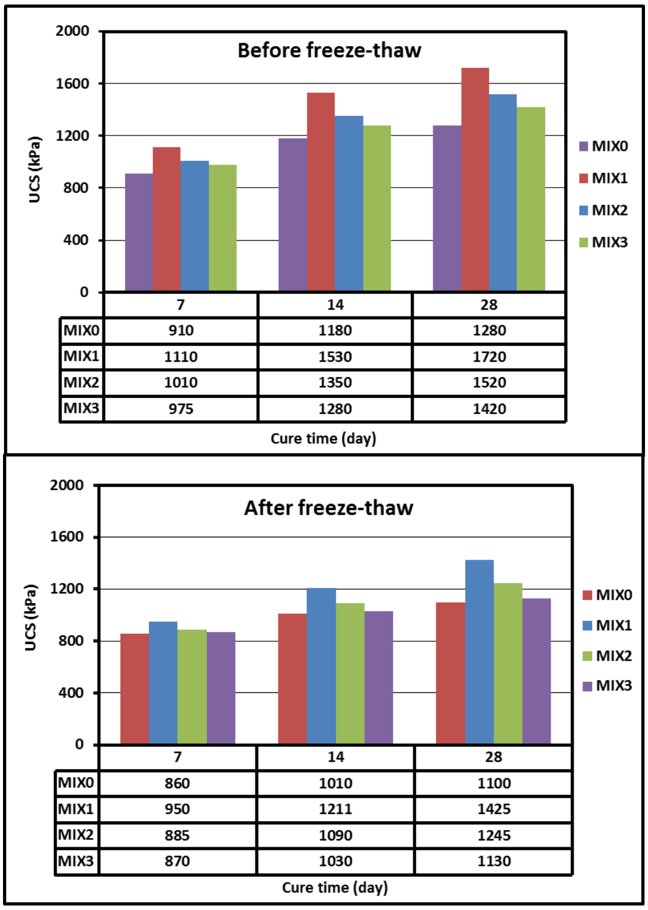

|  | 7 | 14 | 28 |
|---|---|---|---|
| MIX0 | 910 | 1180 | 1280 |
| MIX1 | 1110 | 1530 | 1720 |
| MIX2 | 1010 | 1350 | 1520 |
| MIX3 | 975 | 1280 | 1420 |

|  | 7 | 14 | 28 |
|---|---|---|---|
| MIX0 | 860 | 1010 | 1100 |
| MIX1 | 950 | 1211 | 1425 |
| MIX2 | 885 | 1090 | 1245 |
| MIX3 | 870 | 1030 | 1130 |

**Figure 5.** UCS distribution of samples before-after F-T

### 4.2. XRD analyzes

XRD plots of BTP-reinforced CS samples after F-T are shown in Figure 6. In the after F-T graphs of MIX0, MIX1, MIX2 and MIX3 samples, peaks are observed at the angles corresponding to 16°, 26°, 28° and 30°. It is thought that the changes in the intensity of these peaks are caused by the Si (silicon) mineral (approximately 70% SiO2), which is proportionally more abundant in BTP. Because the effect of the silicon mineral is observed in the XRD graphs after F-T, which reduces the peak intensities of the minerals in the clayey soil.

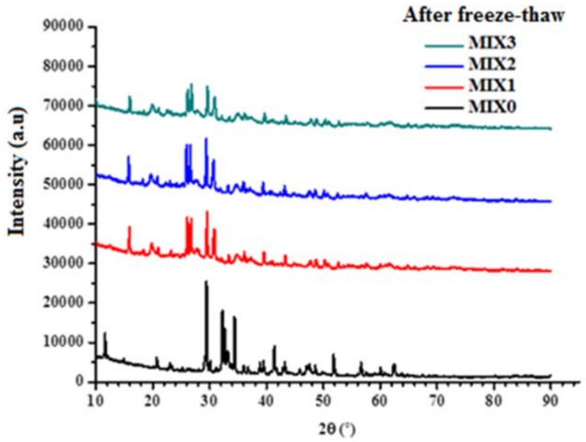

**Figure 6.** XRD graphs of samples after F-T

### 4.3. SEM analyzes

SEM images of BTP-enhanced CS mix samples (MIX0-2, MIX1-2, MIX2-2, MIX3-2) after FT are shown in Figure 7. In the SEM image of CS shown in MIX0-2 after FT, it is seen that the effect of F-T causes fractures and cracks in the internal structure of CS. BTP contribution to CS In parallel with the increase in BTP ratio, it was observed that fractures and cracks were more prominent in MIX2-2 and MIX3-2 mixtures after F-T, but this effect was much less in the MIX1-2 mixture. The reason why the highest strength values in unconfined compressive strength are obtained in MIX1-2 is also revealed in SEM images.

### 4.5. Brunauer-Emmett-Teller (BET) analysis

The surface area measurements, micropore size, and pore size distribution of pelleted mixture samples after F-T was determined by the BET analysis method. With this method, the surface area ($m^2/g$) was calculated by determining the amount of nitrogen gas required to cover the sample surface with a single molecular layer. The surface area measurements of the mixtures after F-T are shown in Table 5 and the pore size distribution graph is shown in Figure 8. When the surface area data of the mixture samples in Table 5 are examined; It was observed that as the BTP ratio in the CS increased, the surface areas decreased. When the pore distribution graph shown in Figure 8 is examined; It has been observed that the pore distributions of the mixture samples have a concentrated micro and mesoporous structure in the range of 1-20 nm.

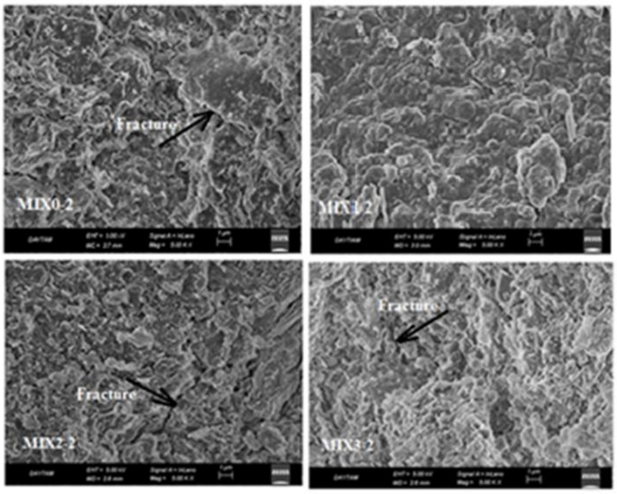

**Figure 7.** SEM images of the samples after F-T

**Table 5.** BET surface area measurement results of the mixtures after F-T

| Mixtures | BET Surface area ($m^2/g$) |
|---|---|
| MIX1 | 43.8546 |
| MIX2 | 40.5498 |
| MIX3 | 40.3348 |

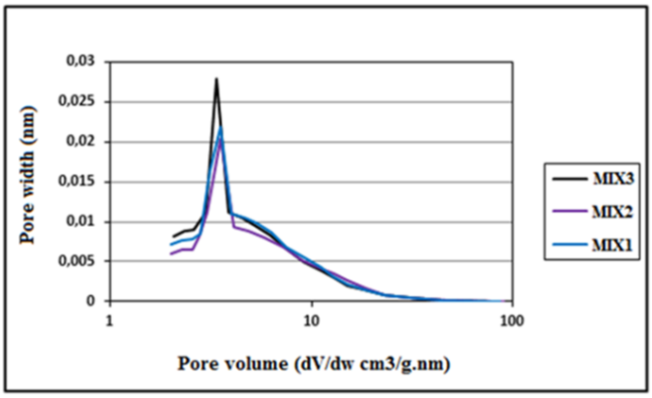

**Figure 8.**The pore distributions of the mixtures after F-T

### 5. Conclusion and Suggestions

The effects of three different mixture samples of BTP reinforced CS on strength after F-T were determined with a UCS device. The structural properties of the samples under the influence of F-T were investigated by XRD and SEM analysis, and their surface areas and pore structure were examined by BET analysis.

The highest strength value of CS soil reinforced with BTP before F-T occurred in the MIX1 mixture with an increase rate of 34.38%. This mixture was followed by MIX2 with an increase rate of 18.75% and MIX3 with an increase rate of 10.94%. After F-T, the highest strength increase occurred in the MIX1 mixture with 29.55%, followed by the MIX2 mixture with a 13.18% increase rate and the MIX3 mixture with a 2.73% increase rate.

BTP added to CS affected the main structure of the clay. This effect is achieved by Si (Silicon), the dominant mineral of BTP. As a result of this effect, it has been observed that the structure of the clay soil becomes more compact as a result of the decrease in porosity. The compact structure is clearly seen in the reduction of the intensity of the peaks in both XRD graphs and SEM images.

In addition, when the surface area and pore distributions of the mixture samples after F-T were examined by BET analysis, it was observed that as the BTP mixture ratio increased in CS, the surface areas decreased and the pore distributions had a concentrated micro and mesoporous structure in the range of 1-20 nm.

As a result, it was concluded that BTP-added CS soils can be used as base or subbase material, especially in cold climate regions and engineering applications. It is evaluated that this study will contribute to future studies on the changes in the strength values of CS+BTP mixtures, especially under the freeze-thaw effect.

## Contributions of the authors

Author 1: Experimental study.

Author 2: Methodology, writing, supervising, reviewing and editing.

## Conflict of Interest Statement

There is no conflict of interest between the authors.

## Statement of Research and Publication Ethics

The study is complied with research and publication ethics

## Acknowledgment

This experimental research was supported by Atatürk University BAP unit with ID number 10401 and code FYL-2022-10401.

## References

[1] J. Zhang, X. Cao, “Stabilization of expansive soil by lime and fly ash”. *J. Wuhan Univ. Technol.* Vol. 17, no. 4, pp.73–77. 2022. Doi:10.1007/BF02838423.

[2] A.J. Puppala, C. Musenda, “Effects of fiber reinforcement on strength and volume change in expansive soils”. *Transportation Research Record* 134-140 (Paper No: 00-0716). 2002.

[3] S.M. Hejazi, M. Sheikhzadeh, S.M. Abtahi, and A. Zadhoush, “A Simple Review of Soil Reinforcement by Using Natural and Synthetic Fibers”, *Construction and Building Materials,* vol. 30, pp.100-116. 2012. Doi: 10.1016/j.conbuildmat.2011.11.045.

[4] N. Yarbasi, “Performance of granular soils reinforced with obsidian (volcanic glass) additives in different proportions subjected to freeze-thaw”, *Pamukkale University Journal of Engineering Sciences* vol. 25, no.6, pp.764-767. 2019. Doi:10.5505/pajes.2019.39049.

[5] N. Yarbaşı, E. Kalkan, “Use of Waste Material (Oltu Stone Waste) for Soil Stabilization”. *International Journal of Latest Technology in Engineering, Management & Applied Science (IJLTEMAS)* Volume VIII, Issue XI, November 2019 | ISSN 2278-2540. 2019.

[6] E. Kalkan, N. Yarbasi, Ö. Bilici,“The Effects of Quartzite on the Swelling Behaviors of Compacted Clayey Soils”. *International Journal of Earth Sciences Knowledge and Applications* vol. 2, no. 2 pp. 92-101. 2020.

[7] N. Yarbaşi, “Effect of Freezing-Thawing on Clayey Soils Reinforced with Human Hair Fibers”. *Journal of Natural Fibers,* vol.17, no. 6, pp. 921-931.2020. https://doi.org/10.1080/15440478.2019.1690614.

[8]. N. Yarbasi, E. Kalkan, “The Mechanical Performance of Clayey Soils Reinforced with Waste PET Fibers”. *International Journal of Earth Sciences Knowledge and Applications* vol. 2, no. , pp. 19-26. 2020.

[9] C. Ince, S. Derogar, N.T. Tiryakiog, Y.C. Toklu, “The influence of zeolite and powdered Bayburt stones on the water transport kinetics and mechanical properties of hydrated lime mortars”. *Construction and Building Materials* vol. 98, pp. 345–352. 2015. https://doi.org/10.1016/j.conbuildmat.2015.08.118.

[10] A.O. Yılmaz, İ. Alp, C. Demir, M. Arslan, H. Kolaylı,“Physical, Mechanical, Petrographic Properties of Bayburt Tuff (Bayburt Stone)”, *TMMOB, Chamber of Mining Engineers*. 2005.

[11] Tekin, H.A. Kamiloglu, E. Yurdagül, “Usage Of Bayburt Stone In Road Infrastructures As A Improvement Material” Conference: *Internaıional Conference On Traffic And Transport Engineerıng,* Belgrade, Volume: 1, October 2012.

[12] F. Yılmaz, H.A. Kamiloglu, and E. Sadoglu, “Soil Stabilization with Using Waste Materials against Freezing Thawing Effect”. *Acta Physica Polonica* A, Vol. 128, Special issue of the International Conference on Computational and Experimental Science and Engineering (ICCESEN 2014). 2015.

[13] I. Tekin, “Properties of NaOH activated geopolymer with marble, travertine and volcanic tuff wastes”. *Construction and Building Materials* vol. 127, pp. 607–617. 2016. http://dx.doi.org/10.1016/j.conbuildmat.2016.10.038.

[14] C. Aykut, “Investigation of the usability of Bayburt stone waste in the production of geopolymer bricks”. Master's thesis, Bayburt University (Turkey), Institute of Science and Technology. 2017.

[15] M. Taş, D. Fidan, F. Yılmaz, “Soil Stabilization with Fly Ash and Bayburt Stone”, *Bayburt University (Turkey) Journal of Science* vol 1, no. 1., 2018.

[16] I. Tekin, D. Tekin. “ Effect Of The Polynaphtalene Sulfonate Based Superplasticizer On Mechanical And Physical Properties Of Blended Cement Replaced With Bayburt Stone At Different Fineness”, *Pamukkale Univ Muh Bilim Derg,* vol. 24, no. 3, pp. 419-425, 2018.

[17] E. Kalkan, M.S. Bayraktutan, “Geotechnical evaluation of Turkish clay deposits”: a case study in Northern Turkey. *Environmental Geology* vol. 55, no.5, pp. 937-950. Doi: 10.1007/s00254-007-1044-8. 2008.

[18] ASTM D 698-12, “Standard Test Methods for Laboratory Compaction Characteristics of Soil Using Standard Effort” (12,400 ft-lbf/ft$^3$ (600 kN-m/m$^3$). 2021.

[19] ASTM D 2166-06, “Standard Test Method for Unconfined Compressive Strength of Cohesive Soil”. 2010.

[20] ASTM D 559-03, “Standard Test Methods for Wetting and Drying Compacted Soil-Cement Mixtures” (Withdrawn 2012).

[21] N. Yarbaşı, R.Kul, “Compressive Strength Of Clayey Soils Reinforced With Bayburt Stone (Bayburt Tuffite)”, International Congress on Innovation Technologies & Engineering "On the occasion of the 40th Anniversary of Ege University, Graduate School of Natural and Applied Sciences" 207-211, Ege University, Izmir, Türkiye, 2022.

Bitlis Eren Üniversitesi Fen Bilimleri Dergisi
BİTLİS EREN UNIVERSITY JOURNAL OF SCIENCE
ISSN: 2147-3129/e-ISSN: 2147-3188
VOLUME: 13 NO: 2 PAGE: 408-417 YEAR: 2024
DOI:10.17798/bitlisfen.1407941

# Estimating the Expected Influence Capacities of Nodes in Complex Networks under the Susceptible-Infectious-Recovered Model

Aybike ŞİMŞEK[1*]

[1]*National Defence University Turkish Military Academy, Department of Computer Engineering*
*Devlet Mah. Kara Harp Okulu Cd. 06420 Ankara / Türkiye,*
*(ORCID:0000-0002-1033-1597)*

**Keywords:** Complex networks, Susceptible-Infectious-Recovered model, Expected influence, Centrality Measures, Node ranking.

**Abstract**
In recent years, epidemic modeling in complex networks has found many applications, including modeling of information or gossip spread in online social networks, modeling of malware spread in communication networks, and the most recent model of the COVID-19 pandemic. If the information disseminated is accurate, for example, maximizing its distribution is desirable, whereas if it is a rumor or a virus, its spread should be minimized. In this context, it is very important to identify super-spreaders that maximize or minimize propagation. Lately, studies for detecting super-spreaders have gained momentum. Most of the studies carried out aim to distinguish the influences of nodes under a specific propagation model (such as SIR) using network centrality measures and subsequently, to rank the nodes accordingly. However, in this study, we developed an algorithm that approximates the expected influence of nodes under the popular SIR model. By considering the behavior of the SIR model and only the shortest paths between nodes, the algorithm ranks the nodes according to this approximated value. Our developed algorithm is named the Expected Value Estimation (EVE). The main contribution of this study is that under the SIR model, the effects of nodes can be calculated quickly and realistically, regardless of the structure of the network. We compared the performance of EVE, using different SIR settings on real-world datasets, with that of many current well-known centrality measures. The experimental studies demonstrated that the solution quality (ranking capability) of EVE is superior to that of its competitors.

## 1. Introduction

Complex networks are highly suitable tools for modeling the real world. They have applications in many different fields such as natural sciences [1], health [2], cyber security [3], economics [4], and social networks [5]–[7]. Moreover, epidemic modeling in complex networks has attracted attention in recent years for its many practical benefits. The spread of a virus outbreak (such as Covid-19) can be estimated and precautions can be taken based on this [8]. By modeling the spread of gossip on the social network, the spread can be prevented [9], [10]. Or, the desired information may reach the maximum number of people [11]. Whether you want to minimize the spread of gossip or maximize the spread of information, in any case, in order to do so, the set having the smallest number of the most influential individuals should be identified [12], [13]. The influences of these individuals under certain epidemic models (such as SIR) should be calculated in order to identify the smallest number of the most influential individuals (i.e., key players). For this, it is necessary to model the propagation by selecting each node individually as the seed. Since propagation models are stochastic models, they must be repeated many times (e.g., about 10.000 iterations) and the average value taken. This operation requires very high

---

[*]Corresponding author: *aysimsek@kho.msu.edu.tr*

*Received: 21.12.2023, Accepted: 20.03.2024*

processing power. On the other hand, researchers have noticed a correlation between the influence capacity of the nodes and network centrality measures, which have been used for a long time to determine the importance of nodes in complex networks. The basic expectation here is that as a centrality measure increases, the influence capacity increases, and as the centrality measure decreases, the influence capacity decreases. Since the calculation of centrality measures requires much less processing power than modeling the propagation thousands of times, studies have turned to this area. For this purpose, basic centrality measures such as Degree, Closeness, Betweenness [14], Katz [15], PageRank [16] were used and new centrality measures were developed. However, many of the measures developed only considered the local and global impacts of the nodes [17]–[22] or network communities [18], [19], [23]–[25]. Recently, another approach has been adopted that combines multiple centrality measures to develop new hybrid centrality measures [26]–[34]. However, many of these studies ignore the dynamics of the propagation model. Unlike other studies the dynamics-sensitive (DS) centrality combines network structure and epidemic model dynamics for ranking nodes [35]. The DS considers all possible random walks between two nodes for estimating the infectious probabilities of nodes. This method may work well for small beta values. However, it will overestimate the infection capabilities of nodes for larger beta values.

In this study, we developed an algorithm that ranks nodes according to their influence capacity, taking into account the propagation behavior in the Susceptible-Infectious-Recovered (SIR) model. We named our developed algorithm the Expected Value Estimation (EVE) because it is based on approximating the expected influence of each node. It is worth mentioning here that the EVE algorithm does not calculate the importance of nodes contrary to the centrality measures. Instead, it calculates the approximate expected influence of the nodes under the SIR model and ranks the nodes accordingly.

### 1.1. Motivation

In the literature, centrality measures are proposed to detect influential nodes in complex networks. However; complex networks show very diverse characteristics, and therefore while a particular centrality measure can well distinguish influential nodes in a given network; it may not be able to on another network. In addition, the influence levels of nodes in the same network may vary under different propagation models. Therefore, trying to determine the influence levels of nodes only based on their centrality will not yield successful results in every network. When determining the influence levels of nodes, it is necessary to consider the dynamics of the given propagation model. Under certain epidemic models (such as SIR), it is necessary to perform heavy Monte-Carlo simulations to distinguish the influence of nodes However, if the dynamics of the SIR propagation model are taken into account, the process can be simplified by ignoring some of the behaviors of this model. Thus, the approximate expected influence of nodes can be calculated and used to rank nodes (similar to a centrality measures). With this motivation, by considering the behavior of the SIR model and only the shortest paths between nodes, the EVE algorithm ranks the nodes according to this approximated value.

## 2. Preliminaries

Before discussing the details of EVE, it would be useful to give some preliminary information.

Let $G = (V, E)$ be an undirected unweighted graph (network). Here, $V$ is the set of nodes (vertices), and $E$ is the set of edges (links).

### 2.1. Definition 1 (Susceptible-Infectious-Recovered Model)

The Susceptible-Infectious-Recovered (SIR) model is a well-known model used for population-based epidemic modeling. In recent years, due to their popularity, SIR and SIR variations have been applied to network topologies [36]. In the SIR model, nodes are found in one of three states: Susceptible (S), Infected (I), and Recovered (R). Nodes in state S are nodes that have the potential to become infected. Nodes in state I are nodes that have already been infected. Nodes in state R are recovered nodes. The transition of nodes between states occurs according to certain probabilities. A node in state I continues to infect its neighbors in state S with a certain probability as long as it remains in state I. This probability of infection is known as $\beta$. In other words; Nodes in state S are infected with probability $\beta$ by nodes in state I. Once a node goes to state I, it cannot return to state S again. Nodes in state I goes to state R with a certain probability. This probability of recovery is known as $\gamma$. Once a node goes to state R, it cannot return to either state S or state I again.

Initially, all other nodes are in a susceptible state, except for nodes that carry the disease (i.e., those that are infected). Starting from the nodes that are initially infected (called ‘seed nodes’), the disease spreads over the network. After a certain period of time, there are no remaining infected nodes on the network and thus, the model is terminated.

### 2.2. Definition 2 (Kendall's tau Ranking Correlation Coefficient) [37]

Let $(a_i, b_i)$ and $(a_j, b_j)$ be tuples of joint A and B ranking lists. If $a_i > a_j$ and $b_i > b_j$ or $a_i < a_j$ and $b_i < b_j$ , then the tuples are concordant. If $a_i > a_j$ and $b_i < b_j$ or $a_i < a_j$ and $b_i > b_j$ , then the tuples are discordant. If $a_i = a_j$ or $b_i = b_j$ , then the tuples are neither concordant nor discordant. Finally, tau is defined as in Equation (1).

$$tau = \frac{N_c - N_d}{0.5N(N-1)} \qquad (1)$$

Here, $N_c$ is the number of concordant pairs, $N_d$ is the number of discordant pairs, and $N$ is the number of all combinations. Positive $tau$ values indicate a positive correlation, and negative $tau$ values indicate a negative correlation.

### 2.3. Definition 3 (Ranking Monotonicity) [38]

When you add a figure to your article, please refer to the relevant picture in the text, such as Figure 1. When using shapes, be attentive to use the Shape Description style. Additionally, there should be a 5 nk space between the figure and its caption [6], [7]. Monotony is a metric of how well the centrality measure assigns each node to different rank levels. The ranking monotonicity (RM) will be '1' if all nodes are assigned to a different ranking level. If all nodes are assigned to the same ranking level, the RM will be '0'. Of course, for a centrality measure, the closer it is to RM 1, the better. The RM is calculated as follows:

$$RM(L) = \left(1 - \frac{\sum_{r \in L} n_r (n_r - 1)}{n(n-1)}\right)^2 \qquad (2)$$

Here, n is the length of the L-ranking list and $n_r$ is the number of elements assigned to the same r rank.

## 3. EVE

Generally speaking, in the SIR model, a node affects its neighbor nodes with a probability β. If not its direct neighbor, it is likely to affect its neighbors' neighbors with probability (β × β). If the network is a tree, the probability of a node influencing another l-hop away node can be calculated as $\beta^l$ since there can be only one path between each pair of nodes. Thus, the expected influence of a node can be calculated using its distance to all other reachable nodes by this node as the sum of $\beta^l$ values. However, real networks rarely exhibit tree structures. Hence, there can be many different paths of different lengths between any two nodes. It is also costly to use all paths to all other nodes to calculate the expected influence of a node. However, the probability of one node influencing another node decreases exponentially with the distance between them, although in practice, the value of $\beta$ is much less than 1. The natural consequence of this is $\beta^n \gg \beta^{n+1}$, where $n \in \mathbb{N}^+$. Based on this information, the expected probability of a node influencing another node can only be approximated using the shortest path between these two nodes. This is because the probability of influence calculated for paths other than the shortest path will be much lower. The calculated values can be used to distinguish the influence capacities of the nodes (similar to a centrality measure).

The working principle of EVE is based on expected value calculation. Therefore, it is useful to first look into the details of how a node infects its neighbor nodes in SIR and how this node recovers. This situation is shown for one iteration in Algorithm 1 [39]. The node u in the algorithm was initially selected as the infected node or one infected at any point in time.

**Algorithm 1. Infection and Recover States of SIR**

```
sn = susceptible neighbors of node u
for each v in sn
    rnd = random number in [0.0,1.0)
    if rnd < $\beta$ then
        mark v as infected
end for
rnd = random number in [0.0,1.0)
if rnd < $\gamma$ then
    mark u as recovered
```

According to Algorithm 1, the node u infects its neighbors with probability β. After the node u infected its neighbors, this node is recovered with probability γ. If $\gamma$ = 1, the node u has absolutely only one attempt to infect its neighbors since it will not be in the Infected state in the next iteration. If $\gamma$ = 0.5, roughly, the node u has two attempts to infect its neighbors since it will be in the Infected state in the next iteration with probability 0.5. If we generalize, the node u has at least ${}^{1}\!/_{\gamma}$ attempts to infect its neighbors. Since the probability of the node u infecting its neighbors is β, the expected value of infecting a neighbor by node u would be $1/\gamma$ times β; that is, $\beta/\gamma$.

Let us explain the situation in Figure 1, where different topologies are shown. Notice that Figure 1-a, b, and c are trees. Therefore, there is only one path between all nodes.

In Figure 1-a, let the node u initially be selected as a seed (infected). The expected influence value (ev) of the node u becomes ev(u) = 1 + $\beta/\gamma$. Here, 1 has been added as node u is already infected. Figure 1-b shows the expected influence value (ev) of the node as:

$$\text{ev(u)} = 1 + {}^{\beta}/_{\gamma}\,(\text{probability of } u \text{ infecting } y).$$

In order to infect the node y, the node u must infect the node x. Next, the node x must infect the node y. The probability of these two events happening together can be obtained by multiplying the probabilities of their respective occurrence. Thus, the expected value of u infecting the node y is $\left({}^{\beta}/_{\gamma} \times {}^{\beta}/_{\gamma}\right)$, i.e., $\left({}^{\beta}/_{\gamma}\right)^2$. Thus, the expected influence value (ev) of the node u becomes ev(u) = $1 + {}^{\beta}/_{\gamma} + \left({}^{\beta}/_{\gamma}\right)^2$.

For Figure 1-c, the expected influence value (ev) of the node u is ev(u) = $1 + 2 \times \left({}^{\beta}/_{\gamma}\right) + 2 \times \left({}^{\beta}/_{\gamma}\right)^2$.

The expected value of a node infecting another node decreases exponentially with the distance between them. If we generalize the ev calculation, we get Equation (3).

$$ev(u) = 1 + nn_1 \times \left({}^{\beta}/_{\gamma}\right) + nn_2 \times \left({}^{\beta}/_{\gamma}\right)^2 + \cdots + nn_h \times \left({}^{\beta}/_{\gamma}\right)^h \qquad (3)$$

Here, nn is the size of the set of node u's neighbors at h-hop distance. The situation is a little different in Figure 1-d. The node y is both a 1-hop and a 2-hop neighbor of the node u. Therefore, the node u can infect the node y directly, as well as through the node x. Thus, the expected value of node u infecting the node y is the sum of these two possibilities, or 1 at most. Ultimately, the expected influence of the node u becomes ev(u) = $1 + \left({}^{\beta}/_{\gamma}\right) + max\left\{1, \left(\left({}^{\beta}/_{\gamma}\right) + \left({}^{\beta}/_{\gamma}\right)^2\right)\right\}$. Let us explain why we use the max function here. For example, if ${}^{\beta}/_{\gamma} = 1$, the expected value of node u infecting the node y would be 2. However, this value can be at most 1, since once a node is infected, it cannot be infected again.

In large and complex networks, there can be many different paths having different lengths from one node to another. It is quite costly to consider all paths. Instead, only the shortest paths can be considered. Thus, as in Figure 1-e, the (x, y) edge is ignored and the approximate ev can be calculated using Equation (3). However, instead of changing the structure of the graph, only neighbors with h-shortest path hop distance can be included when creating $nn_h$sets. Thus, it is guaranteed that $nn_a \cap nn_b = \emptyset$ ; here $a \neq b$ and $a, b \in \{1 \ldots h\}$. If we named as $spn_h$ to the sets created by selecting only neighbors with h-shortest path hop distance, we can calculate the measure we call EVE as in Equation (4).

$$EVE(u) = 1 + spn_1 \times \left({}^{\beta}/_{\gamma}\right) + spn_2 \times \left({}^{\beta}/_{\gamma}\right)^2 + \cdots + spn_h \times \left({}^{\beta}/_{\gamma}\right)^h \qquad (4)$$

Equation (4) does not take into account paths other than the shortest paths. In the literature, β is usually taken as very small (e.g., ≤0.1) and $\boldsymbol{\gamma}$ as large (e.g., = 1). The corollary of this is $\left({}^{\boldsymbol{\beta}}/_{\boldsymbol{\gamma}}\right)^{\boldsymbol{l}} \gg \left({}^{\boldsymbol{\beta}}/_{\boldsymbol{\gamma}}\right)^{\boldsymbol{l+1}}$, where $\boldsymbol{l} \in \mathbb{N}^+$. Thus, it can be considered reasonable to ignore paths other than the shortest paths. In practice, EVE can be calculated as in Algorithm 2. The Sort function sorts the dictionary in descending order. The Power function takes two parameters such as x and y and returns the value $x^y$. As a result, Function EVE returns the list of nodes sorted in descending order according to their EVE values.

**Algorithm 2. EVE**

```
FunctionEVE(G: Graph, $\beta, \gamma$)
Begin
L = {} // L is a dictionary as L[node]=EVE
SP = dictionary of all pairs shortest path of G.
// If there is at least one path between two nodes then
// SP[node,node] is a number. // Otherwise, it is ∞.
V = G's set of nodes
for each u in V
   EVE = 0
   for each v in V
      if SP[u,v]≠ ∞ then
         EVE = EVE + Power($\beta$ / $\gamma$, SP[u,v])
     L[node]=EVE
Sort L descending order by value
return key list of L
End
```

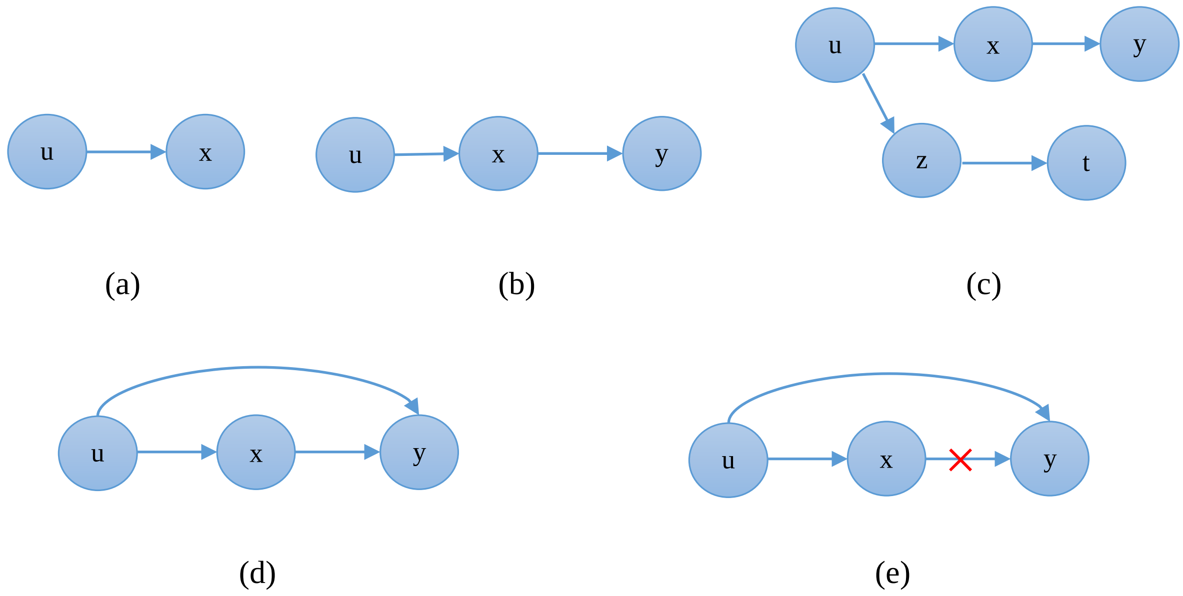

**Figure 1.** Sample graphs for EVE calculation: (a), (b), (c) every node belongs to only one h-hop neighborhood, (d), (e) node-y belongs to different h-hop neighborhoods.

## 4. Experiments

To evaluate the performance of EVE, we determined five competitor centrality measures and experimented with different SIR settings over four real-world datasets. First, let us look at the competing centrality measures and datasets.

### 4.1. Centrality Measures

DC (Degree Centrality) is calculated by dividing the degree of the node by the total number of nodes in the graph minus one [40].

EC (Eigenvector Centrality) is used to determine the importance of a node in the network. The basic logic of EC is that the more adjacent a node is to the important nodes, the more important it is [41].

CC (Closeness Centrality) is a measure of how close a node is to other nodes [42]. The closer the node is to other nodes, the larger the CC.

BC (Betweenness Centrality) is the proportional information on how many of the shortest paths between all pairs are through a node [14].

GC (Gravitational Centrality) is a recent centrality measure inspired by Newton's gravitational formula [30]. Instead of the mass in the original formula, it uses the k-shell values of the nodes and instead of the distance, it uses the length of the shortest path between nodes. Its formula is as follows:

$$GC_i = \frac{ks_i \times ks_j}{\sum_{j \in \mathrm{N}} d(j, i)} \tag{5}$$

Here, $d(\cdot)$ is the length of the shortest path between nodes $i$ and $j$; N is the set of 3-hop neighbors of node $i$.

MLD (multi-local dimension) is a state-of-the-art centrality measure proposed by Wen et. al [43]. MLD considers a node as the center and calculates the ratio of this node's neighbors up to the r-hop distance to the number of all nodes for different radius (r) values. It then calculates a centrality measure for the node based on this value. For the details of MLD, the related study can be examined.

### 4.2. Datasets

We used the following one synthetic and eight real-world networks for the experiments. The properties of the networks are given in Table 1. All the real-world datasets are taken from http://networkrepository.com [44].

**Table 1.** Network dataset features.

| Dataset | $\|V\|$ | $\|E\|$ | $\langle K \rangle$ | $K_{max}$ |
|---|---|---|---|---|
| Barabasi-Albert | 1000 | 9900 | 19.8 | 198 |
| Ca-GrQc | 5242 | 14496 | 5.53 | 81 |
| Email-Enron | 143 | 623 | 8 | 42 |
| Email-Univ | 1133 | 5451 | 9.62 | 71 |
| inf-power | 4941 | 6594 | 2.66 | 19 |
| inf-USAir97 | 332 | 2126 | 12.80 | 139 |
| rt_alwefaq | 4171 | 7123 | 3.41 | 879 |
| rt_bahrain | 4676 | 8007 | 3.42 | 261 |
| rt_damascus | 3052 | 3881 | 2.54 | 648 |

## 4.3. Performance Comparison of the Measures

We evaluated the performance of EVE and the competitor centrality measures from different angles. First, we looked at the Kendall ranking performances. We then compared their Monotonicity performances. Finally, we looked at how many of the nodes in the top 5% of the ranking lists created by the measures corresponded to the ranking lists created according to the SIR simulations.

We applied SIR model to measure influences of nodes. We set $\gamma = 1$, and we tried different values for $\beta$ around the epidemic threshold ($\beta_{th}$). The epidemic threshold is calculated as in (6) [45].

$$\beta_{th} \approx \frac{\langle k \rangle}{\langle k^2 \rangle - \langle k \rangle} \qquad (6)$$

Here $\langle k \rangle$ denotes the average degree, and $\langle k2 \rangle$ denotes the second-order moment of the degree distribution [45].

In the SIR simulations, we set each node as the only infected node in the network. We ended the simulations when there were no infected nodes left in the network. At the end of each simulation, we took the number of recovered nodes in the network as the influence of the node selected as the single infected node at the beginning of that simulation. We repeated the simulation for each node 1000 times and took the average of their influences as the final SIR score. For the simulations we used Python and NetworkX [46].

### 4.3.1. Kendall Ranking

The best results were given by EVE in six experiments, by GC in two experiments, and by EC in one experiment. In addition, the EVE tau values in all experiments are very close to 0.8 or higher. The more detailed results are shown in Figure 2.

The ranking performances of EVE and the competitor centrality measures for $\beta = \beta_{th}$ are shown in Table 2. The best results are emphasized in bold. Ranking performances were calculated using Definition 2, as the Kendall's tau ranking correlation coefficient. The ranking list created by the measure and the list created by SIR simulations were used in the calculations.

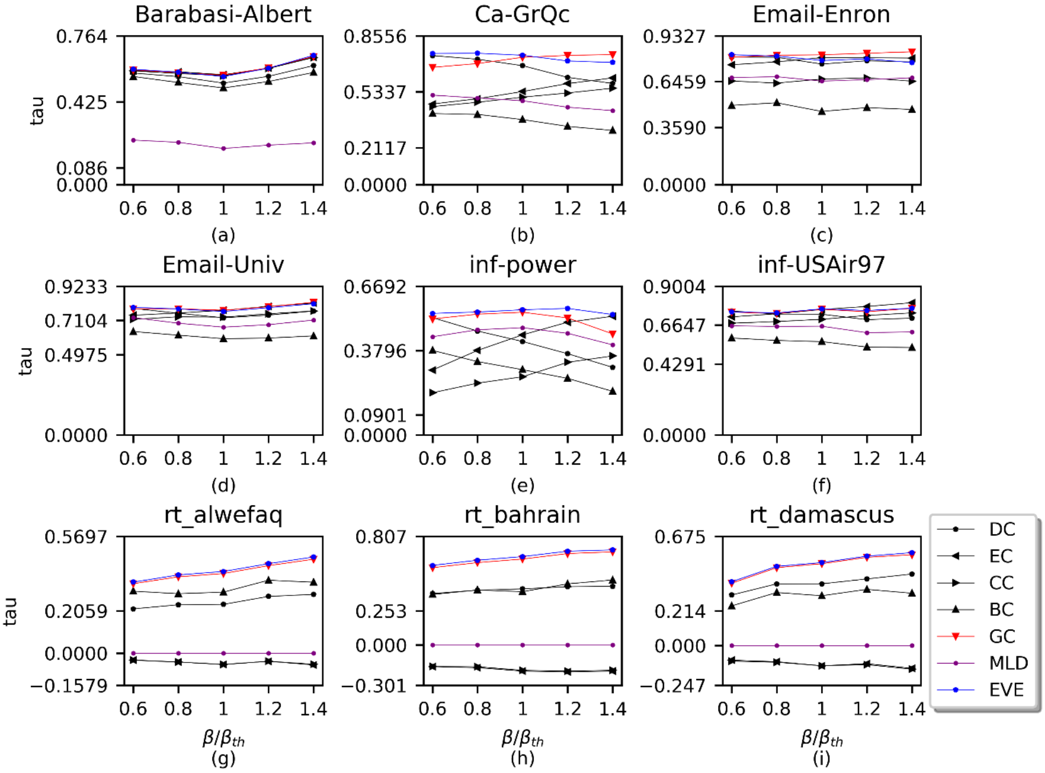

**Figure 2.** Kendall's $tau$ correlation coefficient results of the centrality measures.

**Table 2.** Kendall's $tau$ correlation coefficient results of the centrality measures for $\beta = \beta_{th}$.

| Dataset | DC | EC | CC | BC | GC | MLD | EVE |
|---|---|---|---|---|---|---|---|
| Barabasi-Albert | 0.5214 | **0.5645** | 0.5595 | 0.4965 | 0.5622 | 0.1859 | 0.5550 |
| Ca-GrQc | 0.6840 | 0.5353 | 0.5030 | 0.3740 | 0.7322 | 0.4822 | **0.7439** |
| Email-Enron | 0.7559 | 0.7959 | 0.6617 | 0.4590 | **0.8137** | 0.6490 | 0.7781 |
| Email-Univ | 0.7271 | 0.7734 | 0.7310 | 0.5975 | **0.7737** | 0.6691 | 0.7663 |
| inf-power | 0.4204 | 0.4504 | 0.2620 | 0.2936 | 0.5519 | 0.4825 | **0.5631** |
| inf-USAir97 | 0.7307 | 0.7592 | 0.6998 | 0.5649 | 0.7608 | 0.6582 | **0.7629** |
| rt_alwefaq | 0.2380 | -0.0553 | -0.0562 | 0.2977 | 0.3888 | 0.0 | **0.3988** |
| rt_bahrain | 0.4174 | -0.1950 | -0.1893 | 0.3965 | 0.6397 | 0.0 | **0.6577** |
| rt_damascus | 0.3819 | -0.1259 | -0.1255 | 0.3080 | 0.5064 | 0.0 | **0.5134** |

### 4.3.2. Ranking Monotonicity

The monotonicity values of the ranking lists created by EVE and the competitor centrality measures are shown in Table 3. The values were calculated using Definition 3. Since the ranking lists created by the centrality measures depend only on the network structure, their monotonicity values were calculated only once for each data set. The ranking list created by EVE is dependent on $\beta$. So, its monotony values should be calculated for each $\beta$. On the other hand, the monotonicity of the EVE at different $\beta$ values are very close to the monotonicity of the EVE at $\beta = \beta_{th}$. For the sake of brevity, we only give the monotonicity of the EVE values at $\beta = \beta_{th}$. The monotonicity values calculated for EVE are 1 in three experiments and very close to 1 in the other three experiments. Meanwhile, the EC, CC, GC, and MLD also yielded successful results. GC and EVE have given competitor results for the retweet networks (rt_alwefaq, rt_bahrain, rt_damascus).

Finally, we examined how many of the nodes in the top x% of the ranking lists created by the measure coincided with the nodes in the top x% of the ranking list created according to the SIR simulations. The results are shown in Tables 4-5. The best results are emphasized in bold. Nodes in the top-rank levels formed by the measure are expected to be more influential nodes. Therefore, the nodes at the top of the list and those at the top of the ranking list created according to the SIR simulations must be the same. According to the results, EVE outperforms the competitors in four experiments for top 3% and top5% of the ranking lists.

**Table 3.** Monotonicity values of the centrality measures.

| Dataset | DC | EC | CC | BC | GC | MLD | EVE |
|---|---|---|---|---|---|---|---|
| Barabasi-Albert | 0.9279 | 1.0 | 0.9999 | 1.0 | 1.0 | 1.0 | 1.0 |
| Ca-GrQc | 0.9647 | 0.9973 | 1.0 | 0.7892 | 1.0 | 1.0 | 1.0 |
| Email-Enron | 0.9958 | 1.0 | 1.0 | 0.9998 | 1.0 | 1.0 | 1.0 |
| Email-Univ | 0.97316 | 0.9995 | 0.9995 | 0.9920 | 0.9995 | 0.9995 | 0.9995 |
| inf-power | 0.8043 | 0.6897 | 0.9947 | 0.9543 | 0.9939 | 0.9947 | 0.9947 |
| inf-USAir97 | 0.9830 | 0.9966 | 0.9944 | 0.9403 | 0.9961 | 0.9956 | 0.9956 |
| rt_alwefaq | 0.6933 | 0.9672 | 0.9944 | 0.0878 | 0.2680 | 0.0698 | 0.2635 |
| rt_bahrain | 0.7677 | 0.8805 | 0.9910 | 0.1590 | 0.4866 | 0.1991 | 0.4800 |
| rt_damascus | 0.3999 | 0.3130 | 0.9543 | 0.0506 | 0.2382 | 0.0979 | 0.2359 |

**Table 4.** The number of matching nodes in the top 3% of the ranking list was created according to SIR simulations with the ranking lists created by the measures.

| Dataset | DC | EC | CC | BC | GC | MLD | EVE |
|---|---|---|---|---|---|---|---|
| Barabasi-Albert | 24 | 25 | **26** | 24 | 25 | 23 | 24 |
| Ca-GrQc | 18 | 19 | 13 | 2 | **21** | 0 | 19 |
| Email-Enron | 1 | **4** | 1 | 1 | 3 | 2 | 1 |
| Email-Univ | 20 | **24** | 17 | 14 | 19 | 16 | 21 |
| inf-power | 47 | **88** | 16 | 13 | 86 | 48 | 50 |
| inf-USAir97 | **8** | **8** | 6 | 4 | **8** | 7 | **8** |
| rt_alwefaq | 57 | 17 | 12 | 42 | 49 | 29 | **61** |
| rt_bahrain | 106 | 11 | 5 | 58 | 90 | 23 | **110** |
| rt_damascus | 34 | 3 | 4 | 26 | 36 | 26 | **36** |

**Table 5.** The number of matching nodes in the top 5% of the ranking list was created according to SIR simulations with the ranking lists created by the measures.

| Dataset | DC | EC | CC | BC | GC | MLD | EVE |
|---|---|---|---|---|---|---|---|
| Barabasi-Albert | 40 | **41** | **41** | **41** | **41** | 39 | **41** |
| Ca-GrQc | 36 | 26 | 20 | 7 | **38** | 0 | 37 |
| Email-Enron | 4 | 4 | 3 | 3 | 4 | **5** | 3 |
| Email-Univ | 37 | 36 | 35 | 31 | **38** | 34 | 36 |
| inf-power | 80 | **150** | 46 | 39 | 134 | 91 | 101 |
| inf-USAir97 | 12 | 12 | 10 | 9 | **13** | 12 | 12 |
| rt_alwefaq | 77 | 53 | 43 | 55 | 68 | 71 | **82** |
| rt_bahrain | 161 | 18 | 6 | 97 | 158 | 63 | **181** |
| rt_damascus | 86 | 24 | 23 | 49 | 83 | 63 | **93** |

## 5. Discussion and Conclusions

In this study, we proposed an approach that approximates the influences of nodes in complex networks under the SIR propagation model using the shortest paths between nodes and then applies this to rank the nodes. The EVE is similar to a centrality measure in that it is used for ranking nodes. However, EVE is not a general centrality measure, but a metric specific to the SIR model. As a result of nine datasets and five different SIR settings, EVE performed better than state-of-the-art and well-known centrality measures.

We compared EVE with well-known centrality measures as well as with a state-of-the-art measure such as MLD, and GC, which are successful and innovative methods. The EVE demonstrated that the expected influences of nodes could be better distinguished by using the parameters of the propagation model and the shortest paths (without using the centrality measures of the nodes).

The EVE is calculated using the shortest paths between nodes. This means that all other paths are ignored. In dense networks, there can be many different paths other than the shortest path between two nodes. Therefore, ignoring these paths increase the difference (error) between EVE and the actual expected influence.

The time complexity of the EVE mostly depends on the shortest path calculation. The EVE needs to calculate all-pairs shortest path, and the known best worst-case time complexity for this purpose is $O(|V|^3)$. After the calculation of all-pairs shortest paths, the EVE algorithm works. It has two nested loops that both have $|V|$ as the upper limit. So, time complexity of this part of the algorithm is $O(|V|^2)$. Of two consecutive algorithm parts, the complexity of the larger one is the complexity of the entire algorithm. Thus, the total complexity of EVE becomes $O(|V|^3)$.

As future work, EVE-like algorithms can be developed for other propagation models. Additionally, improvements can be made to EVE to obtain more accurate results on dense networks.

## Acknowledgment

The authors declare that they have no known competing financial interests or personal relationships that could have appeared to influence the work reported in this paper.

## References

[1] J. Gao, B. Barzel, and A.-L. Barabási, “Universal resilience patterns in complex networks,” *Nature*, vol. 530, no. 7590, pp. 307–312, Feb. 2016, doi: 10.1038/nature16948.

[2] A.-L. Barabási, N. Gulbahce, and J. Loscalzo, “Network medicine: a network-based approach to human disease,” *Nat. Rev. Genet.*, vol. 12, no. 1, pp. 56–68, Jan. 2011, doi: 10.1038/nrg2918.

[3] H. Alasmary *et al.*, “Analyzing and Detecting Emerging Internet of Things Malware: A Graph-Based Approach,” *IEEE Internet Things J.*, vol. 6, no. 5, pp. 8977–8988, 2019, doi: 10.1109/JIOT.2019.2925929.

[4] J. Yang, C. Yao, W. Ma, and G. Chen, “A study of the spreading scheme for viral marketing based on a complex network model,” *Phys. A Stat. Mech. its Appl.*, vol. 389, no. 4, pp. 859–870, Feb. 2010, doi: 10.1016/j.physa.2009.10.034.

[5] İ. Tuğal and A. Karcı, “Comparisons of Karcı and Shannon entropies and their effects on centrality of social networks,” *Phys. A Stat. Mech. its Appl.*, vol. 523, pp. 352–363, Jun. 2019, doi:

10.1016/j.physa.2019.02.026.

[6] J. Leskovec, D. Huttenlocher, and J. Kleinberg, “Predicting positive and negative links in online social networks,” in *Proceedings of the 19th international conference on World wide web - WWW ’10*, 2010, p. 641. doi: 10.1145/1772690.1772756.

[7] S. P. Borgatti, A. Mehra, D. J. Brass, and G. Labianca, “Network Analysis in the Social Sciences,” *Science (80-. ).*, vol. 323, no. 5916, pp. 892–895, Feb. 2009, doi: 10.1126/science.1165821.

[8] S. Chang *et al.*, “Mobility network models of COVID-19 explain inequities and inform reopening,” *Nature*, vol. 589, no. 7840, pp. 82–87, Jan. 2021, doi: 10.1038/s41586-020-2923-3.

[9] Y. Yang, X. Wang, Y. Chen, M. Hu, and C. Ruan, “A Novel Centrality of Influential Nodes Identification in Complex Networks,” *IEEE Access*, vol. 8, pp. 58742–58751, 2020, doi: 10.1109/ACCESS.2020.2983053.

[10] J. Zhang, C. Yang, Z. Jin, and J. Li, “Dynamics analysis of SIR epidemic model with correlation coefficients and clustering coefficient in networks,” *J. Theor. Biol.*, vol. 449, pp. 1–13, 2018, doi: 10.1016/j.jtbi.2018.04.007.

[11] S. Banerjee, M. Jenamani, and D. K. Pratihar, “A survey on influence maximization in a social network,” *Knowl. Inf. Syst.*, 2020, doi: 10.1007/s10115-020-01461-4.

[12] D. Kempe, J. Kleinberg, and É. Tardos, “Maximizing the spread of influence through a social network,” in *Proceedings of the ninth ACM SIGKDD international conference on Knowledge discovery and data mining - KDD ’03*, 2003, p. 137. doi: 10.1145/956750.956769.

[13] S. P. Borgatti, “Identifying sets of key players in a social network,” *Comput. Math. Organ. Theory*, vol. 12, no. 1, pp. 21–34, Apr. 2006, doi: 10.1007/s10588-006-7084-x.

[14] L. C. Freeman, “A Set of Measures of Centrality Based on Betweenness,” *Sociometry*, vol. 40, no. 1, p. 35, Mar. 1977, doi: 10.2307/3033543.

[15] L. Katz, “A new status index derived from sociometric analysis,” *Psychometrika*, vol. 18, no. 1, pp. 39–43, Mar. 1953, doi: 10.1007/BF02289026.

[16] L. Page, S. Brin, R. Motwani, and T. Winograd, “The PageRank Citation Ranking: Bringing Order to the Web.,” Stanford InfoLab, 1999. [Online]. Available: http://ilpubs.stanford.edu:8090/422/

[17] J. Sheng *et al.*, “Identifying influential nodes in complex networks based on global and local structure,” *Phys. A Stat. Mech. its Appl.*, vol. 541, p. 123262, 2020, doi: 10.1016/j.physa.2019.123262.

[18] C. Salavati, A. Abdollahpouri, and Z. Manbari, “Ranking nodes in complex networks based on local structure and improving closeness centrality,” *Neurocomputing*, vol. 336, pp. 36–45, 2019, doi: 10.1016/j.neucom.2018.04.086.

[19] Z. Ghalmane, M. El Hassouni, C. Cherifi, and H. Cherifi, “Centrality in modular networks,” *EPJ Data Sci.*, vol. 8, no. 1, 2019, doi: 10.1140/epjds/s13688-019-0195-7.

[20] J. Zhao, Y. Song, and Y. Deng, “A novel model to identify the influential nodes: Evidence theory centrality,” *IEEE Access*, vol. 8, pp. 46773–46780, 2020, doi: 10.1109/ACCESS.2020.2978142.

[21] Z. Lv, N. Zhao, F. Xiong, and N. Chen, “A novel measure of identifying influential nodes in complex networks,” *Phys. A Stat. Mech. its Appl.*, vol. 523, pp. 488–497, 2019, doi: 10.1016/j.physa.2019.01.136.

[22] M. Curado, L. Tortosa, and J. F. Vicent, “A novel measure to identify influential nodes: Return Random Walk Gravity Centrality,” *Inf. Sci. (Ny).*, vol. 628, pp. 177–195, May 2023, doi: 10.1016/j.ins.2023.01.097.

[23] Z. Zhao, X. Wang, W. Zhang, and Z. Zhu, “A community-based approach to identifying influential spreaders,” *Entropy*, vol. 17, no. 4, pp. 2228–2252, 2015, doi: 10.3390/e17042228.

[24] Z. Ghalmane, C. Cherifi, H. Cherifi, and M. El Hassouni, “Centrality in Complex Networks with Overlapping Community Structure,” *Sci. Rep.*, vol. 9, no. 1, pp. 1–29, 2019, doi: 10.1038/s41598-019-46507-y.

[25] Y. Zhao, S. Li, and F. Jin, “Identification of influential nodes in social networks with community structure based on label propagation,” *Neurocomputing*, vol. 210, pp. 34–44, 2016, doi: 10.1016/j.neucom.2015.11.125.

[26] Y. Y. Keng, K. H. Kwa, and C. McClain, “Convex combinations of centrality measures,” *J. Math. Sociol.*, 2020, doi: 10.1080/0022250X.2020.1765776.

[27] S. S. Ali, T. Anwar, and S. A. M. Rizvi, “A Revisit to the Infection Source Identification Problem under Classical Graph Centrality Measures,” *Online Soc. Networks Media*, vol. 17, no. xxxx, p. 100061, May

2020, doi: 10.1016/j.osnem.2020.100061.

[28] M. Alshahrani, Z. Fuxi, A. Sameh, S. Mekouar, and S. Huang, “Efficient algorithms based on centrality measures for identification of top-K influential users in social networks,” *Inf. Sci. (Ny).*, vol. 527, pp. 88–107, Jul. 2020, doi: 10.1016/j.ins.2020.03.060.

[29] M. Şimşek and H. Meyerhenke, “Combined centrality measures for an improved characterization of influence spread in social networks,” *J. Complex Networks*, vol. 8, no. 1, Feb. 2020, doi: 10.1093/comnet/cnz048.

[30] L. Ma, C. Ma, H. Zhang, and B. Wang, “Identifying influential spreaders in complex networks based on gravity formula,” *Phys. A Stat. Mech. its Appl.*, vol. 451, pp. 205–212, Jun. 2016, doi: 10.1016/j.physa.2015.12.162.

[31] X.-L. Yan, Y.-P. Cui, and S.-J. Ni, “Identifying influential spreaders in complex networks based on entropy weight method and gravity law,” *Chinese Phys. B*, vol. 29, no. 4, p. 048902, Apr. 2020, doi: 10.1088/1674-1056/ab77fe.

[32] A. Şimşek, “Lexical sorting centrality to distinguish spreading abilities of nodes in complex networks under the Susceptible-Infectious-Recovered (SIR) model,” *J. King Saud Univ. - Comput. Inf. Sci.*, Jun. 2021, doi: 10.1016/j.jksuci.2021.06.010.

[33] X. Wen, C. Tu, M. Wu, and X. Jiang, “Fast ranking nodes importance in complex networks based on LS-SVM method,” *Phys. A Stat. Mech. its Appl.*, vol. 506, pp. 11–23, Sep. 2018, doi: 10.1016/j.physa.2018.03.076.

[34] L. Sabah and M. Şimşek, “A new fast entropy-based method to generate composite centrality measures in complex networks,” *Concurr. Comput. Pract. Exp.*, vol. 35, no. 10, May 2023, doi: 10.1002/cpe.7657.

[35] J. Liu, J. Lin, Q. Guo, and T. Zhou, “Locating influential nodes via dynamics-sensitive centrality,” *Sci. Rep.*, vol. 6, no. 1, p. 21380, Feb. 2016, doi: 10.1038/srep21380.

[36] D. Tolić, K.-K. Kleineberg, and N. Antulov-Fantulin, “Simulating SIR processes on networks using weighted shortest paths,” *Sci. Rep.*, vol. 8, no. 1, p. 6562, Dec. 2018, doi: 10.1038/s41598-018-24648-w.

[37] M. G. Kendall, “A New Measure of Rank Correlation,” *Biometrika*, vol. 30, no. 1–2, pp. 81–93, Jun. 1938, doi: 10.1093/biomet/30.1-2.81.

[38] J. Bae and S. Kim, “Identifying and ranking influential spreaders in complex networks by neighborhood coreness,” *Phys. A Stat. Mech. its Appl.*, vol. 395, pp. 549–559, Feb. 2014, doi: 10.1016/j.physa.2013.10.047.

[39] G. Rossetti, L. Milli, S. Rinzivillo, A. Sîrbu, D. Pedreschi, and F. Giannotti, “NDlib: a python library to model and analyze diffusion processes over complex networks,” *Int. J. Data Sci. Anal.*, vol. 5, no. 1, pp. 61–79, Feb. 2018, doi: 10.1007/s41060-017-0086-6.

[40] M. Newman, *Networks*, Second. Oxford, UK: Oxford University Press, 2018.

[41] P. Bonacich, “Power and Centrality: A Family of Measures,” *Am. J. Sociol.*, vol. 92, no. 5, pp. 1170–1182, Mar. 1987, doi: 10.1086/228631.

[42] G. Sabidussi, “The centrality index of a graph,” *Psychometrika*, vol. 31, no. 4, pp. 581–603, Dec. 1966, doi: 10.1007/BF02289527.

[43] T. Wen, D. Pelusi, and Y. Deng, “Vital spreaders identification in complex networks with multi-local dimension,” *Knowledge-Based Syst.*, vol. 195, p. 105717, 2020, doi: 10.1016/j.knosys.2020.105717.

[44] R. A. Rossi and N. K. Ahmed, “The Network Data Repository with Interactive Graph Analytics and Visualization,” 2015. [Online]. Available: http://networkrepository.com

[45] Z. Li, T. Ren, X. Ma, S. Liu, Y. Zhang, and T. Zhou, “Identifying influential spreaders by gravity model,” *Sci. Rep.*, vol. 9, no. 1, pp. 1–7, 2019, doi: 10.1038/s41598-019-44930-9.

[46] A. A. Hagberg, D. A. Schult, and P. J. Swart, “Exploring Network Structure, Dynamics, and Function using NetworkX,” in *Proceedings of the 7th Python in Science Conference*, 2008, pp. 11–15.

**Bitlis Eren Üniversitesi Fen Bilimleri Dergisi**
BİTLİS EREN UNIVERSITY JOURNAL OF SCIENCE
ISSN: 2147-3129/e-ISSN: 2147-3188
VOLUME: 13 NO: 2 PAGE: 418-424 YEAR: 2024
DOI:10.17798/bitlisfen.1414588

# Design and Performance Investigation of a Series Compensated Inductive Wireless Power Transfer System for Supplying a Low Power DC Load

Mehmet BÜYÜK[1*]

[1]*Adıyaman University, Department of Electrical and Electronics Engineering, 02040, Adıyaman / Türkiye*
*(ORCID: 0000-0003-3026-4034)*

**Keywords:** Wireless power transfer, Series LC compensation, Low power application, Inductive WPT model.

**Abstract**
In this study, a series compensated WPT system is presented for low power DC load applications. Series LC resonant circuits are applied for both transmitter and receiver sides of WPT system to reduce the impedance at a specified operation frequency, and thus, ensure low power losses. The operation frequency is chosen as 109 kHz for the series compensated WPT system. Then, the series resonant LC filter is designed according to the operation frequency and WPT rating values. In addition, the power electronics systems and their controllers and operation principles are demonstrated in depth. To investigate the performance of the proposed system, a 100 W series compensated WPT model is designed and constructed in a Matlab/Simulink environment. Different simulation results are provided to illustrate the performance of the proposed WPT model. The simulation results show the stable operation of the proposed system under the designed system parameters.

## 1. Introduction

Recently, wireless power transfer (WPT), also called contactless power transfer, has gained widespread development around the world. In a WPT system, electrical energy is transferred from an electric source to an electric load through the coupling of electromagnetic waves without any physical contact between the source and the load [1], [2].

The transfer of electrical energy without a physical connection provides some benefits such as isolation, more flexibility, mobility, reliability, and convenient operation for underwater or hazardous environment applications [1], [2]. The WPT system also has many utilization areas, such as battery charging of electric vehicles (EVs) and portable electronic devices, implantable medical devices, lighting, heating, etc. [3]-[5].

In literature, WPT systems are mainly divided into two categories: inductive WPT (I-WPT) and capacitive WPT (C-WPT) [6], [7]. Extensive work has been done by researchers and academicians for the I-WPT systems owing to their advantage of having more power transfer capability [8], [9]. It is noted in [10] that the market value of the I-WPT around the world has increased from a $1 billion budget in 1995 to an approximate $9.5 billion budget in 2020. It is obvious that the WPT market value has been growing day by day.

The I-WPT systems are classified into four main groups in terms of series or parallel compensation circuits [8], [11]. There are also hybrid compensation circuits. The compensation circuits in I-WPT systems resonate with inductive coils to perform almost zero impedance at a specified frequency [12], [13]. By this way, the efficiency of the system is enhanced. In addition, voltage drop is prevented with an approximate zero impedance.

This paper builds upon previous research in the fields of WPT and series compensation. For instance, Frechter et al. [14] investigated the use of series compensation in resonant inductive WPT systems and demonstrated improvements in efficiency and power delivery range. Similarly,

---

[*]Corresponding author: *mbuyuk@adiyaman.edu.tr*

*Received: 04.01.2024, Accepted: 15.05.2024*

Kuperman [15] proposed a novel series compensation technique for enhancing the voltage regulation of inductive WPT systems, particularly under variable load conditions. On the other hand, the article [16] discusses the topology of the secondary side rectifier while focusing on the operational analysis of the wireless power transfer system. While these studies have provided valuable insights into the potential benefits of series compensation, their focus has primarily been on general WPT applications rather than specifically targeting low-power DC loads. In this study, an I-WPT system is proposed for supplying a low-power DC load. The proposed system is based on series compensation circuits for the both energy sending and receiving sides of the WPT system. In this work, the design of the utilized WPT system is presented in detail. Besides, the power electronics interface for WPT is conducted. A simulation model of the proposed system is modelled and constructed in a simulation environment. The performance of the proposed system is also examined under different loading conditions.

## 2. I-WPT System: Operation Principles and Characteristics

The general structure representation of an I-WPT system for supplying a DC load is illustrated in Figure 1. An I-WPT system consists of a DC power supply, a DC load, coils, and electronics interfaces for both the transmitter and receiver sides. The energy is transferred from the power supply to the DC load through the inductive coils without a physical connection between the transmitter coils and receiver coils. To transfer the energy between the coils without connection, a high-frequency magnetic field is produced by a high frequency current flowing in the transmitter coils. To produce the high-frequency current and magnetic field, power electronics converters are utilized between the power supply and the transmitter coils. On the other hand, the magnetic field produces AC current flow at the receiver coils. Then, this current is rectified through power electronics circuits to supply the DC load.

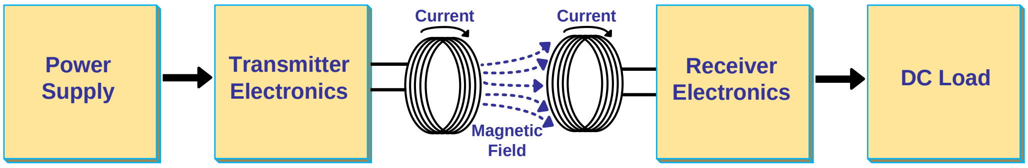

**Figure 1.** The general structure illustration of an I-WPT system for supplying a DC load.

In order to reduce impedances on both sides at the operating frequency and to enhance the efficiency of the WPT system, some compensation circuits are applied to the transmitter and receiver coils. Although there are various compensation circuits, a series compensation circuit is preferred in this study. The structure of the I-WPT with series compensation circuits for the transmitter and receiver sides is demonstrated in Figure 2. It can be seen from the figure that capacitors are used in series with the coils of the transmitter and receiver. Thus, zero impedances are ensured for both sides at a specified frequency, which results in low power losses.

The equivalent electric circuit of a series-compensated I-WPT system is shown in Figure 3. The series resistances of the coils are neglected for mathematical modelling simplicity. The source voltage is modelled as a square wave because the inverter transforms the DC voltage into a square wave ac voltage. Besides, the DC load can be directly added to the equivalent model on the receiver side.

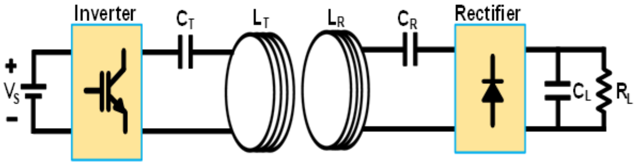

**Figure 2.** WPT system with series compensation circuits on the transmitter and receiver sides.

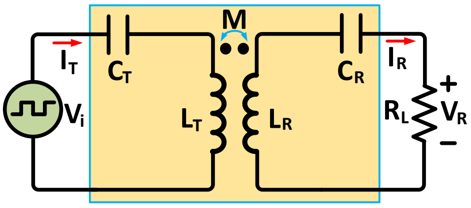

**Figure 3.** Equivalent electric circuit topology of a series-compensated I-WPT system.

The mathematical equations of the series compensated I-WPT system are given as equations (1) and (2). In these equations, the series resistances of the coil wires are neglected to simplify the calculations.

$$jX_T I_T - j\omega M I_R = V_i \tag{1}$$

$$j\omega M I_T - (R_L + jX_R) I_R = 0 \tag{2}$$

where, $V_i$ is the output rms voltage of the inverter. $I_T$ and $I_R$ are the currents on the transmission and receiver sides, respectively. $M$ is the mutual inductance between the transmitter and receiver. $w$ is the angular frequency of the inverter voltage. Besides, $X_T$ and $X_R$ are the impedances of the transmission and receiver sides with series capacitances, respectively.

The series impedances $X_T$ and $X_R$ are zero at the specified operation frequency of the inverter ($w$). Thus, the induced voltage and current at the coil of the receiver side are acquired from equations (1) and (2) as below.

$$V_R = j\omega M I_T \tag{3}$$

$$I_R = \frac{j\omega M I_T}{R_L} \tag{4}$$

Therefore, the relationship between the inverter voltage and the load voltage can be deduced as equation (5). The ratio is also equal to the ratio between the transmission current and the receiver current.

$$\frac{V_R}{V_i} = \frac{I_T}{I_R} = \frac{R_L}{\omega M} \tag{5}$$

## 3. Electronic Circuit and Controller

The power electronic interface of the proposed WPT system consists of an inverter and a rectifier. The inverter is applied to convert the DC source voltage into a high-frequency AC voltage source [15], [16]. On the other hand, the rectifier system is used to transform the high-frequency AC signal into rectified DC voltage [17].

The applied inverter topology in this study and its control algorithm are demonstrated in Figure 4. As shown in the figure, a single-phase H-bridge inverter structure is preferred for the generation of the high frequency AC signal. The single-phase H-bridge inverter circuit includes four switching components, such as MOSFETs, IGBTs, etc. [18].

The switching components are triggered by a high-frequency square wave to obtain a high-frequency voltage for the WPT system [19]. The switching frequency of the inverter is selected so that the series capacitive-inductive components resonate at the selected frequency. As mentioned in the previous section, the resonance frequency of the proposed WPT system is equal to 109 kHz.

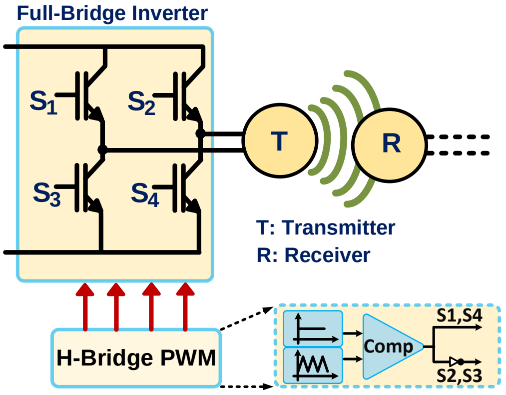

**Figure 4.** The single-phase H-bridge inverter structure and its switching control algorithm.

The other power electronics interface, which is used on the receiver side of the WPT, is a rectifier circuit. In this study, a single-phase uncontrolled rectifier is preferred to providing a suitable voltage form in order to supply the DC load. The structure of the single-phase uncontrolled rectifier is shown in Figure 5. As illustrated in the figure, the rectifier topology used in this work consists of four diodes for the rectification of AC voltage and one capacitor for the ripple reduction of the load voltage.

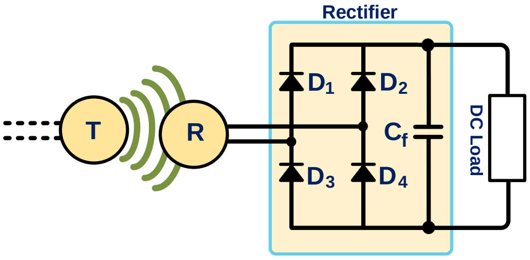

**Figure 5.** The single-phase uncontrolled rectifier circuit scheme.

## 4. Performance Results

In order to analyze and verify the proposed WPT system, a simulation model is designed and implemented in the Matlab/Simulink environment. The parameters of the constructed simulation model are given in Table 1.

**Table 1.** The parameters of the constructed simulation model for the proposed WPT system

| Description ( Symbol) | Value |
|---|---|
| Source Voltage ($V_s$) | 100 V |
| Load Resistance ($R_L$) | 100 Ohm |
| Inverter Operating Frequency ($f_s$) | 109 kHz |
| Transmitter-side Conductance ($C_T$) | 6.18 nF |
| Transmitter-side Inductance ($L_T$) | 430 uH |
| Receiver-side Conductance ($C_R$) | 6.18 nF |
| Receiver-side Inductance ($L_R$) | 430 uH |
| Mutual Inductance ($M$) | 85 uH |

Figure 6 shows the waveforms of the source voltage and inverter output voltage. The source voltage is adjusted to 100 V level. The output voltage of the inverter is a square wave that is obtained by pulsing the switching components of the inverter. The frequency of the inverter output voltage is 109 kHz, where the series capacitance and transmitter inductance resonate. The inverter output voltage changes between 100 V and -100 V levels. In addition, the inverter output voltage and transmitter-side current are demonstrated in Figure 7. Similar to the inverter output voltage, the transmitter-side current has an AC signal with a frequency of 109 kHz. As seen from the figure, the transmitter-side current has a sinus waveform because of the output impedance of the inverter.

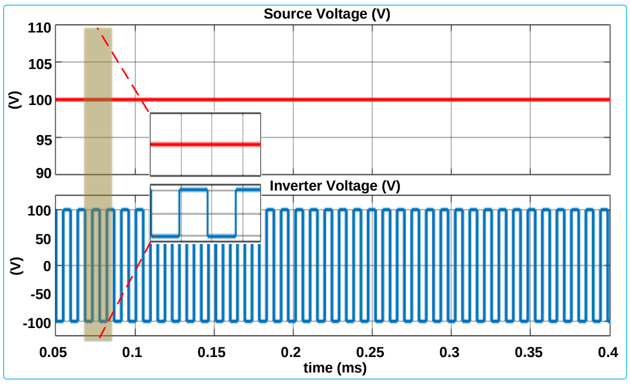

**Figure 6.** The waveforms of the source and inverter voltages.

On the other side, the induced voltage at WPT inductance and the receiver-side current are shown in Figure 8. The induced voltage, similar to the inverter output voltage, has a square wave form with the ranges of 100 V and -100 V levels. Besides, the receiver-side current has a sinusoidal waveform owing to the receiver-side impedance.

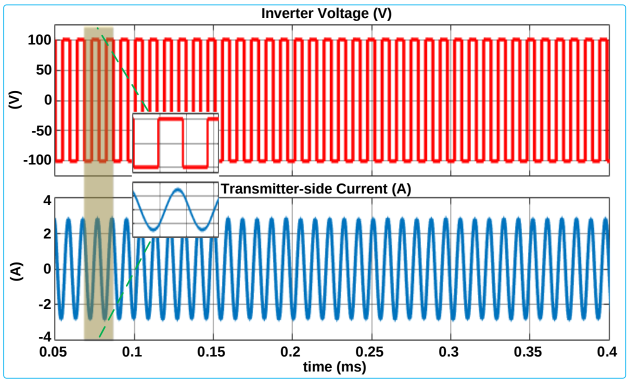

**Figure 7.** The waveforms of the inverter voltage and transmitter-side current.

Furthermore, the voltages of the source, the inverter, the induced voltage, and the load voltage are illustrated in Figure 9. It is obvious that the load voltage is adjusted to be the same as the source voltage through the designed system parameters. Moreover, the load voltage and current are shown in Figure 10. The load is designed to consume an approximate 100 W of power from the source. It can be seen from the simulation results that the WPT system ensures stable operation at the designed parameters.

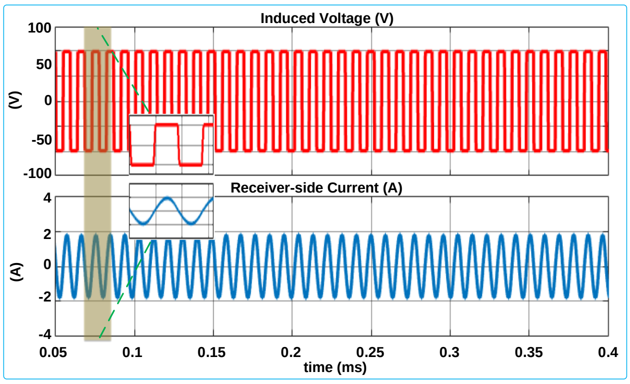

**Figure 8.** The waveforms of the induced voltage and receiver-side current.

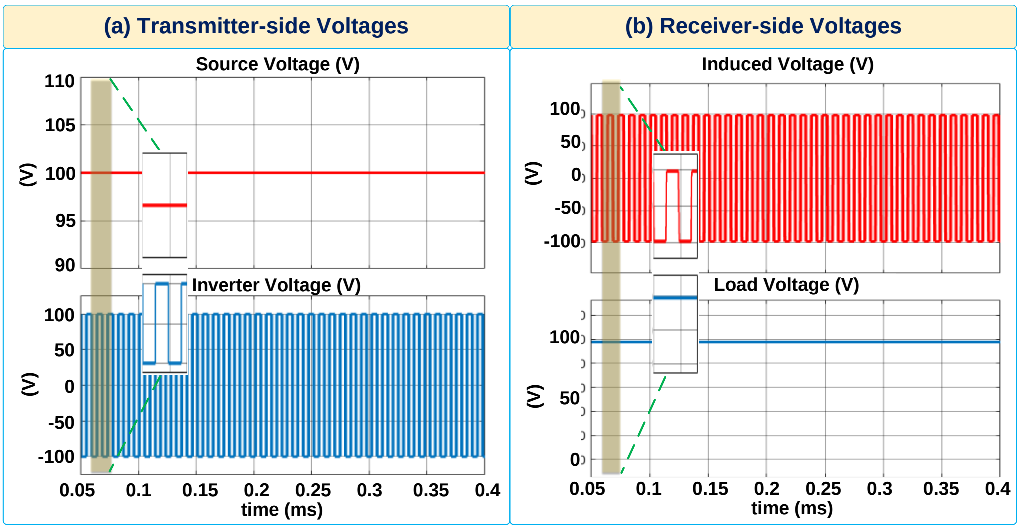

**Figure 9.** The waveforms of the transmitter-side and receiver-side voltages.

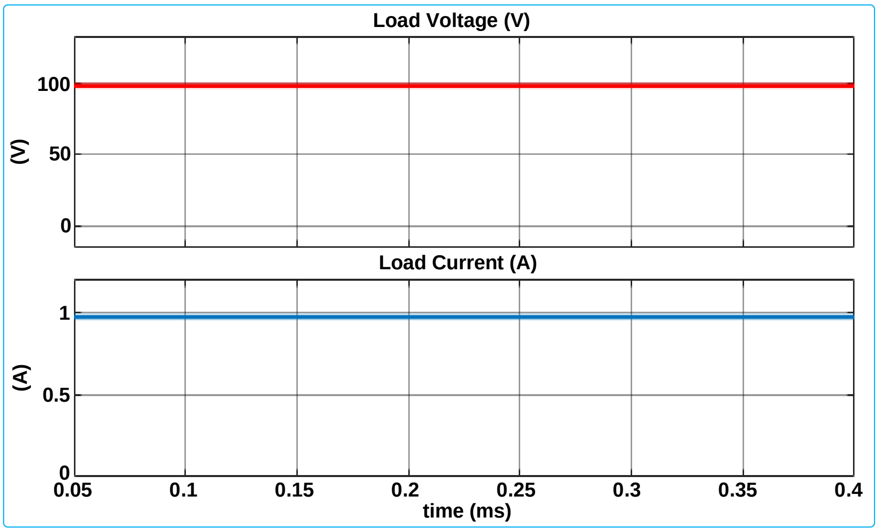

**Figure 10** The waveforms of load voltage and current.

## 5. Conclusions

In this study, we have presented the design and investigation of a series compensated Wireless Power Transfer (WPT) system tailored for low-power DC loads. The operational characteristics of the proposed WPT system have been meticulously introduced, focusing on its series-compensated configuration and resonant operation. The series-compensated WPT system comprises series resonant LC circuits at both the transmitter and receiver sides, with the resonant frequency carefully adjusted to 109 kHz. Through detailed design procedures, the series LC components have been sized and configured to resonate at the specified frequency, ensuring optimal power transfer efficiency.

Moreover, we have provided an in-depth exploration of the electrical equivalent circuit and mathematical equations governing the proposed WPT model. This analytical framework offers valuable insights into the underlying principles driving the system's operation, facilitating a deeper understanding of its behavior. Furthermore, the power electronics interface systems, along with their associated control algorithms and operational characteristics, have been thoroughly presented. These interface systems play a crucial role in regulating the power transfer process and ensuring the stability and efficiency of the WPT system.

To validate the performance of the proposed system, we have modeled and constructed it in the MATLAB/Simulink simulation environment. The designed system parameters have been meticulously configured, and extensive simulations have been conducted to assess its performance under various operating conditions. Our simulation results demonstrate that the proposed WPT system exhibits stable and efficient operation within the designed model and parameters.

## Conflict of Interest Statement

There is no conflict of interest between the authors.

## Statement of Research and Publication Ethics

The study is complied with research and publication ethics

## References

[1] Z. Bi, L. Song, R. De Kleine, C. Mi, and G. Keoleian, "Plug-in vs. wireless charging: Life cycle energy and greenhouse gas emissions for an electric bus system," *Applied Energy,* vol. 146, 05/15 2015.

[2] P. Lazzeroni, V. Cirimele, and A. Canova, "Economic and environmental sustainability of Dynamic Wireless Power Transfer for electric vehicles supporting reduction of local air pollutant emissions," *Renewable and Sustainable Energy Reviews,* vol. 138, p. 110537, 2021/03/01/ 2021.

[3] S. Chhawchharia, S. K. Sahoo, M. Balamurugan, S. Sukchai, and F. Yanine, "Investigation of wireless power transfer applications with a focus on renewable energy," *Renewable and Sustainable Energy Reviews,* vol. 91, pp. 888-902, 2018/08/01/ 2018.

[4] T. Kan, T. Nguyen, J. Wjite, R. Malhan, and C. Mi, "A New Integration Method for an Electric Vehicle Wireless Charging System Using LCC Compensation Topology," *IEEE Transactions on Power Electronics,* vol. 32, pp. 1-1, 01/01 2016.

[5] H. Pan, L. Qi, X. Zhang, Z. Zhang, W. Salman, Y. Yuan*, et al.*, "A portable renewable solar energy-powered cooling system based on wireless power transfer for a vehicle cabin," *Applied Energy,* vol. 195, pp. 334-343, 2017/06/01/ 2017.

[6] Y. H. Sohn, B. H. Choi, E. S. Lee, G. C. Lim, G. Cho, and C. T. Rim, "General Unified Analyses of Two-Capacitor Inductive Power Transfer Systems: Equivalence of Current-Source SS and SP Compensations," *IEEE Transactions on Power Electronics,* vol. 30, pp. 6030-6045, 2015.

[7] Z. Zhang, H. Pang, A. Georgiadis, and C. Cecati, "Wireless Power Transfer—An Overview," *IEEE Transactions on Industrial Electronics,* vol. 66, pp. 1044-1058, 2019.

[8] S. D. Barman, A. W. Reza, N. Kumar, M. E. Karim, and A. B. Munir, "Wireless powering by magnetic resonant coupling: Recent trends in wireless power transfer system and its applications," *Renewable and Sustainable Energy Reviews,* vol. 51, pp. 1525-1552, 2015/11/01/ 2015.

[9] H. Wang, K. T. Chau, C. H. T. Lee, L. Cao, and W. Lam, "Design, Analysis and Implementation of Wireless Shaded-Pole Induction Motors," *IEEE Transactions on Industrial Electronics,* vol. PP, pp. 1-1, 07/10 2020.

[10] Verified Market Research. Available: https://www.verifiedmarketresearch.com/product/wireless-power-transmission-market/

[11] H. Wang, K. T. Chau, C. H. T. Lee, and C. Jiang, "Wireless Shaded-Pole Induction Motor With Half-Bridge Inverter and Dual-Frequency Resonant Network," *IEEE Transactions on Power Electronics,* vol. 36, pp. 13536-13545, 2021.

[12] A. Berger, M. Agostinelli, S. Vesti, J. A. Oliver, J. A. Cobos, and M. Huemer, "A Wireless Charging System Applying Phase-Shift and Amplitude Control to Maximize Efficiency and Extractable Power," *IEEE Transactions on Power Electronics,* vol. 30, pp. 6338-6348, 2015.

[13] M. Stanculescu, M. Iordache, D. Niculae, L. Bobaru, and V. Bucata, "Algorithm for Computing S Parameters and Their Use for Studying Efficiency of Electromagnetic Energy Wireless Transfer Systems," *Revue Roumaine Des Sciences Techniques-Serie Electrotechnique Et Energetique,* vol. 63, pp. 138-144, Apr-Jun 2018.

[14] Y. Frechter and A. Kuperman, "Output Voltage Range of a Power-Loaded Series–Series Compensated Inductive Wireless Power Transfer Link Operating in Load-Independent Regime," *IEEE Transactions on Power Electronics,* vol. 35, pp. 6586-6593, 2020.

[15] A. Kuperman, "Simple Enhancement of Series–Series-Compensated Inductive Wireless Power Transfer Links Operating With Load-Independent Voltage Output at Fixed Frequency to Attain Zero Inverter Phase Angle," *IEEE Transactions on Power Electronics,* vol. 38, pp. 5670-5674, 2023.

[16] M. Zavrel, V. Kindl, M. Frivaldsky, D. Andriukaitis, and D. Navikas, *Optimization of series-series compensated wireless power transfer system using alternative secondary side rectification*, 2023.

[17] K. R. S. Vadivu and R. Ramaprabha, "Improved Steady State and Large Signal Transient Response of Three Level AC-DC Converter Using Hysteresis Modulation based SMC Under DCM," *Revue Roumaine Des Sciences Techniques-Serie Electrotechnique Et Energetique*, vol. 66, pp. 85-90, Apr-Jun 2021.

[18] S. Arezki and M. Boudour, "Study and Regulation of DC Bus Voltages of Wind-Photovoltaic System," *Revue Roumaine Des Sciences Techniques-Serie Electrotechnique Et Energetique*, vol. 59, pp. 35-46, Jan-Mar 2014.

[19] S. Ann and B. Lee, "Analysis of Impedance Tuning Control and Synchronous Switching Technique for a Semi-Bridgeless Active Rectifier in Inductive Power Transfer Systems for Electric Vehicles," *IEEE Transactions on Power Electronics*, vol. 38, pp. 8786-8798, 2021.

Bitlis Eren Üniversitesi Fen Bilimleri Dergisi
BİTLİS EREN UNIVERSITY JOURNAL OF SCIENCE
ISSN: 2147-3129/e-ISSN: 2147-3188
VOLUME: 13 NO: 2 PAGE: 425-431 YEAR: 2024
DOI:10.17798/bitlisfen.1419729

# Modification Technique Influence on the Adsorption Capability of Organobentonites for Reactive and Direct Dyes

Seniha MORSÜMBÜL[1], Emriye Perrin AKÇAKOCA KUMBASAR[1*], Saadet YAPAR[2]

[1]*Ege University, Engineering Faculty Textile Engineering Department, Bornova, Izmir, Türkiye*
[2]*Ege University, Engineering Faculty Chemical Engineering Department, Bornova, Izmir, Türkiye*
*(ORCID: 0000-0002-4929-0681) (ORCID: 0000-0001-5295-9131) (ORCID: 0000-0003-4237-6869)*

**Keywords:** Textile dyes, Decolorization, Adsorption, Organobentonite, Drying.

**Abstract**
In this research, the adsorption of reactive and direct dyes from synthetic textile wastewater using organobentonites modified by two different routes was studied. Except for the drying step, the synthesis conditions were the same, and organobentonites were synthesized by employing a cationic surfactant at a level corresponding to the entire cation exchange capacity of bentonite under microwave irradiation. In the final step, the samples were dried using either a freeze dryer or an air dryer. The structural features of the organobentonites were identified via XRD and FTIR analyses. The obtained equilibrium data indicated that the adsorption process fit the Langmuir isotherm model for both dyes. Although the results indicated that both organobentonites adsorbed two of the dyes, the freeze-dried sample could serve as a more effective adsorbent for removing reactive and direct dyes from wastewater.

## 1. Introduction

The textile sector is known for its substantial water consumption. The various textile finishing processes involved, such as dyeing and washing, result in the discharge of a significant amount of wastewater containing concentrated dyes and chemicals. This discharge poses a major threat to the ecosystem, contributing to elevated levels of chemical and biochemical oxygen demand as well as coloring substances. Consequently, effective treatment of textile wastewater has become an increasingly crucial issue.

It is important for textile companies to develop an economical and environmentally friendly treatment system in order to adapt to today's competitive conditions. In this context, it becomes crucial to research and improve the methods of wastewater treatment. Among these methods, wastewater treatment through the adsorption of pollutants by pristine and/or modified clays has become increasingly notable [1]-[3].

Clay minerals are typically layered aluminum silicates with a large surface area and nanometer-scale size. Moreover, their surfaces are negatively charged and hydrophilic, rendering them unsuitable for the adsorption of organic molecules like textile dyes. The surface properties of clay minerals can be altered by using organic compounds, such as alkyl ammonium ions, to achieve hydrophobic/organophilic surfaces. This modification leads to an enhanced interaction between the organic molecules and the surface [4]-[6]. Therefore, organoclays modified with cationic surfactants exhibit strong interactions with textile dyes, driven by the hydrophobic affinity among the dye molecules and the clay surfaces [7]-[9]. As a result, clays have found widespread use in various environmental applications, such as the removal of pollutants like anionic dyes [10, 11], cationic dyes [12], [13], heavy metals [14]-[16], etc. from wastewater, either alone or in composite form with other materials. However, to our knowledge, the impact of drying conditions on the adsorption of textile dyes by modified bentonites has not been

---

[*]Corresponding author: *perrin.akcakoca@ege.edu.tr*

*Received: 14.01.2024, Accepted: 11.06.2024*

investigated, despite previous studies investigating the impact of chemical modifications on the adsorption capability of bentonites for textile dyes. Thus, the purpose of this study is to comparatively examine the effect of drying conditions applied in the modification of bentonite on its adsorption properties for reactive and direct dyes.

In this study, two different types of organobentonites were synthesized under identical conditions, except for the drying step, where either freeze-drying or air-drying was employed. The modified bentonites obtained through air-drying and freeze-drying were labeled Sample I and Sample II, respectively.

## 2. Material and Method

### 2.1. Materials

The synthetic textile dyes, Reactive Red 141 (RR141) and Direct Red 81 (DR 81), were supplied from Dystar. The molecular configurations of these dyes are illustrated in Figure 1 for RR141 and Figure 2 for DR 81. The bentonite used in the experiments was sourced from the Tokat Reşadiye region of Türkiye. Its cation exchange capacity (CEC) was assessed to be 0.91 meq/g by Yılmaz and Yapar [17]. The surfactant used for the modification, hexadecyltrimethylammonium bromide (HDTMAB) [$CH_3(CH_2)15N(CH_3)3Br$], was obtained from Merck.

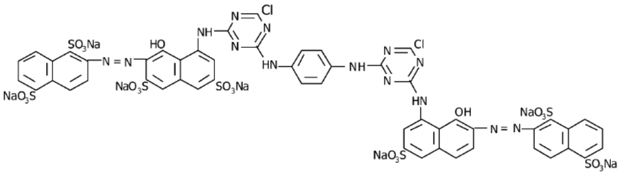

**Figure 1.** Molecular configuration of C.I. Reactive Red 141 [18].

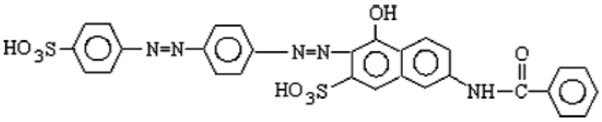

**Figure 2.** Molecular configuration of C.I. Direct Red 81 [19].

### 2.2. Organobentonite Production

The organobentonites were prepared using the procedure described in a prior investigation [20], with the exception of drying conditions. In brief, the sedimentation method was initially used to remove unwanted components such as iron oxide and silica from crude bentonite. Following the sedimentation process, the specimens were subjected to drying in an oven at 60 °C and pulverized using a grinder.

The purified bentonite-water dispersion and HDTMAB solution, prepared following the procedures outlined in the literature [17], were mixed. The mixture was subsequently exposed to microwave irradiation at 360 W for 5 minutes in a microwave oven. This step was followed by multiple washes with purified water until no surfactant particles were detected in the filtered solution. The detection of surfactant presence in the filtered solution was carried out using the methyl orange technique [21]. Following the washing process, the samples were dried using either an air dryer or a freeze dryer. The specifics of the drying parameters can be found in Table 1.

**Table 1.** Drying parameters.

| Sample no | Method of drying | Drying conditions |
|---|---|---|
| I | Oven | T=60 ºC, time = 2 days |
| II | Freeze | T =−45 ºC, P = 0.060 mbar, time=8h |

### 2.3. Material Characterization

The structural characteristics were examined through X-ray diffraction employing a Philips X'Pert Pro diffractometer within the 2 ° to 40 ° ($2\theta$), and FTIR spectra of bentonites were acquired using a Perkin-Elmer FTIR spectrophotometer.

### 2.4. Adsorption Studies

The studies were conducted on Samples I and II by agitating dispersions containing 50 mg of adsorbent in 50 mL of dye solution at different concentrations. Agitation took place at 30 ºC for 24 hours in a water bath (Nuve, ST 402). At the end of the agitation period, the solid phase was separated from the solution through centrifugation, followed by filtration to eliminate the tiny bentonite particles that could affect the absorbance measurements. The dye content in the supernatant was determined using a UV–Vis spectrophotometer (Perkin-Elmer Lambda 25).

The adsorption capacity, denoted as $q_e$ (mg/g), for the adsorbent was computed utilizing Equation 1. Subsequently, the equilibrium concentration, $C_e$ (mg/L) versus the adsorption capacity was plotted.

$$q_e = \frac{(C_0 - C_e)V}{m} \tag{1}$$

where $C_0$ is the initial concentration of dye in the solution (mg/L); $V$ represents the total volume of dye solution used (L); and $m$ is the mass of adsorbent employed (g).

### 2.4. Adsorption Isotherms

The Langmuir equation is shown in Equation 2 [22]:

$$q_e = \frac{q_{\max} K_L C_e}{1 + K_L C_e} \tag{2}$$

Here, $q_{max}$ represents the maximum adsorption capability with full monolayer coverage on the surface (mg/g), and $K_L$ represents the Langmuir constant (L/mg). Equation (2) can be linearized as follows [22]:

$$\frac{C_e}{q_e} = \frac{1}{q_{\max} K_L} + \frac{C_e}{q_{\max}} \tag{3}$$

The constants can be determined by analyzing the intercepts and slopes on the linear graphs of $C_e/q_e$ plotted against $C_e$.

The dimensionless separation factor, $R_L$, is a fundamental aspect of the Langmuir equation. Equation 4 presents the formulation for $R_L$ [22]:

$$R_L = \frac{1}{1 + K_L C_H} \tag{4}$$

where $C_H$ is the highest initial solute concentration and $K_L$ is the Langmuir adsorption constant (L/mg). Table 2 shows the parameter $R_L$ indicated the shape of isotherm.

**Table 2.** The $R_L$ parameters indicate the isotherm type [22].

| Value of $R_L$ | Type of isotherm | Value of $R_L$ |
|---|---|---|
| $R_L>1$ | Unfavorable | $R_L>1$ |
| $R_L=1$ | Linear | $R_L=1$ |
| $0<R_L<1$ | Favorable | $0<R_L<1$ |
| $R_L=0$ | Irreversible | $R_L=0$ |

The Freundlich equation characterizes heterogeneous systems and may be expressed through the heterogeneity factor $1/n$. The equation is presented as follows [22]:

$$q_e = K_F C_e^{1/n} \tag{5}$$

where $K_F$ represents the Freundlich constant (mg/g) $(L/mg)^{1/n}$, and $1/n$ is the heterogeneity factor. The Freundlich model can be linearized by applying the logarithm of Equation (5):

$$\ln q_e = \ln K_F + \frac{1}{n} \ln C_e \tag{6}$$

The constant $K_F$ and the exponent $1/n$ can be derived from analyzing the intercepts and slopes in the linear graphs of ln $q_e$ plotted against ln$C_e$ [22].

### 3. Results and Discussion

### 3.1. XRD Results

The basal spacings ($d_{001}$) for raw bentonite, Sample I, and Sample II are shown in Figure 3. A close examination of the figure reveals that the $d_{001}$ values of the samples were increased in comparison to the raw bentonite. This outcome suggested that quaternary ammonium cations are present within the interlayer of the modified bentonites. Besides, the calculated interlayer spacing of Sample I and Sample II was 0.88 nm and 0.915 nm, respectively. These values correspond to a bilayer arrangement in the interlayer spaces [23], [24].

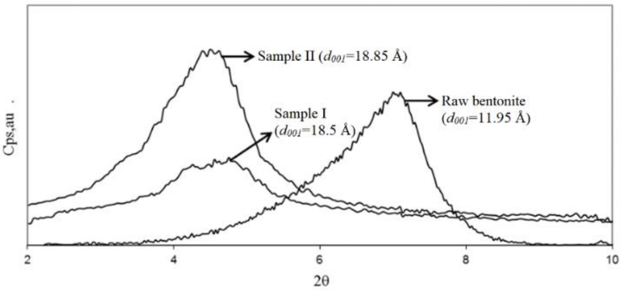

**Figure 3.** X-ray diffraction spectra of raw bentonite, Sample I, and Sample II.

### 3.2. FTIR Results

Figure 4 displays the FTIR spectra of the untreated bentonite, Sample I, and Sample II. The strong peaks at 2850 and 2920 $cm^{-1}$ detected in the samples are assigned to the symmetric and asymmetric stretch vibrations of the methyl and methylene units, respectively [25]. The peaks observed between 1465 and 1475 $cm^{-1}$ also represent their bending vibrations [26], [27]. These peaks, identified in organobentonites, indicate the insertion of surfactant particles between the silica layers of organobentonites. Consequently, this observation can be considered evidence supporting the surface modification of bentonites.

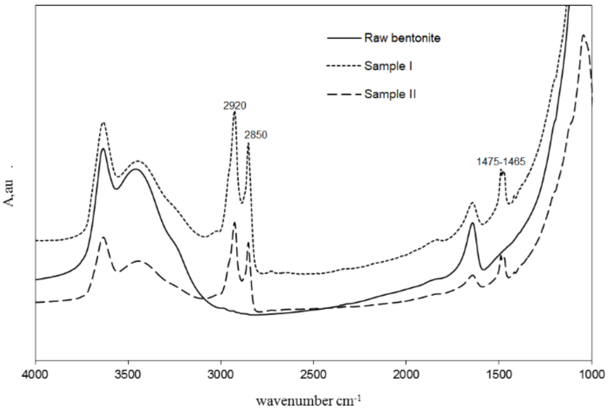

**Figure 4.** FTIR spectra of the untreated bentonite, Sample I, and Sample II.

### 3.3. Adsorption Isotherms

The experiments were conducted using raw bentonite for comparison purposes. The approximately equal concentration values before and after adsorption showed that the natural clay adsorbed almost no Reactive Red 141 and Direct Red 81 dyes. Because of the negative surface charge and the hydrophilic nature of the mineral surface, water is preferably adsorbed, and organic compounds cannot compete with water. In other words, Na-clays are less effective adsorbents for organic molecules. However, the anionic surface property of clay can be altered by using positively charged organic compounds such as alkyl ammonium ions. The modified clay surface (HDTMA-Bentonite) becomes hydrophobic and can strongly interact with organic molecules. Textile dyes are also significantly large organic molecules and can be adsorbed between the dye molecule and HDTMA-Bentonite through hydrophobic interaction.

Studies have been conducted to obtain the adsorption isotherms of HDTMA-bentonite. The Langmuir and Freundlich isotherm equations were employed to model the experimental isotherms. The determination of the $r^2$ values for these equations was conducted to assess the appropriateness of the isotherms. Normalized deviation values ($\Delta Q$) were additionally examined with respect to every isotherm. The $\Delta Q$ values were computed using the following formula:

$$\Delta Q = \frac{1}{N}\sum\left[\left(Q_{calc} - Q_{\exp}\right)/Q_{calc}\right] \tag{7}$$

Here, the subscripts "*exp*" and "*calc*" indicate the experimental and calculated values, respectively, and *N* represents the quantity of experimental data points [28].

Tables 3 and 4 show the Langmuir and Freundlich constants for the adsorption of RR 141 and DR 81, respectively. Additionally, Table 5 displays the normalized deviation values for the samples.

**Table 3.** The Langmuir and Freundlich constants for the adsorption of RR 141.

| SAMPLE | Langmuir isotherm model | | | | Freundlich isotherm model | | |
|---|---|---|---|---|---|---|---|
| | $q_{max}$(mg/g) | $K_L$(L/mg) | $r_L^2$ | $R_L$ | $K_F$ (mg/g)(L/mg)$^{1/n}$ | $n$ | $r_F^2$ |
| I | 82.9 | 0.076 | 0.98 | 0.062 | 19.42 | 3.502 | 0.83 |
| II | 167.97 | 0.308 | 0.98 | 0.016 | 53.97 | 3.489 | 0.72 |

**Table 4.** Langmuir and Freundlich constants for the adsorption of DR 81.

| SAMPLE | Langmuir isotherm model | | | | Freundlich isotherm model | | |
|---|---|---|---|---|---|---|---|
| | $q_{max}$(mg/g) | $K_L$(L/mg) | $r_L^2$ | $R_L$ | $K_F$ (mg/g)(L/mg)$^{1/n}$ | $n$ | $r_F^2$ |
| I | 84.55 | 0.07 | 0.98 | 0.066 | 18.94 | 3.409 | 0.86 |
| II | 173.96 | 0.27 | 0.99 | 0.017 | 53.87 | 3.309 | 0.87 |

**Table 5.** The normalized deviation values (ΔQ) for Samples I and II.

| Sample | Dye | Langmuir isotherm model | Freundlich isotherm model |
|---|---|---|---|
| I | RR 141 | 0.0491 | 0.0797 |
| | DR 81 | 0.0375 | 0.0751 |
| II | RR 141 | 0.1674 | 0.1797 |
| | DR 81 | 0.0112 | 0.1231 |

Considering the $r^2$ and $\Delta Q$ values, it can be concluded that the equilibrium data for RR 141 and DR 81 on Samples I and II adhere to the Langmuir isotherm. The correlation coefficient values for the Langmuir isotherms of both organobentonites ($r^2 \approx 0.99$) indicate a robust positive relationship. The calculated $R_L$ values, intrinsic to the Langmuir isotherm, were also determined to be within the range of 0 and 1 for both modified bentonites, indicating favorable adsorption of the dyes (Table 2).

The adsorption isotherms of RR 141 and DR 81, plotted using both the experimental and calculated data, are illustrated in Figures 5 and 6, respectively.

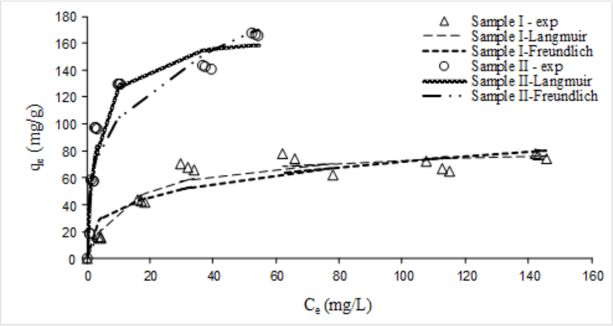

**Figure 5.** The adsorption of RR 141 on Sample I and Sample II.

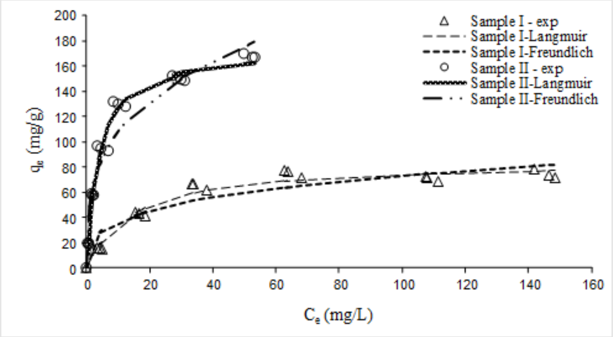

**Figure 6.** The adsorption of DR 81 on Sample I and Sample II.

The adsorption isotherms of the dyes indicate that the quantity of absorbed dye increases as the initial dye concentration increases until it reaches a state of equilibrium (Figs. 5 and 6). The enhanced adsorption capacity of Sample II, in contrast to Sample I, can be ascribed to the distinct surface morphology formed due to variations in drying conditions. During the freeze-drying process, as water evaporates, the frozen water within the product transitions directly to vapor, thus creating a porous structure in the product. This porous structure can affect the properties of the product and may assist in achieving desired characteristics in the adsorption process.

## 4. Conclusion

In the present study, XRD and FTIR analyses demonstrated that HDTMAB was successfully intercalated within the clay. The Langmuir isotherm model, indicating favorable adsorption of both dyes, explained the adsorption behavior of RR141 and RR81. The removal of more than 80% of the dye by freeze-dried organobentonite suggests a relatively more positive impact of freeze-drying than air-drying (which achieved 60% removal) on the removal of reactive and direct dyes from wastewater. The greater adsorption capacity was attributed to the existence of a porous structure formed during the freeze-drying process. In contrast to previous studies that reported the effect of modification on dye adsorption of clay, this study investigates the effect of drying, demonstrating that the applied drying method in the modification process significantly influences the dye adsorption capacity of organobentonite.

## Acknowledgment

The authors gratefully acknowledge the financial support for this research received through Project No. 109M752 of The Scientific and Technical Research Council of Turkey (TUBITAK); through Project No. DPT-2007 K 120780 of the T.R. Prime Ministry State Planning Organization; and through Project No. 10MUH034 of Ege University's scientific research projects.

## Contributions of the authors

The authors' contributions to the paper are equal.

## Conflict of Interest Statement

There is no conflict of interest between the authors.

## Statement of Research and Publication Ethics

The study is complied with research and publication ethics.

**Nomenclature**

| | |
|---|---|
| $q$ | Dye concentration on adsorbent, mg/g |
| $C$ | Dye concentration in aqueous solution, mg/L |
| $V$ | Total volume of dye solution (L) |
| $M$ | Mass of adsorbent, g |
| $R^2$ | Linear regression coefficient |
| $K$ | Adsorption isotherm constant, L/g |
| $T$ | Time, min |
| $T$ | Temperature, C |
| $R_L$ | Characteristic of the Langmuir equation |
| $N$ | Heterogeneity factor |
| RR 141 | C.I. Reactive Red 141 |
| DR 81 | C.I. Direct Red 81 |
| HDTMAB | Hexadecyltrimethyl ammoniumbromide |
| CEC | Cation exchange capacity |
| XRD | X-ray diffraction |
| FTIR | Fourier transform infrared spectroscopy |

***Subscripts***

| | |
|---|---|
| *cal* | Calculated |
| *exp* | Experimental |
| *0* | Initial condition |
| *e* | Equilibrium condition |
| *max* | Maximum |
| *L* | Langmuir isotherm |
| *F* | Freundlich isotherm |
| *t* | The condition at time, t |

## References

[1] D. López-Rodríguez, B. Micó-Vicent, J. Jordán-Núñez, M. Bonet-Aracil, and E. Bou-Belda, “Uses of nanoclays and adsorbents for dye recovery: a textile industry review”, *Applied Sciences* vol. 11, no. 23, pp. 1-27, 2021.

[2] A. K. Dhar, H. A. Himu, M. Bhattacharjee, M.G. Mostufa, and F. Parvin, “Insights on applications of bentonite clays for the removal of dyes and heavy metals from wastewater: a review”, *Environmental Science and Pollution Research*, vol. 30, no. 3, pp. 5440-5474, 2023.

[3] M. El-habacha, Y. Miyah, S. Lagdali, G. Mahmoudy, A. Dabagh, M. Chiban, F. Sinan, S. Iaich, and M. Zerbet, “General overview to understand the adsorption mechanism of textile dyes and heavy metals on the surface of different clay materials”, *Arabian Journal of Chemistry*, vol. 16, no. 11, pp. 1-24, 2023.

[4] S. Barakan and V. Aghazadeh, “The advantages of clay mineral modification methods for enhancing adsorption efficiency in wastewater treatment: a review”, *Environmental Science and Pollution Research*, vol. 28, no.3, pp. 2572-2599, 2021.

[5] R.A Schoonheydta and C.T. Johnston, “Surface and Interface Chemistry of Clay Minerals” in *Handbook of Clay Science*. Elsevier, 2006, ch. 3, pp. 87-113.

[6] G. Lagalya, M. Ogawab, and I. Dekany, “Clay Mineral Organic Interactions” in *Handbook of Clay Science*. Elsevier, 2006, ch. 7.3, pp. 309-377.

[7] J. V. F. L. Cavalcanti, C. C. da Fonseca, G. M. da Silva, I. T. Santiago, L. L. Tenório, M. Sobrinho, and O. S. Baraúna, “Adsorption of textile dye and textile effluent using organoclay from Northeast of Brazil”, *Cerâmica*, vol. 67, pp. 277-283, 2021.

[8] Z. Baouch, B. Kamel Ismet, and B. Bouras, “Adsorption of different dyes from aqueous solutions using organo-clay composites”, *Physical Chemistry Research*, vol. 8, no. 4, pp. 767-787, 2020.

[9] B. M. Al-Sakkaf, S. Nasreen, and N. Ejaz, “Ultrasonic assisted application of organoclay as a sorbent for treatment of textile wastewater”, *Russian Journal of Physical Chemistry A*, vol. 95, no. 8, pp. 1712-1719, 2021.

[10] Y. Zhu, Y. Cui, Y. Peng, R. Dai, H. Chen, and Y. Wang, “Preparation of CTAB intercalated bentonite for ultrafast adsorption of anionic dyes and mechanism study”, *Colloids and Surfaces A: Physicochemical and Engineering Aspects*, vol. 658, pp. 1-11, 2023.

[11] N. Choi, Y. Son, T.H. Kim, Y. Park, and Y. Hwang, Y, “Adsorption behaviors of modified clays prepared with structurally different surfactants for anionic dyes removal”, *Environmental Engineering Research*, vol. 28, no. 2, pp. 1-10, 2022.

[12] A. Oussalah and A. Boukerroui, “Removal of cationic dye using alginate–organobentonite composite beads”, *Euro-Mediterranean Journal for Environmental Integration*, vol. 5, no.3, pp. 1-10, 2020.

[13] N. Daas and H. Zaghouane-Boudiaf, “Synthesis and characterization of porous bentonite adsorbent and its application to remove methylene blue dye from aqueous solutions”, *Desalin. Water Treat*, vol. 249, pp. 271-280, 2022.

[14] Y. Son, Y. Kim, S. Bae, T.H. Kim, and Y. Hwang, "Investigation of chromate adsorption efficacy on organo-bentonite as potential in-situ adsorbent for groundwater remediation", *Journal of Environmental Chemical Engineering*, vol. 10, no 6, pp. 1-10, 2022.

[15] N. Khodabakhshloo, B. Biswas, F. Moore, J. Du, and R. Naidu, "Organically functionalized bentonite for the removal of perfluorooctane sulfonate, phenanthrene and copper mixtures from wastewater", *Applied Clay Science*, vol. 200, pp. 1-11, 2021.

[16] A. Marszałek, G. Kamińska, and N.F.A. Salam, "Simultaneous adsorption of organic and inorganic micropollutants from rainwater by bentonite and bentonite-carbon nanotubes composites", *Journal of Water Process Engineering*, vol. 46, pp. 1-18, 2022.

[17] N. Yılmaz and S. Yapar, "Adsorption properties of tetradecyl- and hexadecyl trimethylammonium bentonites" *Applied Clay Science*, vol. 27, pp. 223-228, 2004.

[18] Ç. Akduman, S. Morsümbül, and E.P. Akçakoca Kumbasar, "The Removal of Reactive Red 141 From Wastewater: A Study of Dye Adsorption Capability of Water-Stable Electrospun Polyvinyl Alcohol Nanofibers", *Autex Research Journal*, vol. 21, no. 1, pp. 20-31, 2021.

[19] N. Junnarkar, D. Srinivas Murty, N.S. Bhatt, and D. Madamwar, D, "Decolorization of diazo dye Direct Red 81 by a novel bacterial consortium", *World Journal of Microbiology & Biotechnolgy*, vol. 22, pp. 163–168, 2006.

[20] S. Elemen, E .P. Akçakoca Kumbasar, and S. Yapar, "Modeling the adsorption of textile dye on organoclay using an artificial neural network", *Dyes and Pigments*, vol. 95, no.1, pp. 102-111, 2012.

[21] L.K. Wang and D.F. Langley, "Determining cationic surfactant concentration", *Industrial Engineering Chemical Product Research Development*, vol. 14, no.3, pp. 210–213, 1975.

[22] B.H. Hameed, A.A Ahmad, and N. Aziz, "Isotherms, kinetics and thermodynamics of acid dye adsorption on activated palm ash", *Chemical Engineering Journal*, vol. 133, pp. 195-203, 2007.

[23] G. Özdemir, and S. Yapar, "Preparation and characterization of copper and zinc adsorbed cetylpyridinium and Nlauroylsarcosinate intercalated montmorillonites and their antibacterial activity", *Colloids and Surfaces B: Biointerfaces*, vol. 188, pp. 1-8, 2020.

[24] S. Yapar, G. Özdemir, A.M.F. Solarte, and R.M.T. Sánchez, "Surface and interface properties of lauroyl sarcosinate-adsorbed CP+-montmorillonite", *Clays and Clay Minerals*, vol. 63, pp. 110–118, 2015.

[25] Z. Li, W.T. Jiang, and H. Hong, "An FTIR investigation of hexadecyltrimethylammonium intercalation into rectorite", *Spectrochimica Acta Part A: Molecular and Biomolecular Spectroscopy*, vol. 71, pp. 1525-1534, 2008.

[26] I. Calabrese, G. Cavallaro, G. Lazzara, M. Merli, L. Sciascia, and M.L. Turco Liveri, "Preparation and characterization of bio-organoclays using nonionic surfactant", *Adsorption*, vol. 22, pp. 105–116, 2016.

[27] Y. Xi, Z. Ding, H. He, and R.L. Frost, "Infrared spectroscopy of organoclays synthesized with the surfactant octadecyltrimethylammonium bromide", *Spectrochimica Acta Part A: Molecular and Biomolecular Spectroscopy*, vol. 61, pp. 515-525, 2005.

[28] Z. Aksu and J.A. Yener, "Comparative adsorption/biosorption study of mono-chlorinated phenols onto various sorbents", *Waste Management*, vol.21, pp. 695-702, 2001.

Bitlis Eren Üniversitesi Fen Bilimleri Dergisi
BİTLİS EREN UNIVERSITY JOURNAL OF SCIENCE
ISSN: 2147-3129/e-ISSN: 2147-3188
VOLUME: 13 NO: 2 PAGE: 432-444 YEAR: 2024
DOI:10.17798/bitlisfen.1421143

# Effect of Chain-Link Fence Attachment on the Crash Performance of an H1 Containment Level Safety Barrier

Ayhan Öner YÜCEL[1]*

[1]*Aydın Adnan Menderes University, Faculty of Engineering, Department of Civil Engineering, Aydın, Türkiye*
*(ORCID: 0000-0001-5888-2809)*

**Keywords:** Longitudinal barrier, Crash simulation, Finite element Analysis, Chain-link fence, EN 1317.

**Abstract**

Longitudinal barriers are among the road safety equipment used to prevent vehicles from leaving the roadway. These systems are designed to be lightweight for economic reasons without compromising their structural adequacy. In this study, the effect of chain-link fence on impact severity and structural performance of a longitudinal barrier was investigated through finite element (FE) analyses. An H1 containment level longitudinal barrier FE model was validated using real crash test results. After modifying the validated system to reduce its weight, crash test simulations (TB11 and TB42) were conducted on the modified system, both with and without chain-link fence attachment. The chain-link fence was placed below the rail and on the traffic side of the post in a manner that had not been applied before. FE analyses found that the chain-link fence minimally altered TB11 test performance. In TB42 simulations without a chain-link fence, the vehicle climbed over the rail, resulting in a test failure. However, when a chain-link fence was used, the same barrier contained and redirected the vehicle, leading to a successful test. It was concluded that using chain-link fences can enhance the crash performance of longitudinal barriers by limiting the barrier lateral deformation. Further detailed studies, supported by real crash tests, on the placement of fences in barriers are recommended.

## 1. Introduction

Longitudinal barriers designed in accordance with the European EN 1317 standard offer specific levels of vehicle containment, effectively redirecting errant vehicles back onto the road [1]. Crash tests are conducted on safety barriers to evaluate their performance levels, with the goal of ensuring that these barriers are structurally adequate and have minimal injury risk to occupants. Different types of longitudinal barriers are grouped by how well they resist deformation. For example, concrete barriers are rigid, steel barriers are semi-rigid when it comes to lateral deformation, and cable barriers are flexible. The focus of this study was on steel barriers. The performance of safety barriers is notably impacted by their geometric features, as highlighted in studies by Molan et al. [2] and Molan and Ksaibati [3]. Key parameters such as barrier height and post spacing play a crucial role in ensuring safety performance [4]. Additionally, the severity of the impact is significantly influenced by both the type and material of the post [4], [5]. The increase in vehicle weights, attributed to the use of batteries in electric vehicles, and the desire to employ lower-cost road restraint systems have prompted researchers to design lightweight, higher-performance systems that prioritize structural adequacy and occupant safety.

Chain-link fences are commonly used systems for various purposes, such as protection against rockfall, debris flows, and security. Recently, their usage of road restraint systems has increased. Silvestri-Dobrovolny et al. [6] evaluated the crash performance of a chain-link fence fixed on the top of

---

*Corresponding author: aoyucel@adu.edu.tr

*Received: 17.01.2024, Accepted: 03.06.2024*

concrete barriers. They are generally used to deter pedestrians from crossing. According to that study, chain-link fence systems are installed at the top or back of concrete barriers in the United States. The general purpose of mounting a chain-link fence is to prevent people from passing or jumping from the barrier in the median or on bridges. The advantages of chain-link fence attachments were listed as easy attachment, withstanding wind loads, and compatibility with MASH. The disadvantage was listed as limited glare screening. A real full-scale crash test was implemented according to MASH Test 3-11 for an F-shape concrete barrier with a chain-link fence mounted on the top [7]. A 2270-kg truck impacted the barrier at a speed of 100 km/h and at an angle of 25°. The system successfully passed the test. Literature reviews showed that there is no study (real crash test or FE analyses) regarding the crashworthiness of longitudinal steel barriers with chain-link fence attachments. In another study, Silvestri Dobrovolny et al. [8] developed and evaluated barrier containment options for the safety of motorcycle riders. They designed a concrete barrier with a chain-link fence mounted on top to decrease the severity of motorcycle crashes. Finite element computer simulations were implemented to evaluate the concrete barrier with chain-link fence attachment. According to FE simulations, the developed system successfully contained the dummy with the help of a mounted chain-link fence system.

Due to the time-consuming and expensive nature of real crash tests, as well as the need for extensive technical infrastructure, the use of finite elements in the crashworthiness evaluation of road restraint systems has become widespread with advancements in computer technologies. Numerous studies have investigated the crash performance of road safety systems through FE analyses [9]-[13]. A 3D finite element model of a chain-link drapery system was developed in ABAQUS software [14]. Real-impact tests in the lab were used to calibrate and validate the model. These tests showed that the FE model accurately depicts the behavior of the chain-link drapery system. Similarly, a chain-link fence finite element model was developed and validated for simulations with the LS-DYNA [8]. They modeled the fence using beam elements and validated the model with real pendulum tests. The results indicated that the FE model of the chain-link fence accurately represents its actual impact behavior. Another chain-link fence FE model was developed by Hoang et al. [15]. They simulated protective fences against rockfalls. The results of the pendulum tests and LS-DYNA outputs were very similar, showing that FE analyses can be used to accurately model the fence's changing behavior.

The primary objective of this study is to investigate the impact of chain-link fence placement in longitudinal barriers on crash performance. Within the scope of this research, an H1 containment level barrier FE model was developed and validated using actual crash test results. The reference model underwent modifications to reduce the system’s weight. TB11 and TB42 crash simulations were conducted using LS-DYNA software for the modified barrier system, both with and without chain-link fence placement. The study assessed the influence of chain-link fence usage on the performance of the modified barrier system, with evaluations focusing on the impact severity on passengers and the structural adequacy of the barrier. The findings of this study could be useful for evaluating the potential use of chain-link fences with longitudinal barriers.

## 2. Material and Method

### 2.1. Longitudinal Barrier Performance Evaluation according to EN 1317

Before road restraint systems are used on European highways, they must undergo testing and certification according to the European standard EN 1317 to assess their crashworthiness [1]. This standard describes test details for different barrier performance classes and certification procedures. EN 1317 comprises eight separate parts, with the first two covering crash test procedures, test vehicle criteria, and general specifications for longitudinal barriers. Terminology, general criteria, and test vehicle specifications are outlined in EN 1317-1 [16]. EN 1317-2 defines test methods for different performance classes and acceptance criteria [1]. This standard delineates containment levels, ranging from low-angle containment to very high containment, along with the required acceptance tests. It describes a total of eleven crash tests involving different vehicle types, masses, impact speeds, and impact angles. In the scope of this study, an H1 containment level steel longitudinal barrier, classified as a higher containment level, was utilized. As indicated in Table 1, TB11 and TB42 crash tests must be conducted for H1 level acceptance. The crash test results must meet EN 1317-2 criteria for successful certification. The TB11 test is performed using a 900 kg car, with the car impacting the barrier at a speed of 100 km/h and at an angle of 20°. The TB42 test involves a rigid Heavy Goods Vehicle (HGV) weighing 10000 kg colliding with the barrier at a speed of 70 km/h and at an angle of 15°.

**Table 1.** The details of tests required for H1 containment level [1]

| Containment level | | Required Test | Speed (km/h) | Angle (°) | Mass (kg) | Type of vehicle |
|---|---|---|---|---|---|---|
| Higher containment | H1 | TB11 | 100 | 20 | 900 | Car |
| | | TB42 | 70 | 15 | 10000 | Rigid HGV |

After conducting full-scale real crash tests, the results are evaluated based on EN 1317-2 specifications. Crash test outcomes are assessed considering the structural adequacy of the barrier, occupant impact severity, and vehicle trajectory. The barrier must meet EN 1317 criteria, including occupant impact severity levels in the car test (TB11), structural adequacy in the HGV test (TB42), and vehicle stability requirements during both tests. In a successful crash test, the vehicle should not roll over, and must be contained and redirected to the traffic side of the barrier, and there should be no complete breakage in the main longitudinal components of barrier system [1]. Within the scope of this study, both the TB11 and TB42 crash test results were investigated. TB11 test results are utilized to assess the impact severity level. The acceleration severity index (ASI) and the theoretical head impact velocity (THIV) indices are employed to quantify the injury risk of vehicle occupants. The ASI reflects impact intensity and is calculated using the accelerations measured during the crash test. The THIV estimates the velocity of the occupant's head during an impact. According to the EN 1317 standard, ASI is determined using Equation (1).

$$ASI(t) = max\left[\sqrt{\left[\left(\frac{a_x}{\hat{a}_x}\right)^2 + \left(\frac{a_y}{\hat{a}_y}\right)^2 + \left(\frac{a_z}{\hat{a}_z}\right)^2\right]}\right] \quad (1)$$

where, $a_x$, $a_y$ and $a_z$ are the acceleration values obtained during the crash testing (measured in g, where g is gravitational acceleration). $\hat{a}_x$, $\hat{a}_y$ and $\hat{a}_z$ refers to limit acceleration values in the longitudinal (x), lateral (y), and vertical (z) directions, respectively. These limit accelerations are given as 12 g, 9 g, and 10 g, respectively.

The THIV index is calculated using the velocities of the theoretical head with respect to the car. The equation used to calculate THIV is given in Equation (2).

$$THIV = \left[V_{head\,x}^2(T) + V_{head\,y}^2(T)\right]^{0.5} \quad (2)$$

where, $V_{head\,x}$ and $V_{head\,y}$ refer to the head velocity with respect to the car in the longitudinal and lateral directions of the vehicle coordinate system, respectively. T refers to the time of flight required for theoretical head displacement, either 600 mm in the x direction or 300 mm in the y direction.

EN 1317-2 establishes ASI and THIV limit values as shown in Table 2 [1]. The impact severity level is determined according to the given ASI ranges. THIV value must be less than 33 km/h for the acceptance of the test in terms of occupant safety. The lower ASI values are desired for reduced impact severity.

**Table 2.** Impact severity levels according to EN 1317-2 [1]

| Impact severity level | Characteristic values | | |
|---|---|---|---|
| A | ASI ≤ 1.0 | and | THIV < 33 km/h |
| B | 1.0 < ASI ≤ 1.4 | | |
| C | 1.4 < ASI ≤ 1.9 | | |

In addition to safety criteria, the structural adequacy of the barrier is crucial for acceptance. The TB42 test is conducted to evaluate the structural performance of H1 containment level barriers. The working width (W) is defined as the maximum lateral deformation of the safety barrier during the crash test. It is measured during the test as the greatest lateral distance between the impact side of the safety barrier and any part of the barrier during the impact. Table 3 presents the working width ranges and corresponding classes.

**Table 3.** Working width classes [1]

| Class | Working width (m) |
|---|---|
| W1 | W≤0.6 |
| W2 | W≤0.8 |
| W3 | W≤1.0 |
| W4 | W≤1.3 |
| W5 | W≤1.7 |
| W6 | W≤2.1 |
| W7 | W≤2.5 |
| W8 | W≤3.5 |

Exit box criteria must also be taken into consideration according to EN 1317 [1]. According to these criteria, all vehicles should be redirected to the road platform at a small angle by the safety barrier after the impact. If the exit angle is large, the errant vehicle may pose a safety risk to other vehicles in the traffic lanes. Following the crash test, the vehicle exit angle and exit box criteria should be checked against the limits specified for vehicle dimensions.

## 2.2. Geometric details and Finite Element (FE) Model of Reference H1 Containment Level Barrier

In this study, a previously tested and certified H1 containment level longitudinal barrier served as a reference system. This system underwent modification and analysis to investigate the impact of chain-link fence placement on its performance. The original safety barrier comprises two main components: C-type posts and W-beam rails. Bolts and nuts are utilized to connect the rails to each other and to attach the rails to the posts. The W-beam rails, made of 2.65 mm thick steel, are connected to 5 mm thick steel C150X75 posts using M16 bolts. Figure 1 illustrates the geometric details of barrier components. The total length of the posts is 1600 mm, with 810 mm embedded into the ground. Consequently, the total height of the post above the ground is 790 mm. The distance between each post in this system is 2 meters. The material grade for the W-beam is S235JR, while the C-type post has a material grade of S355JR. The M16 bolts are composed of Class 8.8 steel material. This H1 safety barrier underwent TB11 and TB42 crash tests in real full-scale conditions, conducted at an accredited crash test center located in France [17], [18].

The finite element (FE) model of the barrier system was created for validation and subsequent analyses. The general view of the H1 containment level safety barrier FE model is illustrated in Figure 2. The 3-dimensional nonlinear finite element software LS-DYNA was used for crash analyses [19]. LS-PrePost software was used to define element types, material models, and other details during the model creation phase. In the development of the FE model, the material properties and geometries of the barrier components were defined to accurately reflect the real crash test results. Rail and post models were created using shell element types. The material properties of steel elements were defined in LS-DYNA using the MAT024 (piecewise linear plasticity) material model. To represent the M16 bolt connection between the post and rail, beam elements were defined. The material properties and failure criteria were established based on the material class of bolts using the MAT098 (simplified Johnson cook) material model. The failure definition in beam connections ensures that the parts remain connected until a certain stress criterion is met. After reaching the limit, the connection fails, and members move freely. Contact definitions between barrier components were established.

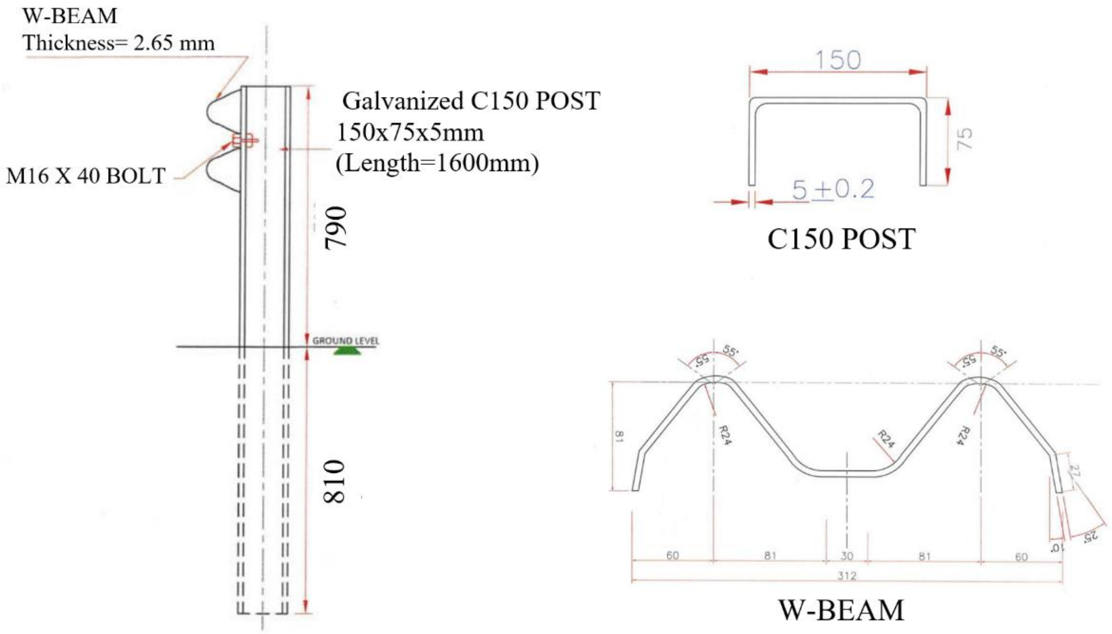

**Figure 1.** The geometric details of H1 containment level safety barrier studied [18]

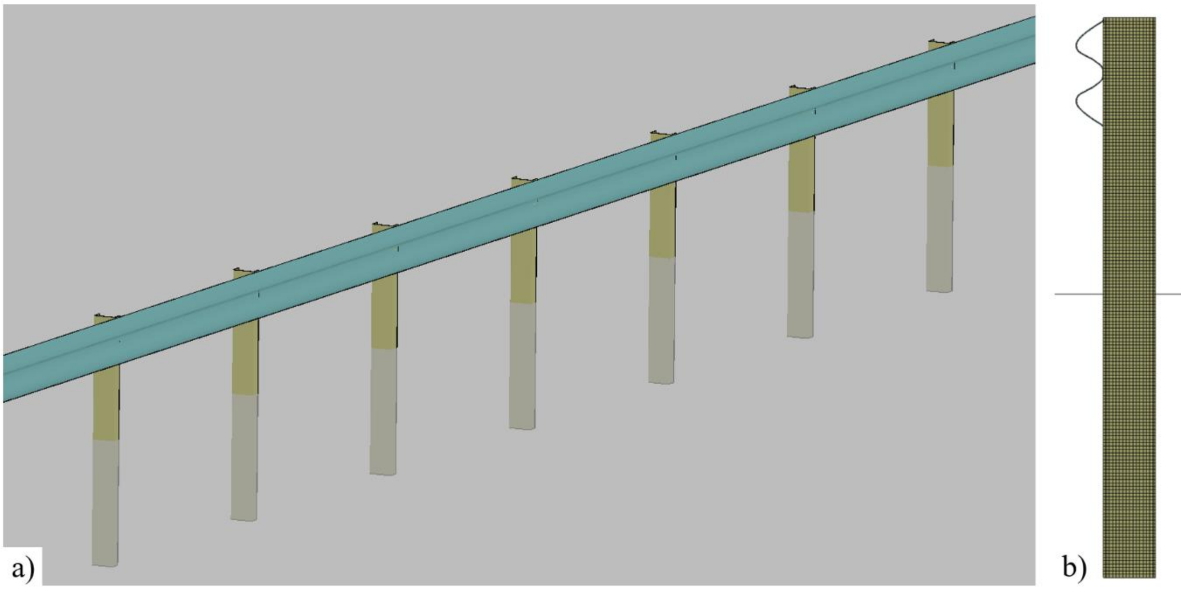

**Figure 2.** The FE model of H1 barrier system: a) General view, b) Side view (mesh view is on)

### 2.3. Validation of Finite Element (FE) Model

The safety barrier FE model must undergo validation using real crash test data before being utilized for further analyses. The barrier performance in the virtual testing should closely align with real-world results to validate the FE model. In this study, the validation and verification process for virtual testing followed the error tolerances outlined in the European standard EN 16303 [20]. To validate the FE model, variations in the test results, such as working width, should be within acceptable limits defined by the standard. Once validated, the model is deemed ready for subsequent crash simulations. Validation was performed using actual full-scale TB42 crash test results. Subsequently, a full-scale FE model for the H1 barrier system under TB42 test conditions was created using LS-DYNA. As previously mentioned, the TB42 test involves a 10000 kg HGV impacting the barrier at a speed of 70 km/h and an angle of 15°. The 10000 kg HGV FE model, developed and validated by the National Crash Analysis Center, was employed [21]. Vehicle and barrier models were integrated into a main file, and their positions were adjusted in accordance with EN 1317-2 and the real crash test conditions. Parameters such as vehicle initial velocity, contacts between vehicle and barrier components, and frictions between surfaces were defined. Additionally, parameters for test outputs, such as the test termination time and plot time intervals, were defined. Figure 3 provides an overview of both the actual full-scale TB42 crash test's initial condition and the corresponding FE model.

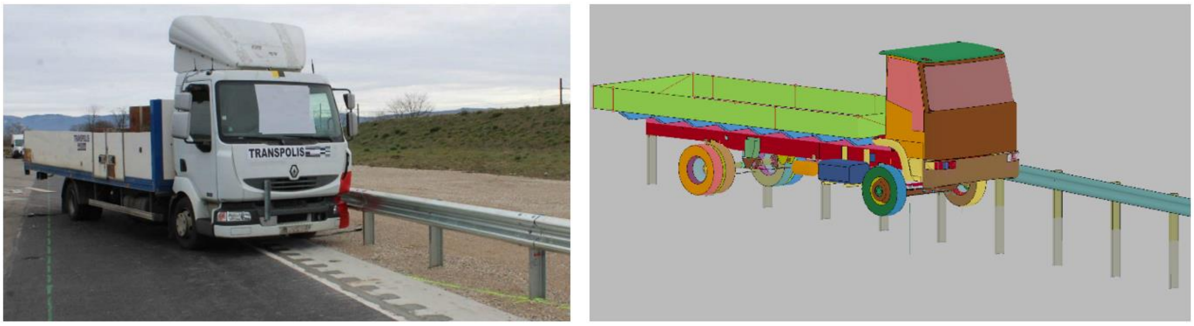

**Figure 3.** General overview of TB42 test before crash: real test (left) [18], FE model (right)

The actual test and FE analysis results were compared for validation. Working width results were compared according to the EN 16303 standard. In the real test, the working width of the barrier ($W_m$) was determined to be 1.14 mm, corresponding to the W4 class. EN 16303 mandates the comparison of working widths between the physical test ($W_m$) and the virtual test ($W_{VT}$). The difference between these two working widths must be less than the calculated value, according to Equation (3).

$$|W_m - W_{VT}| \leq \left(0.1 + 0.1 \times (D_m)\right) \quad (3)$$

where, $W_m$ is the working width of the real test (m), $W_{VT}$ is the working width of the virtual test (m), and $D_m$ is the dynamic deflection of the actual barrier (m). In the virtual test, the working width was determined to be 1.07 m, resulting in a difference of 0.07 m compared to the actual working width of 1.14 m in the real test. The dynamic deflection of the barrier ($D_m$) in the real test was measured to be 1.09 m. Calculating the right-hand side of the equation yielded 0.209 m. As this difference between the working widths was less than the limit value of 0.209 m, the FE model satisfied the working width criteria of EN 16303.

Figure 4 provides a side-by-side comparison between the real crash test and the FE simulation. The collision occurred at a 15° angle with a velocity of about 70 km/h. In the actual test, the collision took place near the 10th post, resulting in the deformation of posts 10-18 during the impact. Approximately 0.52 seconds after the initial impact, the vehicle aligned parallel to the barrier. Although the vehicle moved forward for a while due to wheel movement caused by the collision, it eventually came to a stop without leaving the barrier. The exit angle and exit box criteria in EN 1317-2 were met in this test.

The maximum lateral deformations in barriers during the real crash test and FE analysis are depicted in Figure 5. The strong correlation between the FE simulation and actual crash test outcomes is evident. The validation results confirm the suitability of the FE model for subsequent analyses in this study.

According to real TB11 crash test results, the working width was determined as 0.73 m, and the ASI and THIV parameters were obtained as 1.0 and 23 km/h, respectively [17]. These results led to the certification of this barrier system as an H1-W4-A system.

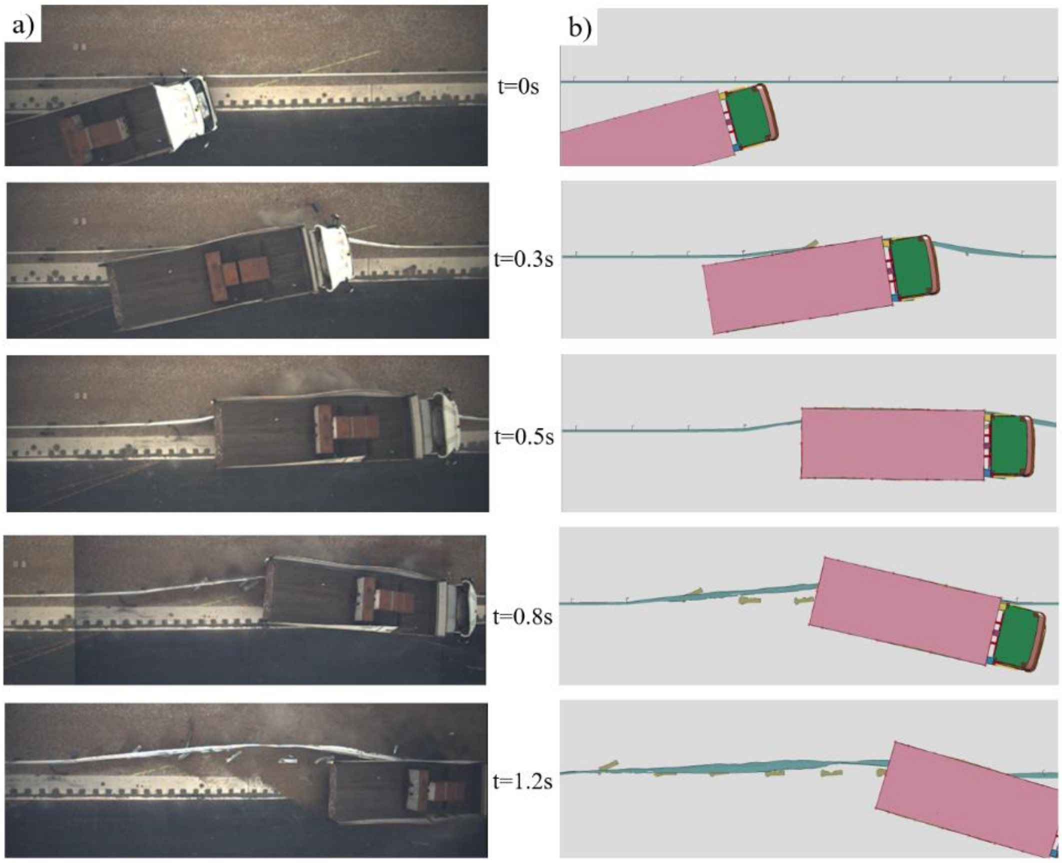

**Figure 4.** Comparison of TB42 results: a) Actual crash test [18], b) FE simulation

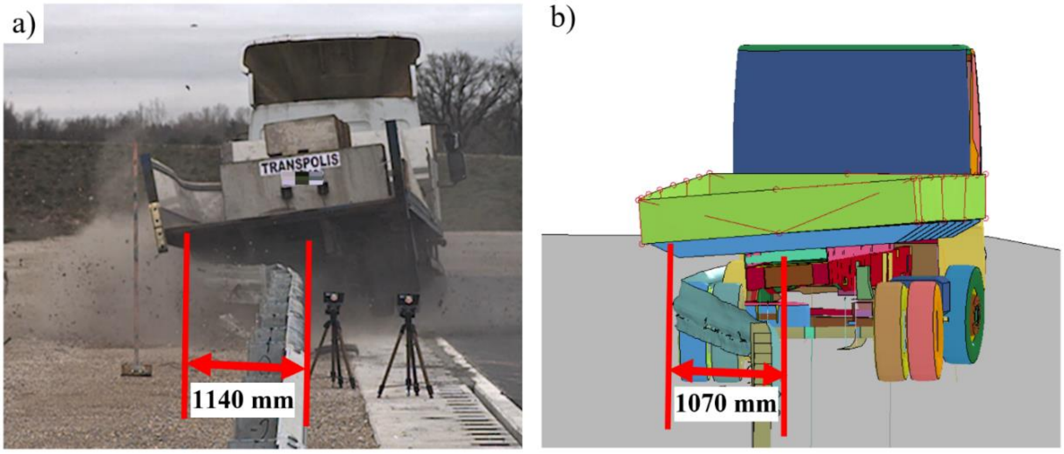

**Figure 5.** Comparison of barrier deformations: a) Full-scale crash test [18], b) FE simulation

## 2.4. Modified Barrier System and Fence Attachment

In this study, the tested and certificated H1-W4-A longitudinal barrier underwent modifications to reduce its weight. The investigation aimed to assess the impact of chain-link fence attachment on barrier performance and vehicle behavior. Analyses were conducted for the modified system, both with and without fence attachment. The 150x75 post and W-beam rail steel material properties remained the same as the reference initial H1-W4-A system, but their thickness was reduced to decrease the overall system weight. The original post length was 1600 mm, with 810 mm in the ground and the remaining 790 mm above the surface. In the modified system, the post length was reduced to 1500 mm, with 800 mm below the ground and 700 mm above the ground. The thickness of the posts, originally 5 mm, was reduced to 4 mm. The W-beam rail thickness decreased from 2.65 mm to 2.5 mm. Additionally, the post-rail connection bolts, initially M16-Class 8.8 bolts, were updated to M10-Class 4.6. The rail and post connections were set 160 mm below the upper end of the posts. While the weight of the reference barrier system's 1 m length was approximately 19.1 kg, the modified barrier system’s weight was reduced to about 16.3 kg per 1 m length. To conduct FE analysis of the modified system, its FE model was created, as illustrated in Figure 6. Geometric details and dimensions are indicated in this figure.

In previous applications involving chain-link fences, they were utilized by fixing them to the top of longitudinal barriers. This was done to protect motorcycle drivers or prevent pedestrian crossings on highways. However, in this study, a different approach was taken. A chain-link fence was attached to the modified barrier system between the W-beam rail and post. The effects of this configuration on barrier performance were investigated through finite element analyses. Figure 7 provides a typical representation of the chain-link fence appearance.

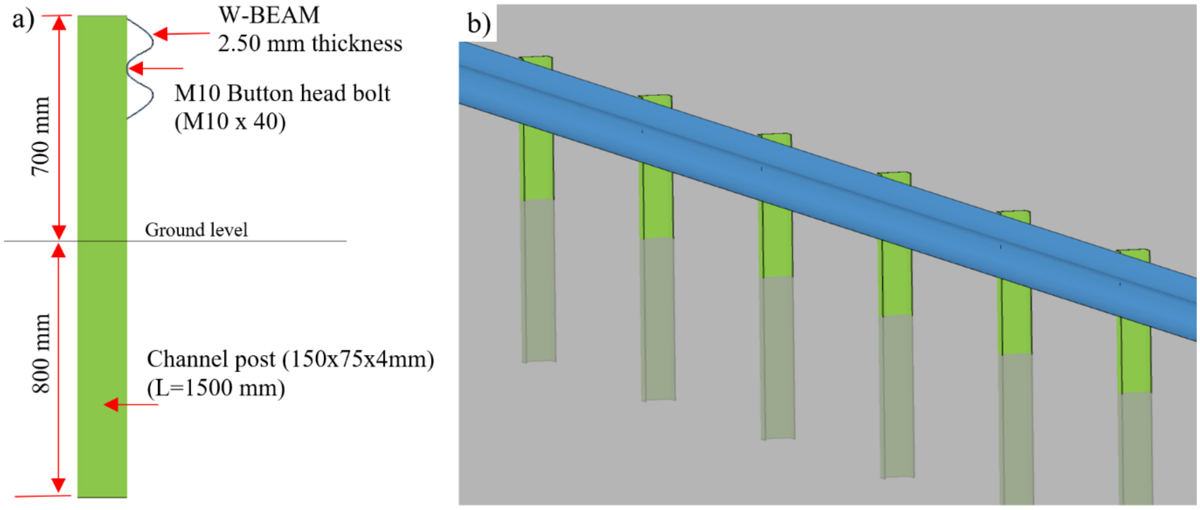

**Figure 6.** FE model of modified barrier system without fence: a) Side view, b) General view

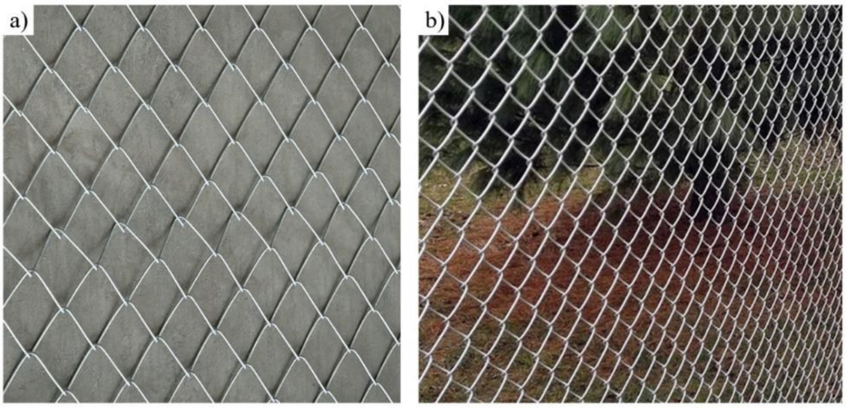

**Figure 7.** The typical view of chain-link fence: a) Example-1 [22], b) Example-2 [23]

In this study, a chain-link fence made from hot-dip galvanized wire material was incorporated into the finite element model preparation. The wire material's properties, produced in accordance with the TS EN 10223-6 standard, were utilized and defined in the FE model [24]. The chosen wire diameter for the chain-link fence was 2.5 mm, with a mesh size of 50 mm x 50 mm. Commonly used wire materials for chain-wire production in Turkey exhibit a minimum tensile strength of 350 N/mm$^2$, and the general material tensile strength falls within the range of 350-750 N/mm$^2$ [22], [25]. Material properties for the chain-link fence in the LS-DYNA model were defined using the MAT024 (piecewise linear plasticity) material model, selecting a tensile strength of 500 N/mm$^2$ and specifying other relevant properties. To model the steel wires, beam elements were used. The chain-link fence was longitudinally positioned between the rail and the post elements, facilitated by rectangular plates. Geometric details and the location of the chain-link fence are depicted in Figure 8. The lower edge of the fence is positioned 100 mm above the ground, with a fence height of 460 mm. A 450x70x3 (mm) steel support plate, made of S235JR grade material, secures the chain-link fence to the system using two bolts. The upper part of this plate is sandwiched between the post and the rail, utilizing the post-rail connection bolt. The lower part of the plate is connected to the post with a second M10-Class 4.6 bolt. The addition of the fixing plate increased the system weight to approximately 16.7 kg per 1m. Additionally, around 0.8 kg of chain-link fence is used in the 1 m barrier system.

To assess the impact severity and barrier structural performance with the inclusion of a chain-link fence, TB11 and TB42 FE simulations were conducted for both the modified system without a fence and the modified system with a fence. A total of four FE analyses were executed using LS-DYNA software. The validated barrier FE model underwent modifications specific to these tests. Vehicle FE models were obtained from the National Crash Analysis Center [21]. The general view of the models before the crash analyses is illustrated in Figure 9.

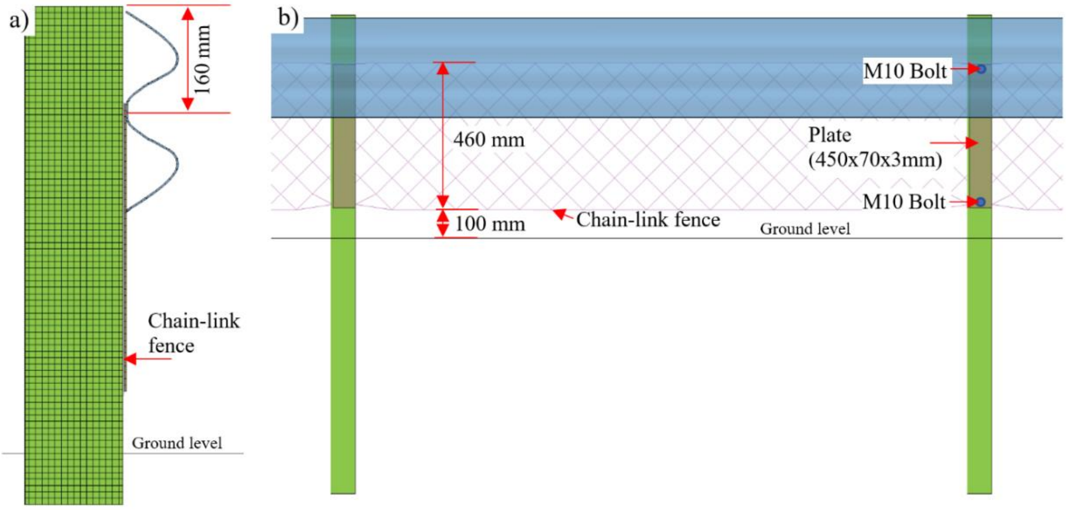

**Figure 8.** FE model of modified barrier system with fence: a) Side view, b) Front View

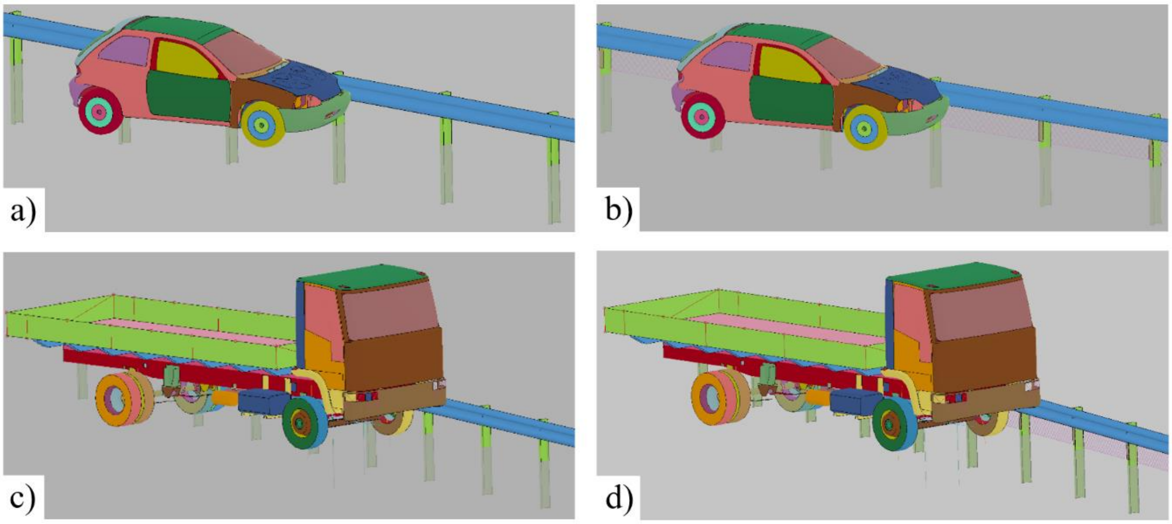

**Figure 9.** TB11 and TB42 FE model with and without fence: a) TB11 simulation without fence, b) TB11 simulation with fence, c) TB42 simulation without fence, d) TB42 simulation with fence

## 3. Results and Discussion

This study investigates the impact severity and barrier performance by analyzing the effect of chain-link fence attachment through FE analyses. Crash simulations were performed using the modified longitudinal barrier system, which was adjusted to reduce the weight of the certified H1 containment level barrier. TB11 and TB42 FE analyses were conducted for both the modified barrier system with and without chain-link fence attachment. The results of the FE simulations are presented and discussed in this section.

### 3.1. TB11 FE Analysis Results

TB11 crash test simulations were conducted for the modified longitudinal barrier, both with and without chain-link fence attachment. The FE analysis results were utilized to assess passenger impact severity and barrier performance. The evaluation employed ASI and THIV indices to determine impact severity levels, along with the assessment of barrier deformation under a car impact. The vehicle impacted the barrier at a speed of 100 km/h and an angle of 20°. Figure 10 illustrates the sequential comparison of TB11 crash test simulations for the modified safety barrier without and with chain-link fence placement. In both tests, 3 posts were detached from the rail due to the failure of M10 bolts. In both scenarios, the barriers effectively contained and redirected the 900 kg car, demonstrating the structural adequacy of the barrier.

Figure 11 shows the deformations in barriers resulting from the crash simulations. The working widths for cases without and with chain-link fence attachments were determined to be 0.72 m and 0.71 m, respectively. The conditions of the deformed region and working widths indicate that the chain-link fence had a minimal effect on the barrier's structural performance in the TB11 test.

In addition to structural evaluation, impact severities were also assessed for both cases. The ASI indices for the modified barrier system without and with a fence were determined to be 0.78 and 0.82, respectively. In both cases, the impact severity level is classified as A, indicating minimal injury risk to occupants. THIV results were calculated for the cases without and with fence placement as 22.8 and 24.7, respectively. Both results met the maximum THIV criteria specified in EN1217-2. Figure 12 presents a comparison of ASI graphs to demonstrate impact severity during crash testing time. FE analysis results indicated that while the implementation of the chain-link fence had a minimal effect on the TB11 test performance, it led to a slight increase in impact severity indices, still well within the EN 1317 limits.

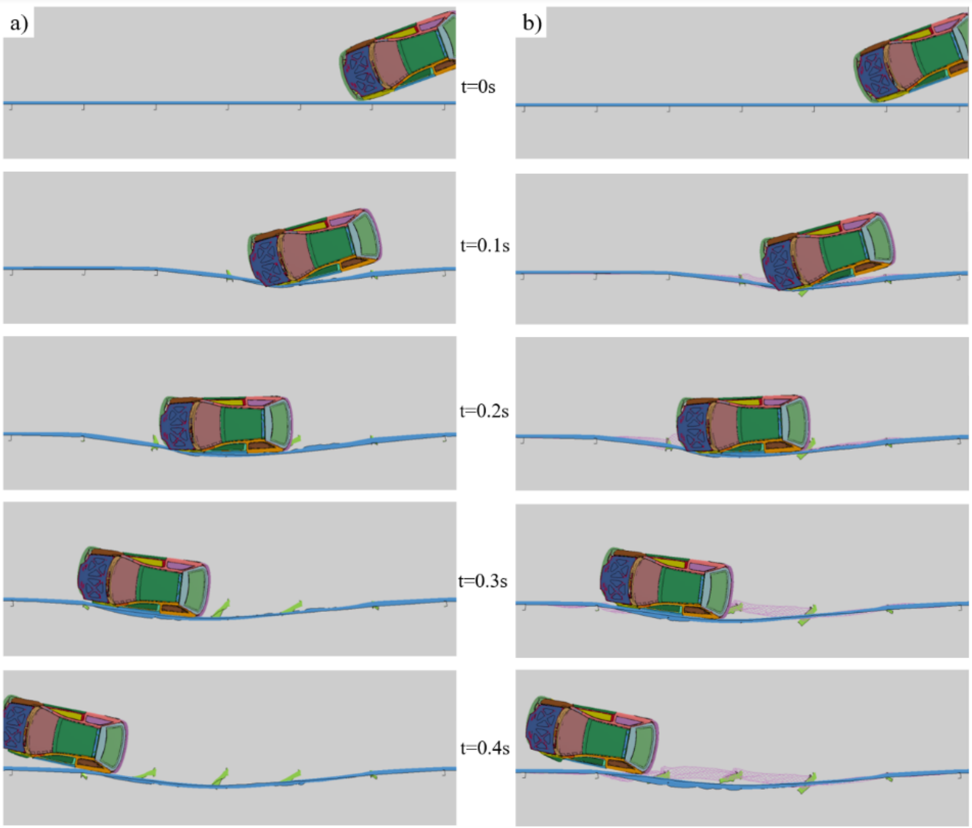

**Figure 10.** Comparison of TB11 simulations without and with fence: a) TB11 simulation without fence, b) TB11 simulation with fence

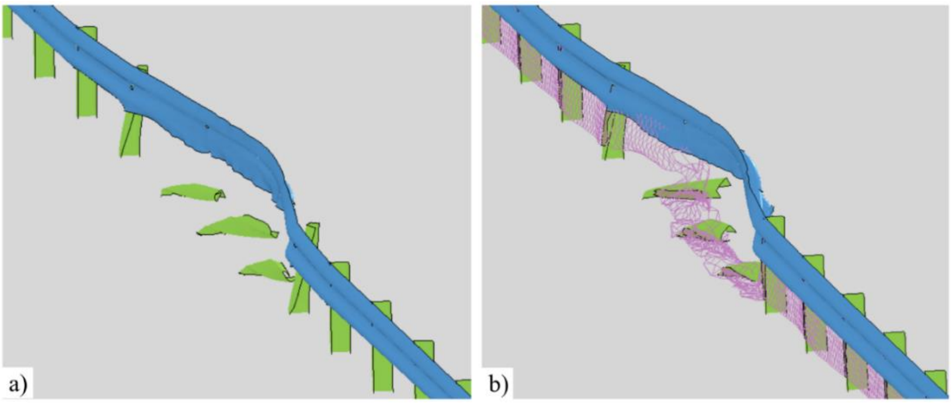

**Figure 11.** Damaged barriers after TB11 simulations: a) Barrier system without fence, b) Barrier system with fence

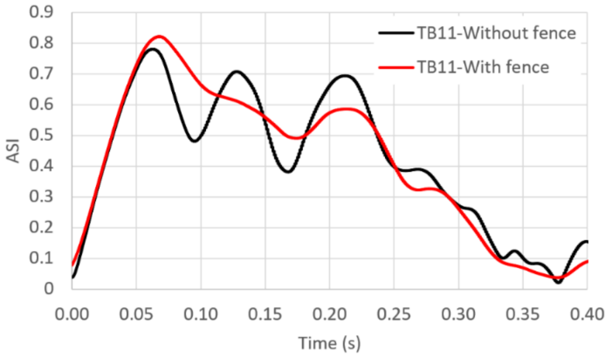

**Figure 12.** ASI graph comparison of two analyses

### 3.2. TB42 FE Analysis Results

TB42 crash simulations were conducted using an HGV model, evaluating the modified longitudinal barrier with and without chain-link fence attachment. The FE analysis results were employed to assess the barrier's structural adequacy in two different cases, examining damage and deformations in barrier components. The vehicle impacted the barrier at a speed of 70 km/h and an angle of 15°. Figure 13 presents a sequential comparison of TB42 crash test simulations for the modified safety barrier without and with chain-link fence placement. In the case without the fence, the vehicle couldn't be contained and redirected by the modified barrier system. Following the impact, the system deformed, and at 0.35 seconds, the front wheel of the vehicle began to climb over the W-beam rail. Eventually, the vehicle overcame the barrier, passed to the back, and ruptured the rail. According to EN 1317-2, this test failed, and the modified barrier system without the fence did not meet H1 containment level requirements. In the second test, the modified barrier with fence attachment successfully contained and redirected the vehicle. After the initial impact, a total of 8 posts were detached from the rail due to the failure of M10 bolts. However, the barrier system functioned properly with the fence attachment, successfully redirecting the vehicle according to EN 1317-2. The working width of the safety barrier was determined to be 1.23 m, corresponding to the W4 working width class, the same as the initial reference heavier barrier system.

Figure 14 displays the final conditions of the barrier systems following the TB42 crash simulations. In the case of the modified barrier system without fence attachment, the vehicle could not be contained. A complete breakage in the longitudinal beam component occurred, resulting in test failure. In the second analysis, however, the presence of the chain-link fence strengthened the system, allowing the barrier to contain and redirect the vehicle successfully.

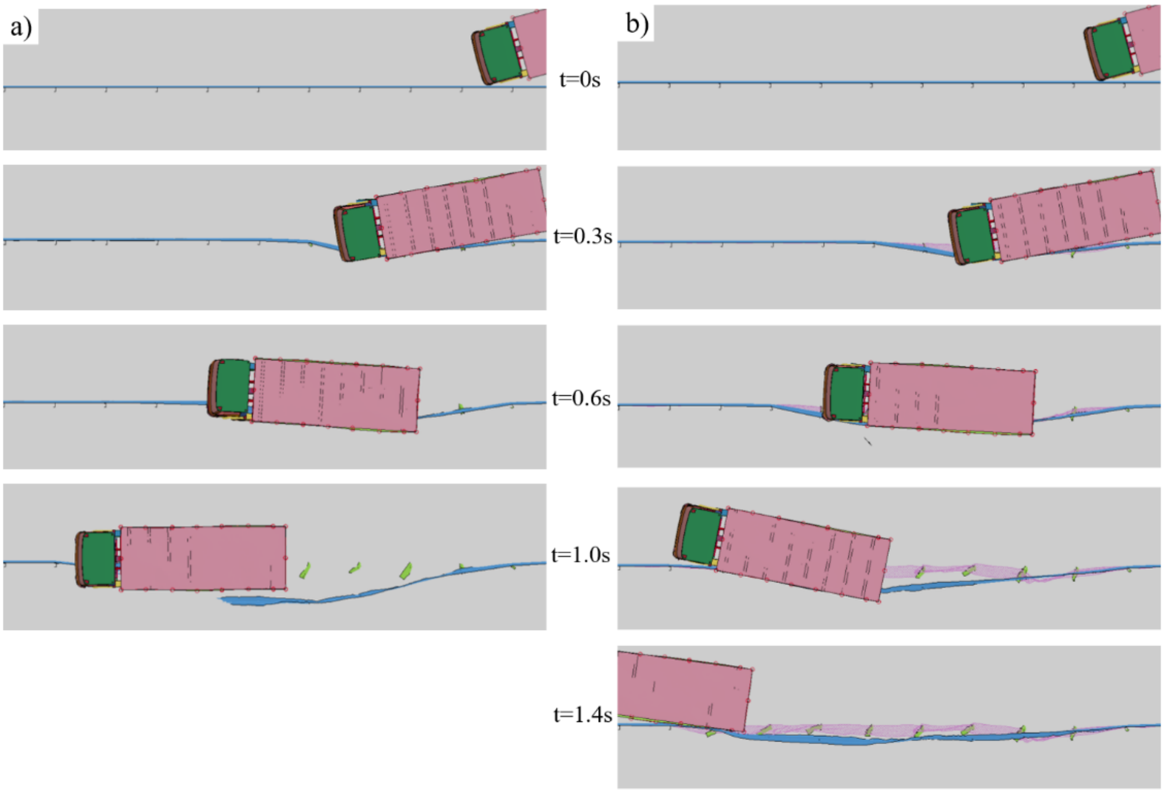

**Figure 13.** Comparison of TB42 simulations without and with fence: a) TB42 simulation without fence, b) TB42 simulation with fence

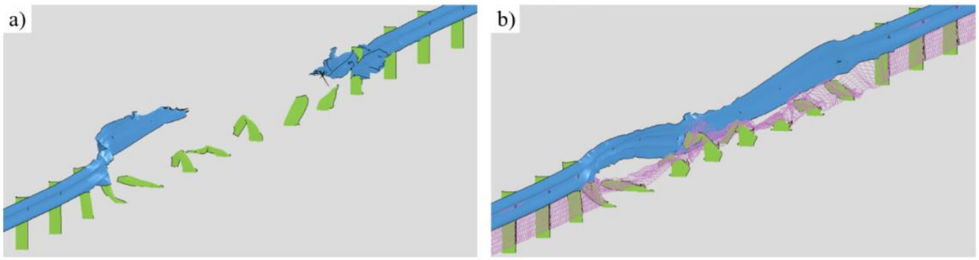

**Figure 14.** Damaged barriers after TB42 simulations: a) Barrier system without fence, b) Barrier system with fence

Table 4 provides a summary of the reference H1 barrier and the modified system crash test results, both with and without fence attachment. TB11 and TB42 FE analysis results demonstrated that the modified longitudinal barrier systems, both without and with fence attachment, met the EN 1317 requirements for the TB11 test. However, the system without a chain-link fence failed in the TB42 crash test simulation. With the attachment of the chain-link fence to the modified barrier, it could effectively contain and redirect the HGV. These findings indicate that the reduced-weight modified barrier system, with the addition of the fence, achieved identical performance to the heavier reference H1-W4-A system. Consequently, chain-link fence attachment emerges as a viable alternative for strengthening existing barrier systems or incorporating into new barrier designs.

**Table 4.** The summary of test results

| Test | Parameter | Real test results of reference H1 barrier | Modified barrier without fence | Modified barrier with fence |
|---|---|---|---|---|
| TB11 | ASI | 1 | 0.78 | 0.82 |
| | THIV (km/h) | 23 | 22.8 | 24.7 |
| | Working width (m) | 0.73 | 0.72 | 0.71 |
| TB42 | Working width (m) | 1.14 | Failed | 1.23 |
| | Working width class | W4 | - | W4 |

## 4. Conclusion

In this study, the impact of chain-link fences on safety barrier performance in terms of impact severity and structural adequacy was investigated through numerical simulations. The numerical model underwent validation using real crash test results, and the validated reference H1 containment level barrier design was modified to reduce system weight. The modified system underwent TB11 and TB42 tests with and without chain-link fence attachment, leading to the following key findings:

- The FE model of H1 containment level barrier was successfully validated with real test results, confirming its suitability for further analyses.
- The attachment of the chain-link fence had minimal effect on TB11 test performance, resulting in a slight increase in impact severity indices that remained within EN 1317 limits.
- The modified barrier without chain-link fence attachment failed the TB42 test, while the system with chain-link fence attachment successfully contained and redirected the 10000 kg HGV in the TB42 test simulation.
- The modified barrier system with fence attachment demonstrated H1-W4-A performance, equivalent to the heavier initial reference system. The use of chain-link fences enhances the performance of a weaker barrier system by limiting the lateral movement of posts.

The results suggest that chain-link fences have the potential for use in improving the performance of existing longitudinal barriers or as a component to reduce system weight in new designs. Further studies, involving simulations and real full-scale crash tests with different containment level safety barriers, are recommended to thoroughly investigate the usability and effectiveness of chain-link fence systems.

## Conflict of Interest Statement

There is no conflict of interest between the authors.

## Statement of Research and Publication Ethics

The study is complied with research and publication ethics.

## References

[1] *Road restraint systems - Part 2: Performance classes, impact test acceptance criteria and test methods for safety barriers including vehicle parapets*, EN 1317-2, European Committee for Standardization, Brussels, Belgium, 2010.

[2] A. M. Molan, M. Moomen, and K. Ksaibati, “Investigating the effect of geometric dimensions of median traffic barriers on crashes: Crash analysis of interstate roads in Wyoming using actual crash datasets,” *J. Safety Res.*, vol. 71, pp. 163–171, 2019.

[3] A. M. Molan and K. Ksaibati, “Impact of side traffic barrier features on the severity of run-off-road crashes involving horizontal curves on non-interstate roads,” *Int. J. Transp. Sci. Technol.*, vol. 10, no. 3, pp. 245–253, 2021, doi: https://doi.org/10.1016/j.ijtst.2020.07.006.

[4] T.-L. Teng, C.-C. Liang, C.-Y. Hsu, C.-J. Shih, and T.-T. Tran, “Impact performance of W-beam guardrail supported by different shaped posts,” *Int. J. Mech. Eng. Appl.*, vol. 4, no. 2, pp. 59–64, 2016.

[5] A. O. Atahan and A. O. Yucel, “Laboratory and field evaluation of recycled content sign posts,” *Resour. Conserv. Recycl.*, vol. 73, pp. 114–121, 2013, doi: https://doi.org/10.1016/j.resconrec.2013.02.002.

[6] C. Silvestri-Dobrovolny, R. Bligh, M. Kiani, and A. Zalani, “Evaluation of Attachments to Concrete Barrier Systems to Deter Pedestrians—Volume 1: Technical Report,” Texas, USA, No. FHWA/TX-23/0-7082-R1-Vol1, 2023.

[7] C. Silvestri-Dobrovolny, R. P. Bligh, M. Kiani, A. Zalani, W. J. L. Schroeder, and D. L. Kuhn, “Evaluation of Attachments to Concrete Barrier Systems to Deter Pedestrians—Volume 2: Crash Report,” Texas, USA, No. FHWA/TX-23/0-7082-R1-Vol2, 2023.

[8] C. Silvestri Dobrovolny, S. Shi, J. Kovar, and R. P. Bligh, “Development and Evaluation of Concrete Barrier Containment Options for Errant Motorcycle Riders,” *Transp. Res. Rec.*, vol. 2673, no. 10, pp. 14–24, 2019, doi: 10.1177/0361198119845900.

[9] T.-L. Teng, C.-C. Liang, and T.-T. Tran, “Effect of various W-beam guardrail post spacings and rail heights on safety performance,” *Adv. Mech. Eng.*, vol. 7, no. 11, p. 1687814015615544, Nov. 2015, doi: 10.1177/1687814015615544.

[10] A. Ö. Yücel, A. O. Atahan, T. Arslan, and U. K. Sevim, “Traffic Safety at Median Ditches: Steel vs. Concrete Barrier Performance Comparison Using Computer Simulation,” *Safety*, vol. 4, no. 4, 2018, doi: 10.3390/safety4040050.

[11] Z. Ren and M. Vesenjak, “Computational and experimental crash analysis of the road safety barrier,” *Eng. Fail. Anal.*, vol. 12, no. 6, pp. 963–973, 2005, doi: https://doi.org/10.1016/j.engfailanal.2004.12.033.

[12] Ł. Pachocki and D. Bruski, “Modeling, simulation, and validation of a TB41 crash test of the H2/W5/B concrete vehicle restraint system,” *Arch. Civ. Mech. Eng.*, vol. 20, no. 2, p. 62, 2020, doi: 10.1007/s43452-020-00065-7.

[13] A. O. Atahan, A. O. Yucel, and O. Guven, “Development of N2–H1 Performance-Level Guardrail: Crash Testing and Simulation,” in *Transportation Research Circular*, *E-C172*, 2013.

[14] S. Tahmasbi, A. Giacomini, C. Wendeler, and O. Buzzi, “3D finite element modelling of chain-link drapery system,” in *ISRM EUROCK*, ISRM, 2018, p. ISRM-EUROCK.

[15] T. T. Le Hoang, H. Masuya, Y. Nishita, and T. Ishii, “Experimental and numerical impact models of protection fences,” *Int. J. Prot. Struct.*, vol. 11, no. 1, pp. 90–108, 2020, doi: 10.1177/2041419619852367.

[16] *Road restraint systems - Part 1: Terminology and General Criteria For Test Methods*, EN 1317-1, European Committee for Standardization, Brussels, Belgium, 2010.

[17] Transpolis SAS, “Barrier for Road edge and Median W-beam - TB11,” TRANSPOLIS S.A.S., Saint-Maurice-de-Rémens, France, 2021.

[18] Transpolis SAS, “Barrier for Road edge and Median W-beam - TB42,” TRANSPOLIS S.A.S., Saint-Maurice-de-Rémens, France, 2021.

[19] *LS-DYNA Keyword User’s Manual*, LSTC, Livermore Software Technology Corporation: Livermore, CA, USA, 2012.

[20] *Road restraint systems - Validation and verification process for the use of virtual testing in crash testing against vehicle restraint system*, BS EN 16303:2020, BSI Standards Publication, 2020.

[21] *Finite element model archive*, NCAC, FHWA/NHTSA National Crash Analysis Center, George Washington University, Apr. 2008 [Online] Available: http:// www.ncac.gwu.edu/vml/models.html.

[22] Guneycelik, “Chain-link fence technical specifications,” guneycelik.com.tr. https://www.guneycelik.com.tr/Tr/tel-orgu.html (accessed Jan. 1, 2024).

[23] Yapimtel, “Galvanized chain-link fence,” yapimtel.com.tr. https://yapimtel.com.tr/urunler/galvaniz-orgu-teli/ (accessed Jan. 1, 2024).

[24] *Steel wire and wire products for fencing and netting - Part 6: Steel wire chain link fencing*, TS EN 10223-6, Turkish Standard, Turkish Standards Institution, Ankara, 2013.

[25] Te-fence, “Chain-link fence,” te-fence.com. https://te-fence.com/chain-link-fence/ (accessed Jan. 1, 2024).

**Bitlis Eren Üniversitesi Fen Bilimleri Dergisi**
BİTLİS EREN UNIVERSITY JOURNAL OF SCIENCE
ISSN: 2147-3129/e-ISSN: 2147-3188
VOLUME: 13 NO: 2 PAGE: 445-459 YEAR: 2024
DOI:10.17798/bitlisfen.1422869

# Detection of Lung Cancer Cells Using Deep Learning Methods

Muhittin GENÇ [1*], Funda AKAR[2]

[1] *Institute of Science and Technology, Erzincan Binali Yıldırım University, Erzincan 24002, Turkey*
[2] *Department of Computer Engineering, Erzincan Binali Yıldırım University, Erzincan 24002, Turkey*
*(ORCID: 0009-0002-5276-9244) (ORCID: 0000-0001-9376-8710)*

**Keywords:** CNN, Deep Learning, Lung Cancer Detection, YOLO

## Abstract

Lung cancer stands out as a high mortality, fatal disease worldwide. Early diagnosis is crucial for effective treatment of this disease; however, treatment options can be limited when it is often diagnosed in advanced stages. This study examines the role of artificial intelligence (AI) techniques in early diagnosis of lung cancer and emphasizes the advantages it provides. Particularly, the ability of deep learning algorithms to extract meaningful features from complex datasets indicates significant potential for detecting early stages of lung cancer. In this context, it is anticipated that AI-supported diagnostic systems have the potential to significantly improve lung cancer diagnostic methods by reducing the workload of radiologists and increasing accuracy rates. In this study, a total of 6 datasets were obtained by applying Gabor filter and Histogram Equalization+CLAHE filter to original datasets. The results obtained in the diagnosis of lung cancer using Convolutional Neural Networks (CNN) and YOLO algorithms are evaluated in two different categories. One of these categories is the investigation of the effect of image preprocessing methods. The other is the investigation of the effect of dataset partitioning into training, testing, and validation on success. According to the results obtained, the highest success rate in terms of F1 Score for the CNN model was achieved in both dataset partitioning (70%-20%-10% and 60%-20%-20%) with the datasets subjected to Histogram Equalization+CLAHE filter. It was obtained as 99%. For the YOLO model, the highest success rate was determined as 96% F1 Score with the same preprocessing technique and dataset partition. The effect of image preprocessing and dataset partitioning on success is not as high in the YOLO model as it is in the CNN model.

## 1. Introduction

Lung cancer is a serious disease that arises from the uncontrolled proliferation of cells in lung tissue, making normal breathing difficult for the patient. This type of cancer begins with the occurrence of DNA structure abnormalities, leading to the formation of an abnormal mass called a tumor, which in turn results in the excessive proliferation of cells [1]. Lung cancer is the deadliest among all cancer types worldwide. As seen in Figure 1, according to data released by the World Health Organization (WHO), approximately 1.8 million people worldwide lost their lives due to lung cancer in 2020, and 2.2 million new cancer cases were reported [2]. In Turkey, within the same year, the incidence rate of lung cancer among all cancer types was determined to be 17.6%, with 41,264 new cases detected [3]. Due to its higher mortality rate compared to other cancer types, early diagnosis of lung cancer is crucial.

In the evolving era of information technology, studies focusing on solutions to this issue have intensified, particularly with the use of artificial intelligence techniques. Artificial intelligence denotes the ability of computers to perform activities specific to human intelligence, such as carrying out various

---

[*]Corresponding author: mgenc@erzincan.edu.tr

*Received: 20.01.2024, Accepted: 18.03.2024*

tasks, solving complex problems, learning, and making decisions. Especially in the field of healthcare, the use of artificial intelligence aims to facilitate physicians in diagnosing diseases and increase operational efficiency. In this study aimed at this purpose, deep learning methods were employed to detect cancerous regions in lung images obtained from Computed Tomography (CT) scans.

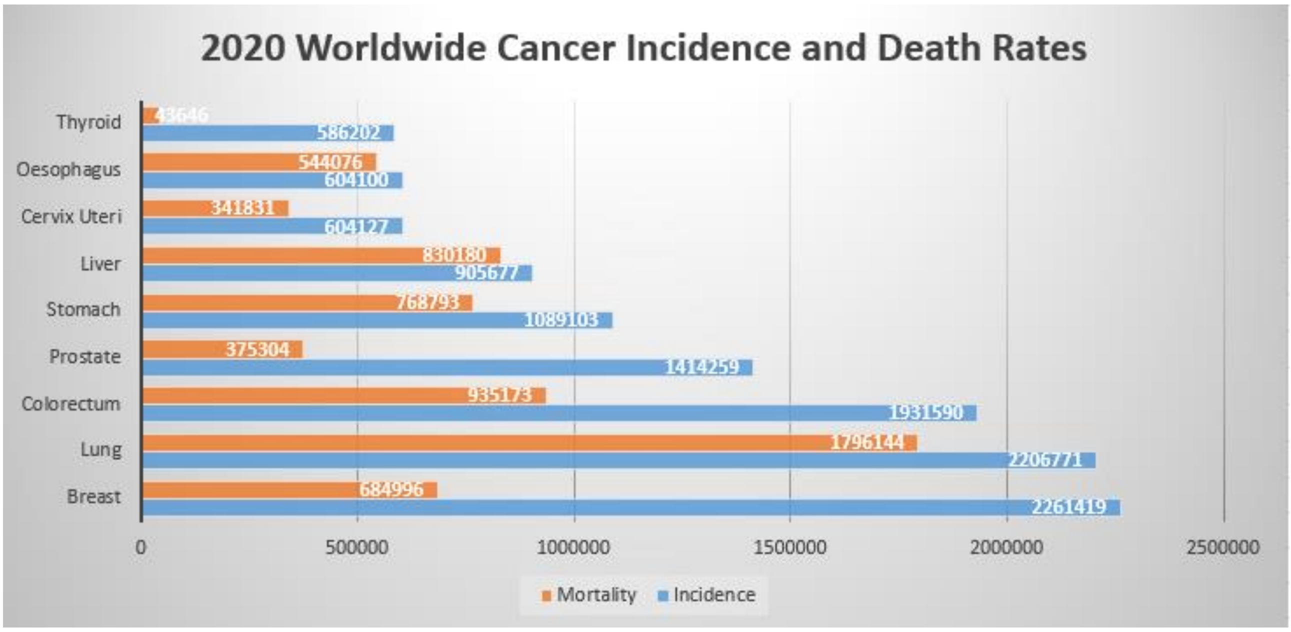

**Figure 1.** Global cancer cases worldwide according to 2020 data [2].

When examining the studies on this topic, it is noticeable that there has been a gradual increase in research, especially after 2019, and a concentration of studies offering solutions using various artificial intelligence methods. Keshani et al. conducted a study using CT images to segment cancerous lungs into regions through active contour modeling. Subsequently, various masking techniques were applied, and nodules were classified using Support Vector Machines (SVM) based on 2D stochastic and 3D anatomical features, achieving a detection accuracy of 89% [4]. Kuruvilla and Gunavathi performed lung segmentation from CT images, extracting various statistical parameters such as standard deviation, skewness, kurtosis, mean, fifth central moment, and sixth central moment. They utilized these parameters for classification using feedforward and backpropagation algorithms of artificial neural networks. The results indicated an accuracy of 91.1% for the first method and 93.3% for the second method [5]. De Carvalho Filho et al. developed a methodology for the detection of lung cancer nodules from CT images using pattern recognition and image processing techniques. They applied clustering algorithms to classify structures resembling lungs after segmenting the images. In the final classification, they employed Micro-Genetic Algorithm in addition to SVM, achieving sensitivity, specificity, and accuracy rates of 85.91%, 97.70%, and 97.55%, respectively [6]. Song et al. utilized three deep learning methods, Convolutional Neural Networks (CNN), Deep Neural Networks (DNN), and Stacked Autoencoders (SAE), to detect benign and malignant nodules from lung CT images. The models achieved accuracies of 84.15% for CNN, 82.37% for DNN, and 82.59% for SAE [7]. Lustberg et al. investigated the use of computer-assisted segmentation in the delineation of organs at risk for lung cancer. They observed that manually performed segmentation took an average of 20 minutes, whereas the atlas-based software reduced this time to 7.8 minutes, and deep learning-based software further reduced it to 10 minutes [8]. In another study, various image processing techniques were applied to improve the quality of CT images, followed by cropping unnecessary details expressing redundancies in the images. The resulting images were modeled by a deep neural network algorithm with an increased number of layers. The obtained results showed an accuracy of 94.56%, sensitivity of 96.2%, and specificity of 94.2% [9]. To enhance the highlighting of cancerous regions in CT images, histogram equalization was performed in another study. They developed a deep learning method using Improved Profuse Clustering Technique (IPCT) and Deep Learning with Instantaneously Trained Neural Networks (DITNN), achieving a 98.42% accuracy after training [10]. A study in 2019 focused on detecting and classifying diseases such as healthy lungs, Chronic Obstructive Pulmonary Disease (COPD), and fibrosis from CT images. Three newly emerged algorithms, namely Improvised Crow Search Algorithm (ICSA), Improvised Grey Wolf Algorithm (IGWA), and Improvised Cuttlefish Algorithm (ICFA), were employed to determine features. For classification, SVM, k-Nearest Neighbor (K-NN), and Decision Tree Classifier were used, and the best combination of classification models and feature extraction methods was observed to be IGWA + K-NN with a 99.4% accuracy [11]. Kasinathan et al. segmented the lungs using CT images, dividing them into subregions after applying Gaussian distribution for feature extraction. They achieved a classification accuracy of 97% using CNN [12]. In a study conducted in 2020, CNN was used to work on a lung CT dataset collected from Iraqi hospitals. A technique with an AlexNet architecture aimed to detect whether the target population in CT scans was benign or malignant, achieving an accuracy of up to 93.5% [13]. Nanglia et al. aimed to improve classification accuracy through a hybrid classification algorithm. They reported a 98.08% accuracy with the model they developed [14]. A study comparing Artificial Neural Networks (ANN), CNN, and Recurrent Neural Networks (RNN) on CT images found that the ANN model marginally outperformed RNN and CNN models with an accuracy of 71.18% [15]. Chen et al. applied the SegNet approach to facilitate the diagnosis of lung cancer from CT images, attempting to detect benign and malignant tumors. The manual detection accuracy for lung cancer was 86.25%, while SegNet achieved an accuracy of 92.50%, DeepLab v3 reached 80.41%, and VGG-19 had an accuracy of 79.58% [16]. In 2021, a research aimed at detecting lung cancer using artificial intelligence techniques employed three different CNN models on the LC25000 Lung and Colon Histopathological Image dataset. Inception_ResNet_V2 achieved a 99.7% accuracy, VGG-19 had 92.99%, and ResNet 50 showed 99.4% accuracy [17]. In the study conducted by Talukder et al. in 2022, they focused on early detection of colon and lung cancer using a hybrid feature extraction method. VGG16, MobileNet, and DenseNet201 models were employed, achieving a detection rate of 99.05% for lung cancer and 100% for colon cancer [18]. Another study on lung cancer utilized Internet of Things (IoT) technology in addition to CT images. Data from both CT and wearable technologies were combined, processed through an Extended Convolutional Neural Network (ECNN), resulting in an accuracy of 96.8% [19]. Haznedar and Simsek analyzed lung and renal cell cancer RNA-Seq data sets from the Cancer Genome Atlas (TCGA) using both classical machine learning methods and deep learning techniques. Among classical machine learning methods, Random Forest yielded the best results with an accuracy range of 93.51% to 91.83%. For deep learning methods, DNN-Adadelta achieved accuracy rates of 95.54% and 96.15% [20]. In another research effort, the VGG16 backbone was combined with Single Shot Detection (SSD) for detecting Osteosarcoma nodules metastasizing to the lungs, resulting in a model with an accuracy of 75.97% [21]. For rapid and accurate diagnosis of lung and colon cancers using CT images, Class Selective Image Processing (CSIP) was applied, and training was performed using an AlexNet neural network model. The accuracy increased from 89.8% before CSIP to 98.8% after its application [22]. A study focused on classifying abnormalities in lung nodules used an optimized hybrid approach of ICSA and CNN-based Long Short-Term Memory (LSTM) methods. Simulation results indicated that the proposed method achieved an accuracy rate of 98% [23]. Shanthi et al. aimed to improve the detection and classification of lung cancer cells by creating a new hybrid algorithm with Naïve Bayes, Decision Tree, and ANN classifiers, incorporating Stochastic Diffusion Search (SDS)-based feature selection. The results showed that the proposed TABU-SDS-NN achieved an accuracy of 94.07% [24]. In a study conducted in 2023, three different CNN models were created for detecting lung cancer cells from CT images. By averaging the results of these three models, a new approach was proposed, and the average accuracy of the three CNNs was measured at 95% [25].

In this study, a comparison of methods for lung cancer diagnosis using CNN and YOLO was conducted with a total of 6 datasets. The impact of image preprocessing methods such as Gabor filter and Histogram Equalization + CLAHE applied prior to the training process of the models on their success was investigated. Additionally, the effect of dataset partitioning, with ratios of 70%-20%-10% and 60%-20%-20%, on the accuracy of the models was also analyzed.

## 2. Material and Method

This study adopts a different approach from other studies in the literature concerning the importance of the mentioned topic. It transforms the dataset into three different datasets, including the original version, by applying various preprocessing methods. The aim of this approach is to determine the impact of the applied preprocessing methods on success.

The first dataset includes the original Cancer Imaging Archive (TCIA) dataset [26], [27]. To enhance success, a second dataset was obtained by applying a Gabor filter to the images. Additionally, images in the original dataset were subjected to histogram equalization followed by Contrast Limited Adaptive Histogram Equalization (CLAHE) to create a third dataset. After expanding the dataset, models were compared in terms of the metrics specified below using CNN and YOLO version 8, whose popularity has increased in recent years.

- Confusion Matrix: A table used to determine the success of models. TP represents true positives, FN represents false negatives, FP represents false positives, and TN represents true negatives (Figure 2).

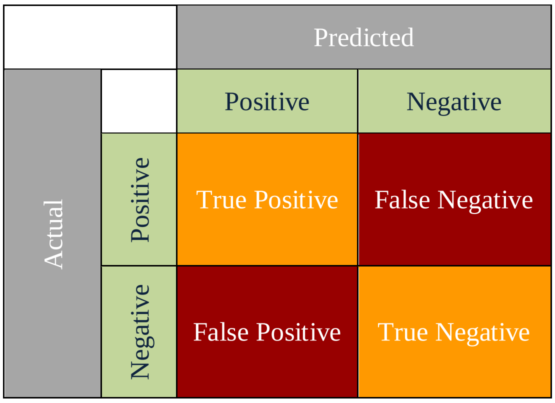

| | | Predicted | |
|---|---|---|---|
| | | Positive | Negative |
| Actual | Positive | True Positive | False Negative |
| | Negative | False Positive | True Negative |

**Figure 2.** Representation of the Confusion Matrix

- Accuracy (ACC): A measure of how accurate the created model is.

$$ACC = \frac{TP+TN}{TP+TN+FP+FN} \qquad (1)$$

- Precision (P): Indicates the positive prediction rate of the model.

$$P = \frac{TP}{TP+FP} \qquad (2)$$

- Recall (R): Also known as sensitivity or true positive rate, formalized as follows:

$$R = \frac{TP}{TP+FN} \qquad (3)$$

- F1 Score: The harmonic mean of precision and recall, considered a better measure than accuracy.

$$F1\,Score = 2 * \frac{Precision*Recall}{Precision*Recall} \qquad (4)$$

- Average Precision (AP): Expressed as the area under the precision-recall curve.

$$AP = \int_0^1 p(r)dr \cong \sum_{k=1}^{n} p(k).\Delta r(k) \qquad (5)$$

- Mean Average Precision (mAP): A metric used to evaluate the performance of the model. mAP measures the accuracy of detected objects and is often evaluated with a threshold value determined using a confidence threshold. While mAP50 represents the case where a confidence threshold of 0.5 is used, mAP50-95 calculates performance at different confidence thresholds between 0.5 and 0.95. This metric indicates the accuracy rate of the objects detected by the model. The mAP value is higher when the model detects objects more accurately. When calculating mAP, precision (AP) measurements are made separately for each class, and then the arithmetic average of these values is taken to obtain the overall mAP value.

$$mAP = \frac{1}{N}\sum_{i=1}^{N} AP_i \qquad (6)$$

**Convolutional Neural Networks (CNNs):** Convolutional Neural Networks are deep learning algorithms that take input images, pass them through various filters to extract features, and produce results by combining them with kernels [28]. The use of CNNs extends beyond image classification, object recognition, and face detection into the medical field, where these advancements facilitate disease diagnosis, ultimately improving survival rates.

**You Only Look Once (YOLO):** YOLO is a deep learning model used in object detection. It is a method that can detect objects in an image in a single pass, making it suitable for real-time applications such as video. Thanks to this feature, YOLO provides a fast and effective solution for object detection tasks.

The flowchart of the study is presented in Figure 3, and sample images for each dataset are shown in Figure 4.

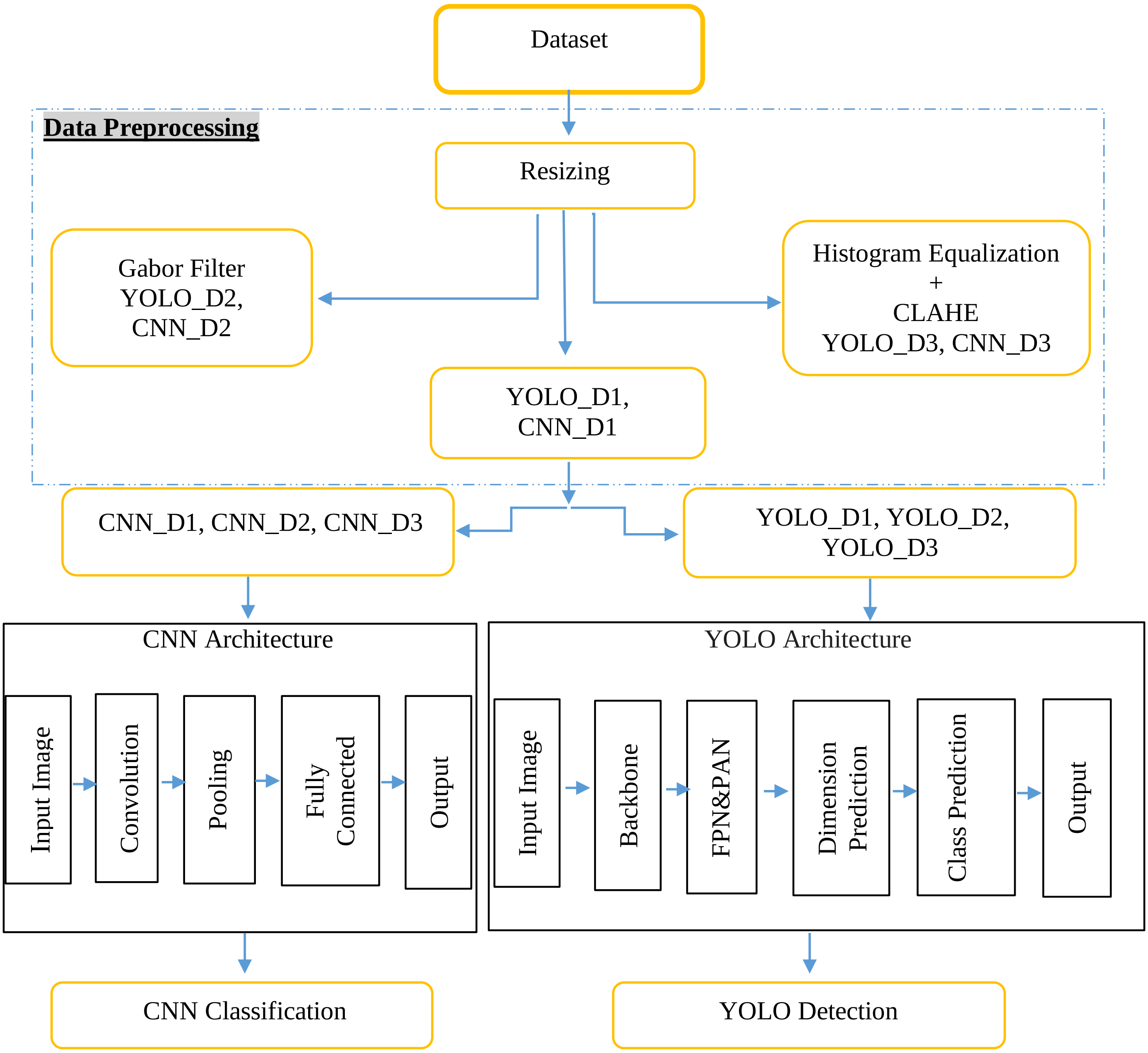

**Figure 3.** Workflow of the Application

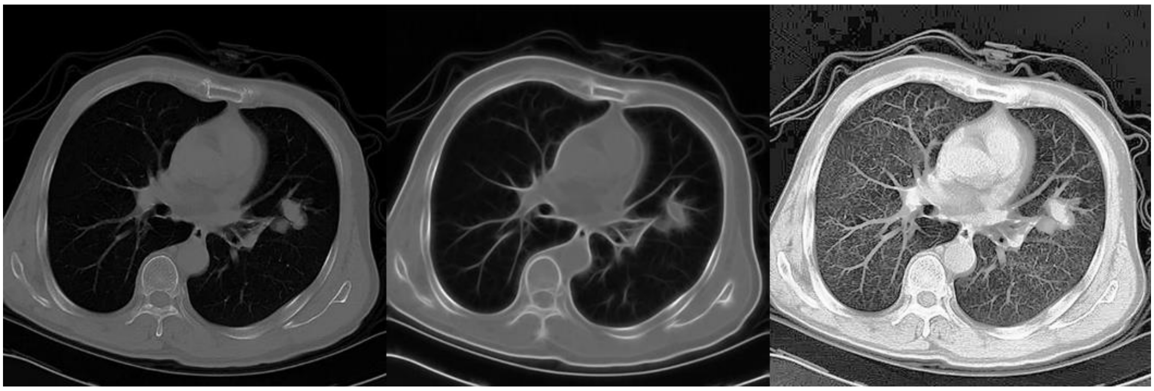

**Figure 4.** Example images from the dataset used for CNN and YOLO models: (a) original image, (b) image with Gabor filter applied, (c) image with histogram equalization and CLAHE applied

### 2.1. Data Preparation

The YOLO dataset consists of 4968 CT images with dimensions of 512x512 pixels. The CNN dataset comprises a total of 7940 images with dimensions of 512x512 pixels, half of which are cancerous and the other half normal. The images in the CNN dataset are reduced to a size of 64x64 pixels. This size reduction aims to save runtime and resource usage. Since the YOLO model achieves higher success on large-scale images, no dimension changes are made to the YOLO dataset.

Two different partitioning methods are employed to analyze the datasets. In the first partitioning, 70% of the dataset is used for training, 20% for validation, and 10% for testing. In the second partitioning, these ratios are set at 60% for training, 20% for validation, and 20% for testing. As the YOLO and CNN datasets are transformed into three separate datasets, the subsequent representations in this study are provided in the Table 1.

**Table 1.** Naming of datasets

| Dataset | Description of the Dataset |
|---|---|
| D1 | Original dataset |
| D2 | The dataset created by applying the gabor filter |
| D3 | The dataset created by applying histogram equalization + CLAHE |

## 2.2. Data Preprocessing

Data preprocessing is a crucial step that helps improve the quality of images. In this study, various preprocessing steps, including resizing, formatting, and converting images to the desired format, were applied to the images in the dataset. In addition to the original dataset (D1), a Gabor filter was first applied to both datasets to investigate its impact on performance (D2). Subsequently, a new dataset was created for the original dataset by applying histogram equalization + CLAHE processing (D3). As a result, three different datasets, each subjected to different preprocessing methods for YOLO and CNN, were obtained. Classification processes were then carried out on these datasets.

### CNN Model

Three different convolution processes of 32x3x3, 64x3x3, and 64x3x3 were applied to the input image. After each convolution process, pooling of 4x4, 2x2, and 2x2 was sequentially applied to reduce the height and width of the image. Additionally, a dropout parameter of 0.5 was used after each convolution to prevent overfitting and memorization by the model. Finally, the model was passed through the sigmoid activation function to obtain results. These processes aim to extract various features from the input image and support the model in learning more generally. The model was run for 50 epochs on a computer with an Intel Core i5 7200U 2.5 GHz processor and 8 GB RAM. This process was performed for three different datasets and two different split procedures. Training times are detailed in Table 2.

### YOLO Model

The training of the YOLO model, based on the YOLO v8 architecture, was conducted for 60 epochs using Python programming language and Google Colaboratory with Google Drive. To expedite and facilitate the training process, a Tesla T4 GPU provided by Google was employed. The processing of the dataset and training duration are detailed in Table 2. The preference for the Tesla T4 GPU was motivated by the ability to complete the training in a few hours, compared to several days with a CPU. This choice aimed to save time and enhance the efficiency of the training process.

**Table 2.** Training durations for CNN and YOLO

| | CNN | | YOLO | |
|---|---|---|---|---|
| **Dataset** | **%70-%20-%10** | **%60-%20-%20** | **%70-%20-%10** | **%60-%20-%20** |
| D1 | 3 hours 23 min | 3 hours 28 min | 2 hours 27 min | 2 hours 57 min |
| D2 | 3 hours 37 min | 3 hours 36 min | 2 hours 19 min | 2 hours 50 min |
| D3 | 3 hours 05 min | 3 hours 02 min | 2 hours 31 min | 2 hours 54 min |

### 3. Research Findings

The results of the 12 studies conducted with a total of 6 datasets obtained through the division process of 2 different datasets for the 2 models used are presented in Table 3 and Table 4.

The images in the datasets used for CNN are labeled as cancerous and normal. Therefore, as shown in Table 3, two values are observed for cancerous/normal in each of the F1 Score, Precision, and Recall values. However, in the YOLO datasets, since the training process is conducted solely on cancerous images, such a scenario is not applicable for YOLO.

**Table 3.** CNN Model Results

| | Dataset | Preprocessing | Train Acc | Train Loss | Val Acc | Val Loss | Test Acc | Test Loss | F1-Score Cancer - Normal | Precision Cancer - Normal | Recall Cancer - Normal |
|---|---|---|---|---|---|---|---|---|---|---|---|
| CNN | Dataset 60-20-20 | Original (D1) | 0.985 | 0.061 | 0.894 | 0.480 | 0.89 | 0.47 | 0.89-0.90 | 0.97-0.84 | 0.81-0.98 |
| | | Gabor Filter (D2) | 0.998 | 0.004 | 0.920 | 0.250 | 0.95 | 0.29 | 0.92-0.93 | 0.98-0.87 | 0.86-0.98 |
| | | Histogram Equalization+ CLAHE (D3) | 0.996 | 0.01 | 0.989 | 0.0241 | 0.992 | 0.024 | 0.99-0.99 | 0.98-1.0 | 1.0-0.98 |
| | Dataset 70-20-10 | Original (D1) | 0.985 | 0.685 | 0.935 | 0.307 | 0.80 | 0.67 | 0.93-0.94 | 0.98-0.90 | 0.89-0.98 |
| | | Gabor Filter(D2) | 1.0 | 0.0027 | 0.925 | 0.256 | 0.98 | 0.082 | 0.92-0.93 | 1.0-0.87 | 0.85-1.0 |
| | | Histogram Equalization+ CLAHE (D3) | 0.999 | 0.059 | 0.995 | 0.182 | 0.993 | 0.020 | 0.99-0.99 | 0.99-1.0 | 1.0-0.99 |

**Table 4.** YOLO Model Results

| | Dataset | Preprocessing | Train mAP (50) | Train mAP (50-95) | Val mAP (50) | Val mAP (50-95) | F1-Skor/ Threshold | Precision/ Threshold | P-R | Recall |
|---|---|---|---|---|---|---|---|---|---|---|
| YOLO V8 | Dataset 60-20-20 | Original (D1) | 0.980 | 0.621 | 0.98 | 0.621 | 0.96/ 0.471 | 1.0/0.862 | 0.980 mAP@ 0.5 | 0.98 |
| | | Gabor Filter (D2) | 0.978 | 0.601 | 0.978 | 0.602 | 0.96/ 0.478 | 1.0/0.837 | 0.978 mAP@ 0.5 | 0.98 |
| | | Histogram Equalization+ CLAHE (D3) | 0.981 | 0.616 | 0.981 | 0.615 | 0.96/ 0.512 | 1.0/0.831 | 0.981 mAP@ 0.5 | 0.98 |
| | Dataset 70-20-10 | Original (D1) | 0.976 | 0.612 | 0.975 | 0.611 | 0.95/ 0.492 | 1.0/0.836 | 0.976 mAP@ 0.5 | 0.98 |
| | | Gabor Filter(D2) | 0.974 | 0.604 | 0.973 | 0.603 | 0.96/ 0.361 | 1.0/0.838 | 0.974 mAP@ 0.5 | 0.97 |
| | | Histogram Equalization+ CLAHE (D3) | 0.977 | 0.61 | 0.977 | 0.61 | 0.96/ 0.249 | 1.0/0.831 | 0.977 mAP@ 0.5 | 0.98 |

Ideally, both high Recall and high Accuracy are aimed for in a model, yet this situation may vary depending on the specific problem and application. In the CNN-based study, it was observed that the dataset with the applied Gabor filter (D2) achieved higher accuracy in both ways the dataset was split, although the training time with D2 was found to be longer compared to other datasets. Considering other evaluation parameters (F1-Score, Precision, and Recall), it can be seen that the dataset obtained by histogram equalization + CLAHE (D3) yields better results, and the processing time is significantly lower compared to D1 and D2 datasets. Additionally, the dataset split, while not having a highly significant impact on the model's success, led to a noticeable change. The split of 70%-20%-10% produced higher values. According to the model evaluation with the test data not used in the training stage, D3 outperformed all other datasets. In conclusion, preprocessing applied to the images in the dataset was found to enhance the model's performance.

In the case of YOLO-based studies, it was observed that the success rate of the D2 dataset decreased compared to D1 at the mAP (50) threshold, while D3 had a better accuracy compared to other methods. The dataset split also showed a small change in the model's success. Here, the 60%-20%-20% split yielded higher success rates in all three datasets. It was observed that the preprocessing applied to the images in the dataset was not as effective on the success of the YOLO model as it was in the CNN model.

Another success metric, the confusion matrix, shows how accurate the models predictions are. Figures 5 and 6 present confusion matrices and accuracy curves for the CNN model with D1, D2, and D3 datasets in the case of a 60%-20%-20% split. Similarly, Figures 7 and 8 show the confusion matrices and accuracy curves for the CNN model with D1, D2, and D3 datasets in the case of a 70%-20%-10% split. Upon examination, it can be observed that, for both split scenarios, D3 yields more successful results compared to other methods, and D2 is closer to D1 but exhibits a higher level of accuracy than D1.

When analyzing the accuracy curves in Figures 6 and 8, it is observed that, for both split scenarios, D3 exhibits less fluctuation compared to other methods, indicating a more stable performance. This analysis demonstrates that the D3 dataset performs more effectively for the CNN model, providing more reliable results.

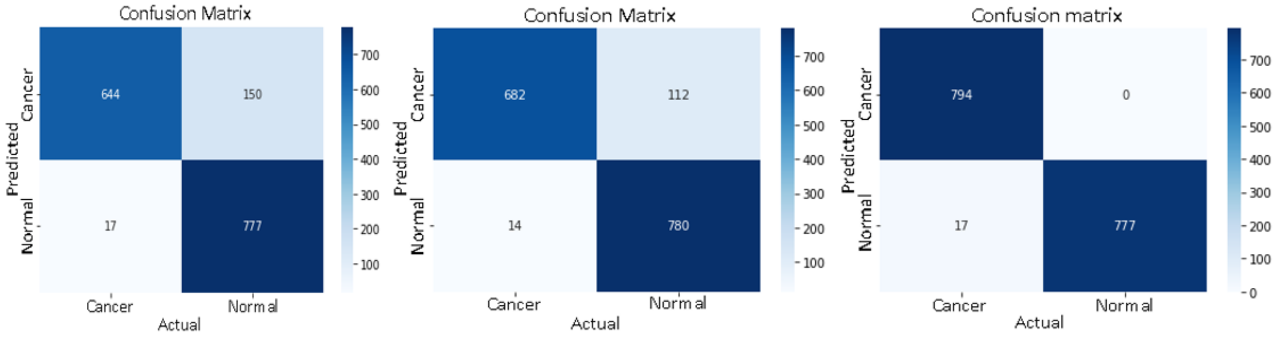

(a) (b) (c)

**Figure 5.** CNN model for 60%-20%-20% split: (a) confusion matrix for D1, (b) confusion matrix for D2, and (c) confusion matrix for D3

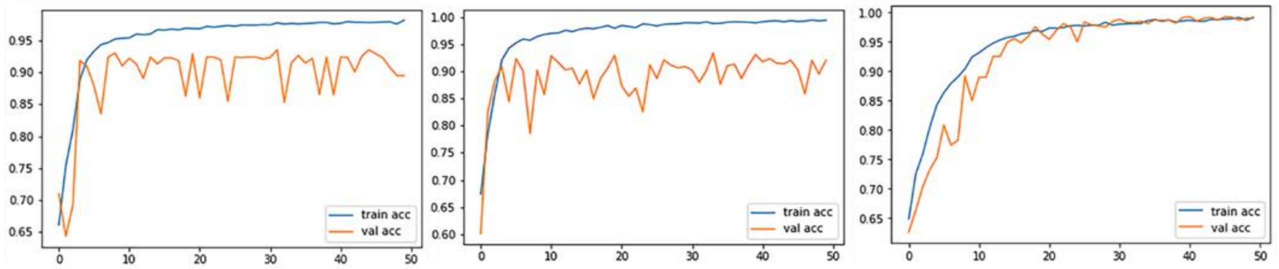

(a) (b) (c)

**Figure 6.** CNN model for 60%-20%-20% split: (a) accuracy curves for D1, (b) accuracy curves for D2, and (c) accuracy curves for D3

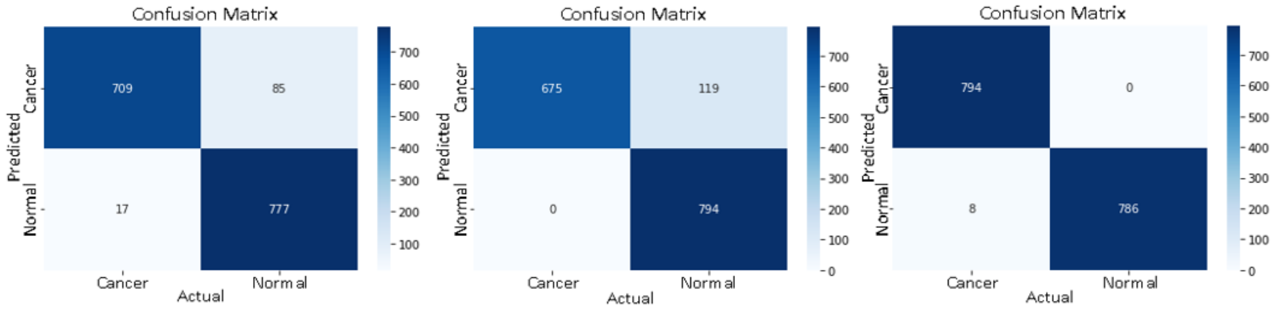

(a) (b) (c)

**Figure 7.** CNN model for 70%-20%-10% split: (a) confusion matrices for D1, (b) confusion matrices for D2, and (c) confusion matrices for D3

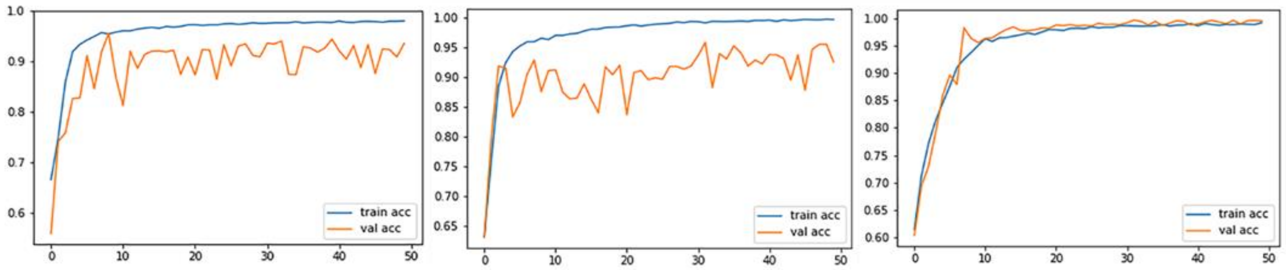

(a) (b) (c)

**Figure 8.** CNN model for 70%-20%-10% split: (a) accuracy curves for D1, (b) accuracy curves for D2, and (c) accuracy curves for D3

Figure 9 and Figure 10 show the confusion matrices of the YOLO model for the 60%-20%-20% and 70%-20%-10% split scenarios, respectively, for D1, D2, and D3 datasets. When examining the confusion matrices, it is observed that D3 achieved better results by correctly predicting nodule 1 with 96% and nodule 2 with 100% in Figure 9, and nodule 1 with 98% and nodule 2 with 97% in Figure 10 compared to other datasets. Additionally, in cases where the model could not make any detections, it was noted that it perceived and labeled the images as the background. This observation is crucial for assessing the detection capability of the model.

For the YOLO model in the 60%-20%-20% split, the accuracy and loss curves for the D1, D2, and D3 datasets, along with changes in performance parameters with increasing epoch counts, are respectively illustrated in Figures 11, 12, and 13. In the 70%-20%-10% split, the accuracy and loss curves for the D1, D2, and D3 datasets are shown in Figures 14, 15, and 16. The mAP(50) and mAP(50-95) values started to increase as the epoch count increased, reaching over 97% for mAP(50) and up to 62% for mAP(50-95). Additionally, it was observed that the classification loss dropped below 0.5. Moreover, in both splits, the mAP curves for the D3 dataset exhibited a more stable pattern compared to the other datasets. As can be seen from Figure 11, 12, and Figure 14, 15, the performance metrics of YOLO obtained after training with D1 and D2 datasets indicate less fluctuation in the graphs of the D1 dataset for both dataset partitioning methods (%60-%20-%20 and %70-%20-%10) compared to the D2 dataset. This suggests that the D1 dataset exhibits a more stable structure for both partitioning methods compared to the D2 dataset.

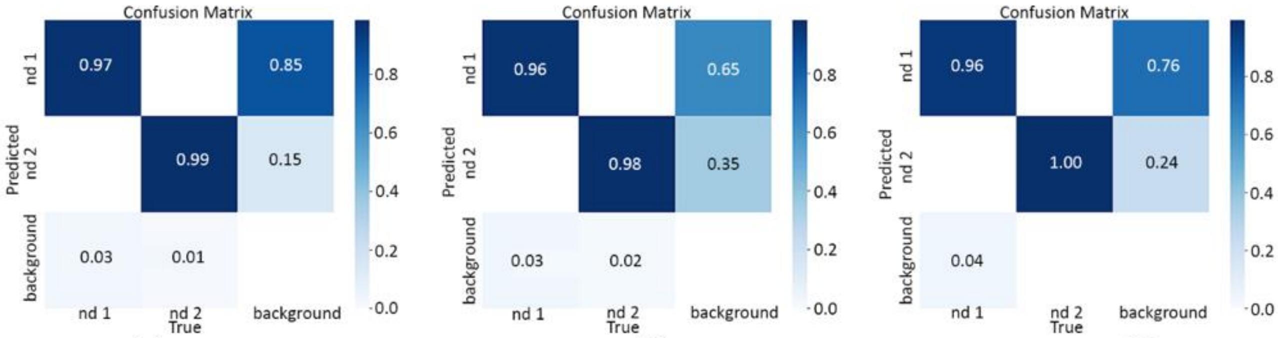

(a) (b) (c)

**Figure 9.** Confusion matrices for the YOLO model in the 60%-20%-20% split for (a) D1, (b) D2, and (c) D3

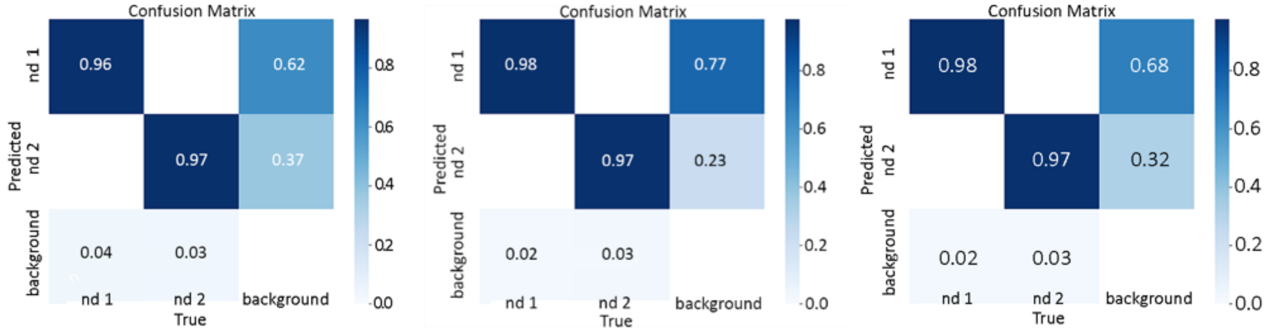

(a) (b) (c)

**Figure 10.** Confusion matrices for the YOLO model in the 70%-20%-10% split for (a) D1, (b) D2, and (c) D3

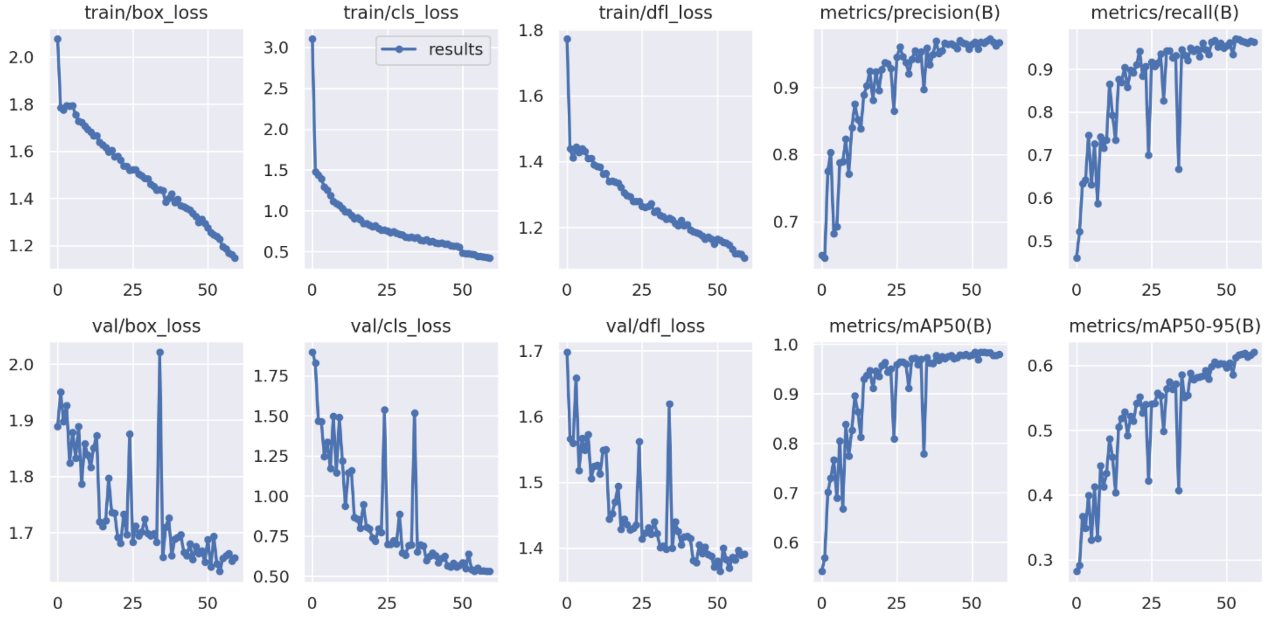

**Figure 11.** Accuracy and loss curves for YOLO model with %60-%20-%20 split for dataset D1

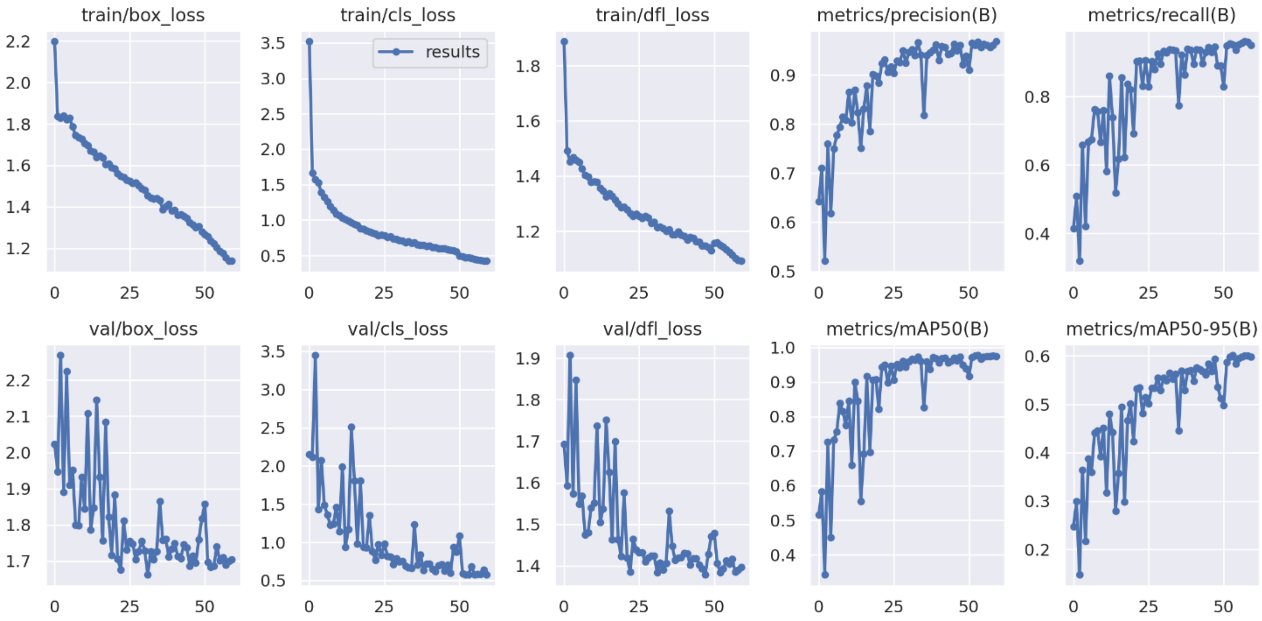

**Figure 12.** Accuracy and loss curves for YOLO model with %60-%20-%20 split for dataset D2

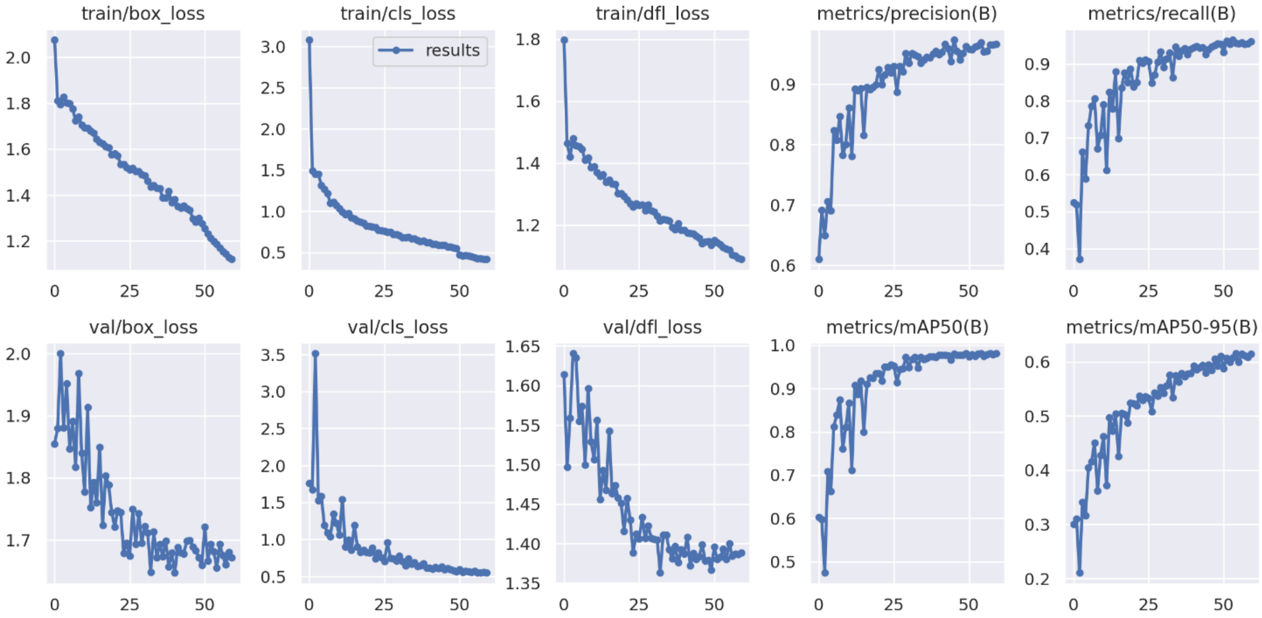

**Figure 13.** Accuracy and loss curves for YOLO model with %60-%20-%20 split for dataset D3

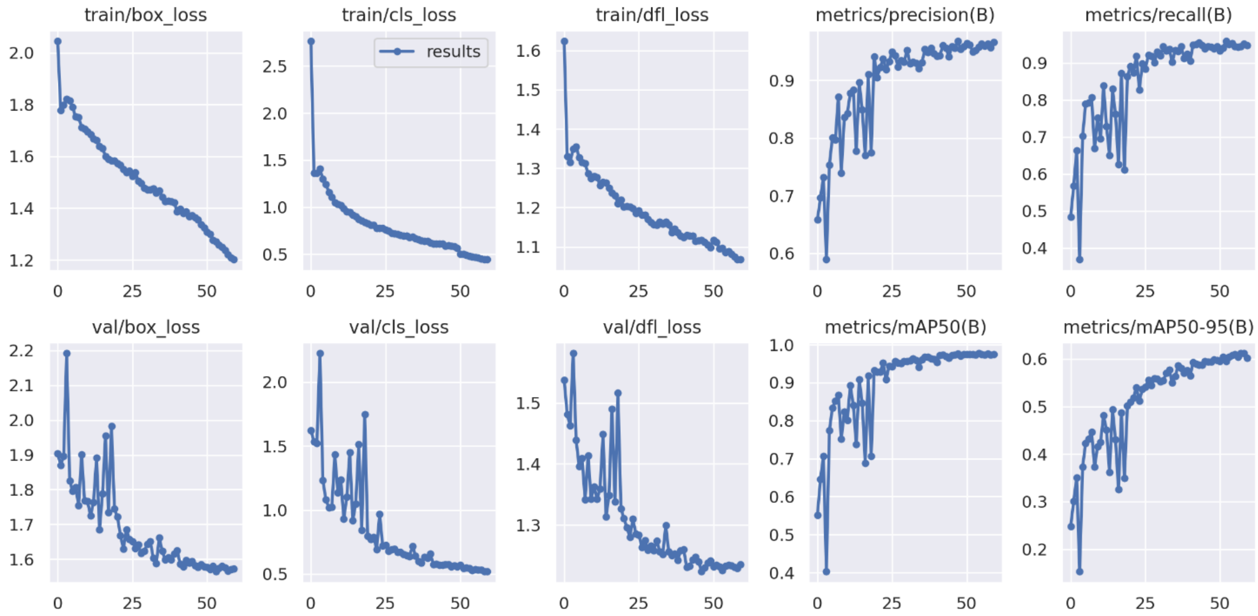

**Figure 14.** Accuracy and loss curves for YOLO model with %70-%20-%10 split for dataset D1

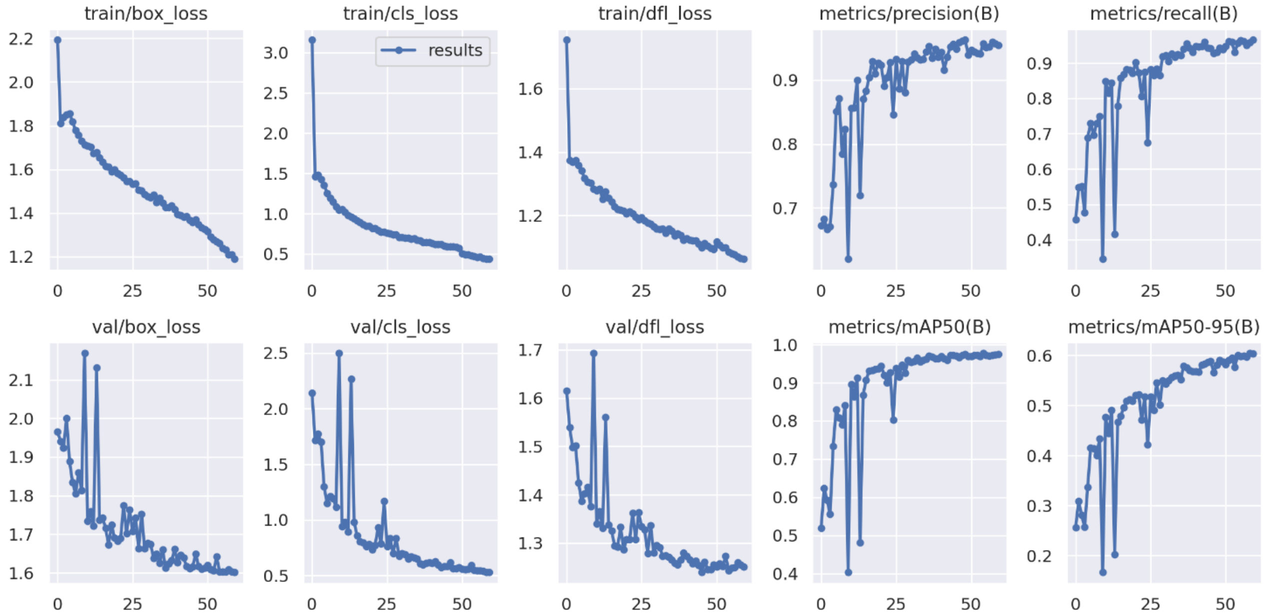

**Figure 15.** Accuracy and loss curves for YOLO model with %70-%20-%10 split for dataset D2

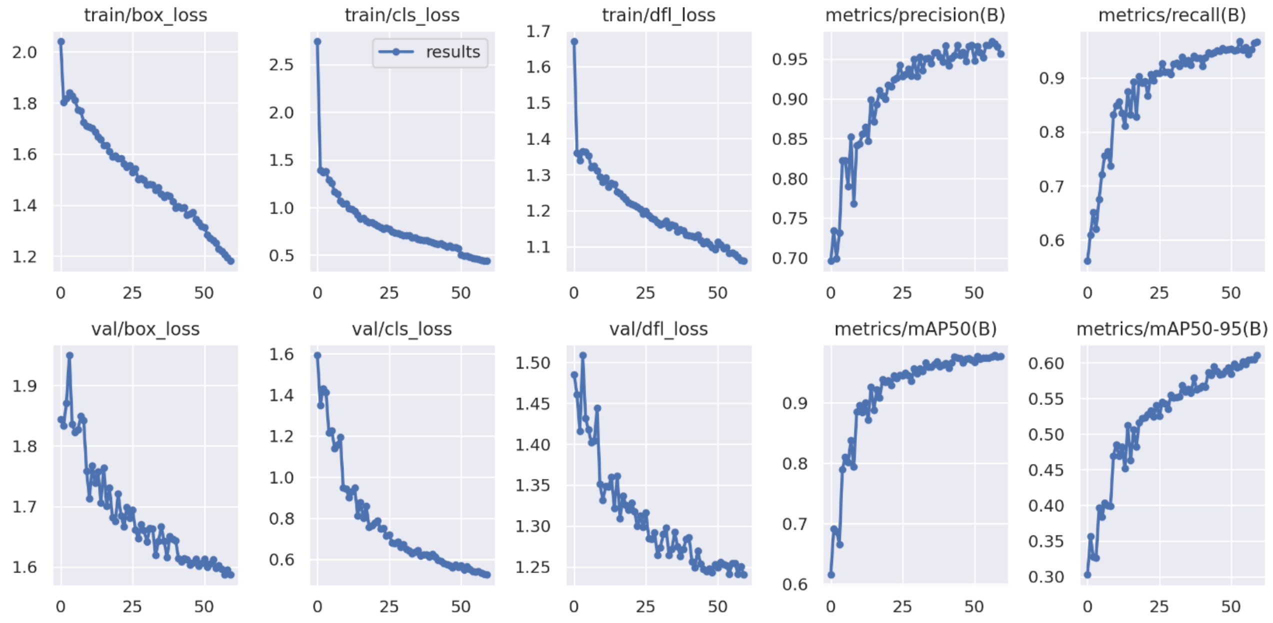

**Figure 16.** Accuracy and loss curves for YOLO model with %70-%20-%10 split for dataset D3

## 4. Conclusion and Suggestions

This research investigates the use of artificial intelligence components, namely CNN and YOLO algorithms, for the early diagnosis of lung cancer and evaluates the effectiveness of these algorithms. The dataset used for the CNN model consists of a total of 7940 images, with half being cancerous and the other half healthy. For the YOLO model, the dataset comprises 4968 CT images. The datasets were segmented using different image preprocessing techniques, and the impact of these techniques on the performance of models was thoroughly examined. The proposed CNN model achieved an accuracy of 98.5% when trained with the original dataset (D1), 99.85% with the dataset obtained by applying histogram equalization + CLAHE filter (D3), and 100% with the dataset where the Gabor filter was applied (D2). The F1 score, a metric considered better than accuracy, reached the highest value of 99% with the D3 dataset. The F1 score values for the other datasets were observed to be 94% for D1 and 93% for D2.

For the YOLO model, the highest success rate in terms of mAP scale was achieved with the D3 dataset, where histogram equalization + CLAHE was applied (98.1%). The mAP values for the other datasets were measured as 98% for D1 and 97.8% for D2. In terms of F1 score, all datasets had approximately the same value for the YOLO model. Success parameters and graphical analyses indicate that the histogram equalization + CLAHE method outperforms other methods. Additionally, it was observed that image preprocessing and dataset segmentation have a significant impact on success rates.

## References

[1] C. Yan and N. Razmjooy, “Optimal lung cancer detection based on CNN optimized and improved Snake optimization algorithm,” *Biomed Signal Process Control*, vol. 86, p. 105319, 2023, doi: https://doi.org/10.1016/j.bspc.2023.105319.

[2] Global Cancer Observatory, “World,” 2020. Accessed: Dec. 02, 2023. [Online]. Available: https://gco.iarc.fr/today/data/factsheets/populations/900-world-fact-sheets.pdf

[3] Global Cancer Observatory, “Turkey,” 2020. Accessed: Jan. 18, 2024. [Online]. Available: https://gco.iarc.fr/today/data/factsheets/populations/792-turkey-fact-sheets.pdf

[4] M. Keshani, Z. Azimifar, F. Tajeripour, and R. Boostani, “Lung nodule segmentation and recognition using SVM classifier and active contour modeling: A complete intelligent system,” *Comput Biol Med*, vol. 43, no. 4, pp. 287–300, May 2013, doi: 10.1016/j.compbiomed.2012.12.004.

[5] J. Kuruvilla and K. Gunavathi, "Lung cancer classification using neural networks for CT images," *Comput Methods Programs Biomed*, vol. 113, no. 1, pp. 202–209, Jan. 2014, doi: 10.1016/j.cmpb.2013.10.011.

[6] A. O. De Carvalho Filho, W. B. De Sampaio, A. C. Silva, A. C. de Paiva, R. A. Nunes, and M. Gattass, "Automatic detection of solitary lung nodules using quality threshold clustering, genetic algorithm and diversity index," *Artif Intell Med*, vol. 60, no. 3, pp. 165–177, 2014, doi: 10.1016/j.artmed.2013.11.002.

[7] Q. Z. Song, L. Zhao, X. K. Luo, and X. C. Dou, "Using Deep Learning for Classification of Lung Nodules on Computed Tomography Images," *J Healthc Eng*, vol. 2017, 2017, doi: 10.1155/2017/8314740.

[8] T. Lustberg *et al.*, "Clinical evaluation of atlas and deep learning based automatic contouring for lung cancer," *Radiotherapy and Oncology*, vol. 126, no. 2, pp. 312–317, Feb. 2018, doi: 10.1016/j.radonc.2017.11.012.

[9] S. K. Lakshmanaprabu, S. N. Mohanty, K. Shankar, N. Arunkumar, and G. Ramirez, "Optimal deep learning model for classification of lung cancer on CT images," *Future Generation Computer Systems*, vol. 92, pp. 374–382, Mar. 2019, doi: 10.1016/j.future.2018.10.009.

[10] P. M. Shakeel, M. A. Burhanuddin, and M. I. Desa, "Lung cancer detection from CT image using improved profuse clustering and deep learning instantaneously trained neural networks," *Measurement (Lond)*, vol. 145, pp. 702–712, Oct. 2019, doi: 10.1016/j.measurement.2019.05.027.

[11] N. Gupta, D. Gupta, A. Khanna, P. P. Rebouças Filho, and V. H. C. de Albuquerque, "Evolutionary algorithms for automatic lung disease detection," *Measurement*, vol. 140, pp. 590–608, 2019, doi: https://doi.org/10.1016/j.measurement.2019.02.042.

[12] G. Kasinathan, S. Jayakumar, A. H. Gandomi, M. Ramachandran, S. J. Fong, and R. Patan, "Automated 3-D lung tumor detection and classification by an active contour model and CNN classifier," *Expert Syst Appl*, vol. 134, pp. 112–119, Nov. 2019, doi: 10.1016/j.eswa.2019.05.041.

[13] H. F. Al-Yasriy, M. S. Al-Husieny, F. Y. Mohsen, E. A. Khalil, and Z. S. Hassan, "Diagnosis of Lung Cancer Based on CT Scans Using CNN," in *IOP Conference Series: Materials Science and Engineering*, IOP Publishing Ltd, Nov. 2020. doi: 10.1088/1757-899X/928/2/022035.

[14] P. Nanglia, S. Kumar, A. N. Mahajan, P. Singh, and D. Rathee, "A hybrid algorithm for lung cancer classification using SVM and Neural Networks," *ICT Express*, vol. 7, no. 3, pp. 335–341, 2021, doi: https://doi.org/10.1016/j.icte.2020.06.007.

[15] S. Doppalapudi, R. G. Qiu, and Y. Badr, "Lung cancer survival period prediction and understanding: Deep learning approaches," *Int J Med Inform*, vol. 148, p. 104371, 2021, doi: https://doi.org/10.1016/j.ijmedinf.2020.104371.

[16] X. Chen, Q. Duan, R. Wu, and Z. Yang, "Segmentation of lung computed tomography images based on SegNet in the diagnosis of lung cancer," *J Radiat Res Appl Sci*, vol. 14, no. 1, pp. 396–403, Dec. 2021, doi: 10.1080/16878507.2021.1981753.

[17] N. Baranwal, P. Doravari, and R. Kachhoria, "Classification of Histopathology Images of Lung Cancer Using Convolutional Neural Network (CNN)." [Online]. Available: https://orcid.org/0000-0002-1113-7884

[18] Md. A. Talukder, Md. M. Islam, M. A. Uddin, A. Akhter, K. F. Hasan, and M. A. Moni, "Machine learning-based lung and colon cancer detection using deep feature extraction and ensemble learning," *Expert Syst Appl*, vol. 205, p. 117695, 2022, doi: https://doi.org/10.1016/j.eswa.2022.117695.

[19] A. B. Pawar *et al.*, "Implementation of blockchain technology using extended CNN for lung cancer prediction," *Measurement: Sensors*, vol. 24, p. 100530, 2022, doi: https://doi.org/10.1016/j.measen.2022.100530.

[20] B. Haznedar and N. Y. Simsek, "A Comparative Study on Classification Methods for Renal Cell and Lung Cancers Using RNA-Seq Data," *IEEE Access*, vol. 10, pp. 105412–105420, 2022, doi: 10.1109/ACCESS.2022.3211505.

[21] C. Loraksa, S. Mongkolsomlit, N. Nimsuk, M. Uscharapong, and P. Kiatisevi, "Development of the Osteosarcoma Lung Nodules Detection Model Based on SSD-VGG16 and Competency Comparing With Traditional Method," *IEEE Access*, vol. 10, pp. 65496–65506, 2022, doi: 10.1109/ACCESS.2022.3183604.

[22] S. Mehmood *et al.*, "Malignancy Detection in Lung and Colon Histopathology Images Using Transfer Learning With Class Selective Image Processing," *IEEE Access*, vol. 10, pp. 25657–25668, 2022, doi: 10.1109/ACCESS.2022.3150924.

[23] M. Kanipriya, C. Hemalatha, N. Sridevi, S. R. SriVidhya, and S. L. Jany Shabu, "An improved capuchin search algorithm optimized hybrid CNN-LSTM architecture for malignant lung nodule detection," *Biomed Signal Process Control*, vol. 78, p. 103973, 2022, doi: https://doi.org/10.1016/j.bspc.2022.103973.

[24] S. Shanthi, V. S. Akshaya, J. A. Smitha, and M. Bommy, "Hybrid TABU search with SDS based feature selection for lung cancer prediction," *International Journal of Intelligent Networks*, vol. 3, pp. 143–149, 2022, doi: https://doi.org/10.1016/j.ijin.2022.09.002.

[25] A. A. Shah, H. A. M. Malik, A. Muhammad, A. Alourani, and Z. A. Butt, "Deep learning ensemble 2D CNN approach towards the detection of lung cancer," *Sci Rep*, vol. 13, no. 1, p. 2987, 2023, doi: 10.1038/s41598-023-29656-z.

[26] K. Clark *et al.*, "The Cancer Imaging Archive (TCIA): Maintaining and Operating a Public Information Repository," Journal of Digital Imaging.

[27] Mehmet Fatih AKCA, "Veri seti." Accessed: Jan. 19, 2024. [Online]. Available: https://universe.roboflow.com/mehmet-fatih-akca/yolotransfer/dataset/2

[28] R. Chauhan, K. K. Ghanshala, and R. C. Joshi, "Convolutional Neural Network (CNN) for Image Detection and Recognition," in *2018 First International Conference on Secure Cyber Computing and Communication (ICSCCC)*, 2018, pp. 278–282. doi: 10.1109/ICSCCC.2018.8703316.

Bitlis Eren Üniversitesi Fen Bilimleri Dergisi
BİTLİS EREN UNIVERSITY JOURNAL OF SCIENCE
ISSN: 2147-3129/e-ISSN: 2147-3188
VOLUME: 13 NO: 2 PAGE: 460-466 YEAR: 2024
DOI:10.17798/bitlisfen.1425717

# Quantum Chemical Computations, Molecular Docking, and ADMET Predictions of Cynarin

Sevtap CAGLAR YAVUZ*

*Department of Medical Services and Technicians, Ilic Dursun Yildirim Vocational School, Erzincan Binali Yildirim University, Erzincan 24700, Turkey*
*(ORCID: 0000-0001-6497-2907)*

**Keywords:** Cynarin, DFT, HOMO-LUMO, Molecular docking, Spartan '10.

**Abstract**
Cynarin (1,3-o-dicaffeoylquinic acid) is one of the biologically active functional food components which is the most well-known caffeoylquinic acid derivative found in artichoke. The structural and electronic features of cynarin compound were investigated theoretically using density functional theory (DFT). The highest occupied molecular orbital (HOMO) and the least occupied molecular orbital (LUMO) are the most significant orbitals in molecules, these orbitals are quite helpful to know several molecular features such as the chemical reactivity, kinetic stability, electronegativity, chemical potential, electrophilicity index, chemical hardness and softness and electronegativity. Molecular orbital analysis HOMO-LUMO was used to explore the stability of the molecule. Moreover, physicochemical properties, drug-likeness, and toxicity estimation of the cynarin compound were appraised owing to ADMET (including absorption, distribution, metabolism, excretion, and toxicology). Molecular docking was carried out to examine the biological activity of the cynarin compound. 5A19, a liver cancer biomarker, is human methionine adenosyl-transferase enzymes (MATs). Cynarin-MAT enzyme binding energy value was calculated as -7.9 kcal/mol. As a result, this in silico study confirmed that cynarin has the potential to be a drug by revealing its protective effect against liver diseases.

## 1. Introduction

Studies conducted in different disease groups have reported that a diet rich in vegetables and fruits has a significant protective potential effect against the risk of illnesses such as hypertension, diabetes, cardiovascular diseases and cancer [1]. Artichoke (Cynara Scolymus), a vegetable known and consumed for centuries, has been accepted as a potential phytotherapeutic agent for various conditions such as cardiovascular, hepatic, liver and gastric diseases [2], [3]. It is known that artichoke leaf extract contains saponins, caffeic acid derivatives, flavonoid derivatives, fatty acids and various polyphenolic components [4], [5]. It is stated that many phytochemical substances in the composition of artichoke can inhibit cancer-related angiogenesis by preventing the secretion of cancer agents. At the same time, in artichoke; It has been reported that there are many powerful polyphenol-type antioxidants that may contribute to the protection and therapy of prostate cancer, breast cancer, and leukemia [6]. The composition of artichoke contains basic phenolic substances such as cinnamic acids, chlorogenic acid, cynarin, 1,5-o-dicaffeoylquinic acid, 3,4-o-dicaffeoylquinic acid, and basic flavonoid substances such as apigenin and luteolin [7], [8]. Cynarin is one of the active biological chemicals found in artichoke and is found in high levels in the leaves of the plant. Therefore, most of the natural drugs acquired from this plants are made ready from the leaves. Cynarin is a caffeolquinic acid and is largely concentrated in the leaves [9]. Cynarin is a phenolic acid compound that is liable for its cholagogue and choleretic features. Due to these functions, it is quite significant for liver health. In addition to its liver-protective effect,

---

*Corresponding author: sevtap.yavuz@erzincan.edu.tr

*Received: 25.01.2024, Accepted: 03.06.2024*

cynarin has been observed to inhibits cholesterol biosynthesis and provides low-density lipoprotein (LDL) oxidation [10]. The chemical structure of cynarin is shown in Figure 1.

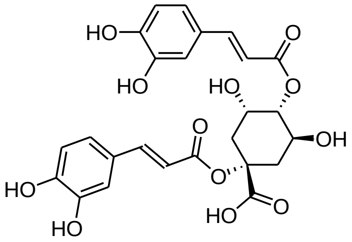

**Figure 1.** Chemical structure of cynarin.

MATs catalyze the formation of S-adenosylmethionine, the major biological methyl donor, and these enzymes play a significant act in the protection of life. Their dysregulation is significantly linked to liver and colon cancers [11].

In computer-aided drug design (CADD) studies, theoretical computational methods are used to simulate drug-receptor interactions. CADD studies enable the design and accurate evaluation of molecules that have the potential to become drugs in the discovery phase [12]. Thanks to computational approaches, the logic of designing natural pharmacologically active molecules that can target proteins of interest by using bioactive natural compounds of plant origin, such as cynarin, for potential drug development has improved significantly.

Many studies have been conducted by researchers for cynarin, which has a wide range of biological activities: Some of these include janus kinase (JAK) inhibition [13], matrix metalloproteinase-9 (MMP-9) inhibition [14], spike (S) glycoprotein inhibition [15], inhibition on human colon cancer HT-29 and RKO. Cells [16], effects on inflammatory response in EA.hy926 human endothelial cells [17], and effects on amelanotic melanoma C32 and renal adenocarcinoma ACHN [18] have been reported.

The main objective of this study is to review the available knowledge regarding the specifically related to liver and colon cancer prevention potency of the cynarin, and to summarise its mechanism of action. In this study, it was aimed to examine the inhibition of cynarin with MATs using in silico methods. Further, ADMET analysis of cynarin natural compound was done. Molecular reactivity analysis (HOMO-LUMO) of the cynarin compound and other electronic parameters acquired from this analysis, molecular electrostatic potential (MEP) analysis, and geometry optimization were computed with the DFT/B3LYP theory and 6-311G* basis set, and the results were displayed.

## 2. Material and Method

### 2.1. Computational methods

Quantum mechanical computations were carried out for the compound cynarin with DFT using B3LYP standard of principle and 6-311G* as the basis set in Spartan '10 software [19]. The acquired outcomes were visualized by the same program. SwissADME (http://www.swissadme.ch/) online tool was used to predict drug-like attributes, and ADMETlab 2.0 (https://admetmesh.scbdd.com/) and Pro Tox-II (https://tox-new.charite.de/protox_II/) online tools were used to predict ADMET properties such as druggability and toxicity risk. AutoDock Vina (in UCSF [University of California, San Francisco] Chimera) [20] is one of the most right programs used in docking analysis. Molecular docking analysis was realized to estimate the binding locations, using AutoDock Vina in UCSF Chimera software (version 1.16) [21], and the crystal structure of target was provided from the protein data bank (https://www.rcsb.org) in the pdb format. The target protein contains human MATs (PDB ID: 5A19). The chemical structure of cynarin compound was received at 3D SDF format from the PubChem site (https://pubchem.ncbi.nlm.nih.gov/).

## 3. Results and Discussion

### 3.1. Computational structural analysis

Frontier orbitals, that is, HOMO and LUMO, are display an important role to estimate the chemical reactivity and stability of molecules [22]. The energy range (ΔE) of these orbitals is a useful method for determining chemical reactivity, kinetic stability, and predicting the softness ($\sigma$) and hardness ($\eta$) of a molecule. It is also used to predict some the electronic structure-based descriptor such as electronegativity ($\chi$), chemical potential ($\mu$), and electrophilicity index ($\omega$). The HOMO and LUMO representations for the cynarin compound were given in Figure 2. The HOMO, LUMO, and HOMO-LUMO gap energies for cynarin are -5.6382, -1.7769, and 3.8613 eV, respectively, as display in Table 1.

**Table 1.** The HOMO, LUMO energies and ΔE energy ranges of cynarin compound in the gaseous media

| Cynarin | | | | |
|---|---|---|---|---|
| Medium | $E_{HOMO(a.u.)}$ | $E_{LUMO(a.u.)}$ | $\Delta E_{(a.u.)}$ | $\Delta E_{(eV)}$ |
| gaseous | -0.2072 | -0.0653 | 0.1419 | 3.8613 |

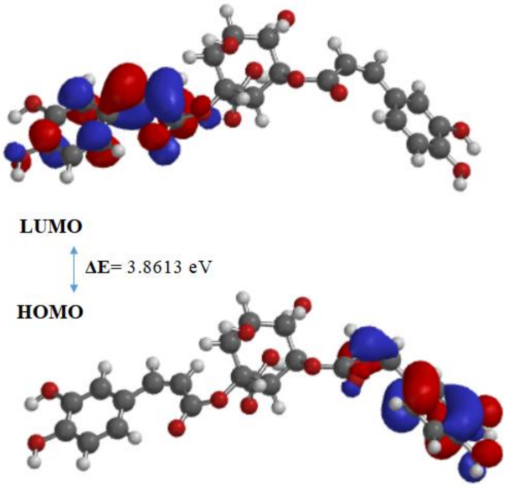

**Figure 2.** HOMO and LUMO energy plots of cynarin compound.

Global chemical reactivity descriptors were calculated from the energies of these orbitals. The ionization potential ($I=-E_{HOMO}$) and electron affinity ($A=-E_{LUMO}$) related immediately to the energies of the HOMO and LUMO orbitals and are computed to be -5.6382 and -1.7769 eV for cynarin, respectively. Hardness ($\eta=(I-A)/2$) and softness ($S=1/2\eta$) provide important information about the reactive behavior of a molecule. Compounds with high chemical reactivity and low stability are described as soft, while hardness is defined as the opposite of softness. The computed electronic structure descriptors of the cynarin compound were given in Table 2. The computed results of chemical hardness and softness for cynarin are 1.9307 eV and 0.2589 eV, respectively. Electronegativity ($\chi=(I+A)/2$), is a relative measure of an atom's ability to attract electrons when creating a chemical bond. It was computed to be 3.7075 eV for cynarin. The electrophilicity index ($\omega=\mu^2/2\eta$) is a descriptor proposed by Parr and Yang and indicates the quantitative expression of the global electrophilic strength of a molecule [23]. The calculated value of the electrophilicity index for cynarin is 3.5597 eV. It was calculated to be -3.7075 eV the chemical potential ($\mu=-(I+A)/2$) of cynarin. A substance with a low chemical potential also has a low effectiveness against other substances [24]. The maximum charge transfer ΔNmax of the cynarin compound is 1.9202 eV.

HOMO-LUMO energy gap (ΔE) values major than 1.5 eV express that the molecules are thermodynamically steady and resistant [25]. According to the calculation result, the energy difference of 3.8613 eV showed that the cynarin was thermodynamically steady. The high HOMO-LUMO energy difference of the cynarin compound makes it harder and less chemically reactive. There is low electron flow due to the high energy difference. This cause the cynarin compound to be low reactive.

**Table 2.** The calculated electronic structure parameters of the cynarin compound

| Parameters | Value (eV) |
|---|---|
| $E_{HOMO}$ | -5.6382 |
| $E_{LUMO}$ | -1.7769 |
| $\Delta E = E_{LUMO}-E_{HOMO}$ | 3.8613 |
| $I = -E_{HOMO}$ | 5.6382 |
| $A = -E_{LUMO})$ | 1.7769 |
| $\eta = (I-A)/2$ | 1.9307 |
| $S = 1/2\eta$ | 0.2589 |
| $\chi = (I+A)/2$ | 3.7075 |
| $\mu = -(I+A)/2$ | -3.7075 |
| $\omega = \mu^2 /2\eta$ | 3.5597 |
| $\Delta nmax = -\mu/\eta$ | 1.9202 |

Molecular electrostatic potential maps (MEPs) provide a three-dimensional view of the charge distribution within a molecule [26]. The electrostatic potential rises in the order of red < orange < yellow < green < blue [27]. While the most negative potential (the region with high electron density) is shown in red; the color blue is used to show the most positive potential (the region where partial positive charges are located). The yellow colour represents regions with fewer electrons than the other regions and the green colour represents neutral regions with zero potential. Positive regions indicate nucleophilic reactivity and negative regions indicate electrophilic reactivity. Interpretation of MEP maps assumes a vital role in the determination of active sites in the chemical binding of the molecule and the synthesis of new chemicals [28].

In order to understand the charge distribution of the cynarin compound, the calculation results made with the B3LYP/6-311G* level were visualized in three dimensions using the Spartan '10 program. These MEP surface maps obtained for the cynarin compound are shown in Figure 3. As in Figure 3, it can be seen that the highest nucleophilic potential is found on the hydrogen atoms of the –COOH groups, and the highest electrophilic potential is situated on oxygen atoms of hydroxyl groups.

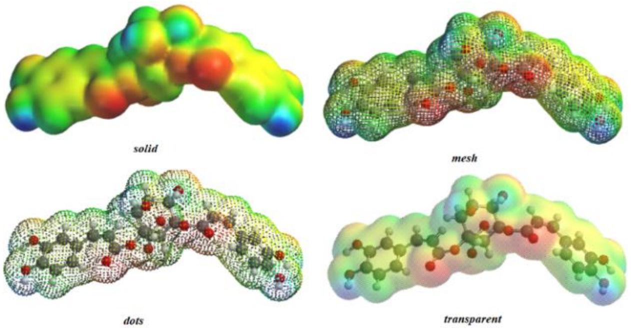

**Figure 3.** Showing the molecular electrostatic potential maps of the cynarin.

### 3.2. Molecular docking studies and ADMET properties

Binding patterns and affinity interactions between small molecules and binding pockets of proteins was able to be examined owing to molecular docking interaction. Cynarin was docked with protein target in liver cancer, specifically the receptors of MATs (PDB ID: 5A19).

There is more than one solved structure information defined for the MATs enzyme in the protein database. The enzyme (PDB code: 5A19) obtained by x-ray crystallization method from the protein data bank (www.rscb.org) was randomly selected as the MAT enzyme. The protein-ligand complex was selected considering the best obtained pose according to binding energy value. The binding free energy of cynarin compound in case of is -7.9 kcal/mol. The good energy value of the docking result for the cynarin compound is given in Table 3. Receptor-ligand interaction to three-dimensional (3D) was visualized using the Biovia Discovery Studio Visualizer program [29]. The receptor was prepared by removing water molecules, ions, and some small molecules for docking analysis.

**Table 3.** Molecular docking results of the cynarin PDB ID: 5A19

| Molecule Name | Binding Energy (kcal/mol) | RMSD | Amino Acid Residues |
|---|---|---|---|
| Cynarin | -7.9 | 1.824 | GLU122, VAL129 LYS133, ARG347, TYR351, GLY355, ARG356 |

The interactions of the conventional hydrogen bond (GLU122, GLY355, ARG347, and ARG356), π-alkyl (VAL129 and LYS133), and π -π T-shaped (TYR351) were observed on cynarin compound with adenosyl-transferase enzyme. Interaction types such as, conventional hydrogen bond, Van der Waals forces, π-alkyl bonds, and π -π T-shaped, also encountered in docking analyses are significant for the structural integrity of many biological molecules with the inclusion of proteins and DNA, and are also very important for drug-receptor interactions.

As a result of the docking process between 5A19 and cynarin, the best binding conformation with a binding energy of -7.9 kcal/mol obtained between 5A19 and the ligand was shown in Figure 4. The binding energy value found in the molecular docking study is a pointer that the docking process is successful.

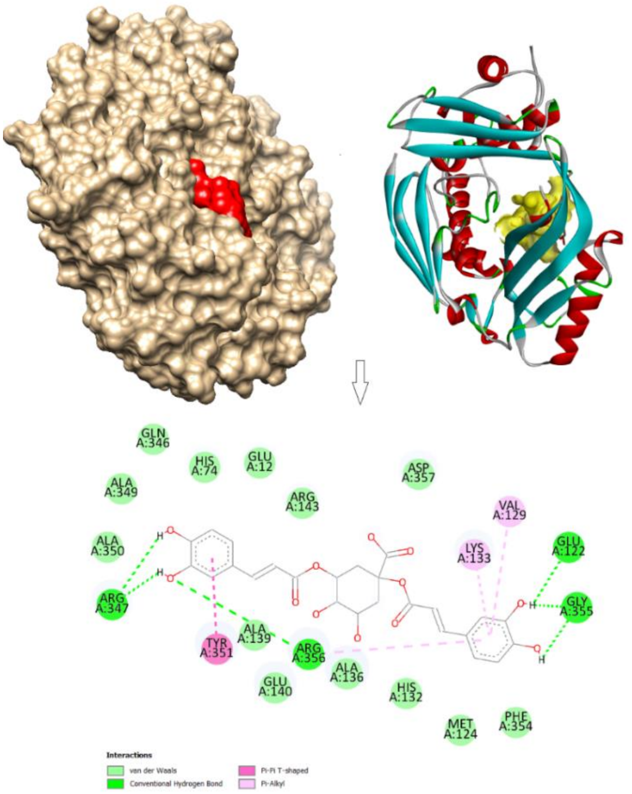

**Figure 4.** The three-dimensional interaction, the 2D structure, and the best binding pose of cynarin compound.

The drug-like features of the cynarin compound were calculated according to Lipinski's five criteria with the relief of the SwissADME web tool, and the relevant parameters were shown in Table 4.

**Table 4.** Estimated physicochemical properties of the cynarin according to the SwissADME program

| | SwissADME Physicochemical Properties |
|---|---|
| Formula | $C_{25}H_{24}O_{12}$ |
| *Molecular weight* | 516.45 g/mol |
| Number heavy atoms | 37 |
| Number aromatic heavy atoms | 12 |
| Fraction Csp$^3$ | 0.24 |
| Number rotatable bonds | 9 |
| *Number hydrogen bond acceptors* | 12 |
| *Number hydrogen bond donors* | 7 |
| *Molar refractivity* | 126.90 |
| TPSA | 211.28 Å$^2$ |
| Lipophilicity | |
| *LogP$_{o/w}$* | 1.11 |
| Water Solubility | |
| LogS | -3.65 |
| Solubility | 1.17e-01 mg/ml |
| Absorption | |
| GI absorption | Low |
| Distribution | |
| BBB permeation | No |
| P-gp substrate | Yes |
| Metabolism | |
| CYP1A2 inhibitor | No |
| CYP2C19 inhibitor | No |
| CYP2C9 inhibitor | No |
| CYP2D6 inhibitor | No |
| CYP3A4 inhibitor | No |
| LogK$_p$ (skin permeation) | -8.37 cm/s |
| *(Table 4 devamı)* | |
| Drug-likeness | |
| Lipinski | No; 3 violations: MW>500, NorO>10, NHorOH>5 |
| Ghose | No; 1 violation: MW>480 |
| Veber | No; 1 violation: TPSA>140 |
| Medicinal Chemistry | |
| PAINS | 1 alert: catechol_A |
| Brenk | 3 alerts: catechol, michael_acceptor_1, more_than_2_esters |
| Leadlikeness | No; 2 violations: MW>350, Rotors>7 |
| Synthetic Accessibility | 4.81 |
| Bioavailability Score | 0.11 |

There are some criteria such as Lipinski, Ghose and Veber to establish whether the compounds have a drug-like structure and their activity in living organisms [30].

In this study, the drug similarity properties of the cynarin compound were examined using Lipinski criteria. According to Lipinski's rule, an effective drug taken orally should not cause violations of more than one parameter. According to Lipinski's rule of five, chemical structure limitations are described as molecular weights ≤500, hydrogen bond acceptor numbers ≤10, hydrogen bond donor numbers ≤5, lipophilicity of compounds ≤5, and molar refractivity between 40-130 [31], [32]. According to Lipinski's rule indicates that there is a condition that would prevent the cynarin compound from being an orally active drug in humans (Table 5).

**Table 5.** Drug-like properties of cynarin compound according to Lipinski's five rule

| Lipinski's rule of five | Acceptable range | Cynarin Theoric | Cynarin Result |
|---|---|---|---|
| Molecular weight | ≤500 | 516.45 | + |
| Number hydrogen bond donors | ≤5 | 7 | - |
| Number hydrogen bond acceptors | ≤10 | 12 | - |
| LogP | ≤5 | 1.11 | + |
| Molar refractivity | 40-130 | 126.90 | + |

Toxicity estimation is an important parameter the drug discovery course that helps identify of molecules with the major potential for safe and influential use in humans [33]. The predictive toxicity study was accomplished by Pro-Tox II webserver. The predicted outcome for cynarin compound was demonstrated in Table 6. Accordingly, the cynarin compound did not show hepatotoxic, carcinogenic, mutagenic, and cytotoxic efficiency but it had immunotoxic efficiency. According to Pro Tox-II, the cynarin was categorized as predicted toxicity class 5. Category 5 indicates that it has relatively low acute toxicity. However, it is known that under certain conditions it may pose a danger to some populations.

**Table 6.** The toxicity computation of SDG molecule by Pro-Tox II web tool

| Toxicity Model Report (Predicted Toxicity Class: 5) | | |
|---|---|---|
| Classification | Target | Prediction |
| Organ toxicity | Hepatotoxicity | Inactive |
| Toxicity end points | Carcinogenicity | Inactive |
| Toxicity end points | Immunotoxicity | Active |
| Toxicity end points | Mutagenicity | Inactive |
| Toxicity end points | Cytotoxicity | Inactive |

## 4. Conclusion and Suggestions

The quantum chemical descriptors for the cynarin molecule have been executed by energy minimization, by DFT at the B3LYP level, using the basis set 6-311G*. The HOMO-LUMO energy gap of the cynarin compound has 3.8613 eV, theoretically that it has low chemical reactivity and high kinetic stability. As to the indicated outcomes of MEP computations, the cynarin compound has contained both nucleophilic active regions and electrophilic attack regions. Cynarin compound has low binding energy (-7.9 kcal/mol) which could be regarded as revealing its protective effect against liver diseases. The cynarin compound did not show any cytotoxic, hepatotoxic, mutagenic or carcinogenic efficacy with respect to the Pro Tox II prediction, but had an immunotoxic effect. Therefore, cynarin may be appropriate compound for further analysis drug development in liver cancer with targeted features.

## Acknowledgment

The author would like to thank for all referees for their valuable contributions and recommendations.

## References

[1] M. J. Wargovich, “Experimental evidence for cancer preventive elements in foods,” *Cancer Lett*, vol. 114, no. 1-2, pp. 11-17, 1997.

[2] S. Bekheet and V. Sota, “Biodiversity and medicinal uses of globe artichoke (Cynara scolymus L.) plant,” J *Biodivers Conserv Bioresour Manag*, vol. 5, no. 1, pp. 39-54, 2019.

[3] H. O. Santos, A. A. Bueno, J. F. Mota, “The effect of artichoke on lipid profile: A review of possible mechanisms of action,” *Pharmacol Res*, vol. 137, pp. 170-178, 2018.

[4] M. Wang, J. E. Simon, I. F. Aviles, K. He, Q. Y. Zheng, Y. Tadmor, “Analysis of antioxidative phenolic compounds in artichoke (Cynara scolymus L.),” *J Agric Food Chem*, vol. 51, no. 3, pp. 601-608, 2003.

[5] M. A. Farag, S. H. El-Ahmady, F. S. Elian, L. A. Wessjohann, “Metabolomics driven analysis of artichoke leaf and its commercial products via UHPLC–q-TOF-MS and chemometrics,” *Phytochemistry*, vol. 95, pp. 177-187, 2013.

[6] N. F. Hassabou, and A. F. Farag, “Anticancer effects induced by artichoke extract in oral squamous carcinoma cell lines,” *J Egypt Natl Canc Inst*, vol. 32, no. 1, pp. 1-10. 2020.

[7] R. Llorach, J. C. Espin, F. A. Tomas-Barberan, F. Ferreres, “Artichoke (Cynara scolymus L.) byproducts as a potential source of health-promoting antioxidant phenolics,” *J Agric Food Chem*, vol. 50, no. 12, pp. 3458-3464, 2002.

[8] G. Löhr, A. Deters, A. Hensel, “In vitro investigations of Cynara scolymus L. extract on cell physiology of HepG2 liver cells,” *Braz J Pharm Sci*, vol. 45, pp. 201-208, 2009.

[9] E. Speroni, R. Cervellati, P. Govoni, S. Guizzardi, C. Renzulli, M. C. Guerra, “Efficacy of different Cynara scolymus preparations on liver complaints,” *J Ethnopharmacol*, vol. 86, no. 2-3, pp. 203-211, 2003.

[10] E. Christaki, E. Bonas, P. Floray-Paneri, “Nutritional And Functional Properties of Cynara Crops (Clobe Artichoke and Cardoon) and Their Potential Applications: A Review,” *Int J Appl Sci Technol*, vol. 2, no. 2, pp. 64-68, 2012.

[11] S. C. Lu, L. Alvarez, Z. Z. Huang, L. Chen, W. An, F. J. Corrales, M. A. Avila, G. Kanel, J. M. Mato, “Methionine adenosyltransferase 1A knockout mice are predisposed to liver injury and exhibit increased expression of genes involved in proliferation,” *Proc Natl Acad Sci*, vol. 98, no. 10, pp. 5560-5565, 2001.

[12] G. Sliwoski, S. Kothiwale, J. Meiler, E. W. Lowe, “Computational methods in drug discovery,” *Pharmacol Rev*, vol. 66, no. 1, pp. 334-395, 2014.

[13] H. J. Liao and J. T. Tzen, “The potential role of phenolic acids from Salvia miltiorrhiza and Cynara scolymus and their derivatives as JAK inhibitors: An in silico study,” *Int J Mol Sci*, vol. 23, no. 7, pp. 4033, 2022.

[14] M. H. Malekipour, F. Shirani, S. Moradi, A. Taherkhani, “Cinnamic acid derivatives as potential matrix metalloproteinase-9 inhibitors: molecular docking and dynamics simulations,” *Genom Inform*, vol. 21, no. 1, pp. e9, 2023.

[15] G. AbrahamDogo, O. Uchechukwu, U. Umar, A. J. Madaki, J. C. Aguiyi, “Molecular docking analyses of phytochemicals obtained from African antiviral herbal plants exhibit inhibitory activity against therapeutic targets of SARS-CoV-2,” *Res Sq*, pp. 1-15. 2020.

[16] M. Villarini, M. Acito, R. di Vito, S. Vannini, L. Dominici, C. Fatigoni, R. Pagiotti, M. Moretti, “Pro-apoptotic activity of artichoke leaf extracts in human HT-29 and RKO colon cancer cells,” *Int J Environ Res Public Health*, vol. 18, no. 8, pp. 4166, 2021.

[17] D. B. Kim, B. Unenkhuu, G. J. Kim, S.W. Kim, H. S. Kim, “Cynarin attenuates LPS-induced endothelial inflammation via upregulation of the negative regulator MKP-3. Animal Cells and Systems,” vol. 26, no. 3, 119-128, 2022.

[18] E. N. Simsek and T. Uysal, “In vitro investigation of cytotoxic and apoptotic effects of Cynara L. species in colorectal cancer cells,” *Asian Pac J Cancer*, vol. 14, no. 11, pp. 6791-6795, 2013.

[19] P. G. Seybold, “Quantum chemical estimation of the acidities of some inorganic oxoacids,” *Mol Phys*, vol. 113, no. 3-4, pp. 232-236, 2015.

[20] S. S. Butt, Y. Badshah, M. Shabbir, M. Rafiq, “Molecular docking using chimera and autodock vina software for nonbioinformaticians,” *JMIR Bioinfor Biotech*, vol. 1, no. 1, pp. e14232, 2020.

[21] R. Al-Ghani, W. P. Nirwani, T. N. Novianti, A. G. P. Sari, “In silico anti-inflammatory activity evaluation from usnea misaminensis through molecular docking approach,” *Chem Mater*, vol. 1, no. 3, pp. 77-82, 2022.

[22] S. C. Yavuz, “Theoretical electronic properties, Admet prediction, and molecular docking studies of some imidazole derivatives,” *J Sci Rep A*, vol. 51, pp. 340-357, 2022.

[23] A. Yiğit and Z. S. Turhan, “Theoretical Investigation of some synthesized 3-arylamino-5-[2-(substituted 1-imidazole) ethyl 1]-1, 2, 4-triazole derivatives,” *Yuzuncu Yil University J Inst Nat Appl Sci*, vol. 28, no. 1, pp. 76-91, 2023.

[24] P. W. Atkins and J. de Paula, *Physical chemistry for the life sciences*, Oxford, England: W. H. Freeman, 2006.

[25] P. T. Tasli, T. Soganci, S. O. Kart, H. H. Kart, M. Ak, “Quantum mechanical calculations of different monomeric structures with the same electroactive group to clarify the relationship between structure and ultimate optical and electrochemical properties of their conjugated polymers,” *J Phys Chem Solids*, vol. 149, pp. 109720, 2021.

[26] J. S. Murray and P. Politzer, “The electrostatic potential: an overview,” *Wiley Interdiscip Rev Comput Mol Sci*, vol. 1, no. 2, pp. 153-163, 2011.

[27] P. Jayaprakash, M. L. Caroline, S. Sudha, R. Ravisankar, G. Vinitha, P. Ramesh, E. Raju, “Synthesis, growth, optical and third order nonlinear optical properties of l-phenylalanine d-mandelic acid single crystal for photonic device applications,” *J Mater Sci Mater Electron*, vol. 31, pp. 20460-20471, 2020.

[28] F. C. Asogwa, U. D. Izuchukwu, H. Louis, C. C. Eze, C. M. Ekeleme, J. A. Ezugwu, I. Benjamin, S. I. Attah, E. C. Agwamba, O. C. Ekoh, A. S. Adeyinka, “Synthesis, characterization and theoretical investigations on the molecular structure, electronic property and anti-trypanosomal activity of benzenesulphonamide-based carboxamide and its derivatives,” *Polycycl Aromat Comp*, vol. 43, no. 10, pp. 8690-8709, 2023.

[29] Dassault Systèmes BIOVIA, Discovery studio visualizer. v16.1.0.15350, San Diego: Dassault Systèmes, 2016.

[30] A. Daina, O. Michielin, V. Zoete, “SwissADME: A free web tool to evaluate pharmacokinetics, druglikeness and medicinal chemistry friendliness of small molecules,” *Sci Rep*, vol. 7, pp. 42717-42729, 2017.

[31] C. A Lipinski, F. Lombardo, B. W. Dominy, P. J. Feeney, “Experimental and computational approaches to estimate solubility and permeability in drug discovery and development settings,” *Adv Drug Deliv Rev,* vol. 46, no.1–3, pp. 3–26, 2001.

[32] B. E. Oyinloye, T. A. Adekiya, R. T. Aruleba, O. A. Ojo, B. O. Ajiboye, “Structure-based docking studies of GLUT4 towards exploring selected phytochemicals from Solanum xanthocarpum as a therapeutic target for the treatment of cancer,” *Curr Drug Discov Technol*. vol. 16, no. 4, pp. 406-416, 2019.

[33] F. P, Guengerich, J. S. MacDonald, “Applying mechanisms of chemical toxicity to predict drug safety,” *Chem Res Toxicol*, vol. 20, no. 3, pp. 344-369, 2007.

Bitlis Eren Üniversitesi Fen Bilimleri Dergisi
BİTLİS EREN UNIVERSITY JOURNAL OF SCIENCE
ISSN: 2147-3129/e-ISSN: 2147-3188
VOLUME: 13 NO: 2 PAGE: 467-473 YEAR: 2024
DOI:10.17798/bitlisfen.1426092

# On Equiform Rectifying, Normal and Osculating Curves in Minkowski Space-Time

Özgür BOYACIOĞLU KALKAN[1*]

[1] *Afyon Vocational School, Ahmet Necdet Sezer Campus, Afyon Kocatepe University,*
*Afyonkarahisar 03200, Turkey*
*(ORCID: 0000-0003-1665-233X)*

**Keywords:** Rectifying curves, Normal curves, Osculating curves, Equiform Frenet frame

This article addresses the equiform rectifying, normal, and second type osculating curves within Minkowski space-time $E_1^4$. We expose the requisite and satisfactory criteria for a curve to qualify as a rectifying, normal, and second kind osculating curve with respect to equiform geometry within Minkowski space-time $E_1^4$. We derive the correlation between the curvatures of these curves to be congruent to a rectifying, normal and second kind osculating curve according to equiform geometry in Minkowski space-time $E_1^4$.

## 1. Introduction

In Euclidean space $E^3$, a curve is characterized through the Frenet frame $\{T, N, B\}$. The planes, spanned by the vectors, $\{T, B\}$, $\{N, B\}$ and $\{T, N\}$ are respectively called as the rectifying plane, normal plane, and osculating plane. A curve is called as a rectifying (resp. normal, osculating) curve if its position vector always lies in its rectifying (resp. normal, osculating) plane. In other words, the rectifying, normal, and osculating planes of these curves consistently include a specific point. A widely recognized principle states that when all the normal or osculating planes of a curve in three-dimensional Euclidean space $E^3$ intersect at a specific point, then the curve either lies on a sphere or is a planar curve, depending on the context. Furthermore, it is established knowledge that if all rectifying planes of a non-planar curve in $E^3$ intersect at a specific point, then the ratio between torsion and curvature for such a curve is accepted as a non-constant linear function [3]. Chen defined the concept of the rectifying curve in his study [2]. Given that the position vector of rectifying curve establishes instantaneous rotation axis at each point along the curve, the author also showed that these curves are necessary for mechanics, kinematics and differential geometry. In Minkowski 3-space $E_1^3$, rectifying curves exhibit analogous geometric properties to those in Euclidean 3-space $E^3$. Spacelike, timelike and null rectifying curves in $E_1^3$ were examined in [8]. Furthermore, the characterizations of rectifying curves were introduced in 4-dimensional Euclidean and Minkowski spaces in [1], [7], [9]. The equiform geometry of rectifying curves were studied in Galilean 4-space in [19].

Normal and osculating curves have been examined in various studies in three and four-dimensional spaces. The characterizations of the normal and osculating curves in 3-dimensional Euclidean and Minkowski spaces were introduced in [10], [11], [13]. In addition, the characterizations of the normal and osculating curves in 4-dimensional Minkowski space were obtained in [12], [14], [15], [16]. The equiform geometry of normal and osculating curves were introduced in Galilean 4-space in [20], [21].

This paper focuses on equiform rectifying, normal and second kind osculating curves in $E_1^4$. We examine the characteristics of rectifying, normal and second kind osculating curves based on their equiform curvature functions, establishing essential and sufficient conditions for any curve to qualify as

---

[*] Corresponding author: *bozgur@aku.edu.tr*

*Received: 26.01.2024, Accepted: 03.04.2024*

rectifying, normal and second kind osculating curve, respectively.

## 2. Preliminaries

The Minkowski space $E_1^4$ is a Euclidean space provided with the indefinite flat metric given by

$$\langle x, y\rangle = -x_1y_1 + x_2y_2 + x_3y_3 + x_4y_4$$

is called Lorentzian inner product. For any vector $\vartheta \in E_1^4$ can have one of three causal characters; it can be spacelike $\langle \vartheta, \vartheta\rangle > 0$ or $\vartheta = 0$, timelike if $\langle \vartheta, \vartheta\rangle < 0$ and null if $\langle \vartheta, \vartheta\rangle = 0$ and $\vartheta \neq 0$. The pseudo-norm of a vector non null $\vartheta$ is defined by $\|\vartheta\| = \sqrt{|\langle \vartheta, \vartheta\rangle|}$ [4], [6], [17].

Let $\alpha = \alpha(s)$ is a regular spacelike curve in $E_1^4$ with timelike vector field $\delta_3$. The Frenet formulae in $E_1^4$ can be written as

$$\begin{bmatrix} t'(s) \\ \delta_1'(s) \\ \delta_2'(s) \\ \delta_3'(s) \end{bmatrix} = \begin{bmatrix} 0 & k_1(s) & 0 & 0 \\ -k_1(s) & 0 & k_2(s) & 0 \\ 0 & -k_2(s) & 0 & k_3(s) \\ 0 & 0 & k_3(s) & 0 \end{bmatrix} \begin{bmatrix} t(s) \\ \delta_1(s) \\ \delta_2(s) \\ \delta_3(s) \end{bmatrix} \tag{2.1}$$

where $k_1, k_2$ and $k_3$ are curvature functions of spacelike curve $\alpha$. Here, $\{t, \delta_1, \delta_2, \delta_3\}$ satisfy the following equations $\langle t, t\rangle = \langle \delta_1, \delta_1\rangle = \langle \delta_2, \delta_2\rangle = 1$ $\langle \delta_3, \delta_3\rangle = -1$ and $\langle t, \delta_1\rangle = \langle t, \delta_2\rangle = \langle t, \delta_3\rangle = \langle \delta_1, \delta_2\rangle = \langle \delta_1, \delta_3\rangle = \langle \delta_2, \delta_3\rangle = 0$ [6], [18].

Now we define rectifying, normal and osculating curves in $E_1^4$.

The curve $\alpha$ is termed as rectifying curve in $E_1^4$ whose position vector consistently resides in the orthogonal complement $\vec{\delta}_1^{\perp}$ of its principal normal vector field $\vec{\delta}_1$. Hence, position vector of rectifying spacelike curve can be expressed as:

$$\alpha(s) = \mu_1(s)t(s) + \mu_2(s)\delta_2(s) + \mu_3(s)\delta_3(s) \tag{2.2}$$

for some differentiable functions $\mu_1(s)$, $\mu_2(s)$ and $\mu_3(s)$ in arclength function $s$ [7].

Subsequently, a normal curve in $E_1^4$ can be defined as a curve whose position vector consistently resides in its normal space. As a result, the position vector of normal spacelike curve can be written as:

$$\alpha(s) = \varsigma_1(s)\delta_1(s) + \varsigma_2(s)\delta_2(s) + \varsigma_3(s)\delta_3(s) \tag{2.3}$$

for some differentiable functions $\varsigma_1(s), \varsigma_2(s)$ and $\varsigma_3(s)$ in arclength function $s$ [12].

Finally, we establish the definition of first kind or second kind osculating curve in $E_1^4$ where its position vector concerning a selected origin consistently lies in the orthogonal complement $\delta_3^{\perp}$ or $\delta_2^{\perp}$, respectively. Therefore, position vector of spacelike and timelike first kind osculating curve can be written as:

$$\alpha(s) = \lambda_1(s)t(s) + \lambda_2(s)\delta_1(s) + \lambda_3(s)\delta_2(s) \tag{2.4}$$

and position vector of spacelike and timelike second kind osculating curve can be written as:

$$\alpha(s) = \lambda_1(s)t(s) + \lambda_2(s)\delta_1(s) + \lambda_3(s)\delta_3(s) \tag{2.5}$$

where $\lambda_1(s), \lambda_2(s)$ and $\lambda_3(s)$ are differentiable functions in arclength function $s$ [14].

For a regular spacelike curve $\alpha : I \to E_1^4$, let the equiform parameter of $\alpha(s)$ defined by $\sigma = \int k_1\, ds$ where $\rho = \dfrac{1}{k_1}$ is the radius of curvature of the curve α. Hence, it follows $\rho = \dfrac{ds}{d\sigma}$. Let $\{T, \eta, \zeta_1, \zeta_2\}$ be the equiform Frenet frame of the curve $\alpha$, where $T(\sigma) = \rho t(s)$ is equiform tangent vector, $\eta(\sigma) = \rho\delta_1(s)$ is equiform principal normal vector, $\zeta_1(\sigma) = \rho\delta_2(s)$ is equiform first binormal vector and $\zeta_2(\sigma) = \rho\delta_3(s)$ is equiform second binormal vector. Moreover, equiform curvatures of the curve $\alpha = \alpha(\sigma)$ are defined by $K_1(\sigma) = \dot{\rho}$, $K_2(\sigma) = \dfrac{k_2}{k_1}$ and $K_3(\sigma) = \dfrac{k_3}{k_1}$. Thus, the equiform Frenet formulae in $E_1^4$ is written as follows:

$$\begin{bmatrix} T'(\sigma) \\ \eta'(\sigma) \\ \zeta_1'(\sigma) \\ \zeta_2'(\sigma) \end{bmatrix} = \begin{bmatrix} K_1(\sigma) & 1 & 0 & 0 \\ -1 & K_1(\sigma) & K_2(\sigma) & 0 \\ 0 & -K_2(\sigma) & K_1(\sigma) & K_3(\sigma) \\ 0 & 0 & K_3(\sigma) & K_1(\sigma) \end{bmatrix} \begin{bmatrix} T(\sigma) \\ \eta(\sigma) \\ \zeta_1(\sigma) \\ \zeta_2(\sigma) \end{bmatrix} \tag{2.6}$$

where $\left( '=\dfrac{d}{d\sigma} \right)$, $\langle T,T\rangle = \langle \eta,\eta\rangle = \langle \zeta_1,\zeta_1\rangle = \rho^2$, $\langle \zeta_2,\zeta_2\rangle = -\rho^2$ and $\langle T,\eta\rangle = \langle T,\zeta_1\rangle = \langle T,\zeta_2\rangle = \langle \eta,\zeta_1\rangle = \langle \eta,\zeta_2\rangle = \langle \zeta_1,\zeta_2\rangle = 0$ [5].

The paper focuses on rectifying, normal and second kind osculating curves within the context of equiform geometry in $E_1^4$, characterizing these curves based on their equiform curvature functions.

## 3. Spacelike Equiform Rectifying Curves in $E_1^4$

**Theorem 3.1.** Assume that $\alpha$ is a unit speed spacelike curve in $E_1^4$ with spacelike vector fields $T,\zeta_1$ and timelike vector field $\zeta_2$. Then $\alpha$ is a rectifying curve if and only if

$$\left(\frac{1}{K_3}\left(\frac{1}{K_2}+(c+s)\left(\frac{1}{K_2}\right)'\right)\right)' = \frac{(c+s)K_3}{\rho K_2} - \frac{K_1}{K_3}\left(\frac{1}{K_2}+(c+s)\left(\frac{1}{K_2}\right)'\right) \tag{3.1}$$

where $K_1, K_2, K_3$ are non-zero equiform curvatures and $c$ is non-zero constant.

**Proof**, Let $\alpha$ be a unit speed spacelike rectifying curve in $E_1^4$ with equiform curvatures $K_1$, $K_2$ and $K_3$ with respect to the equiform invariant parameter $\sigma$. Hence, by definition we have

$$\alpha(\sigma) = \mu_1(\sigma)T(\sigma) + \mu_2(\sigma)\zeta_1(\sigma) + \mu_3(\sigma)\zeta_2(\sigma) \tag{3.2}$$

for some differentiable functions $\mu_1$, $\mu_2$ and $\mu_3$ in $E_1^4$. Differentiating (3.2) with respect to $\sigma$ and using Eq. (2.6), the following equation is gathered

$$\begin{aligned} T &= \left(\mu_1' + \mu_1 K_1\right)T + (\mu_1 - \mu_2 K_2)\eta \\ &\quad + \left(\mu_2' + \mu_2 K_1 + \mu_3 K_3\right)\zeta_1 + \left(\mu_3' + \mu_3 K_1 + \mu_2 K_3\right)\zeta_2. \end{aligned}$$

It follows that

$$\begin{cases} \mu_1' + \mu_1 K_1 - 1 = 0, \\ \mu_1 - \mu_2 K_2 = 0, \\ \mu_2' + \mu_2 K_1 + \mu_3 K_3 = 0, \\ \mu_3' + \mu_2 K_3 + \mu_3 K_1 = 0 \end{cases} \tag{3.3}$$

and therefore

$$\begin{cases} \mu_1 = \dfrac{c+s}{\rho}, \qquad \mu_2 = \dfrac{c+s}{\rho K_2}, \\ \mu_3 = -\dfrac{1}{K_3}\left(\dfrac{1}{K_2}+(c+s)\left(\dfrac{1}{K_2}\right)'\right). \end{cases} \tag{3.4}$$

where $c$ is non-zero constant. In this way, the functions $\mu_1(\sigma)$, $\mu_2(\sigma)$ and $\mu_3(\sigma)$ can be expressed in terms of the equiform curvatures $K_1$, $K_2$ and $K_3$. Thus

$$\begin{aligned} \alpha(\sigma) &= \frac{c+s}{\rho}T(\sigma) + \frac{c+s}{\rho K_2}\zeta_1(\sigma) \\ &\quad - \left(\frac{1}{K_3}\left(\frac{1}{K_2}+(c+s)\left(\frac{1}{K_2}\right)'\right)\right)\zeta_2(\sigma). \end{aligned} \tag{3.5}$$

Furthermore, employing the last equation in (3.3) and the relation (3.4), it can be deduced that the equiform curvature functions $K_1$, $K_2$ and $K_3$ satisfy the equation

$$\left(\frac{1}{K_3}\left(\frac{1}{K_2}+(c+s)\left(\frac{1}{K_2}\right)'\right)\right)' = \frac{(c+s)K_3}{\rho K_2} - \frac{K_1}{K_3}\left(\frac{1}{K_2}+(c+s)\left(\frac{1}{K_2}\right)'\right). \tag{3.6}$$

Consider the vector $X \in E_1^4$ expressed as

$$\begin{aligned} X(\sigma) &= \alpha(\sigma) - \frac{c+s}{\rho}T(\sigma) - \frac{c+s}{\rho K_2}\zeta_1(\sigma) \\ &\quad + \left(\frac{1}{K_3}\left(\frac{1}{K_2}+(c+s)\left(\frac{1}{K_2}\right)'\right)\right)\zeta_2(\sigma). \end{aligned}$$

Then, we can easily find $X' = 0$, that is, $X$ is a constant vector. Hence, $\alpha$ is rectifying curve.

**Theorem 3.2.** There are no spacelike rectifying curves in $E_1^4$ with constant equiform curvatures $K_1$, $K_2$ and $K_3$.

**Proof.** The clarity of the statement is evident from Theorem 3.1.

**Theorem 3.3.** Assume that $\alpha$ is a unit speed spacelike curve in $E_1^4$ with non-zero equiform curvatures $K_1$, $K_2$ and $K_3$ with respect to the equiform invariant parameter $\sigma$. Hence, $\alpha$ is rectifying curve if

$$K_2 = \text{constant}, \quad K_3 = \text{constant}, \qquad K_1 = \frac{(c+s)}{\rho} K_3^2 \tag{3.7}$$

where $c$ is non-zero constant.

**Proof.** Suppose that $K_2 = \text{constant}$ and $K_3 = \text{constant}$. By using the equation (3.6), we get (3.7).

**Corollary 3.1.** Let $\alpha$ be a unit speed spacelike curve with non-zero equiform curvatures $K_1, K_2, K_3$ and vector fields $T$, $\zeta_1$ and $\zeta_2$ in $E_1^4$. If $\alpha$ is a rectifying curve then the following relations satisfied:

(i) The principal tangent component of position vector of rectifying curve is expressed as

$$\langle \alpha, T \rangle = \rho(c+s).$$

(ii) The first and second binormal components of position vector of rectifying curve can be expressed as

$$\langle \alpha, \zeta_1 \rangle = \rho \frac{c+s}{K_2},$$

$$\langle \alpha, \zeta_2 \rangle = \frac{\rho^2}{K_3}\left( \frac{1}{K_2} + (c+s)\left( \frac{1}{K_2} \right)' \right).$$

## 4. Spacelike Equiform Normal Curves in $E_1^4$

**Theorem 4.1.** Assume that $\alpha$ is a unit speed spacelike curve in $E_1^4$ with spacelike vector fields $\eta$, $\zeta_1$ and timelike vector field $\zeta_2$. Then α is a normal curve if and only if

$$\left( \frac{1}{K_3}\left( K_2 + \left( \frac{K_1}{K_2} \right)' + \frac{K_1^2}{K_2} \right) \right)' = \frac{K_1 K_3}{K_2} - \frac{K_1}{K_3}\left( K_2 + \left( \frac{K_1}{K_2} \right)' + \frac{K_1^2}{K_2} \right) \tag{4.1}$$

where $K_1$, $K_2$ and $K_3$ are non-zero equiform curvatures.

**Proof** Let $\alpha$ be a unit speed spacelike curve in $E_1^4$ with non-zero equiform curvatures $K_1$, $K_2$ and $K_3$ with respect to the equiform invariant parameter $\sigma$. Hence, by definition we have

$$\alpha(\sigma) = \varsigma_1(\sigma)\eta(\sigma) + \varsigma_2(\sigma)\zeta_1(\sigma) + \varsigma_3(\sigma)\zeta_2(\sigma) \tag{4.2}$$

for some differentiable functions $\varsigma_1, \varsigma_2$ and $\varsigma_3$ in $E_1^4$. Differentiating (4.2) with respect to $\sigma$ and using the Eq. (2.6), the following equation is gathered

$$\begin{aligned} T = {} & -\varsigma_1 T + (\varsigma_1' + \varsigma_1 K_1 - \varsigma_2 K_2)\eta \\ & + (\varsigma_1 K_2 + \varsigma_2' + \varsigma_2 K_1 + \varsigma_3 K_3)\zeta_1 \\ & + (\varsigma_2 K_3 + \varsigma_3 K_1 + \varsigma_3')\zeta_2. \end{aligned}$$

It follows that

$$\begin{cases} -\varsigma_1 - 1 = 0, \\ \varsigma_1' + \varsigma_1 K_1 - \varsigma_2 K_2 = 0, \\ \varsigma_1 K_2 + \varsigma_2' + \varsigma_2 K_1 + \varsigma_3 K_3 = 0, \\ \varsigma_2 K_3 + \varsigma_3 K_1 + \varsigma_3' = 0 \end{cases} \tag{4.3}$$

and therefore

$$\begin{cases} \varsigma_1 = -1, \qquad \varsigma_2 = -\dfrac{K_1}{K_2}, \\ \varsigma_3 = \dfrac{1}{K_3}\left( K_2 + \left( \dfrac{K_1}{K_2} \right)' + \dfrac{K_1^2}{K_2} \right). \end{cases} \tag{4.4}$$

In this way, the functions $\varsigma_1(\sigma)$, $\varsigma_2(\sigma)$ and $\varsigma_3(\sigma)$ can be expressed in terms of the equiform curvatures $K_1$, $K_2$ and $K_3$. Thus

$$\begin{aligned} \alpha(\sigma) = {} & -\eta(\sigma) - \frac{K_1}{K_2}\zeta_1(\sigma) \\ & + \frac{1}{K_3}\left( K_2 + \left( \frac{K_1}{K_2} \right)' - \frac{K_1^2}{K_2} \right)\zeta_2(\sigma). \end{aligned} \tag{4.5}$$

Additionally, employing the last equation in (4.3) and the relation (4.4), it is straightforward to determine that equiform curvature functions $K_1$, $K_2$ and $K_3$ satisfy the equation

$$\frac{K_1 K_3}{K_2} - \frac{K_1}{K_3}\left( K_2 + \left( \frac{K_1}{K_2} \right)' + \frac{K_1^2}{K_2} \right) = \left( \frac{1}{K_3}\left( K_2 + \left( \frac{K_1}{K_2} \right)' + \frac{K_1^2}{K_2} \right) \right)'. \tag{4.6}$$

Consider the vector $X \in E_1^4$ expressed as

$$X(\sigma)=\alpha(\sigma)+\eta(\sigma)+\frac{K_1}{K_2}\zeta_1(\sigma)$$
$$-\frac{1}{K_3}\left(K_2+\left(\frac{K_1}{K_2}\right)'+\frac{K_1^2}{K_2}\right)\zeta_2(\sigma)$$

gives $X'=0$, and $X$ is a constant vector. Hence, $\alpha$ is a normal curve.

**Theorem 4.2.** Assume that $\alpha$ is a unit speed spacelike curve in $E_1^4$ with non-zero constant equiform curvatures $K_1$, $K_2$ and $K_3$ with respect to the equiform invariant parameter $\sigma$. Then $\alpha$ is normal curve if $K_1^2+K_2^2=K_3^2$.

**Proof.** The clarity of the statement is evident from Theorem 4.1.

**Theorem 4.3.** Assume that $\alpha$ is a unit speed spacelike curve in $E_1^4$ with non-zero equiform curvatures $K_1$, $K_2$ and $K_3$ with respect to the equiform invariant parameter $\sigma$. Then $\alpha$ is a normal curve if

$$K_1=\text{constant},\quad K_2=\text{constant},$$
$$K_3=\pm e^{K_1(\sigma+c)}\sqrt{\frac{1+K_1^2}{e^{2K_1(\sigma+c)}\pm\left(1+K_1^2\right)}} \tag{4.7}$$

where $c$ is non-zero constant.

**Proof.** Suppose that $K_1=a_1$, $K_2=a_2$ and $K_2+\frac{K_1^2}{K_2}=a_3$, where $a_1,a_2,a_3$ are non-zero constants. By using the equation (4.6), we get

$$K_3'=a_1K_3-\frac{a_1}{a_2a_3}K_3^3. \tag{4.8}$$

Then the solution of differential equation (4.8) gives (4.7).

**Corollary 4.1.** Let $\alpha$ be a unit speed spacelike curve with non-zero equiform curvatures $K_1,K_2,K_3$ and vector fields $\eta$, $\zeta_1$, $\zeta_2$ in $E_1^4$. If $\alpha$ is a normal curve, then the following relations are satisfied:

(i) The principal normal component of position vector of normal curve can be expressed as

$$\langle\alpha,\eta\rangle=-\rho^2.$$

(ii) The first and second binormal components of position vector of normal curve can be expressed as

$$\langle\alpha,\zeta_1\rangle=-\rho^2\frac{K_1}{K_2},$$
$$\langle\alpha,\zeta_2\rangle=-\frac{\rho^2}{K_3}\left(K_2+\left(\frac{K_1}{K_2}\right)'+\frac{K_1^2}{K_2}\right).$$

## 5. Spacelike Equiform Second Kind Osculating Curves in $E_1^4$

**Theorem 5.1.** Assume that $\alpha$ is a unit speed spacelike curve in $E_1^4$ with spacelike vector fields $T$, $\eta$ and timelike vector field $\zeta_2$. Hence, α is a second kind osculating curve if and only if

$$\left(\frac{K_3}{K_2}\right)''=-\frac{K_3}{K_2}+\frac{1}{c}e^{\int K_1 d\sigma},\quad c\in R. \tag{5.1}$$

**Proof** Let $\alpha$ be a unit speed spacelike osculating curve in $E_1^4$ with non-zero equiform curvatures $K_1$, $K_2$ and $K_3$ with respect to the equiform invariant parameter $\sigma$. Hence, by definition we have

$$\alpha(\sigma)=\lambda_1(\sigma)T(\sigma)+\lambda_2(\sigma)\eta(\sigma)+\lambda_3(\sigma)\zeta_2(\sigma) \tag{5.2}$$

for some differentiable functions $\lambda_1,\lambda_2$ and $\lambda_3$ in $E_1^4$. Differentiating (5.2) with respect to $\sigma$ and using the Eq. (2.6), the following equation is gathered

$$T=(\lambda_1'+\lambda_1K_1-\lambda_2)T+(\lambda_1+\lambda_2'+K_1\lambda_2)\eta$$
$$+(\lambda_2K_2+\lambda_3K_3)\zeta_1+(\lambda_3'+\lambda_3K_1)\zeta_2.$$

It follows that

$$\begin{cases}\lambda_1'+\lambda_1K_1-\lambda_2-1=0,\\ \lambda_1+\lambda_2'+K_1\lambda_2=0,\\ \lambda_2K_2+\lambda_3K_3=0,\\ \lambda_3'+\lambda_3K_1=0\end{cases} \tag{5.3}$$

and therefore

$$\begin{cases}\lambda_1=c\left(\frac{K_3}{K_2}\right)'e^{-\int K_1 d\sigma},\\ \lambda_2=-c\left(\frac{K_3}{K_2}\right)e^{-\int K_1 d\sigma},\\ \lambda_3=ce^{-\int K_1 d\sigma}\end{cases} \tag{5.4}$$

where $c$ is non-zero constant. Accordingly, the functions $\lambda_1(\sigma)$, $\lambda_2(\sigma)$ and $\lambda_3(\sigma)$ can be expressed in terms of the equiform curvatures $K_1$, $K_2$ and $K_3$. Thus

$$\alpha(\sigma)=ce^{-\int K_1 d\sigma}\left[\begin{array}{l}\left(\frac{K_3}{K_2}\right)' T(\sigma)-\left(\frac{K_3}{K_2}\right)\eta(\sigma)\\ +\zeta_2(\sigma)\end{array}\right]. \qquad (5.5)$$

Furthermore, utilizing the first equation in (5.3) and the Eq. (5.4), the equiform curvature functions $K_1$, $K_2$ and $K_3$ satisfy the equation

$$\left(\frac{K_3}{K_2}\right)''=-\frac{K_3}{K_2}+\frac{1}{c}e^{\int K_1 d\sigma}, \qquad c\in\square .$$

(5.6)

Consider the vector $X\in E_1^4$ expressed as

$$X(\sigma)=\alpha(\sigma)-c\left(\frac{K_3}{K_2}\right)' e^{-\int K_1 d\sigma}T(\sigma)$$
$$+c\frac{K_3}{K_2}e^{-\int K_1 d\sigma}\eta(\sigma)-ce^{-\int K_1 d\sigma}\zeta_2(\sigma)$$

gives $X'=0$, and $X$ is a constant vector. Hence, $\alpha$ is a second kind osculating curve.

**Theorem 5.2.** There are no spacelike second kind osculating curves in $E_1^4$ with non-zero constant equiform curvatures $K_1$, $K_2$ and $K_3$.

**Proof.** The clarity of the statement is evident from Theorem 5.1.

**Theorem 5.3.** Let $\alpha$ be a unit speed spacelike second kind osculating curve in $E_1^4$ with non-zero equiform curvatures $K_1$, $K_2$ and $K_3$ with respect to the equiform invariant parameter $\sigma$. Hence, $\alpha$ is a second kind osculating curve if

$K_1=\text{constant}$,

$$\frac{K_3}{K_2}=-\int\left(\int\frac{K_3}{K_2}d\sigma\right)d\sigma+\frac{1}{cK_1^2}e^{K_1\sigma}+d_1\sigma+d_2 \qquad (5.7)$$

where $c,d_1,d_2\in R$ .

**Proof.** Suppose that $K_1=\text{constant}$ . By utilizing the equation (5.6), we obtain differential equation

$$\left(\frac{K_3}{K_2}\right)''=-\frac{K_3}{K_2}+\frac{1}{c}e^{K_1\int d\sigma}, \quad c\in R. \qquad (5.8)$$

Solution of the differential equation (5.8) can be formulated as

$$\frac{K_3}{K_2}=-\int\left(\int\frac{K_3}{K_2}d\sigma\right)d\sigma+\frac{1}{cK_1^2}e^{K_1\sigma}+d_1\sigma+d_2,$$

where $c,d_1,d_2\in R$.

**Corollary 5.1.** Let $\alpha$ be a unit speed spacelike curve with non-zero equiform curvatures $K_1$, $K_2$ and $K_3$ and vector fields $T,\eta$ and $\zeta_2$ in $E_1^4$. If $\alpha$ is a second kind osculating curve then the following relations are satisfied:

(i) The tangential and principal normal components of position vector of second kind osculating curve are expressed as respectively

$$\langle\alpha,T\rangle=c\rho^2\left(\frac{K_3}{K_2}\right)' e^{-\int K_1 d\sigma},$$
$$\langle\alpha,\eta\rangle=-c\rho^2\frac{K_3}{K_2}e^{-\int K_1 d\sigma}.$$

(ii) The second binormal component of position vector of second kind osculating curve is expressed as

$$\langle\alpha,\zeta_2\rangle=-c\rho^2 e^{-\int K_1 d\sigma}.$$

## 6. Conclusion

This study gives rectifying, normal and second kind osculating curves according to equiform geometry in $E_1^4$. We examine rectifying, normal, and second-kind osculating curves based on their curvature functions and identify the essential and sufficient conditions for rectifying, normal and second kind osculating curves to be congruent to rectifying, normal and second kind osculating curves according to equiform geometry in $E_1^4$, respectively.

## Acknowledgment

The author would like to extend her gratitude to the contributors of the referenced literature for providing valuable scientific insights and ideas that contributed to this study.

## Statement of Research and Publication Ethics

The study adheres to research and publication ethics.

## References

[1] A. T. Ali and M. Önder, “Some characterizations of spacelike rectifying curves in the Minkowski space-time”, *Glob J Sci Front Res Math Decision Sci*, vol. 12, no. 1, pp. 57-64, 2012.

[2] B. Y. Chen, “When does the position vector of a space curve always lie in its rectifying plane?”, *Amer. Math. Monthly*, vol. 110, pp. 147-152, 2003.

[3] B. Y. Chen and F. Dillen, “Rectifying curves as centrodes and extremal curves”, *Bull. Inst. Math. Academia Sinica*, vol. 2, pp. 77-90, 2005.

[4] B. O’Neill, “*Semi-Riemannian geometry with applications to relativity*”, Academic Press, London: 1983.

[5] H.S. Abdel-Aziz, M.K. Khalifa Saad, and A.A. Abdel-Salam, “Equiform Differential Geometry of Curves in Minkowski Space-Time”, 2015, arXiv:1501.02283v1 [math DG] January.

[6] J. Walrave, “Curves and surfaces in Minkowski space”, Ph.D. dissertation, Leuven University,1995.

[7] K. İlarslan and E. Nešovic, “Some characterizations of rectifying curves in the Euclidean space $E^4$”, *Turkish. J. Math.*, vol. 32, no. 1, pp. 21-30, 2008.

[8] K. İlarslan, E. Nešovic, and M. Petrovic-Torgasev, “Some characterizations of rectifying curves in the Minkowski 3-space”, *Novi Sad J. Math.*, vol. 33, no. 2, pp. 23-32, 2003.

[9] K. İlarslan and E. Nešovic, “Some characterizations of null, pseudo null and partially null rectifying curves in Minkowski space-time”, *Taiwanese J. Math.*, vol. 12, no. 5, pp. 1035-1044, 2008.

[10] K. İlarslan, “Spacelike normal curves in Minkowski space $E_1^3$”, *Turkish J. Math.*, vol. 29, no. 1, 53-63, 2005.

[11] K. İlarslan and E. Nešovic, “Timelike and null normal curves in Minkowski space $E_1^3$”, *Indian J. Pure Appl. Math.*, vol. 35, no. 7, 881-888, 2004.

[12] K. İlarslan and E. Nešovic, “Spacelike and timelike normal curves in Minkowski space-time”, *Publ. Inst. Math. (Belgrad) (N.S.)*, vol. 85, no. 99, pp. 111-118, 2009.

[13] K. İlarslan and E. Nešovic, “Some characterizations of osculating curves in the Euclidean spaces”, *Demonstratio Mathematica*, vol. 16, pp. 931-939, 2008.

[14] K. İlarslan and E. Nešovic, “The first kind and the second kind osculating curves in Minkowski space-time”, *Compt. Rend. Acad. Bulg. Sci.*, vol. 62, no. 6, pp. 677-686, 2009.

[15] K. İlarslan and E. Nešovic, “Some characterizations of null osculating curves in the Minkowski space-time”, *Proceedings of the Estonian Academy of Sciences*, vol. 6, no. 1, pp. 1-8, 2012.

[16] K. İlarslan, N. Kılıç, and H. Altın Erdem, “Osculating curves in 4-dimensional semi-Euclidean space with index 2”, *Open Mathematics*, vol. 15, pp. 562-567, 2017.

[17] R. Lopez, “Differential geometry of curves and surfaces in Lorentz-Minkowski space”, *Int. Electron. J. Geom.*, vol. 3, pp. 67-101, 2010.

[18] S. Yılmaz and M. Turgut, “On the Differential Geometry of the curves in Minkowski space-time”, *Int. J. Contemp. Math. Sci.*, vol. 3, no. 7, pp. 1343-1349, 2008.

[19] M. Elzawy and S. Mosa, “Equiform rectifying curves in Galilean space $G^4$”, *Scientific African*, vol 22, e01931, 2023.

[20] M. Fakharany, A. El-Abed, M. Elzawy and S. Mosa, “On the geometry of equiform normal curves in the Galilean space $G^4$”, *Inf. Sci. Lett.*, vol. 11, no. 5, pp. 1711-1715, 2022.

[21] D. W. Yoon, J. W. Lee and C. W Lee, “Osculating curves in the Galilean 4-space”, *International Journal of Pure and Applied Mathematics*, vol. 100, no. 4, pp. 497-506, 2015.

Bitlis Eren Üniversitesi Fen Bilimleri Dergisi
BİTLİS EREN UNIVERSITY JOURNAL OF SCIENCE
ISSN: 2147-3129/e-ISSN: 2147-3188
VOLUME: 13 NO: 2 PAGE: 474-481 YEAR: 2024
DOI:10.17798/bitlisfen.1432493

# Species Delimitation of Some *Melanargia* Species (Lepidoptera, Nymphalidae, Satyrinae) in The Southeastern Anatolia Region Based On The mtCOI Gene

Hikmet BAYRAKTUTAN[1], Sibel KIZILDAĞ[1*]

[1]*Department of Biology, Van Yuzuncu Yil University, 65080 Van, TÜRKİYE*

*(ORCID: 0009-0007-7814-0301) (ORCID: 0000-0003-0182-5154)*

**Keywords:** DNA barcoding, *Melanargia*, mtCOI gene, Species delimitation, Systematics.

**Abstract**

Among the Palearctic species, butterflies of the genus *Melanargia* are known for their black and white wing patterns. The morphological character polarization of this genus is full of varying combinations of subgenus, species complex, and subspecies status. Its taxonomy is open to debate, especially in species and subspecies categories, with definitions mostly based on wing color. In recent years, cryptic species, phenotypically masked species, and species with intense intraspecific variation have been identified through the determination of lineages under the leadership of molecular systematics. The mtCOI gene, which is especially described as a species signature, is an important DNA barcode used for Lepidoptera.

In the presented study, the mtCOI gene sequence of the populations of *Melanargia larissa*, *M.grumi*, *M.hylata*, *M.syriaca*, and *M.russiae* species in the South-eastern Anatolia region was determined for the first time. To determine the boundaries of these species, gene characterization and genetic distances were carried out according to the Kimura-2 Parameter, and putative species analyses were carried out by the ABGD method. Trees were constructed with Maximum likelihood and Bayesian inference algorithms to determine the phylogenetic relationships between species of the genus. In light of these analyses, it has been shown that the genetic distance of morphological species *M. larissa*, *M. grumi*, *M.hylata*, and *M. syriaca* is not at the species level and that *M.larissa* maintains its species status according to the principle of priority. In addition, the *M.russiae* population presented in this study forms a monophyletic clade with other populations of the same species in the phylogenetic tree, proving that this taxon is a distinct species

## 1. Introduction

The *Melanargia* genus was established by Meigen in 1828 and belongs to the family Satyridae. It is distributed from Europe to the easternmost part of Russia and is represented by 24 valid species [1]. Members of the genus have been classified under three subgenera for a long time due to their distribution in these geographical regions: *Melanargia*, *Parce* and *Turcargia*. *Melanargia* subgenus is known for its single species, *M. galathea*. This species is the type species of *Melanargia* and is found in Europe, southwestern Russia and in our country only in the Northern Anatolian forest belt. The type species of the second subgenus, *Parce*, is *Melanargia russiae*. This species has an intermittent distribution in the alpine zone in Europe, Anatolia and Central Asia and is found locally in the high mountains in eastern Turkey. Although the type species of the *Turcargia* subgenus is *Melanargia larissa*, this subgenus also includes *M.grumi*, *M.hylata*,

---

[*] Corresponding author: sibelkizildag@yyu.edu.tr

*Received: 06.02.2024, Accepted: 29.04.2024*

*M.syriaca*, and *M.titea*, and these species are recorded in some countries in the southwestern Palearctic [2]. The species of genus *Melanargia*, commonly known as 'marbled whites' due to their checker black-white wing patterns, are characterized by a wide vein at the base of the forelimbs and are easily distinguished from other genera in the Satyrini subtribe [3]. The taxonomic structure of the genus, and evaluation of taxa as subgenera or species groups is still debated. In particular, the existing morphological variations of these butterflies are quite confusing in determining their taxonomic status. The density of black patterns, especially on the upper wings of individuals examined between different species of the genus or within the same species, makes it difficult to determine species delimitation. Individuals within populations of nearly every species contain variations with very light or very dark patterns. Although new species were added to this genus until recently, the character polarization of the species has not been fully established. As the importance of molecular taxonomy in systematic research is realized, the phylogenetic relationships between members of this genus have begun to be understood. Nazari et al. [4] investigated the taxonomic and phylogenetic relationships using the genital morphologies and mtCOI, ribosomal 18S rRNA and nuclear wg genes of all known Palaearctic butterfly species of the genus Melanargia. Thus, the taxonomic structure of the genus and the evaluation of taxa as subgenera or species groups have been opened to discussion at the molecular level. With the results of this study, they proposed three subgenera of the genus as *Melanargia*, *Halimede* and *Argeformia* with revized species/subspecies. A new *Melanargia* species (*M.sadjadii*) was recognized in northern Iran, near the Caspian Sea, by Carbonel and Naderi [5], which is very similar to *Mtitea wiskotti* with its external morphology and sparse black spots on its wings, and to Mevartianae with its genital structure. Later, Nazari et al. [4], they gave new status as a subspecies of *M.evartianae* for *M.sadjadii* with molecular analysis.

The Mitochondrial Cytochrome Oxidase I (COI) gene is an important barcoding sequence widely used for species identification, delimitation, and also used nucleotide characterization of the gene to reveal variation in species or subspecies categories [6], [7], [8]. The aim of this study was to barcode some *Melanargia* species in Southeastern Turkey for the first time and to contribute to the molecular taxonomy of the *Melanargia* genus through species delimitation analyses. In this region, the *Melanargia* genus is represented by the species larissa, syriaca, grumi, hylata and russiae [9], [10], [11], [12], [13]. The Van population of *M.russiae* was compared with other populations reported from different geographies. In addition, the barcodes of the species within the "larissa" complex, whose morphological distinction is still controversial, were evaluated for the first time with new recording data in Turkey, and their phylogenetic species levels were discussed with molecular analyses.

## 2. Material and Method

*Melanargia* specimens used for molecular analysis were collected, morphologically identified, and then preserved by Muhabbet Kemal and Ahmet Ömer Koçak from the South-eastern Anatolia Region between 2015 and 2018.

**Table 1**. Label information of materials whose species delimitation are evaluated.

| No | Taxon name | Collected location and date with collectors | Location code* | CESA ID** |
|---|---|---|---|---|
| **1** | *Melanargia grumi* | TR- Adıyaman Pr Kahta, Aydınpınar 6.5.2018, M.Kemal & A.Koçak leg. (Cesa) | | LepDNA Saty01–Cesa, |
| **2** | *Melanargia grumi* ssp.*grumi* | TR – Mardin Pr., Nusaybin Kalecik 560m, 10.5. 2015, I. Akdeniz leg. (Cesa) | 47Gd | LepDNA Saty 08-Cesa |
| **3** | *Melanargia grumi* ssp. | TR – Bitlis Mutki, Kavakbaşı 1670m, 9.6.2018, M.Kemal & A.Koçak leg. (Cesa) | 13F22 | LepDNA Saty 09-Cesa |
| **4** | *Melanargia hylata karabagi* | TR- Hakkari Pr. Ağaçdibi, 15.6.2018, M.Kemal &A.Koçak leg. (Cesa) | 30B | LepDNA Saty02–Cesa |

| | | | | |
|---|---|---|---|---|
| **5** | *Melanargia hylata* | TR- Van Pr., Bahçesaray Paşaköy 1600m, 6.7.2016, M. Kemal & A.Koçak leg. (Cesa) | 65Ai | LepDNA Saty 04-Cesa |
| **6** | *Melanargia larissa masageta* | TR- Malatya Pr., Beydağı TP 1275m, 20.6.2015, M. Kemal & A.Koçak leg. (Cesa) | 44L | LepDNA Saty 03-Cesa |
| **7** | *Melanargia syriaca* ssp. *kocaki* | TR- Bitlis Pr., Güroymak 1600m, 4.7.2015, M.Kemal & A.Koçak leg. (Cesa) | 13D | LepDNA Saty 06-Cesa |
| **8** | *Melanargia syriaca* ssp. *kocaki* | TR-Muş Pr., Buğlan Pass 1640m, 21.7.2019, M.Kemal & A.Koçak leg. (Cesa) | 49Ea | LepDNA Saty 07-Cesa |
| **9** | *Melanargia russiae* ssp. | Van Pr., Gürpınar, Başet Mt., Dijik 2710m, 10.7.2019, M.Kemal & A.Koçak leg. (Cesa) | 65Gv | LepDNA Saty 10-Cesa |

* The location codes of the materials used in the study are taken from the study of Koçak and Kemal (2019) [14].

** Informations of the sequenced barcodes were keeped in the Cesa barcode store. (https://entcesa.tripod.com/Cesacollection.pdf)

Legs from each individual belonging to nine populations of these butterflies were cleaned with ethanol. Total genomic DNA (tgDNA) was isolated from the muscle tissue of the hindlimb femur of each sample using the RED Extract-N-Amp Tissue PCR Kit (Sigma-Aldrich, St. Louis, Missouri, USA) [15]. The mitochondrial COI gene 658 bp sequence was amplified by PCR reaction using LepF1 and LepR1 primers for each individual. Used cycling parameters were as follows: Initial denaturation at 94 °C for 2 min, followed by 5 cycles of 40 s denaturation at 95°C, 40 s annealing at 45°C, 1 min extension at 72°C, and additional 36 cycles of 40 s denaturation at 94°C, 40 s annealing at 51°C, 1 min extension at 72°C, with a final extension of 72 °C for 10 min. Purification and bidirectional sequencing of PCR products were performed by the Macrogen company (Macrogen, Amsterdam, Netherlands).

Forward and reverse DNA fragments of each bidirectionally sequenced sample in Ab1 format were created contigs after nucleotides controlled, and also converted to .fasta format in the CodonCode Aligner v.8.0.2. A data set was created with used the CLUSTALW alignment algorithm in MEGA 7.0 software by all possible pairwise aligning 9 *Melanargia* barcodes obtained from Southeastern Turkey with other 93 *Melanargia* barcodes registered in online portals. [16], [17]. In the same program, nucleotide compositions were computed for gen characterization of available five species and genetic distances between *Melanargia* populations and species were measured using the Kimura-2 parameter [18]. In the ALTER online portal, the alignment sequences were converted from fasta format to philip and nexus format and then used for Maximum-likelihood (ML) and Bayesian inference (BI) algorithms in the respectively. The ML tree was constructed in CIPRES Science Gateway XSEDE v.8.2.4 using RAxML Blackbox efficiency with 1000 replicates [19]. TPM1uf substitution model was selected as the best evolutionary model according to Akaike criteria in the program JModeltest v.2.1.7 [20], but TPM1uf substitution model were replaced by the GTR model for the closest over-parameterized model [21]. Therefore, BI analysis nucleotide change commands were arranged according to GTR +I +G model with the Markov chain Monte Carlo algorithm in MrBayes 3.2.6 software [22]. Markov chain Monte Carlo (MCMC) simulations were run for 3 000 000 generations, sampling every 100 generations. In the context of Bayesian statistics, summarized tree was obtained through the posterior probability distribution after the first 7500 trees were burned. The topology of both algorithm trees was visualized using FigTree v.1.4.2. DNA barcodes were identified as putative species by the Automated Barcode Gap Discovery (ABGD) method based on a preliminary P value ranging from 0.005 to 0.1 [23].

## 3. Results and Discussion

Gene characters of current populations of *Melanargia* spp. were determined according to the first, second and third nucleotide positions of the mtCOI gene sequences of *Melanargia* species (Table2). The AT deviation was calculated at the first nucleotide position in the variable region of the mtCOI gene nucleotide characters of *M.hylata* and *M.russiae* populations. The second nucleotide positions were conserved in the variable region of

*M.larissa*, and the third nucleotide positions in the variable region of *M.russiae* and *M.grumi*. In addition, both the second and third nucleotide positions of *M.hylata* and *M.syriaca* variable regions were conserved. The most numbers of singletons in the mtCOI gene characterization variable region were determined in *Mhylata* populations and the lowest in *M.grumii* populations.

**Table 2.** Barcode characterizations of the COI gene from different populations of *Melanargia* spp.

| Species | Nucleotide Position | Variable Site (%) | Informative Site (%) | T (%) | C (%) | A (%) | G (%) | AT (%) | GC (%) |
|---|---|---|---|---|---|---|---|---|---|
| | 1st | 92.3 | 66.5 | 49.0 | 7.7 | 42.3 | 0.9 | 91.3 | 8.6 |
| *M. grumii* | 2nd | 7.6 | 25.5 | 25.0 | 16.9 | 32.0 | 26.0 | 57.0 | 42.9 |
| | 3rd | 0.0 | 6.8 | 43.0 | 24.7 | 16.0 | 16.0 | 59.0 | 40.7 |
| | All | 1.9 | 98.1 | 39.2 | 16.4 | 30.1 | 14.3 | 69.3 | 30.7 |
| | 1st | 100.0 | 66.2 | 49.0 | 7.7 | 42.7 | 0.5 | 91.7 | 8.2 |
| *M. hylata* | 2nd | 0.0 | 25.5 | 25.0 | 16.9 | 31.5 | 26.5 | 56.5 | 43.4 |
| | 3rd | 0.0 | 6.8 | 43.0 | 24.7 | 16.0 | 16.0 | 59.0 | 40.7 |
| | All | 1.6 | 98.3 | 39.1 | 16.5 | 30.0 | 14.4 | 69.1 | 30.9 |
| | 1st | 94.7 | 66.4 | 48.0 | 9.1 | 42.3 | 0.9 | 90.3 | 10.0 |
| *M. larissa* | 2nd | 0.0 | 25.8 | 25.0 | 16.9 | 31.5 | 26.5 | 56.5 | 43.4 |
| | 3rd | 5.2 | 6.3 | 43.0 | 24.7 | 15.5 | 16.4 | 58.5 | 41.1 |
| | All | 2.8 | 97.1 | 39.1 | 16.5 | 29.9 | 14.5 | 69.0 | 31.0 |
| | 1st | 100.0 | 66.5 | 50.0 | 7.3 | 42.7 | 0.5 | 92.7 | 7.8 |
| *M. syriaca* | 2nd | 0.0 | 25.8 | 25.0 | 16.9 | 31.5 | 26.5 | 56.5 | 43.4 |
| | 3rd | 0.0 | 6.5 | 43.0 | 24.7 | 16.0 | 16.0 | 59.0 | 40.7 |
| | All | 2.1 | 97.8 | 39.4 | 16.3 | 30.1 | 14.3 | 69.5 | 30.6 |
| | 1st | 88.8 | 66.1 | 49.0 | 8.2 | 40.9 | 2.3 | 89.9 | 10.5 |
| *M. russiae* | 2nd | 11.1 | 25.3 | 26.0 | 16.4 | 31.1 | 26.9 | 57.1 | 43.3 |
| | 3rd | 0.0 | 5.9 | 43.0 | 24.7 | 16.0 | 16.0 | 59.0 | 40.7 |
| | All | 2.7 | 97.2 | 39.3 | 16.3 | 29.3 | 15.1 | 68.6 | 31.4 |

When the genetic distance relations between the *Melanargia* populations obtained from Southeastern Turkey, and constituting the materials of this study are examined, the four morphological species do not diverge at the species level (Table3). It has been determined that the 1.40-1.88% genetic distance between the *Melanargia syriaca kocaki* populations and other larissa-hylata-syriaca populations is sufficient at the molecular level for the subspecies level of the *syriaca kocaki* population. It is clear that the *M.russiae* population is a strong species with a genetic difference range of 6.20-6.74% from other populations.

**Table 3.** Genetic distances of the mtCOI sequence between *Melanargia* populations using the Kimura 2-parameter model.

| **The populations in the study** | **K2P-Genetic distances** | | | | | | | |
|---|---|---|---|---|---|---|---|---|
| *M. grumi*-Adıyaman | | | | | | | | |
| *M. grumi*-Mardin | **0.00** | | | | | | | |
| *M. grumi*-Bitlis | 0.46 | **0.46** | | | | | | |
| *M. larissa masageta*-Malatya | 0.61 | 0.61 | **1.08** | | | | | |
| *M. hylata karabagi*-Hakkari | 0.77 | 0.77 | 0.61 | **0.77** | | | | |
| *M. hylata*-Van | 1.08 | 1.08 | 0.92 | 1.08 | **0.31** | | | |
| *M. syriaca kocaki*-Muş | 1.88 | 1.88 | 1.40 | 1.88 | 1.40 | **1.71** | | |
| *M. syriaca kocaki*-Bitlis | 1.88 | 1.88 | 1.40 | 1.88 | 1.40 | 1.71 | **0.00** | |
| *M. russiae*-Van | 6.38 | 6.38 | 6.56 | 6.74 | 6.20 | 6.56 | 6.74 | **6.74** |

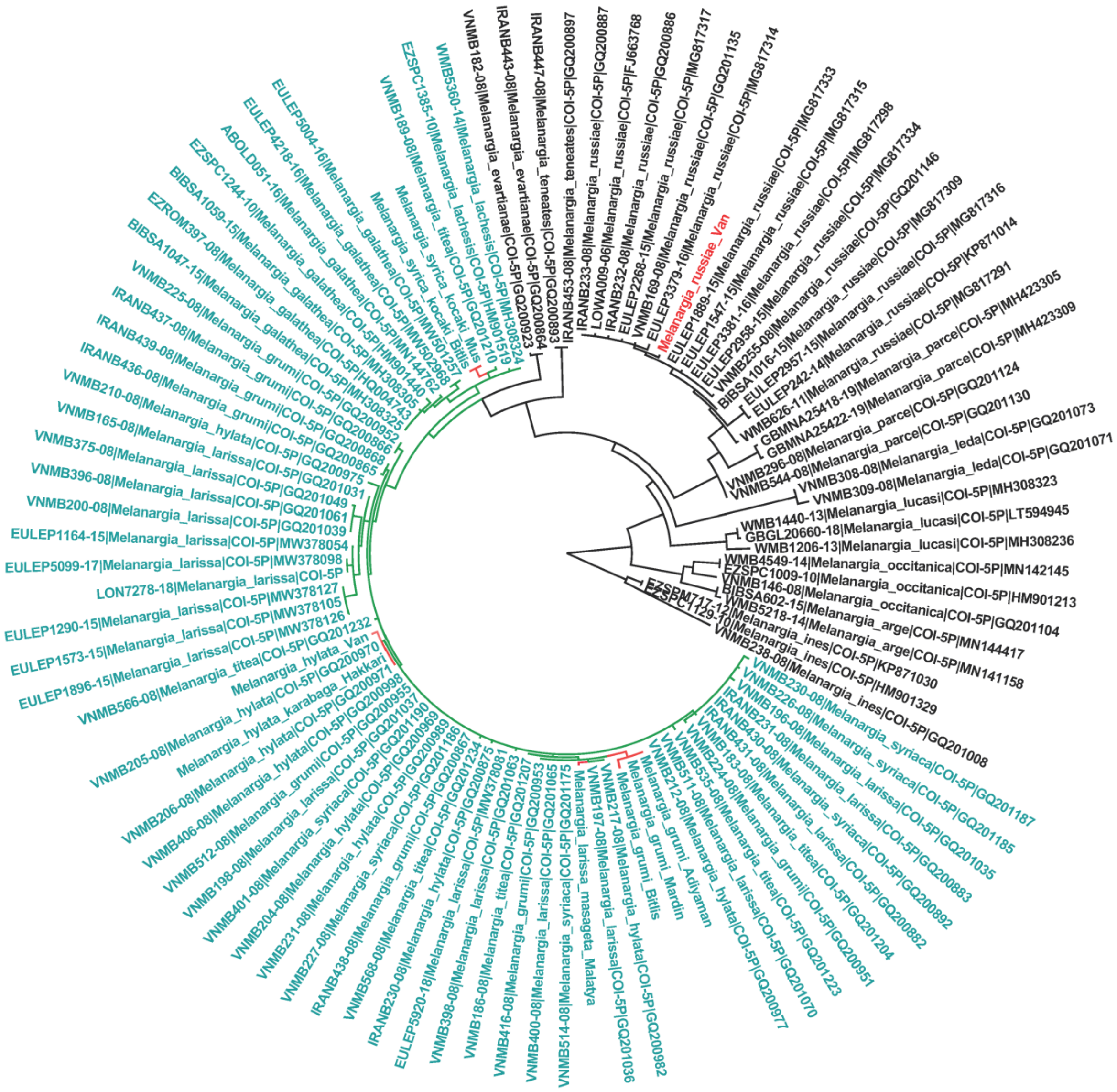

**Figure 1.** Circular phylogenetic tree created by ML algorithm when viewed from inside to outside, blue taxa (grumi+hylata+syriaca+titea=larissa) lineage representing a single species (red branches represent Turkish populations). In the M.russiae clade, the Turkish population written in red is shown.

Because maximum likelihood (ML) and Bayesian inference (BI) trees show similar tree topologies, the phylogenetic relationships of Melanargia species are shown in the circular ML tree without support values given in the text. (Figure1). Both phylogenetic analyses were identified well-supported major clades of *Melanargia*. The first major clade includes of *Melanargia ines* (100/1.00). The second major clade (100/1.00) consists of two distinct groups. The first group includes the *M.arge* and *M.occitanica* clade (100/1.00). The other group consisted of monophyletic and non-monophyletic taxa. Monophyletic taxa (*M.lucasi*, *M.leda*, *M.parce*, *M.russiae*, *M.tenetates*, *M.evartianae*, *M.galathea*, *M.lachesis*) formed branches with strong support values. Non-monophyletic taxa (*M.grumi* , *M.hylata*, *M.syriaca*, *M.titea*, *M.larissa*) are crowded ingroups indicated by the blue text.

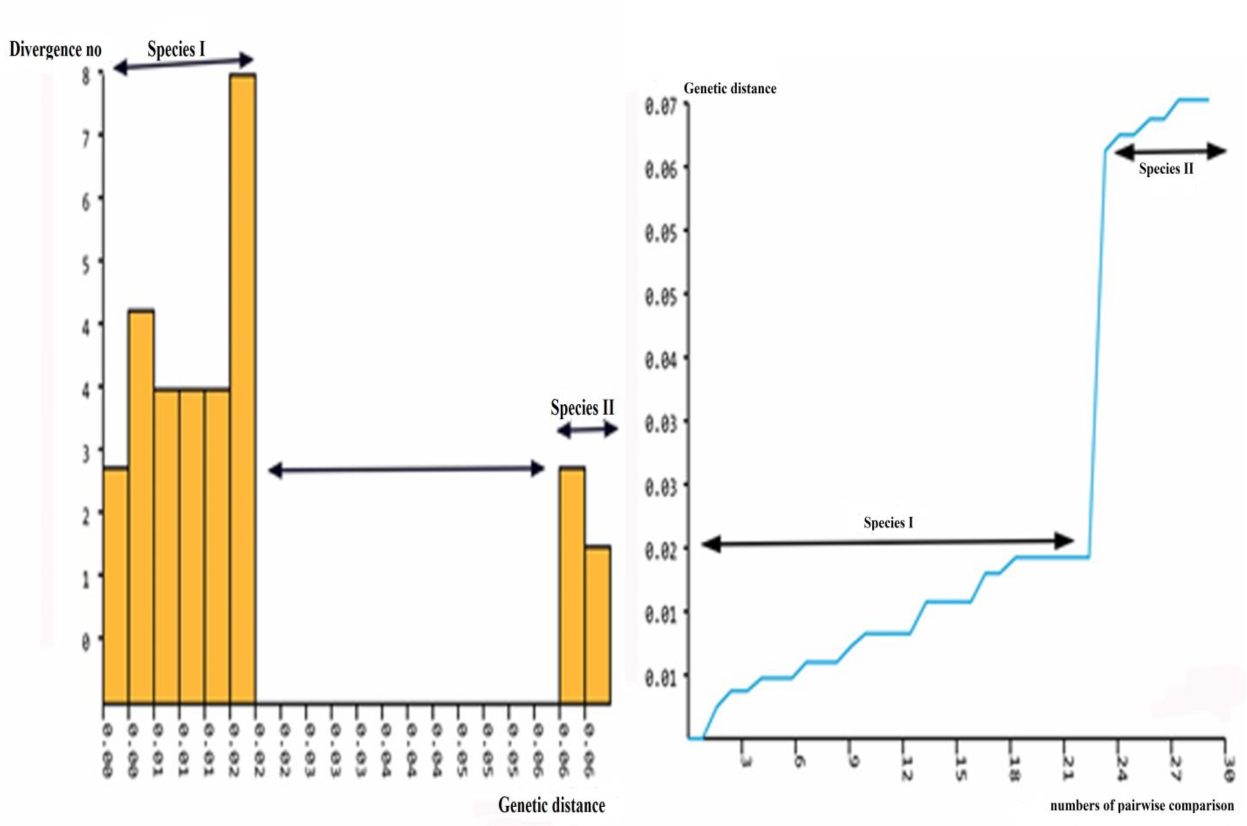

**Figure 2.** Histogram of pairwise K2P distances of nine Turkish populations aligned sequences (A) with ranked distances (B).

In the presented study, it was determined that the genetic distance range of individuals belonging to *Melanargia* populations consisted of two groups (Figure2). The first group is in the range of 0.00-1.88 and the second group is in the range of 6.38-6.74. In the ABGD test, in both pairwise and multiple comparisons of 9 populations, the nucleotide change for group I does not exceed 2% for 4 morphological species (*M.larissa*, *M.grumi*, *M.hylata* and *M.syriaca*). The *M.russiae* population in the second group was genetically separated from other populations in the first group as a distinct species with an average genetic distance of 6.5% according to its lower and upper limits.

## 4. Conclusion and Suggestions

In the study, as a result of genetic distance, species delimitation and phylogenetic analysis of the mtCOI gene sequence among 9 Turkish populations belonging to five morpho-species, these were determined that these populations belonged to only two species. The first species is *M.russiae*, which is morphologically defined as the same, and the second species, which is *M.larissa* according to the principle of priority, is a group of populations belonging to four morphological species (grumi+hylata+larissa+syriaca). For this reason, we support the evaluation of *M.syriaca kocaki* and *M.hylata karabagi* populations within/under the *M.larissa* species. In our study, populations within the larissa group showed very limited genetic differences. Although insufficient phylogenetic signal in this complex cannot be ruled out for mtCOI, Nazari et al. [4] reported that the signal in the 18S rRNA and nuclear wg genes was weak in the phylogeny resolution of this complex. Thus, the lack of molecular divergence for Lepidoptera is not limited to mitochondrial genes. In same study, they conducted with *Melanargia* samples from different geographies, except for the populations of the southeastern Anatolia region, they reported that *M.larissa* is a strong species, and its eleven subspecies, most of them with new statuses.

Molecular analysis of *Melanargia* populations according to the mtCOI gene sequence showed that *M.lucasi*, *M.leda*, *M.parce*, *M.russiae*, *M.tenetates*, *M.evartianae*, *M.galathea*, *M.lachesis* and *M.larissa* are the strong species. In the presented phylogenetic tree, *M.parce* demonstrated two different branches. These two distinct lineages represent two morphologically masked but genetically distinct species. Although the morphological species *M.titea* shares common habitats with the larissa complex only with *M.syriaca* in Hatay [4], it was clustered in the phylogenetic tree with the Muş and Bitlis populations of *M.syriaca* presented in this study. As an appearance, *M.titea* is easily distinguished from the larissa complex.

In this study, the effectiveness of DNA barcoding was tested for the identification and discovery of species from the species-rich fauna of south-eastern Turkey. According to our results, the variations in wing color taken into account in *Melanargia* taxonomy do not lead to a meaningful conclusion with molecular analyses. In our phylogenetic tree, the stable placement of taxa that have completed their speciation and the cladistic chaos of taxa that have not yet reached species saturation (grumi+hylata+syriaca+titea in larissa) can be clearly seen. Moreover, the results of mtCOI gene characterization of *Melanargia* Turkish populations were also showed signals like admixture or subdivisions, inbreeding, or introgression. Although these taxa, which have a wide distribution area, may change in appearance due to ecological pressures in different geographies, their genetic distance from each other is not at the species level because gene flow continues between them.

**Acknowledgment**
Special thanks are given to Prof. Dr. Ahmet Ömer KOÇAK and Dr. Muhabbet KEMAL for their continuous help and use of the Cesa Collection. This work was supported by the Research Council of Van Yüzüncü Yil University (YYUBAP, Project No.: FYL-2020-8839), Van, Turkey

**Conflict of Interest Statement**
There is no conflict of interest between the authors.

**Statement of Research and Publication Ethics**
The study is complied with research and publication ethics

## References

[1] J. C. Habel, R. Vila, M. Husemann, T. Schmitt and L. Dapporto, “Differentiation in the marbled white butterfly species complex driven by multiple evolutionary forces”, *J. Biogeogr.*, pp. 1-13, 2016, doi:10.1111/jbi.12868

[2] A. Ö. Koçak, M. Kemal, “Çatak butterflies with faunal, taxonomical and zoogeographical notes (Papilionoidea, Hesperioidea, Lepidoptera)”. *Misc. Pap.*, vol. 138, pp. 82-85, 2002.

[3] C. Peña, , S. Nylin, A. V. L. Freitas, & N. Wahlberg, “Biogeographic history of the butterfly subtribe Euptychiina (Lepidoptera, Nymphalidae, Satyrinae)”. *Zool. Scr.*, vol. 39, pp. 243-258, 2010.

[4] V. Nazari, W. Hagen, G. C. Bozano, “Molecular systematics and phylogeny of the ‘Marbled Whites’ (Lepidoptera: Nymphalidae, Satyrinae, Melanargia Meigen)”. *Syst. Entomol.*, vol. 35, pp. 132-147, 2010, doi: 10.1111/j.1365-3113.2009.00493.x.

[5] F. Carbonell, A. Naderi, “*Melanargia sadjadii* n. sp., du nord de l’Iran (Lepidoptera, Nymphalidae)”. *Bull. Soc. entomol. Fr.*, vol. 111, no. 4, pp. 465-468, 2006,

[6] P. D. Hebert, M. Y. Stoeckle, T. S. Zemlak and Francis C. M., “Identification of birds through DNA barcodes”. *PLoS Biol.*, vol. 2, e312, 2004.

[7] M. Bai, X. Qing2, K. Qiao, X. Ning, S. Xiao, X. Cheng and G. Liu. “Mitochondrial COI gene is valid to delimitate Tylenchidae (Nematoda: Tylenchomorpha) species”. *J Nematol.*, vol. 52, e2020-38. 2020.

[8] L. M. Nneji, A. C. Adeola, A. O. Ayoola, S. O. Oladipo, Y. Wang, Y. D. Malann, O. Anyaele, I. C. Nneji, M. Rahman, C. S. Olory. “DNA barcoding and species delimitation of butterflies (Lepidoptera) from Nigeria”. *Mol. Biol. Rep.*, vol. 47, pp. 9441-9457. 2020.

[9] A. Ö. Koçak, “A new subspecies of Melanargia larissa from Turkey (Lepidoptera: Satyridae)”. *Atalanta*, vol. 7, no. 1, pp. 40-41, 1976.

[10] A. Ö. Koçak, “New lepidoptera from Turkey V”. *Atalanta*, vol. 8, no. 2, pp. 126-147, 1977.

[11] S. Wagener, “Zwei neue Melanargia formen aus Anatolian”. *Atalanta*, vol. 14, no. 4, pp. 247-299, 1983.

[12] S. Wagener, “Zur Taxonomie, Nomenklatur und verbreitung von Melanargia titea (Klug, 1832) (Lepidoptera:Satyridae)”. *Nota Lepid.*, vol. 6, no. 2/3, pp. 175-188, 1983.
[13] A. Ö. Koçak, M. Kemal, “A synonymous and distributional list of the species of the Lepidoptera of Turkey”. *Memoirs.*, vol. 8, pp. 1-487, 2018.
[14] A. Ö. Koçak, M. Kemal, “First updated geographical codes used in the publications of the Cesa”. *Priamus,* vol. 17, no. 4, pp. 319-360, 2019.
[15] M. Kemal, İ. Yıldız, S. Kızıldağ, H. Uçak and A. Ö. Koçak, “Taxonomical and molecular evaluation of *Apochima agassiz* in East Turkey, with a description of a new genus (Lepidoptera, Geometridae, Ennominae)”. *Misc. Pap.,* vol. 169, pp. 1-13, 2018.
[16] Anonymous, “Barcode Of Life Data System (BoldSystems)”. [Online]. Available: http://www.boldsystems.org/index.php. [Accessed: Jan. 9, 2024].
[17] Anonymous. “National Center for Biotechnology Information (NCBI)”. [Online]. Available: https://www.ncbi.nlm.nih.gov/nuccore/?term=*Melanargia*+COI. [Accessed: Jan. 9, 2024].
[18] M. Kimura, “A simple method for estimating evolutionary rate of base substitutions through comparative studies of nucleotide sequences”. *J. Mol. Evol.,* vol. 16, pp. 111-120, 1980.
[19] A. Stamatakis, “RAxML Version 8: A tool for Phylogenetic Analysis and Post-Analysis of Large Phylogenies”. *Bioinform.*, vol. 30, no. 9, pp. 1312–1313, 2014, doi: 10.1093/bioinformatics/btu033.
[20] D. Posada, “jModelTest: phylogenetic model averaging”. *Mol. Biol. Evol.,* vol. 25, no. 7, pp. 1253-6, 2008, doi: 10.1093/molbev/msn083.
[21] T. Lecocq, N. J. Vereecken, D. Michez, S. Dellicour, P. Lhomme, Patterns of Genetic and Reproductive Traits Differentiation in Mainland vs. Corsican Populations of Bumblebees. *Plos one*, vol. 8, no. 6, e65642. doi:10.1371/journal.pone.0065642. 2013.
[22] F. Ronquist, J. P. Huelsenbeck, “MrBayes 3: Bayesian phylogenetic inference under mixed models”. *Bioinform.,* vol. 19, pp. 1572-1574. 2003,doi: 10.1093/bioinformatics/btg180.
[23] Anonymous.“Automatic Barcode Gap Discovery (ABGD)”. [Online]. Available: https://bioinfo.mnhn.fr/abi/public/abgd/abgdweb.html. [Accessed: Jan. 21, 2024].

**Bitlis Eren Üniversitesi Fen Bilimleri Dergisi**
BİTLİS EREN UNIVERSITY JOURNAL OF SCIENCE
ISSN: 2147-3129/e-ISSN: 2147-3188
VOLUME: 13 NO: 2 PAGE: 482-491 YEAR: 2024
DOI:10.17798/bitlisfen.1433870

# Bayesian Parameter Estimation for Geometric Process with Rayleigh Distribution

Asuman YILMAZ[1*]

[1*]*Van Yüzüncü Yıl University, Faculty of Economics and Administrative Sciences,*
*Department of Econometrics,*
*Van, Türkiye*
*ORCID:0000-0002-8653-6900*

**Keywords:** Rayleigh Distribution, Geometric Process, Maximum Likelihood Estimator, Bayesian Parameter Estimation, Simulation Study.

**Abstract**
The main purpose of this study is to deal with the parameter estimation problem for the geometric process (GP) when the distribution of the first occurrence time of an event is assumed to be Rayleigh. For this purpose, maximum likelihood and Bayesian parameter estimation methods are discussed. Lindley and Markov chain Monte Carlo (MCMC) approximation methods are used in Bayesian calculations. Additionally, a novel method called the Modified-Lindley approximation has been proposed as an alternative to the Lindley approximation. An extensive simulation study was conducted to compare the performances of the prediction methods. Finally, a real data set is analyzed for illustrative purposes.

## 1. Introduction

The counting process is an appropriate and frequently employed method for the statistical analysis of the times at which successive events occur. Let us consider a set of data with successive arrival times. If successive arrival times are independently and identically distributed (iid), the renewal process (RP) can be utilized to analyze this data. Although this method appears to be theoretically easy, real-world situations frequently have a monotone trend in the data set because of the effect of aging and accumulated wear [1], meaning that the successive arrival times may be independently distributed but not identically distributed. Non-homogeneous Poisson process and geometric process (GP) are two more procedures that can be used in the literature to analyze a set of successive arrival times with a trend. The GP was first introduced by Lam [1-2], as a generalization of a renewal process. See the following definition to understand it, [3].

**Definition 1:** A set of nonnegative random variables $\{X_i\ , i = 1,2, \dots\}$ is said to be a GP, If $a^{i-1}X_i, i = 1,2, \dots$ are iid random variables, where $a > 0$ is the ratio of GP. The GP is stochastically decreasing when $a > 1$, increasing when $a < 1$. It will become a RP if $a = 1$. In other words, it is simple to determine the density function of $X_i$ from Definition 1, if $\{X_i\ , i = 1,2, \dots\}$ is a GP and the density function of $X_1$ is $f$.

$$f_{x_i}(x) = a^{i-1}f\left(a^{i-1}x_i\right) \qquad (1)$$

Furthermore, with $E(X_1) = \mu$ and $Var(X_1) = \sigma^2$, the expected value (EV) and the variance (Var) of $X_i$,are given as follows:

$$E(X_i) = \frac{\mu}{a^{i-1}} \text{ and } Var(X_i) = \frac{\sigma^2}{a^{2(i-1)}},$$

where μ and $\sigma^2$ are EV and Var of the first occurrence time $X_1$, respectively.

Lam introduced and applied the GP to maintenance and repair problems, see [1-2]. Several researchers have researched the basic properties of GP, such as [3-4]. Furthermore, the parameter estimation problems for the GP have recently been presented based on the assumption that the random variable $X_1$ follows particular distributions, for example, the lognormal distribution Yeh and Chan [5], gamma distribution Kara et al.[6], Weibull distribution Aydoğdu et al. [7], the inverse Rayleigh distribution Usta [8], generalized Rayleigh distribution Biçer et al. [9] and Rayleigh distribution Biçer et al.[10].

---

[*] Corresponding author: asumanduva@yyu.edu.tr

*Received: 08.02.2024, Accepted: 21.05.2024*

In studies on the GP, different classical parameter estimation methods, including maximum likelihood estimators (MLEs), have been used to estimate the parameters of the process. Since GP was introduced, it has been studied by many researchers, see Kara et al. [11] and also the references cited therein. In these studies on the GP, classical (maximum likelihood and modified maximum likelihood) methods were used to estimate the parameters of the process. However, there are not many studies on the Bayesian parameter estimation problem in GP. Recently, the Bayesian estimators for GP with Lindley and Weibull distributions, respectively, are developed by Yılmaz et al. [12] and Usta [13].

This scenario has motivated us to investigate the Bayesian parameter estimation problem in the GP. On the other hand, Bayesian inference is an alternative framework in estimation problems and received a great deal of attention in recent years.

One of the main advantages of Bayesian statistics is that it allows us to use prior information to analyze unknown parameters. Thus, stronger inferences are obtained. Additionally, Bayesian models outperform classical models, particularly for small sample sizes.

Therefore, in this paper, we have discussed Bayesian inference in GP with Rayleigh distribution.

Here, we assume that the first inter-arrival time $X_1$ distribution in GP follows a Rayleigh distribution with parameter λ. The remainder of the article is organized as follows: In section 2, the Rayleigh distribution is briefly given. The MLEs of the parameters $a$ and λ are obtained. The limiting distributions of the MLEs are investigated. The Bayes estimators of the unknown parameters under square error loss function (SELF) are constructed. For the Bayesian computation, Lindley's, Modified Lindley (M-Lindley), and Gibbs sampling methods are used. In Section 3, a Monte Carlo Simulation study is carried out to compare the performance of the various estimation methods developed in the previous sections. A real-life data set is presented in Section 4. Finally, some concluding remarks are provided in Section 5.

## 2. Material and Method

In this section of the study, Rayleigh Distribution, maximum likelihood method and Bayesian parameter estimation methods are investigated.

### 2.1 Rayleigh Distribution

The Rayleigh distribution is one of the most widely used distributions for modeling positive data in reliability, health, and engineering. Let the distribution of the first occurrence time $X_1$ in GP has a Rayleigh distribution. The probability density function (pdf) and the cumulative density function (cdf) of the Rayleigh distribution are given by

$$f(x) = \frac{x}{\lambda^2} e^{\frac{-x^2}{2\lambda^2}}, \quad x > 0, \lambda > 0 \qquad (2)$$

and

$$F(x) = 1 - e^{\frac{-x^2}{2\lambda^2}} \qquad x > 0, \lambda > 0, \qquad (3)$$

respectively. In Equations (2)-(3), λ represents the scale parameter of the distribution.

Note that, the EV and the Var of the Rayleigh distribution are

$$E(X) = \frac{\lambda\sqrt{\pi}}{\sqrt{2}} \text{ and } Var(X) = \frac{(4-\pi)\lambda^2}{2}, (4)$$

respectively. The MLEs and Bayesian methods are given as follows.

### 2.2 Maximum Likelihood Estimators

Assume that $X_1, X_2, \dots, X_n$ is a set of data that follows a GP with ratio $a$ and $X_1$ has the Rayleigh distribution with parameter λ. Afterward, using Equation (1), and the likelihood function for $X_i,\ i = 1,2, \dots n$ is then obtained

$$L(a, \lambda; x) = \prod_{i=1}^{n} a^{i-1} f\left(a^{i-1} x_i\right) = \frac{a^{n(n-1)}}{\lambda^{2n}} \prod_{i=1}^{n} x_i e^{\frac{-\left(a^{i-1}x_i\right)^2}{2\lambda^2}} . \qquad (5)$$

The MLEs of the parameters $a$ and λ are obtained by taking logarithms of Equation (5), differentiating with respect to $a$ and λ, and equating the normal equations to zero as follows:

$$lnL(a, \lambda; x) = n(n-1)lna - 2nln\lambda + \sum_{i=1}^{n} lnx_i - \sum_{i=1}^{n} \frac{\left(a^{i-1}x_i\right)^2}{2\lambda^2} . \qquad (6)$$

Then, differentiating Equation (6) with respect to $a$ and λ, and equating the normal equations to zero given as

$$\frac{\partial lnL(a,\lambda)}{\partial a} = \frac{n(n-1)}{a} - \frac{1}{a\lambda^2} \sum_{i=1}^{n} \left(a^{i-1}x_i\right)^2 (i-1) \qquad (7)$$

and

$$\frac{\partial lnL(a,\lambda)}{\partial\lambda} = \frac{-2n}{\lambda} + \frac{1}{\lambda^3}\sum_{i=1}^{n}\left(a^{i-1}x_i\right)^2 \qquad (8)$$

Then, from Equations (7) and (8), the parameter λ is found as follows:

$$\lambda = \left(\frac{1}{2n}\sum_{i=1}^{n}\left(a^{i-1}x_i\right)^2\right)^{\frac{1}{2}}. \qquad (9)$$

By substituting Equation (9) into (7), the resulting equation in $a$ becomes

$$\frac{n(n-1)}{a} - \left(2n\sum_{i=1}^{n}(i-1)x_i^2 a^{2i-3}\right) \left(\sum_{i=1}^{n}\left(a^{i-1}x_i\right)^2\right)^{-1} = 0. \qquad (10)$$

These equations are simultaneously solved to yield the MLEs for $\hat{a}$ and $\hat{\lambda}$. Equation (10) must instead be solved iteratively because there are no explicit solutions to the equation. In this study, the Newton Rapson method is used.

Now, we built the asymptotically distribution of the MLEs. With a mean vector $(\mathrm{a},\lambda)$,and covariance $(I^{-1})$the joint distribution of $\hat{a}$ and $\hat{\lambda}$ is asymptotically normal (AN), thus,

$$\begin{pmatrix}\hat{a}\\ \hat{\lambda}\end{pmatrix} \sim AN\left(\begin{pmatrix}a\\ \lambda\end{pmatrix}, I^{-1}(\mathrm{a},\lambda)\right). \qquad (11)$$

Here $I(a,\lambda) = \left[I_{ij}\right]_{2x2}$ where is defined as the Fisher information matrix $I$ and is obtained as shown below:

$$I^{-1}(\mathrm{a},\lambda) = \begin{bmatrix} I_{11} & I_{12}\\ I_{21} & I_{22}\end{bmatrix} = \begin{bmatrix} -E\left(\frac{\partial^2 logL}{\partial^2 a}\right) & -E\left(\frac{\partial^2 logL}{\partial a\partial\lambda}\right)\\ -E\left(\frac{\partial^2 logL}{\partial\lambda\,\partial \mathrm{a}}\right) & -E\left(\frac{\partial^2 logL}{\partial^2\lambda}\right)\end{bmatrix}. \qquad (12)$$

Since $E\left(a^{i-1}X_i\right)^2 = 2\lambda^2$, the expected values of the second derivatives are calculated as follows:

$$I_{11} = \frac{-n(n-1)}{a^2} + \frac{1}{a^2\lambda^2}\sum_{i=1}^{n}(i-1)E\left(a^{i-1}X_i\right)^2$$
$$\frac{-2}{a^2\lambda^2}\sum_{i=1}^{n}(i-1)^2E\left(a^{i-1}X_i\right)^2 \approx \frac{4n^3}{3a^2},$$

$$I_{12} = \frac{-2}{a\lambda^3}\sum_{i=1}^{n}(i-1)E\left(a^{i-1}X_i\right)^2 \approx \frac{-2n^2}{a\lambda},$$

and

$$I_{22} = \frac{-2n}{\lambda^2} + \frac{3}{\lambda^4}\sum_{i=1}^{n}E\left(a^{i-1}X_i\right)^2 \approx \frac{4n}{\lambda^2}.$$

The symbol ≈ stands for “asymptotically equivalent”. Therefore, the asymptotic variance-covariance matrix of $\hat{a}$ and $\hat{\lambda}$ is obtained by $I^{-1}(\mathrm{a},\lambda)$,

$$I^{-1}(\mathrm{a},\lambda) = \begin{bmatrix} \frac{3a^2}{n^3} & \frac{3a\lambda}{2n^2}\\ \frac{3a\lambda}{2n^2} & \frac{\lambda^2}{n}\end{bmatrix}. \qquad (13)$$

Then, by using equation (11), the marginal asymptotic distribution of $\hat{a}$ and $\hat{\lambda}$ can be seen as

$$\hat{a}\sim AN\left(a,\frac{3a^2}{n^3}\right) \text{ and } \hat{\lambda}\sim \mathrm{AN}\left(\lambda,\frac{\lambda^2}{n}\right).$$

Thus, the all the proposed estimators are asymptotically unbiased. Furthermore, these estimators are also consistent because the asymptotic variance of each estimator goes to zero as n goes to infinity.

### 2.3. Bayesian Inference

The Bayesian estimation under the Lindley, M-Lindley, and Markov chain Monte Carlo (MCMC) approximation techniques based on the SELF of parameters $a$ and λ in GP with Rayleigh distribution is discussed in this section. The Bayesian estimation framework has drawn a lot of interest recently. A suitable loss function and prior distribution play a significant role in making the best decision in Bayesian parameter estimation. In line with this purpose, SELF is one of the widely used loss functions.

This loss function is obtained by the following

$$L_{SELF}\left(\hat{\lambda},\ \lambda\right) = \left(\hat{\lambda} - \lambda\right),^2 \qquad (14)$$

where $\hat{\lambda}$ is the estimate of the parameter λ, see [14].

Before seeing the new data, what was known or thought to be true is expressed by the prior distribution. It is assumed that λ has independent Gamma prior distribution in this study. The independent Gamma prior distribution is reasonable since it is flexible and appropriate. When the values of the hyper-parameters in the gamma prior are taken to be zero, the prior is non-informative. Several writers have employed independent gamma priors on the shape and scale parameters for lifespan distributions, see [15]-[16].

The prior distribution of the ratio parameter $a$ would be the uniform distribution since the parameter has bounded support. Consequently, the prior pdfs of parameters $a$ and λ, independent uniform, and gamma priors may be given as

$$\pi_1(a) = (\Phi_2 - \Phi_1)^{-1}$$

and

$$\pi_2(\lambda) = \frac{\beta^\alpha}{\Gamma(\alpha)} \lambda^{\alpha-1} e^{-\beta\lambda}.$$

Then, the joint prior pdfs of $a$ and $\lambda$ is given as

$$\pi(a,\lambda) = \pi_1(a)\pi_2(\lambda) =$$
$$(\Phi_2 - \Phi_1)^{-1} \frac{\beta^\alpha}{\Gamma(\alpha)} \lambda^{\alpha-1} e^{-\beta\lambda}. \quad (15)$$

Here, it is assumed that the hyper-parameters $(\alpha,\beta)$ and $(\Phi_1,\Phi_2)$ are known and positive.

Combining (5) with (15) and using Bayes theorem, the joint posterior density function of $a$ and $\lambda$ is given by:

$$\pi(a,\lambda|x) = \frac{L(a,\lambda;\mathrm{x})\pi(a,\lambda)}{\int\int(a,\lambda;\mathrm{x})\pi(a,\lambda)dad\lambda} \propto$$
$$\frac{a^{n(n-1)}}{(\Phi_2-\Phi_1)} \frac{\lambda^{\alpha-1-2n}}{e^{\beta\lambda}} \prod_{i=1}^{n} x_i e^{\frac{-\left(a^{i-1}x_i\right)^2}{2\lambda^2}}. \quad (16)$$

The marginal conditional posterior pdfs of $a$ and $\lambda$ are thus provided in Equation (16), $\pi_a(a|\lambda,\mathrm{x}) \propto$

$$\frac{a^{n(n-1)}}{(\Phi_2-\Phi_1)} \prod_{i=1}^{n} x_i e^{\frac{-\left(a^{i-1}x_i\right)^2}{2\lambda^2}}, \quad (17)$$

and

$$\pi_2(\lambda|a,\mathrm{x}) \propto \lambda^{\alpha-1-2n} e^{-\beta\lambda} \prod_{i=1}^{n} x_i e^{\frac{-\left(a^{i-1}x_i\right)^2}{2\lambda^2}}, \quad (18)$$

respectively. The EV of the conditional posterior pdfs shown in (17) and (18) provides the Bayes estimators for the parameters $a$ and $\lambda$. However, an explicit solution for the estimates does not yield by expected values of the conditional posterior pdfs. Therefore, we are taking into consideration the Lindley, M-Lindley, and MCMC techniques to compute the Bayes estimators of the parameters $a$ and $\lambda$ for GP with Rayleigh distribution. Summaries of these methods are given below.

### 2.4. Lindley Approximation

For calculating the ratio of the two integrals, Lindley [17] proposed an approximation method. This method may be used for calculating the posterior mean of an arbitrary function $u(a,\ \lambda)$, as shown below:

$$\hat{u} = E\big(u(a,\lambda|x)\big) = \frac{\int_0^\infty\int_0^\infty u(a,\lambda)\pi(a,\lambda)L(a,\lambda;\mathrm{x})dad\lambda}{\int_0^\infty\int_0^\infty \pi(a,\lambda)L(a,\lambda;\mathrm{x})dad\lambda}. \quad (19)$$

Here, $u(a,\lambda)$ is a function of $a$ and $\lambda$ only, $\pi(a,\lambda)$is the joint prior density function, $L(a,\lambda;\mathrm{x})$and is the likelihood function.

By using Lindley approximation, Equation (19) can be written by the following formula:

$$u \approx u(\hat{a},\hat{\lambda}) + 0.5[u_{11}\sigma_{11} + u_{22}\sigma_{22} + 2u_{12}\sigma_{12} + 2u_1(\sigma_{11}\rho_1 + \sigma_{21}\rho_2) + 2u_2(\sigma_{12}\rho_1 + \sigma_{22}\rho_2)] + 0.5\Big[L_{111}(u_1\sigma_{11}^2 + u_2\sigma_{11}\sigma_{12}) + L_{112}\left(3u_1\sigma_{11}\sigma_{12} + u_2(\sigma_{11}\sigma_{22} + 2\sigma_{12}^2)\right) + L_{122}(u_1(\sigma_{11}\sigma_{22} + 2\sigma_{12}^2) + 3u_2\sigma_{12}\sigma_{22}) + L_{222}(u_1\sigma_{12}\sigma_{22} + u_2\sigma_{22}^2)\Big]. \quad (20)$$

Here, $\hat{a}$ and $\hat{\lambda}$ are the MLEs of $a$ and $\lambda$ respectively.

$u_1 = \frac{\partial u(a,\lambda)}{\partial a}, u_{11} = \frac{\partial^2 u(a,\lambda)}{\partial a^2}, \quad u_2 \frac{\partial u(a,\lambda)}{\partial\lambda}, u_{22} = \frac{\partial^2 u(a,\lambda)}{\partial^2\lambda}, u_{12} = \frac{\partial^2 u(a,\lambda)}{\partial \mathrm{a}\partial\lambda}, \rho_1 = \frac{\partial In\pi(a,\lambda)}{\partial a},$

$\rho_2 = \frac{\partial In\pi(a,\lambda)}{\partial\lambda}, L_{111} = \frac{\partial^3 InL}{\partial^3 a}, L_{112} = \frac{\partial^3 InL}{\partial^2 a\partial\lambda}, L_{122} = \frac{\partial^3 InL}{\partial^2\lambda\partial\mathrm{a}}, \ L_{222} = \frac{\partial^3 InL}{\partial^3\lambda},$

and $\sigma_{ij}, i,j = 1{,}2$ are the elements of the inverse Fisher information matrix.

Hence, it follows from Equation (20) that the Bayes estimators of the parameters $a$ and $\lambda$, say $\hat{a}_L$ and $\hat{\lambda}_L$,are given:

If $u(a,\lambda) = a$,$\hat{u}_1 = 1, \hat{u}_{11} = \hat{u}_{12} = \hat{u}_2 = \hat{u}_{22} = 0$, then

$$\hat{a}_L = \hat{a} + \hat{\sigma}_{21}\hat{\rho}_2 + 0.5\left[\hat{L}_{111}\hat{\sigma}_{11}^2 + 3\hat{L}_{112}\hat{\sigma}_{11}\hat{\sigma}_{12} + \hat{L}_{122}\left((\hat{\sigma}_{11}\hat{\sigma}_{22} + 2\sigma_{12}^2)\right) + \hat{L}_{222}\hat{\sigma}_{12}\hat{\sigma}_{22}\right]. \quad (21)$$

If,$(a,\lambda) = \lambda, \hat{u}_2 = 1, \hat{u}_{22} = \hat{u}_{12} = \hat{u}_2 = \hat{u}_{11} = 0$, then

$$\hat{\lambda}_L = \hat{\lambda} + \hat{\sigma}_{22}\hat{\rho}_2 + 0.5\left[\hat{L}_{111}\hat{\sigma}_{11}\hat{\sigma}_{12} + \hat{L}_{112}(\hat{\sigma}_{11}\hat{\sigma}_{22} + 2\hat{\sigma}_{12}^2) + 3\hat{L}_{122}\hat{\sigma}_{11}\hat{\sigma}_{22} + \hat{L}_{222}\hat{\sigma}_{22}^2\right], \quad (22)$$

respectively.

Here,

$$\hat{L}_{111} = \frac{2n(n-1)}{\hat{a}^3} - \frac{2}{\hat{\lambda}^2\hat{a}^3}\sum_{i=1}^{n}\left(\hat{a}^{i-1}x_i\right)^2(i-1)(i-2)(2i-3)$$

$\hat{L}_{222} = \frac{-4n}{\hat{\lambda}^3} + \frac{12}{\hat{\lambda}^5}\sum_{i=1}^{n}\left(\hat{a}^{i-1}x_i\right)^2,$

$\hat{L}_{112} = \frac{2}{\hat{\lambda}^2\hat{a}^3}\sum_{i=1}^{n}\left(\hat{a}^{i-1}x_i\right)^2(i-1)(2i-3),$

$\hat{L}_{122} = \frac{-6}{\hat{a}\hat{\lambda}^4}\sum_{i=1}^{n}\left(\hat{a}^{i-1}x_i\right)^2(i-1),$

$\hat{\rho}_1 = 0, \ \hat{\rho}_2 = \frac{\alpha-1}{\hat{\lambda}} - \hat{\beta},$

and $\sigma_{ij}\ , i,j = 1{,}2$ are the elements of the variance-covariance matrix defined in Equation (13).

### 2.5 Modified-Lindley Approximation

In Lindley approximation, the Bayes estimators of $a$ and λ are obtained by incorporating all $\left(L_{ijk}\right)$into (21) and (22), respectively. However, in our case, it will be quite complicated. Therefore, we present the M-Lindley approximation as a novel approximation technique. The EVs of the terms in the expression $\left(L_{ijk}\right)$ form the basis of this approximation technique. In other words, $E\left(L_{ijk}\right)$ $(i,j,k=1,2,3)$ exists, it can be obtained under the M-Lindley approximation.

Therefore, if all of the L terms are available, Equation (20) can be estimated as follows:

$$\hat{u} \approx u(\hat{a},\hat{\lambda}) + 0.5[u_{11}\sigma_{11} + u_{22}\sigma_{22} + 2u_{12}\sigma_{12} + 2u_1(\sigma_{11}\rho_1 + \sigma_{21}\rho_2) + 2u_2(\sigma_{12}\rho_1 + \sigma_{22}\rho_2)] + 0.5\Big[E(L_{111})(u_1\sigma_{11}^2 + u_2\sigma_{11}\sigma_{12}) + E(L_{112})\Big(3u_1\sigma_{11}\sigma_{12} + u_2(\sigma_{11}\sigma_{22} + 2\sigma_{12}^2)\Big) + E(L_{122})(u_1(\sigma_{11}\sigma_{22} + 2\sigma_{12}^2) + 3u_2\sigma_{12}\sigma_{22}) + E(L_{222})(u_1\sigma_{12}\sigma_{22} + u_2\sigma_{22}^2)\Big], \tag{23}$$

where all the remaining terms will be the same as the Lindley approximation.

Hence, it follows from Equation (23) that the Bayes estimators of the parameters $a$ and λ, say $\hat{a}_{M-L}$ and $\hat{\lambda}_{M-L}$are given as follows:

If $u(a,\lambda)=a$, $\hat{u}_1=1, \hat{u}_{11}=\hat{u}_{12}=\hat{u}_2=\hat{u}_{22}=0$, then

$$\hat{a}_{M-L} = \hat{a} + \hat{\sigma}_{21}\hat{\rho}_2 + 0.5\Big[E(\hat{L}_{111})\hat{\sigma}_{11}^2 \; 3E(\hat{L}_{112})\hat{\sigma}_{11}\hat{\sigma}_{12} + \hat{L}_{122}\Big((\hat{\sigma}_{11}\hat{\sigma}_{22} + 2\sigma_{12}^2)\Big) + E(\hat{L}_{222})\hat{\sigma}_{12}\hat{\sigma}_{22}\Big],$$

If,$(a,\lambda)=\lambda, \hat{u}_2=1, \hat{u}_{22}=\hat{u}_{12}=\hat{u}_2=\hat{u}_{11}=0$, then

$$\hat{\lambda}_{M-L} = \hat{\lambda} + \hat{\sigma}_{22}\hat{\rho}_2 + 0.5\Big[E(\hat{L}_{111})\hat{\sigma}_{11}\hat{\sigma}_{12} + E(\hat{L}_{112})(\hat{\sigma}_{11}\hat{\sigma}_{22} + 2\hat{\sigma}_{12}^2) + 3E(\hat{L}_{122})\hat{\sigma}_{11}\hat{\sigma}_{22} + E(\hat{L}_{222})\hat{\sigma}_{22}^2\Big].$$

In our case, the Bayesian estimators of $a$ and λ using the M-Lindley approximation are derived as:

$\hat{a}_{M-L} = \hat{a} + \hat{\sigma}_{12}\hat{\rho}_2 + \frac{3\hat{a}}{2n^2}$ and

$\hat{\lambda}_{M-L} = \hat{\lambda} + \hat{\sigma}_{22}\hat{\rho}_2 + \frac{2\hat{\lambda}}{n}$.

Here,

$E(L_{111}) \approx \frac{-2n^4}{a^3}, E(L_{222}) = \frac{20n}{\lambda^3}$,

$E(L_{122}) \approx \frac{-6n^2}{a\lambda^2}$ and $E(L_{112}) \approx \frac{8n^3}{\lambda a^2}$,

$\sigma_{11}, \sigma_{12}, \sigma_{22}$ and $\rho_1, \rho_2$ will be the same as the Lindley approximation.

### 2.6 Markov Chain Monte Carlo Method

Here, the Gibbs sampling method is used to produce samples from the posterior distributions. It is a subclass of the MCMC, see [18]. We know that the posterior conditional density function of $a$ and λ is given as follows in Equations (17)-(18),

$$\pi_a(a|\lambda,\mathrm{x}) \propto \frac{a^{n(n-1)}}{(\Phi_2-\Phi_1)}\prod_{i=1}^{n} x_i e^{\frac{-\left(a^{i-1}x_i\right)^2}{2\lambda^2}} \text{ and}$$

$$\pi_\lambda(\lambda|\mathrm{a},\mathrm{x}) \propto \frac{\lambda^{\alpha-1-2n}}{e^{\beta\lambda}}\prod_{i=1}^{n} x_i e^{\frac{-\left(a^{i-1}x_i\right)^2}{2\lambda^2}} \;,$$

respectively. It is clear from these equations that the conditional density function of $a$ and λ cannot be found in the form the well-known density functions. So, we can use the Metropolis- Hasting (M-H) algorithm, introduced by Metropolis et al. [19], with normal proposal distribution to generate random samples from these distributions.

The steps of the Gibbs sampling method are as follows:

**Step1:** Start with an initial guess $a_0=\hat{a}$ and $\lambda_0=\hat{\lambda}$.

**Step2:** Set $j=1$.

**Step 3:** Using the M-H algorithm, generate a posterior sample for $a_0^{(j)}$and $\lambda_0^{(j)}$from Equations (17) and (18), respectively.

**Step 4:** Set $j=j+1$

**Step 5:** Repeat Step 3-4 N times and obtain MCMC sample as$(a_1,\lambda_1), \ldots, , (a_N,\lambda_N)$.

So, the Bayes estimator of the parameters $a$ and λ under SELF, say $\hat{a}_{MCMC}$ and, $\hat{\lambda}_{MCMC}$ are computed as follows:

$$\hat{a}_{MCMC} = \frac{1}{N}\sum_{i=1}^{N} a_j \text{and } \hat{\lambda}_{MCMC} = \frac{1}{N}\sum_{i=1}^{N} \lambda\,.$$

### 3. Simulation Study

In this Section, we carried out an extensive Monte Carlo simulation study to compare the performances of Bayesian and classical estimators with respect to mean, bias and mean square error (MSE) values for the different sample size. In the context of the Bayesian parameter estimation, two different informative priors are used. Firstly, we take $\alpha = 2, \beta = 1$ and $\Phi_2 = 1.5, \Phi_1 = 0.5$ and, call them Prior-I. Then we chose $\alpha = \beta = 0$ and $\Phi_2 = 1.5, \Phi_1 = 0.5$ and, call them Prior-II. The Bayesian estimators of the parameters $a$ and λ are calculated under SELF using the Lindley, M-Lindley, and MCMC approximation methods based on these priors. The ratio parameters are $a = 0.90, 0.95, 1.05$ and $1.10$ and the sample $n = 20, 30, 50, 100, 190$ are used in the simulation study. A sequence of random variables $\{Y_i,\ i = 1,2,\ldots\}$ each having Rayleigh distribution with the parameter λ is generated by using MATLAB2013. The data set $\{X_i,\ i = 1,2,\ldots\}$ then becomes a realization of the GP with ratio $a$ by the transformation $X_i = \frac{Y_i}{a^{i-1}}$. Since the simulation results are similar, the results are summarized only for $a = 0.90, 1.10$ and λ = 0.5, 0.8, 1 and 2. Additionally, the results obtained for n=190 are not added to the study because they are similar to the results obtained for n=100 in terms of bias and MSE. The mean, bias and MSE values of the estimators based on 2000 replications are given in Table 1-4.

The bias and MSE values are given as follows:

$Bias = \frac{1}{2000}\sum_{1=1}^{2000}\left(\hat{\theta}_i - \theta\right)$ and

$MSE = \frac{1}{2000}\sum_{1=1}^{2000}\left(\hat{\theta}_i - \theta\right).^2$

Here $\hat{\theta}_i$is the $ith$ simulated estimate of the parameter interest and θ is the true parameter value.

**Table1.** The mean and MSE values for the estimators of parameters a and λ when a=0.90,1.10 and λ=0.5.

| | | Prior-I | | | | | | | Prior-II | | | | | |
|---|---|---|---|---|---|---|---|---|---|---|---|---|---|---|
| | | $a$ | | | | λ | | | $a$ | | | λ | | |
| N | $a$ | Method | Mean | Bias | MSE | Mean | Bias | MSE | Mean | Bias | MSE | Mean | Bias | MSE |
| 20 | $a = 0.9$ | MLE | 0.90007 | 0.0007 | $3.1x10^{-4}$ | 0.5030 | -0.0030 | 0.0131 | 0.8999 | -0.0001 | $3.29x10^{-4}$ | 0.4973 | -0.0027 | 0.0124 |
| | | Lindley | 0.8957 | -0.0043 | $6.3x10^{-4}$ | 0.4980 | -0.0020 | 0.0125 | 0.8985 | -0.0005 | $6.55x10^{-4}$ | 0.4967 | -0.0033 | 0.0116 |
| | | M-Lindley | 0.8952 | -0.0048 | $7.2x10^{-4}$ | 0.4975 | -0.0035 | 0.0124 | 0.8987 | -0.0003 | $7.96x10^{-4}$ | 0.4961 | -0.0039 | 0.0116 |
| | | MCMC | 0.9005 | 0.0005 | $1.1x10^{-4}$ | 0.5022 | 0.0022 | 0.0032 | 0.9003 | 0.0003 | $8.80x10^{-5}$ | 0.5021 | 0.0021 | 0.0085 |
| 30 | | MLE | 0.8998 | -0.0002 | $9.63x10^{-5}$ | 0.4951 | -0.0049 | 0.0076 | 0.8999 | -0.0001 | $9.92x10^{-5}$ | 0.4951 | -0.0049 | 0.0076 |
| | | Lindley | 0.8996 | -0.0004 | $1.27x10^{-4}$ | 0.4981 | -0.0019 | 0.0079 | 0.8997 | -0.0003 | $1.26x10^{-4}$ | 0.4964 | -0.0036 | 0.0074 |
| | | M-Lindley | 0.8997 | -0.0003 | $1.42x10^{-4}$ | 0.4983 | -0.0017 | 0.0077 | 0.8998 | -0.0002 | $1.73x10^{-4}$ | 0.4966 | -0.0034 | 0.0074 |
| | | MCMC | 0.9000 | 0.0000 | $2.45x10^{-5}$ | 0.5032 | 0.0032 | 0.0056 | 0.8999 | -0.0001 | $2.43x10^{-5}$ | 0.5065 | 0.0065 | 0.0022 |
| 50 | | MLE | 0.8999 | -0.0001 | $1.88x10^{-5}$ | 0.4983 | -0.0017 | 0.0046 | 0.8999 | -0.0001 | $2.14x10^{-5}$ | 0.4981 | -0.0019 | 0.0046 |
| | | Lindley | 0.8998 | -0.0002 | $2.47x10^{-5}$ | 0.4989 | -0.0011 | 0.0047 | 0.8999 | -0.0001 | $3.41x10^{-5}$ | 0.4976 | -0.0024 | 0.0044 |
| | | M-Lindley | 0.8998 | -0.0002 | $2.61x10^{-5}$ | 0.4987 | -0.0013 | 0.0045 | 0.8999 | -0.0001 | $3.59x10^{-5}$ | 0.4974 | -0.0026 | 0.0045 |
| | | MCMC | 0.9000 | 0.0000 | $5.08x10^{-6}$ | 0.5018 | 0.0018 | 0.0033 | 0.9000 | 0.0000 | $5.08x10^{-6}$ | 0.5033 | 0.0033 | 0.0033 |
| 100 | | MLE | 0.9000 | 0.0000 | $2.33x10^{-6}$ | 0.4999 | -0.0001 | 0.0025 | 0.9001 | 0.0001 | $2.58x10^{-6}$ | 0.5024 | 0.0024 | 0.0026 |
| | | Lindley | 0.8999 | -0.0001 | $2.77x10^{-6}$ | 0.4997 | -0.0003 | 0.0020 | 0.9000 | 0.0000 | $3.36x10^{-6}$ | 0.5021 | 0.0021 | 0.0020 |
| | | M-Lindley | 0.8999 | -0.0001 | $2.81x10^{-6}$ | 0.4995 | -0.0005 | 0.0018 | 0.9000 | 0.0000 | $3.42x10^{-6}$ | 0.5021 | 0.0021 | 0.0018 |
| | | MCMC | 0.9000 | 0.0000 | $8.41x10^{-6}$ | 0.5011 | 0.0011 | 0.0012 | 0.9000 | 0.0000 | $8.03x10^{-6}$ | 0.5026 | 0.0026 | 0.0007 |
| 20 | $a = 1.1$ | MLE | 1.1004 | 0.0004 | $5.13x10^{-4}$ | 0.4989 | -0.0011 | 0.0116 | 1.1005 | 0.0005 | $5.01x10^{-4}$ | 0.4994 | -0.0006 | 0.0117 |
| | | Lindley | 1.0989 | -0.0011 | $5.87x10^{-4}$ | 0.4948 | -0.0042 | 0.0110 | 1.0987 | -0.0013 | $8.49x10^{-4}$ | 0.4894 | 0.0116 | 0.0116 |
| | | M-Lindley | 1.0987 | -0.0013 | $6.93x10^{-4}$ | 0.4934 | -0.0066 | 0.0111 | 1.0983 | -0.0017 | $1.17x10^{-4}$ | 0.4899 | 0.0101 | 0.0117 |
| | | MCMC | 1.1009 | 0.0009 | $1.34x10^{-4}$ | 0.5031 | 0.0031 | 0.0096 | 1.1004 | 0.0004 | $1.32x10^{-4}$ | 0.5075 | 0.0075 | 0.0083 |
| 30 | | MLE | 1.0999 | -0.0001 | $1.14x10^{-4}$ | 0.4993 | -0.0007 | 0.0088 | 1.1002 | 0.0002 | $1.42x10^{-4}$ | 0.5010 | 0.0010 | 0.0078 |
| | | Lindley | 1.0996 | -0.0004 | $1.82x10^{-4}$ | 0.4994 | -0.0006 | 0.0085 | 1.0997 | -0.0003 | $2.49x10^{-4}$ | 0.5011 | 0.0011 | 0.0074 |
| | | M-Lindley | 1.0997 | -0.0003 | $2.02x10^{-4}$ | 0.4996 | -0.0004 | 0.0080 | 1.0997 | -0.0003 | $2.78x10^{-4}$ | 0.5008 | 0.0008 | 0.0070 |
| | | MCMC | 1.0998 | -0.0002 | $3.67x10^{-5}$ | 0.5010 | 0.0010 | 0.0062 | 1.0998 | -0.0002 | $3.65x10^{-5}$ | 0.5005 | 0.0005 | 0.0052 |
| 50 | | MLE | 1.1002 | 0.0002 | $3.11x10^{-5}$ | 0.4995 | -0.0005 | 0.0051 | 1.1002 | 0.0002 | $3.25x10^{-5}$ | 0.5017 | 0.0017 | 0.0050 |
| | | Lindley | 1.0998 | -0.0002 | $3.82x10^{-5}$ | 0.4996 | -0.0004 | 0.0049 | 1.0998 | -0.0002 | $4.66x10^{-5}$ | 0.5008 | 0.0008 | 0.0048 |
| | | M-Lindley | 1.0999 | -0.0001 | $4.00x10^{-5}$ | 0.4997 | -0.0003 | 0.0048 | 1.0999 | -0.0001 | $4.89x10^{-5}$ | 0.5006 | 0.0006 | 0.0045 |
| | | MCMC | 1.1002 | 0.0002 | $7.69x10^{-6}$ | 0.4998 | -0.0002 | 0.0032 | 1.1003 | 0.0003 | $8.10x10^{-6}$ | 0.5018 | 0.0018 | 0.0034 |
| 100 | | MLE | 1.1000 | 0.0000 | $3.69x10^{-6}$ | 0.5002 | 0.0002 | 0.0024 | 1.1000 | 0.0000 | $3.92x10^{-6}$ | 0.5002 | 0.0002 | 0.0024 |
| | | Lindley | 1.0998 | -0.0002 | $4.54x10^{-6}$ | 0.5006 | 0.0006 | 0.0020 | 1.0998 | -0.0002 | $5.18x10^{-6}$ | 0.5001 | 0.0001 | 0.0020 |
| | | M-Lindley | 1.0997 | -0.0003 | $4.61x10^{-6}$ | 0.5005 | 0.0005 | 0.0018 | 1.0999 | -0.0001 | $5.27x10^{-6}$ | 0.5000 | 0.0000 | 0.0020 |
| | | MCMC | 1.1001 | 0.0001 | $5.91x10^{-6}$ | 0.5008 | 0.0008 | 0.0013 | 1.1000 | 0.0000 | $6.83x10^{-6}$ | 0.5001 | 0.0001 | 0.0017 |

**Table2.** The mean and MSE values for the estimators of parameters a and λ when a=0.90,1.10 and λ=0.8.

| | | Prior-I | | | | | | | Prior-II | | | | | |
|---|---|---|---|---|---|---|---|---|---|---|---|---|---|---|
| | | $a$ | | | | λ | | | $a$ | | | λ | | |
| n | a | Method | Mean | Bias | MSE | Mean | Bias | MSE | Mean | Bias | MSE | Mean | Bias | MSE |
| 20 | $a = 0.9$ | MLE | 0.90007 | 0.0007 | $3.17x10^{-4}$ | 0.7984 | -0.0016 | 0.0286 | 0.9002 | 0.0002 | $3.26x10^{-4}$ | 0.7972 | -0.0028 | 0.0304 |
| | | Lindley | 0.8950 | -0.0050 | $5.47x10^{-4}$ | 0.7965 | -0.0035 | 0.0270 | 0.8988 | -0.0012 | $5.25x10^{-4}$ | 0.7941 | -0.0059 | 0.0297 |
| | | M-Lindley | 0.8951 | -0.0049 | $7.24x10^{-4}$ | 0.7956 | -0.0044 | 0.0270 | 0.8981 | -0.0019 | $5.56x10^{-4}$ | 0.7955 | -0.0045 | 0.0298 |
| | | MCMC | 0.9004 | 0.0004 | $9.27x10^{-5}$ | 0.8030 | 0.0030 | 0.0194 | 0.9002 | 0.0002 | $7.70x10^{-5}$ | 0.8037 | 0.0037 | 0.0190 |
| 30 | | MLE | 0.9001 | 0.0001 | $9.28x10^{-5}$ | 0.7964 | -0.0036 | 0.0199 | 0.9001 | 0.0001 | $8.93x10^{-5}$ | 0.7985 | -0.0015 | 0.0200 |
| | | Lindley | 0.8982 | -0.0008 | $1.38x10^{-4}$ | 07962 | -0.0038 | 0.0196 | 0.8993 | -0.0007 | $1.74x10^{-4}$ | 0.7983 | -0.0017 | 0.0199 |
| | | M-Lindley | 0.8989 | -0.0001 | $1.57x10^{-4}$ | 0.7962 | -0.0038 | 0.0196 | 0.8991 | -0.0009 | $1.74x10^{-4}$ | 0.7975 | -0.0025 | 0.0199 |
| | | MCMC | 0.9000 | 0.0000 | $2.51x10^{-5}$ | 0.8018 | 0.0018 | 0.0159 | 0.9003 | 0.0003 | $2.44x10^{-5}$ | 0.8034 | 0.0034 | 0.0157 |
| 50 | | MLE | 0.8998 | -0.0002 | $2.06x10^{-5}$ | 0.8058 | 0.0058 | 0.0136 | 0.8999 | -0.0001 | $2.15x10^{-5}$ | 0.7976 | -0.0024 | 0.0131 |
| | | Lindley | 0.8995 | -0.0005 | $2.62x10^{-5}$ | 0.8048 | 0.0048 | 0.0135 | 0.8996 | -0.0004 | $3.4510^{-5}$ | 0.7963 | -0.0037 | 0.0130 |
| | | M-Lindley | 0.8994 | -0.0006 | $2.76x10^{-5}$ | 0.8046 | 0.0046 | 0.0135 | 0.8994 | -0.0006 | $3.64x10^{-5}$ | 0.7961 | -0.0039 | 0.0130 |
| | | MCMC | 0.8998 | -0.0002 | $5.45x10^{-6}$ | 0.8029 | 0.0029 | 0.0128 | 0.9000 | 0.0000 | $5.06x10^{-6}$ | 0.8011 | 0.0011 | 0.0120 |
| 100 | | MLE | 0.8999 | -0.0001 | $2.45x10^{-6}$ | 0.8001 | 0.0001 | 0.0059 | 0.8999 | -0.0001 | $2.40x10^{-6}$ | 0.7973 | -0.0027 | 0.0064 |
| | | Lindley | 0.8999 | -0.0001 | $3.05x10^{-6}$ | 08004 | 0.0004 | 0.0058 | 0.8997 | -0.0003 | $3.37x10^{-6}$ | 0.7979 | -0.0021 | 0.0060 |
| | | M-Lindley | 0.8999 | -0.0001 | $3.08x10^{-6}$ | 07995 | 0.0005 | 0.0058 | 0.8997 | -0.0003 | $3.44x10^{-6}$ | 0.7981 | -0.0019 | 0.0060 |
| | | MCMC | 0.9000 | 0.0000 | $8.03x10^{-6}$ | 0.8005 | 0.0005 | 0.0037 | 0.9000 | 0.0000 | $8.13x10^{-6}$ | 0.8004 | 0.0004 | 0.0038 |
| 20 | | MLE | 1.1003 | 0.0003 | $4.82x10^{-4}$ | 0.7979 | -0.0021 | 0.0300 | 1.0990 | -0.0010 | $5.52x10^{-4}$ | 0.7915 | -0.0085 | 0.0328 |
| | | Lindley | 1.0953 | -0.0047 | $6.92x10^{-4}$ | 0.7936 | -0.0064 | 0.0290 | 1.0987 | -0.0013 | $8.31x10^{-4}$ | 0.7923 | -0.0077 | 0.0314 |

| | | | | | | | | | | | | | | |
|---|---|---|---|---|---|---|---|---|---|---|---|---|---|---|
| | | M-Lindley | 1.0955 | -0.0045 | $8.64x10^{-4}$ | 0.7901 | -0.0099 | 0.0290 | 1.0989 | -0.0011 | $9.73x10^{-4}$ | 0.7916 | -0.0084 | 0.0317 |
| | | MCMC | 1.0994 | 0.0006 | $1.29x10^{-4}$ | 0.8104 | 0.0104 | 0.0189 | 1.0988 | -0.0012 | $1.73x10^{-4}$ | 0.7923 | -0.0067 | 0.0104 |
| 30 | $a = 1.1$ | MLE | 1.0997 | -0.0003 | $1.41x10^{-4}$ | 0.7997 | -0.0023 | 0.0211 | 1.1005 | 0.0005 | $1.47x10^{-4}$ | 0.8039 | 0.0039 | 0.0215 |
| | | Lindley | 1.0979 | -0.0021 | $2.04x10^{-4}$ | 0.7980 | -0.0020 | 0.0206 | 1.0998 | -0.0002 | $2.44x10^{-4}$ | 0.7992 | -0.0008 | 0.0213 |
| | | M-Lindley | 1.0974 | -0.0026 | $2.31x10^{-4}$ | 0.7970 | -0.0030 | 0.0206 | 1.0997 | -0.0003 | $2.72x10^{-4}$ | 0.7982 | -0.0018 | 0.0213 |
| | | MCMC | 1.0999 | -0.0001 | $3.79x10^{-5}$ | 0.8080 | 0.0080 | 0.0161 | 1.1001 | 0.0001 | $3.70x10^{-5}$ | 0.8053 | 0.0053 | 0.0055 |
| 50 | | MLE | 1.0999 | -0.0001 | $3.19x10^{-5}$ | 0.7982 | -0.0018 | 0.0128 | 1.0998 | -0.0002 | $3.13x10^{-5}$ | 0.7986 | - 0.0014 | 0.0133 |
| | | Lindley | 1.0997 | -0.0003 | $4.21x10^{-5}$ | 0.7975 | -0.0025 | 0.0127 | 1.0998 | -0.0002 | $5.44x10^{-5}$ | 0.7973 | -0.0027 | 0.0132 |
| | | M-Lindley | 1.0994 | -0.0006 | $4.43x10^{-5}$ | 0.7977 | -0.0023 | 0.0127 | 1.0997 | -0.0003 | $5.75x10^{-5}$ | 0.7981 | -0.0019 | 0.0132 |
| | | MCMC | 1.1002 | 0.0002 | $7.85x10^{-6}$ | 0.8030 | 0.0030 | 0.0083 | 1.1000 | 0.0000 | $7.80x10^{-6}$ | 0.8019 | 0.0019 | 0.0088 |
| 100 | | MLE | 1.1000 | 0.0000 | $3.60x10^{-6}$ | 0.7990 | 0.0063 | 0.0024 | 1.1000 | 0.0000 | $3.87x10^{-6}$ | 0.7998 | -0.0002 | 0.0064 |
| | | Lindley | 1.0998 | -0.0002 | $4.37x10^{-6}$ | 0.7988 | 0.0063 | 0.0020 | 1.0999 | -0.0001 | $5.14x10^{-6}$ | 0.7994 | -0.0006 | 0.0060 |
| | | M-Lindley | 1.0997 | -0.0003 | $4.46x10^{-6}$ | 0.7987 | 0.0062 | 0.0018 | 1.0999 | -0.0001 | $5.23x10^{-6}$ | 0.7993 | -0.0007 | 0.0059 |
| | | MCMC | 1.1001 | 0.0001 | $6.43x10^{-6}$ | 0.8017 | 0.0047 | 0.0013 | 1.1000 | 0.0000 | $6.08x10^{-6}$ | 0.7995 | -0.0005 | 0.0035 |

**Table3.** The mean and MSE values for the estimators of parameters a and λ when a=0.90,1.10 and λ=1.

| | | | Prior-I | | | | | | Prior-II | | | | | |
|---|---|---|---|---|---|---|---|---|---|---|---|---|---|---|
| | | | $a$ | | | λ | | | $a$ | | | λ | | |
| n | a | Method | Bias | Mean | MSE | Bias | Mean | MSE | Bias | Mean | MSE | Bias | Mean | MSE |
| 20 | a=0.9 | MLE | 0.8998 | -0.0002 | $3.42x10^{-4}$ | 0.9902 | 0.0098 | 0.0513 | 0.9005 | 0.0005 | $3.46x10^{-4}$ | 1.0058 | 0.0058 | 0.0507 |
| | | Lindley | 0.8996 | -0.0004 | $5.71x10^{-4}$ | 0.9866 | -0.0134 | 0.0499 | 0.8988 | -0.0002 | $7.51x10^{-4}$ | 1.0029 | 0.0029 | 0.0494 |
| | | M-Lindley | 0.8997 | -0.0003 | $7.33x10^{-4}$ | 0.9895 | 0.0115 | 0.0499 | 0.8986 | -0.0004 | $9.22x10^{-4}$ | 0.9982 | -0.0018 | 0.0493 |
| | | MCMC | 0.9003 | 0.0003 | $8.91x10^{-5}$ | 1.0122 | 0.0122 | 0.0343 | 0.9907 | 0.0007 | $9.27x10^{-5}$ | 1.0039 | 0.0039 | 0.0343 |
| 30 | | MLE | 0.9007 | 0.0007 | $9.58x10^{-5}$ | 1.0060 | 0.0060 | 0.0298 | 0.8999 | -0.0001 | $1.51x10^{-4}$ | 0.9956 | -0.0044 | 0.0314 |
| | | Lindley | 0.8998 | -0.0002 | $1.55x10^{-4}$ | 1.0025 | 0.0025 | 0.0295 | 0.8995 | -0.0005 | $2.62x10^{-4}$ | 0.9967 | -0.0033 | 0.0309 |
| | | M-Lindley | 0.8996 | -0.0004 | $1.77x10^{-4}$ | 1.0016 | 0.0016 | 0.0293 | 0.8994 | -0.0006 | $2.94x10^{-4}$ | 0.9968 | -0.0032 | 0.0309 |
| | | MCMC | 0.9005 | 0.0005 | $3.14x10^{-5}$ | 1.0013 | 0.0013 | 0.0207 | 0.8999 | -0.0001 | $4.64x10^{-4}$ | 1.0109 | 0.0109 | 0.0278 |
| 50 | | MLE | 0.9001 | 0.0001 | $1.70x10^{-5}$ | 1.0046 | 0.0046 | 0.0190 | 0.8998 | -0.0002 | $1.84x10^{-5}$ | 0.9960 | -0.0040 | 0.0192 |
| | | Lindley | 0.8999 | -0.0001 | $2.33x10^{-5}$ | 1.0028 | 0.0028 | 0.0189 | 0.8997 | -0.0003 | $2.71x10^{-5}$ | 0.9970 | -0.0030 | 0.0180 |
| | | M-Lindley | 0.8998 | -0.0002 | $2.35x10^{-5}$ | 1.0026 | 0.0026 | 0.0182 | 0.8997 | -0.0003 | $2.90x10^{-5}$ | 0.9973 | -0.0027 | 0.0171 |
| | | MCMC | 0.9000 | 0.0000 | $8.58x10^{-6}$ | 1.0028 | 0.0028 | 0.0150 | 0.8998 | -0.0002 | $4.81x10^{-5}$ | 0.9986 | -0.0014 | 0.0146 |
| 100 | | MLE | 0.9000 | 0.0000 | $2.41x10^{-6}$ | 0.9974 | -0.0026 | 0.0102 | 0.8999 | -0.0001 | $3.84x10^{-6}$ | 0.9989 | -0.0011 | 0.0097 |
| | | Lindley | 0.8999 | -0.0001 | $2.53x10^{-6}$ | 0.9970 | -0.0030 | 0.0080 | 0.8999 | -0.0001 | $3.95x10^{-6}$ | 0.9986 | -0.0024 | 0.0095 |
| | | M-Lindley | 0.8999 | -0.0001 | $2.57x10^{-6}$ | 0.9973 | -0.0027 | 0.0075 | 0.8999 | -0.0001 | $4.01x10^{-6}$ | 0.9988 | -0.0012 | 0.0093 |
| | | MCMC | 0.9001 | 0.0001 | $7.29x10^{-6}$ | 1.0010 | 0.0010 | 0.0066 | 0.9001 | 0.0001 | $7.52x10^{-6}$ | 0.9990 | -0.0010 | 0.0065 |
| 20 | a=1.1 | MLE | 1.0995 | 0.0005 | $5.69x10^{-4}$ | 0.9864 | -0.0136 | 0.0473 | 1.1001 | 0.0001 | $4.87x10^{-5}$ | 0.9853 | -0.0147 | 0.0457 |
| | | Lindley | 1.0988 | -0.0012 | $8.49x10^{-4}$ | 0.9829 | 0.0171 | 0.0457 | 1.0996 | -0.0004 | $9.56x10^{-4}$ | 0.9886 | -0.0114 | 0.0445 |
| | | M-Lindley | 1.0984 | -0.0016 | $7.37x10^{-4}$ | 0.9793 | -0.0207 | 0.0457 | 1.0994 | -0.0006 | $9.22x10^{-4}$ | 0.9854 | -0.0116 | 0.0445 |
| | | MCMC | 1.0992 | -0.0008 | $1.28x10^{-4}$ | 1.0127 | 0.0127 | 0.0320 | 1.0102 | 0.0002 | $1.42x10^{-5}$ | 1.0101 | 0.0102 | 0.0340 |
| 30 | | MLE | 1.0998 | -0.0002 | $9.67x10^{-5}$ | 0.9982 | -0.0018 | 0.0324 | 1.0998 | -0.0002 | $3.68x10^{-5}$ | 0.9969 | -0.0031 | 0.0319 |
| | | Lindley | 1.0997 | -0.0003 | $1.75x10^{-4}$ | 0.9989 | -0.0011 | 0.0290 | 1.0997 | -0.0003 | $5.18x10^{-5}$ | 0.9967 | -0.0033 | 0.0315 |
| | | M-Lindley | 1.0997 | -0.0003 | $2.00x10^{-4}$ | 0.9980 | -0.0020 | 0.0285 | 1.0996 | -0.0004 | $5.38x10^{-5}$ | 0.9964 | -0.0036 | 0.0312 |
| | | MCMC | 1.0996 | -0.0004 | $3.76x10^{-5}$ | 0.9983 | -0.0017 | 0.0184 | 1.0998 | -0.0002 | $1.08x10^{-5}$ | 1.0034 | 0.0034 | 0.0285 |
| 50 | | MLE | 1.1002 | 0.0002 | $2.10x10^{-5}$ | 1.0060 | 0.0060 | 0.0212 | 1.0999 | -0.0001 | $3.57x10^{-5}$ | 1.0036 | 0.0036 | 0.0194 |
| | | Lindley | 1.0986 | -0.0014 | $3.42x10^{-5}$ | 1.0046 | 0.0046 | 0.0180 | 1.0998 | -0.0002 | $5.27x10^{-5}$ | 0.9985 | -0.0015 | 0.0190 |
| | | M-Lindley | 1.0987 | -0.0013 | $3.68x10^{-5}$ | 1.0044 | 0.0044 | 0.0176 | 1.0998 | -0.0002 | $5.43x10^{-5}$ | 0.9987 | -0.0013 | 0.0188 |
| | | MCMC | 1.1001 | 0.0001 | $6.27x10^{-6}$ | 1.0033 | 0.0033 | 0.0157 | 1.0999 | -0.0001 | $1.03x10^{-5}$ | 1.0030 | 0.0030 | 0.0155 |
| 100 | | MLE | 1.1000 | 0.0000 | $3.46x10^{-6}$ | 0.9969 | -0.0031 | 0.0100 | 1.1001 | 0.0001 | $3.80x10^{-6}$ | 1.0027 | 0.0027 | 0.0107 |
| | | Lindley | 1.0998 | -0.0002 | $3.53x10^{-6}$ | 0.9966 | -0.0034 | 0.0096 | 1.0999 | -0.0001 | $4.87x10^{-6}$ | 1.0024 | 0.0024 | 0.0096 |
| | | M-Lindley | 1.0998 | -0.0002 | $3.60x10^{-6}$ | 0.9966 | -0.0034 | 0.0094 | 1.0999 | -0.0001 | $4.96x10^{-6}$ | 1.0022 | 0.0022 | 0.0094 |
| | | MCMC | 1.1000 | 0.0000 | $8.53x10^{-6}$ | 0.9970 | -0.0030 | 0.0086 | 1.1000 | 0.0000 | $6.47x10^{-6}$ | 1.0018 | 0.0018 | 0.0069 |

**Table 4**. The mean and MSE values for the estimators of parameters a and λ when a=0.90,1.10 and λ=2.

| | | | Prior-I | | | | | | Prior-II | | | | | |
|---|---|---|---|---|---|---|---|---|---|---|---|---|---|---|
| | | | $a$ | | | λ | | | $a$ | | | λ | | |
| n | | Method | Mean | Bias | MSE | Mean | Bias | MSE | Mean | Bias | MSE | Mean | Bias | MSE |
| 20 | $a = 0.9$ | MLE | 0.8995 | -0.0005 | $3.52x10^{-4}$ | 1.9794 | -0.0206 | 0.2006 | 0.9010 | 0.0010 | $2.91x10^{-4}$ | 2.0126 | 0.0126 | 0.1760 |
| | | Lindley | 0.8997 | -0.0003 | $7.99x10^{-4}$ | 1.9712 | -0.0288 | 0.1990 | 0.8995 | -0.0005 | $7.32x10^{-4}$ | 2.0063 | 0.0063 | 0.1743 |
| | | M-Lindley | 0.8998 | -0.0002 | $6.94x10^{-4}$ | 1.9680 | -0.0320 | 0.1991 | 0.8989 | -0.0011 | $9.42x10^{-4}$ | 2.0033 | 0.0033 | 0.1740 |
| | | MCMC | 0.8999 | -0.0001 | $8.40x10^{-5}$ | 2.0169 | 0.0169 | 0.1473 | 0.9009 | 0.0009 | $9.29x10^{-5}$ | 2.0024 | 0.0024 | 0.1530 |
| 30 | | MLE | 0.8998 | -0.0002 | $8.86x10^{-5}$ | 1.9886 | -0.0114 | 0.1291 | 0.9005 | 0.0005 | $8.48x10^{-5}$ | 2.0114 | 0.0114 | 0.1251 |
| | | Lindley | 0.8997 | -0.0003 | $1.44x10^{-4}$ | 1.9847 | -0.0153 | 0.1288 | 0.8997 | -0.0003 | $1.91x10^{-5}$ | 2.0050 | 0.0050 | 0.1244 |
| | | M-Lindley | 0.8994 | -0.0006 | $1.65x10^{-4}$ | 1.9839 | -0.0161 | 0.1275 | 0.8997 | -0.0003 | $2.33x10^{-5}$ | 2.0041 | 0.0041 | 0.1243 |
| | | MCMC | 0.8999 | -0.0001 | $2.36x10^{-5}$ | 2.0153 | 0.0153 | 0.1153 | 0.9006 | 0.0006 | $2.70x10^{-5}$ | 2.0029 | 0.0029 | 0.1129 |
| 50 | | MLE | 0.9001 | 0.0001 | $2.26x10^{-5}$ | 2.0047 | 0.0047 | 0.0808 | 0.8999 | -0.0001 | $2.15x10^{-5}$ | 1.9945 | -0.0055 | 0.0754 |
| | | Lindley | 0.8998 | -0.0002 | $3.09x10^{-5}$ | 2.0034 | 0.0034 | 0.0806 | 0.8999 | -0.0001 | $3.42x10^{-5}$ | 1.9920 | -0.0080 | 0.0752 |
| | | M-Lindley | 0.8998 | -0.0002 | $3.29x10^{-5}$ | 2.0033 | 0.0033 | 0.0805 | 0.8999 | -0.0001 | $3.59x10^{-5}$ | 19919 | -0.0081 | 0.0752 |
| | | MCMC | 0.9000 | 0.0000 | $6.45x10^{-6}$ | 2.0056 | 0.0056 | 0.0607 | 0.9000 | 0.0000 | $4.72x10^{-5}$ | 1.9970 | -0.0030 | 0.0686 |
| 100 | | MLE | 0.9000 | 0.0000 | $1.96x10^{-6}$ | 1.9989 | -0.0011 | 0.0404 | 0.9001 | 0.0001 | $3.08x10^{-6}$ | 2.0020 | 0.0020 | 0.0408 |
| | | Lindley | 0.8999 | -0.0001 | $3.02x10^{-6}$ | 1.9992 | -0.0008 | 0.0400 | 0.9000 | 0.0000 | $3.83x10^{-6}$ | 2.0014 | 0.0014 | 0.0405 |
| | | M-Lindley | 0.8999 | -0.0001 | $3.08x10^{-6}$ | 1.9993 | -0.0007 | 0.0398 | 0.9000 | 0.0000 | $3.89x10^{-6}$ | 2.0013 | 0.0013 | 0.0405 |
| | | MCMC | 0.9000 | 0.0000 | $9.77x10^{-6}$ | 1.9990 | -0.0010 | 0.0299 | 0.9000 | 0.0000 | $9.70x10^{-6}$ | 2.0008 | 0.0008 | 0.0389 |
| 20 | $a = 1.1$ | MLE | 1.1002 | 0.0002 | $2.56x10^{-4}$ | 1.9889 | -0.0111 | 0.1844 | 1.0995 | -0.0005 | $5.52x10^{-4}$ | 1.9848 | -0.0152 | 0.2161 |
| | | Lindley | 1.0990 | -0.0010 | $6.52x10^{-4}$ | 1.9790 | -0.0210 | 0.1825 | 1.0994 | -0.0006 | $2.56x10^{-3}$ | 1.9822 | -0.0178 | 0.2115 |
| | | M-Lindley | 1.0988 | -0.0009 | $8.80x10^{-4}$ | 1.9773 | -0.0227 | 0.1826 | 1.0993 | -0.0007 | $1.26x10^{-3}$ | 1.9794 | -0.0206 | 0.2112 |
| | | MCMC | 1.0993 | -0.0007 | $8.74x10^{-4}$ | 2.0121 | 0.0121 | 0.1479 | 1.0999 | -0.0001 | $1.17x10^{-4}$ | 2.0163 | 0.0163 | 0.1488 |
| 30 | | MLE | 1.1002 | 0.0002 | $4.66x10^{-5}$ | 1.9963 | -0.0037 | 0.1309 | 1.1003 | 0.0003 | $1.10x10^{-4}$ | 1.9843 | -0.0152 | 0.1214 |
| | | Lindley | 1.0997 | -0.0003 | $2.10x10^{-4}$ | 1.9966 | -0.0034 | 0.1307 | 1.0996 | -0.0004 | $1.52x10^{-4}$ | 1.9802 | -0.0198 | 0.1204 |
| | | M-Lindley | 1.0996 | -0.0004 | $2.75x10^{-4}$ | 1.9964 | -0.0036 | 0.1306 | 1.0997 | -0.0003 | $1.68x10^{-4}$ | 1.9799 | -0.0201 | 0.1196 |
| | | MCMC | 1.1002 | 0.0002 | $4.66x10^{-5}$ | 2.0030 | 0.0030 | 0.1250 | 1.1002 | 0.0002 | $3.30x10^{-4}$ | 2.0130 | 0.0130 | 0.1080 |
| 50 | | MLE | 1.1000 | 0.0000 | $3.08x10^{-5}$ | 2.0011 | 0.0011 | 0.0798 | 1.1000 | 0.0000 | $1.80x10^{-5}$ | 1.9972 | -0.0028 | 0.0799 |
| | | Lindley | 1.0954 | -0.0046 | $5.10x10^{-5}$ | 1.9984 | -0.0016 | 0.0797 | 1.0999 | -0.0001 | $2.94x10^{-5}$ | 1.9978 | -0.0022 | 0.0796 |
| | | M-Lindley | 1.0950 | -0.0050 | $5.36x10^{-5}$ | 1.9982 | -0.0018 | 0.0795 | 1.0998 | -0.0002 | $3.14x10^{-5}$ | 1.9976 | -0.0024 | 0.0789 |
| | | MCMC | 1.1000 | 0.0000 | $1.06x10^{-5}$ | 2.0019 | 0.0019 | 0.0609 | 1.1001 | 0.0001 | $4.96x10^{-5}$ | 2.0020 | 0.0020 | 0.0693 |

| | | | | | | | | | | | | | |
|---|---|---|---|---|---|---|---|---|---|---|---|---|---|
| 100 | | MLE | 1.1000 | 0.0000 | $6.16x10^{-6}$ | 1.9976 | -0.0024 | 0.0383 | 1.1001 | 0.0001 | $3.89x10^{-6}$ | 2.0053 | 0.0053 | 0.0411 |
| | | Lindley | 1.0999 | -0.0001 | $8.15x10^{-6}$ | 1.9971 | -0.0029 | 0.0380 | 1.0999 | -0.0001 | $3.37x10^{-6}$ | 2.0049 | 0.0049 | 0.0393 |
| | | M-Lindley | 1.0998 | -0.0002 | $8.31x10^{-6}$ | 1.9970 | -0.0030 | 0.0377 | 1.0999 | -0.0001 | $3.43x10^{-6}$ | 2.0043 | 0.0043 | 0.0390 |
| | | MCMC | 1.1002 | 0.0002 | $6.06x10^{-6}$ | 1.9988 | -0.0012 | 0.0298 | 1.1000 | 0.0000 | $6.87x10^{-6}$ | 2.0040 | 0.0040 | 0.0300 |

The following conclusions can be drawn from the Monte Carlo simulation.

- As the sample size increases, bias and MSE values decrease in most of the cases. This is an expected case because all estimators are asymptotically unbiased and consistent as given in Section 2.
- When the proposed Bayesian Methods and the MLEs are compared, Bayesianmethods have smaller bias and MSE values for estimating parameters $a$ and λ the most of the cases.
- Considering Bayesian methods, the performance of the MCMC approximation method is generally demonstrated slightly better than Lindley and M-Lindley approximation methods in the case. Also, the performances of Lindley and M-Lindley approximation methods under both Prior-I and Prior-II are more or less the same with respect to bias and MSE values in all cases. When Prior-I and Prior-II are compared, Prior-II is somewhat more efficient.

## 4. Application

In this Section, we take a real data set from the literature to apply the proposed methods. This data set is about coal mining disaster data. It is found in Andrews and Herzberg [20]. The 190 observations in the data set demonstrate the days between successive disasters in Great Britain, see [21]. Moreover, Biçer et al. [10] analyzed the same data set for the Rayleigh distribution. They obtained that the $a$ ration parameter is less than 1 and the data set consists with a GP. They showed with the $Z^*$ test statistic ($Z^* = 1.0049, p - value$ =0.8938) that this data set is appropriate with the Rayleigh distribution. For more details about $Z^*$ test statistic, see Tiku [22]. Additionally we use Anderson-Darling (A-D) test statistic ($A - D = 0.2414, p - value = 0.7368$) to test whether the data set is fit with Rayleigh distribution. These test results on whether the coal mining disaster data set is suitable for the Rayleigh geometric process. Therefore, this data set can be modeled with GP. We have the same result as other authors who analyzed this data set. However, they are only considered classical parameter estimators. In our study, in addition to the classical parameter estimation, the proposed Bayesian parameter estimators are also taken consideration into for the Rayleigh distribution. The MLEs and Bayesian estimators of the parameters $a$ and λ by using MLE, Lindley, M-Lindley, and MCMC approximation methods are given in Table 5.

**Table 5**. Estimation of parameters the time between failure times of a coal mining disaster data

| | Prior-I | | Prior-II | |
|---|---|---|---|---|
| Method | $\hat{a}$ | $\hat{\lambda}$ | $\hat{a}$ | $\hat{\lambda}$ |
| MLE | 0.9916 | 91.2931 | 0. 9916 | 91.2931 |
| Lindley | 0.9923 | 92.3196 | 0.9887 | 93.3755 |
| M-Lindley | 0.9920 | 91.7736 | 0.9880 | 94.8301 |
| MCMC | 0.9936 | 91.0412 | 1.0102 | 92.4682 |

There are some differences among the estimators even though they are close to one another. We select the most appropriate estimators using the simulation results provided in Section 3. We observed in simulation that the estimators obtained by MCMC method outperform the others. For this reason, in these examples, we recommend using MCMC estimators.

## 5. Results and Discussion

Here, MLEs and Bayesian parameter estimation methods for GP are discussed, assuming that the distribution of the first occurrence time is Rayleigh with the scale parameter λ. As far as we know, this is the first study to compare Bayesian and classical parameter estimation methods. The asymptotic distributions of the MLEs are also constructed. These features are very useful for practitioners. Bayesian estimators under Prior-I and Prior-II based on SELF are considered. In Bayesian computation, Lindley and MCMC approximation methods are used. We also proposed the M-Lindley approximation as an alternative to the Lindley approximation. We conducted a simulation study to evaluate the performance of these methods. It is clear from the simulation study that the M-Lindley approximation is very close to the Lindley approximation in terms of bias and MSE values. Additionally, the MCMC approximation has slightly better performance than the Lindley and M-Lindley approximations in terms of bias and

MSE values. Therefore, considering the computational difficulties, we propose to use the M-Lindley and MCMC approximations instead of the Lindley and MLEs methods.

**Conflict of Interest Statement**

There is no conflict of interest between the authors.

**Statement of Research and Publication Ethics**

The study is complied with research and publication ethics

**References**

[1] Y. Lam, "A note on the optimal replacement problem,"*Advances in Applied Probability*, vol. 20, pp. 479-482, 1988

[2]Y**.** Lam, "Geometric processes and replacement problem," *Acta Math Appl Sin*., vol. 4, pp. 366-377, 1988.

[3] W.J. Braun, W. Li, and Y.P. Zhao, "Properties of the geometric and related processes*,".Nav Res Log*., vol. 52, pp.607–616, 2005.

[4] Y. Lam, Y.H. Zheng, and Y.L. Zhang, "Some limit theorems in geometric process," *Acta Math Appl Sin*., vol. 19, pp. 405– 416, 2003.

[5] L. Yeh, and S. K. Chan, "Statistical inference for geometric processes with lognormal distribution," *Computational statistics & data analysis*, vol. 27, no. 1, pp. 99-112, 1998.

[6] M. Kara, G. Güven, B. Şenoğlu, and H. Aydoğdu, "Estimation of the parameters of the gamma geometric process," *Journal of Statistical Computation and Simulation*, vol. 92, no. 12, pp. 2525-2535, 2022.

[7] H. Aydoğdu, B. Şenoğlu, and M. Kara, "Parameter estimation in geometric process with Weibull distribution." *Applied Mathematics and Computation*, vol. *217, no*.6, pp. 2657-2665,2010.

[8] I**.**Usta, "Statistical inference for geometric process with the inverse Rayleigh distribution*," Sigma Journal of Engineering and Natural Sciences*, vol. 37, no. 3, pp. 871-882,2019.

[9] C. Biçer, H.D. Biçer, M. Kara, and A. Yılmaz, "Statistical inference for geometric process with the generalized rayleigh distribution*," Facta Universitatis, Series: Mathematics and Informatics*, 1107-1125, 2021.

[10] C. Biçer, H.D. Biçer, M.Kara, and H. Aydoğdu, "Statistical inference for geometric process with the Rayleigh distribution," *Communications Faculty of Sciences University of Ankara Series A1 Mathematics and Statistics*, vol. 68, no. 1, pp. 149-160,2019.

[11] M. Kara, H. Aydoğdu, and Ö. Türkşen, 2015. "Statistical inference for geometric process with the inverse Gaussian distribution," *Journal of Statistical Computation and Simulation*, vol. 85, no. 16, pp. 3206-3215, 2015.

[12] A. Yılmaz, M. Kara, and H. Kara, *"*Bayesian inference for geometric process with lindley distribution and its applications*," Fluctuation and Noise Letters*, vol. 21, no. 05, 2250048,2022.

[13] I. Usta, "Bayesian estimation for geometric process with the Weibull distribution,"*Communications in Statistics-Simulation and Computation*, vol. 53, no. pp. 1-27, 2022.

[14] S. Ali, M. Aslam and S.M.A. Kazmi, 2013. "A study of the effect of the loss function on Bayes Estimate, posterior risk and hazard function for Lindley distribution*". Applied Mathematical Modelling* 37, 6068-6078,2013.

[15] M.Y. Danish, and M. Aslam, 2013. "Bayesian estimation for randomly censored generalized exponential distribution under asymmetric loss functions," *Journal of Applied Statistics*, vol. 40, no. 5, pp. 1106-1119, 2013.

[16] A.Helu, and H. Samawi, H. 2015. "The inverse Weibull distribution as a failure model under various loss functions and based on progressive first-failure censored data," *Quality Technology & Quantitative Management*, vol. 12, no. 4, pp. 517-535, 2015.

[17] D.V. Lindley, "Approximate Bayesian methods," *Trabajos Estadistica Investig Oper*., vol. 31, pp. 223-245, 1980.

[18] A.F. Smith, and G. O. Roberts, *"*Bayesian computation via the Gibbs sampler and related Markov chain Monte Carlo methods," *Journal of the Royal Statistical Society: Series B (Methodological)*.vol. 55, pp. 3-23, 1993.

[19] N. Metropolis, A.W. Rosenbluth, and M.N. Rosenbluth, "Equation of state calculations by fast computing machines," *J Chem Phys*., vol. 21, pp. 1087-1092, 1953.

[20] D. Andrews, and A. Herzberg, *Data*. New York: Springer,1985.

[21] Y.Lam, "Nonparametric inference for geometric process," *Communications in Statistics - Theory and Methods*. vol 21, pp. 2083–105,1992.

[22]M.L. Tiku, "Goodness of fit statistics based on the spacings of complete or censored samples*," Australian Journal of Statistics*, vol. 22, no. 3, pp. 260-275,1980

**Bitlis Eren Üniversitesi Fen Bilimleri Dergisi**
BİTLİS EREN UNIVERSITY JOURNAL OF SCIENCE
ISSN: 2147-3129/e-ISSN: 2147-3188
VOLUME: 13 NO: 2 PAGE: 492-504 YEAR: 2024
DOI:10.17798/bitlisfen.1434925

# Optimizing Speech to Text Conversion in Turkish: An Analysis of Machine Learning Approaches

İzel Zeynep GENÇYILMAZ [1], Kürşat Mustafa KARAOĞLAN [1*]

[1] *Department of Computer Engineering, Faculty of Engineering, Karabuk University, Karabuk (ORCID: 0009-0009-0025-3394) (ORCID: 0000-0001-9830-7622)*

**Keywords:** Speech to Text Conversion, Natural Language Processing, Convolutional Neural Network, Convolutional Recurrent Neural Network, Machine Learning, Deep Learning.

**Abstract**
The Conversion of Speech to Text (CoST) is crucial for developing automated systems to understand and process voice commands. Studies have focused on developing this task, especially for Turkish-specific voice commands, a strategic language in the international arena. However, researchers face various challenges, such as Turkish's suffixed structure, phonological features and unique letters, dialect and accent differences, word stress, word-initial vowel effects, background noise, gender-based sound variations, and dialectal differences. To address the challenges above, this study aims to convert speech data consisting of Turkish-specific audio clips, which have been limitedly researched in the literature, into texts with high-performance accuracy using different Machine Learning (ML) models, especially models such as Convolutional Neural Network and Convolutional Recurrent Neural Network (CRNN). For this purpose, experimental studies were conducted on a dataset of 26,485 Turkish audio clips, and performance evaluation was performed with various metrics. In addition, hyperparameters were optimized to improve the model's performance in experimental studies. A performance of over 97% has been achieved according to the F1-score metric. The highest performance results were obtained with the CRNN approach. In conclusion, this study provides valuable insights into the strengths and limitations of various ML models applied to CoST. In addition to potentially contributing to a wide range of applications, such as supporting hard-of-hearing individuals, facilitating notetaking, automatic captioning, and improving voice command recognition systems, this study is one of the first in the literature on CoST in Turkish.

## 1. Introduction

Natural Language Processing (NLP) is a pivotal field in computer science, focusing on enabling computers to understand and interpret human languages [1]. Language can be classified into three primary types: spoken, written, and sign language [2]. The conversion of spoken words into written text not only assists individuals with hearing impairments in comprehending others but also enhances our capacity to concentrate on presentations or lectures without note-taking. Conversion of Speech to Text (CoST) integration with smart devices and home systems, like Siri or Alexa, further enriches our daily interactions. Historically, speech analysis techniques have evolved significantly. In the early 2000s, speech analysis heavily relied on the utilization of the Hidden Markov Model (HMM) and Gaussian Mixture Model techniques [3]. HMMs employed a statistical modeling approach to comprehend the correlation between hidden states and transition probabilities, necessitating extensive data to achieve satisfactory results in tasks like classification or recognition [4]. In the context of speech processing, HMMs exhibited limited accuracy rates, particularly in terms of accuracy in data-scarce environments [5].

Consequently, attaining a high success rate in CoST presented challenges in the 2000s. However, in the 2010s, Long Short-Term Memory (LSTM) and Gated Recurrent Unit (GRU) models emerged, known for their enhanced accuracy [6]. LSTM, a variation of Recurrent Neural Network (RNN), was designed to address the challenge of long-term dependencies, thus incorporating a memory cell controlled by gates that

---

[*] Corresponding author: kkaraoglan@karabuk.edu.tr

*Received:10.02.2024, Accepted:20.03.2024*

determine the information to be retained or forgotten within the network [7]. Leveraging this attribute empowers LSTM to keep past information proficiently, amplifying its efficacy when dealing with intricate sequential assignments like natural language or speech signal processing [8]. On the other hand, GRU, a more efficient counterpart to LSTM, offers quicker processing and reduced computational demands. Nevertheless, despite these advantages, GRU sometimes they may fall short in NLP tasks that require the recognition of extended sequences, like CoST, or context-dependent aspects of language where LSTM networks often excel due to their enhanced ability to retain long-term data dependencies [9]. This discrepancy arises from its limited ability to capture long-term dependencies as effectively as LSTM. Over the past few years, significant progress has been witnessed in deep learning techniques and their integration into NLP, leading to rapid improvement in success rates [10]. Through the strategic utilization of methodologies like deep neural network (DNN), Convolutional Neural Network (CNN), and RNN, remarkable strides have been made, resulting in notably elevated levels of performance [11], [12]. While significant strides have been achieved in deep learning for speech processing, several challenges must be addressed. These hurdles encompass a need for substantial labelled data, the pursuit of model interpretability, and varying environmental conditions [13]. These environmental factors contain various variables, ranging from word count, gender-specific voices, and ethnic origins to audio quality, duration, and vocabulary representation within the dataset. Addressing these intricacies is pivotal for further advancement in the field. Our study tackles these challenges by employing and comparing different ML techniques. Utilizing a comprehensive Kaggle dataset, curated by Kurtkaya, which comprises 26,485 one-second Turkish audio recordings across 14 various commands, our objectives are twofold [14].

This study aims to enhance the accuracy and efficiency of CoST in Turkish, thereby significantly contributing to the broader field of NLP and automated voice recognition systems. The comparison of various Machine Learning (ML) techniques, focusing on deep learning and CNN, endeavors to find the most effective and accurate results. By optimizing parameters such as the number of epochs and other hyperparameters, an improvement in the model's performance is sought, and novel insights are provided by contrasting the findings of this study with other similar works.

This study is organized into four main sections. The first section provides an introduction. The second section is a comprehensive literature review that sets the stage for the research, delves into the goals and overarching framework, gives details of the methodology, and explores the approaches and techniques employed. The third section evaluates criteria, hyperparameters, and comparative results. The fourth and final section discusses the detailed findings and offers suggestions for future research.

## 2. Material and Method

The dataset details are outlined initially, followed by a discussion on the pre-processing steps and the proposed approach to speech recognition. The architecture of the proposed model is detailed after that, with a specific focus on constructing the CNN and CRNN models. The dataset encompasses a collection of 26,485 audio recordings featuring a spectrum of 14 distinct commands. Each audio recording has been meticulously standardized to precisely 1 second, with a chosen sampling frequency of 16 kHz. Table 1 provides a comprehensive statistical overview, encapsulating key aspects and metrics that define the dataset's composition and characteristics.

**Table 1.** Summary of Dataset Characteristics and Features

| Feature | Description |
|---|---|
| **Total Audio Files** | 26485 |
| **Command Instances** | Open - (Aç): 1995<br>Cancel - (İptal): 1952<br>Left - (Sol) : 1910<br>Up - (Yukarı) : 1892<br>Stop - (Dur) : 1887<br>Forward - (İleri) : 1886<br>Yes - (Evet) : 1885<br>Right - (Sağ) : 1883<br>Close - (Kapa) : 1882<br>Continue - (Devam) : 1880<br>Start - (Başlat) : 1879<br>Down - (Aşağı) : 1870<br>No - (Hayır) : 1843 |
| **Sampling Frequency** | 16 kHz |

### 2.1. Speech Classification

In this section, the description of speech classification is provided, along with some fundamental terminologies encountered during our speech processing work. Waveform is a diagrammatic representation that aids in examining the displacement of sound waves over time alongside other essential parameters [15]. Frequency pertains to the rate at which the waveform repeats within one second. The highest point on the waveform is called the crest, while the lowest point is known as the trough. Amplitude signifies the distance from the center line to the crest or trough [16]. Spectrogram visually depicts an audio signal's evolving frequency spectrum over time [17]. This powerful tool is employed for sound signal analysis and finds utility in tasks such as identifying different sounds in a recording, analyzing pitch and timbre, monitoring the temporal evolution of sound, and detecting and categorizing noise [18].

Mel-Frequency Cepstral Coefficient (MFCC) denotes a method of extracting features that represent the spectral characteristics of an audio signal [19]. MFCCs apply Mel filtering to the logarithm of the signal's power spectrum. Subsequently, they compute the discrete cosine transform of the filtered signal. Popular libraries like Librosa or Sox are commonly utilized to extract MFCC coefficients from audio signals [20]. Sound classification encompasses the automated attribution of labels to audio recordings.
Diverse techniques are employed to accomplish this objective, with spectrograms and MFCCs emerging as the most prevalent approaches [21]. Spectrograms are leveraged to distil distinctive attributes from assorted sound recordings. In the subsequent feature extraction stage, our model leverages MFCCs to apply ML techniques. Several vital advantages underpin the choice of MFCCs over spectrograms.
Firstly, spectrograms often possess high-dimensional characteristics, slowing the model training process and requiring powerful computational resources. In contrast, MFCCs offer a more compact and efficient representation. Secondly, while spectrograms linearly process frequencies, MFCCs are designed to emulate the non-linear auditory perception of the human ear. This is particularly beneficial in CoST, as it allows for a more natural interpretation of audio data. However, it is noteworthy that spectrograms can be more effective than MFCCs in handling high frequencies [22]. Lastly, spectrograms' critical limitation is their reduced capability to accurately represent the temporal variations in sound within specific time intervals [23]. MFCCs, by design, provide a more detailed and precise reflection of these material changes, making them a more suitable choice for our CNN model's requirements [24].

In the study, one of the procedural steps involved using the 'path' column in the 'dataBase.xlsx' file, primarily to reference and retrieve audio files with .wav and .mp3 extensions from various directories using the' os.walk(directory_path)' command. For organizational purposes, these files were initially stored on an empty list. Subsequently, we prepared additional empty lists for labeling and calculating MFCC. The MFCC for each audio file was computed using the 'librosa.feature.mfcc' command. The labelling process utilized the file paths of the audio files, a method chosen for its straightforwardness as each audio file was systematically stored in its corresponding folder. Labelling was executed using the' os.path.

Since the folder names and labels encompass the names of 14 distinct commands, these were initially in string format. However, we converted these string labels into integer values to enhance the model's performance. This numerical representation is crucial as it facilitates the model's ability to process and understand the data more effectively.

Another vital aspect of our methodology was dividing data into training and test sets, with the test size set at 20%. This split is essential for evaluating the model's performance under varied conditions [25]. The research encompassed an array of ML models: Support Vector Machine (SVM), K-Nearest Neighbors, Decision Tree (DT), Random Forest (RF), Gaussian Naive Bayes (GNB), LSTM, GRU, CNN, and Convolutional Recurrent Neural Networks (CRNN). The prediction phase involved using the trained models to classify audio clips into their respective voice command categories. This step has been performed to determine the practical applicability of the models in real-world scenarios, such as voice command recognition systems. In the final phase, the performance of each model was compared using key metrics such as Accuracy, Precision, Recall, F1-Score, Receiver Operating Characteristic (ROC) curve, and Area Under the Curve (AUC).

Furthermore, hyperparameters were optimized to improve the performance of the models. This phase yielded insights into the strengths and weaknesses of each model, while also elucidating the potential and limitations of various ML approaches in CoST.

To concisely encapsulate, the steps in our study were as follows:

- Retrieval of audio files from the designated directory.
- Calculation of MFCCs for each audio file using Librosa.
- Utilization of the folder names as labels for the audio files.
- Segregation of the dataset into training and testing subsets.
- Employing various ML techniques.

- Comparing the results and optimizing hyperparameters for improved outcomes.

Figure 1 is provided to enhance understanding of the proposed approach structure.

## 2.2. Architecture of CNN Model

The CNN architecture is a deep learning model widely utilized for tasks like image classification [26], [27].

.

Nevertheless, thanks to recent advancements in learning methodologies, CNN has also demonstrated remarkable achievements in speech processing [20], [28], [29], [30], [31]. Convolutional layers employ filters to process the input data, generating feature maps [32].

$$\mathbf{x_l}(\mathbf{t},\mathbf{f}) = \sum_{\mathbf{a}=-\mathbf{p}}^{\mathbf{p}} \sum_{\mathbf{b}=-\mathbf{p}}^{\mathbf{p}} \mathbf{w_{ab}} \mathbf{x_{l-1}}(\mathbf{t}+\mathbf{a})(\mathbf{f}+\mathbf{b}) + \mathbf{b} \quad (1)$$

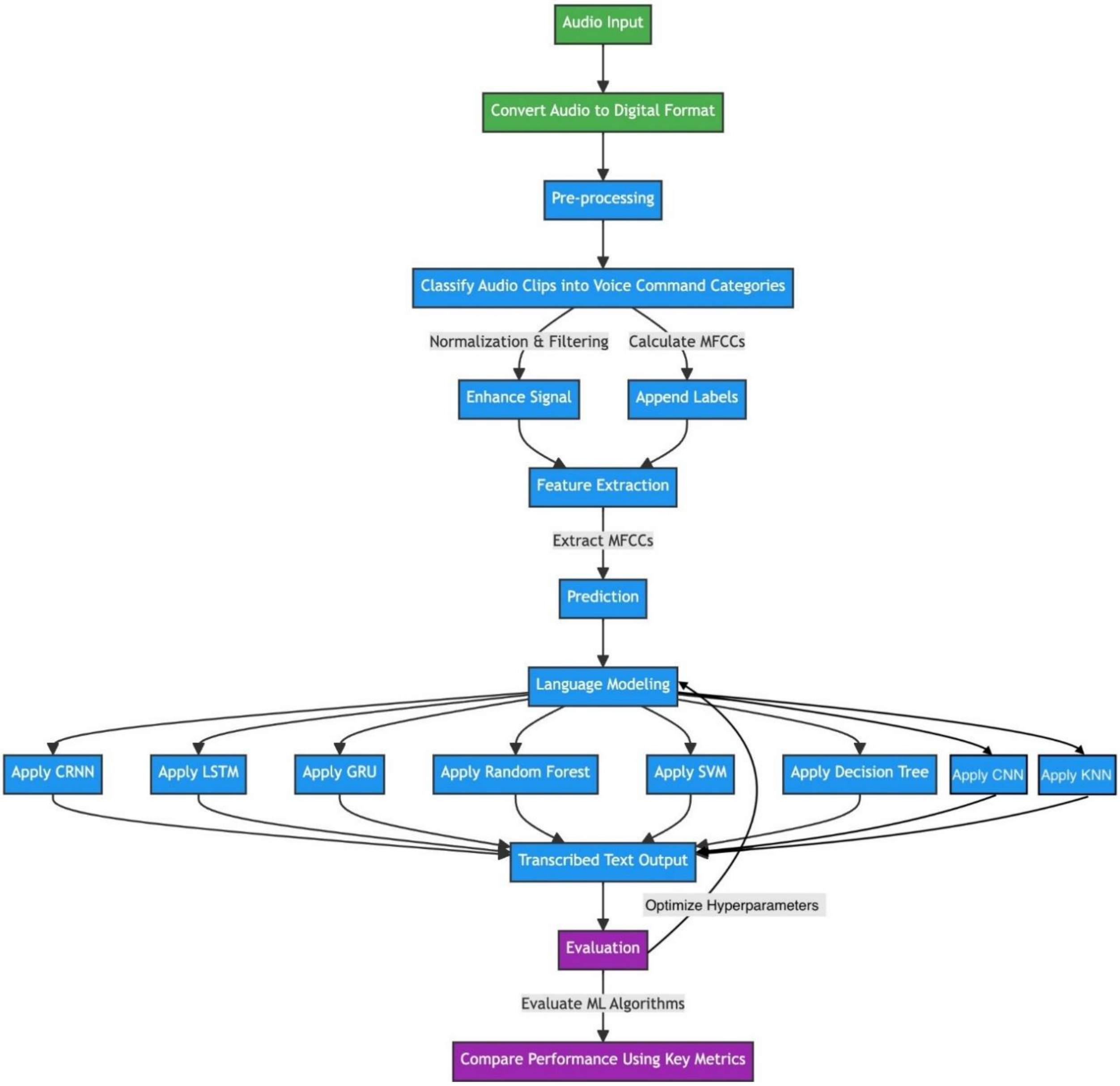

**Figure 1.** Structure of the proposed CoST approach.

Formula (1) is a mathematical expression of a convolution operation commonly used in neural networks [33]. The equation above represents the value at time t in the l-th layer and frequency f. The formula includes two nested sums. In the first sum, the variables a and b take values from -p to p. In the second sum, the variables a and b also take values from -p to p. The convolution operation in speech processing, like the spatial dimensions in image processing, is performed by summing neighboring values in the time and frequency dimensions [34]. Weights represent the learnable parameters of the filters, and the bias term (b) is added to the weighted sum.

The formula calculates an output in the current layer by taking the surrounding sum of the inputs from the previous layer and appropriately weighing each output [35]. With this formula, in CNN architecture, the network learns to extract relevant features from the input spectrogram and performs the task of speech recognition [36], [37]. The Keras Sequential model facilitates the construction of linearly arranged neural architectures, enabling the seamless integration of layers, like fully connected or convolutional layers, each with singular input and output tensors [38]. Its efficacy is simplifying unidirectional data flow in various standard neural network applications. The usage of the Sequential API is convenient. The reason for using Sequential in our model is that it allows us to easily stack the desired layers in the desired order, enabling the straightforward creation of a model.

The model is architecturally composed of five layers intricately designed to work harmoniously. The first and second layers are similar, each consisting of a Convolutional 2D (Conv2D) layer, followed by a MaxPooling2D layer, and a Dropout layer. These layers are for feature extraction and reducing overfitting [39], [40]. The third layer is a Flatten layer, serving as a bridge between the convolutional and dense layers by converting the 2D feature maps into a 1D feature vector, crucial for subsequent processing [41]. In the fourth layer, we have a fully connected Dense layer coupled with a Dropout layer.

The dense layer plays a key role in combining the complex features learned by earlier layers in a flexible, non-linear way [42]. The fifth and final layer is another Dense layer, responsible for output and utilizing a SoftMax activation function, making it suitable for multi-class classification tasks. Overall, the model includes two Convolutional layers, two Max-Pooling layers, one Flatten layer, two Dense layers, and three Dropout layers, with one layer designated for output. It is meticulously compiled with the Categorical Cross Entropy loss function and optimized using the Adam optimizer, ensuring effective training and performance. For a clearer understanding of the model's structure and layers, refer to the following table:

**Table 2.** Details of the applied layers

| Layers | |
|---|---|
| **Number** | **Types** |
| 1 | Conv2D, MaxPooling2D, Dropout |
| 2 | Conv2D, MaxPooling2D, Dropout |
| 3 | Flatten |
| 4 | Dense (Fully connected), Dropout |
| 5 | Dense (Output with SoftMax) |

The first layer applies convolution operations to the audio signal, using 32 filters of size 3x3, each capturing distinct frequency components and their temporal changes. The command "model.add(Conv2D(32, kernel_size=(3, 3), activation='ReLU', input_shape=(X_train.shape[1], X_train.shape[2], 1)))" implements this convolution operation.

The second layer's MaxPooling operation reduces the feature map's size, decreasing the number of parameters and risk of overfitting while improving computational efficiency [32], [43]. The command "model.add(MaxPooling2D(pool_size=(2, 2)))" is used for this purpose, employing a 2x2 pooling region. The Dropout layer, applied in both the first and fourth layers with a rate of 25%, aims to mitigate overfitting by randomly deactivating input units during each update cycle [40]. Following this, the procedures of Conv2D, MaxPooling2D, and Dropout layers are repeated, with the second Conv2D layer employing 48 filters. This increase in filters allows for capturing a broader range of complex features.

The Flatten layer converts the multi-dimensional feature map into a one-dimensional vector, formatted for input into a fully connected dense layer. The command "model.add(Flatten())" facilitates this transformation.

The subsequent Dense layer, connected to every neuron in the preceding layer, enhances the model's ability to recognize intricate patterns. The command "model.add (Dense (128, activation='ReLU'))" sets the neuron count and incorporates the 'ReLU' activation function.

The final output layer, with neurons equal to the total class count, employs the "softmax" activation function to provide probabilistic class predictions. The model is trained using the categorical cross-entropy loss function, which is ideal for multi-class classification. The Adam optimizer dynamically adapts the learning rate for each parameter, facilitating faster convergence and achieving superior performance compared to traditional optimization algorithms. [44]. The model's weights are adjusted throughout the training process to minimize the loss function, enabling it to recognize speech commands effectively.

### 2.3. The Architecture of CRNN Model

The architecture of the proposed CRNN model combines the strengths of both CNN and LSTM layers using the sequential model framework. This approach ensures seamless data flow from one layer to the next.

The model has five essential layers, each serving a specific function. Initially, the model begins with a Conv2D layer, which applies 2D convolutions to the input data, extracting critical features from the audio signals. In this initial stage, the layer utilizes 32 filters of size 3x3 each, employing the 'ReLU' activation function to maintain positive values while setting negative values to zero. Following the Conv2D layer, the MaxPooling2D layer selects the highest value among neighboring pixels within a 2x2 area, effectively reducing the dimensions of the feature maps. This helps the model generalize better by reducing its sensitivity to minor variations in the data. It achieves this by introducing stochasticity using a dropout mechanism, which randomly deactivates a portion (e.g., 25%) of the units in each layer during training. This prevents overfitting and encourages the model to learn more robust representations [39]. As the model progresses, an additional Conv2D layer with 64 filters is introduced, mirroring the initial layer in its composition.

The data shape transforms within the Reshape layer, adapting it seamlessly for processing by the subsequent LSTM layer. This LSTM layer, equipped with 64 internal units, is designed to handle sequential data, like sentences or time series, expertly. The network culminates in two Dense layers. The first one, housing 128 neurons, utilizes the ReLU activation function to introduce non-linearity. This layer is followed by another Dropout mechanism, strategically removing 25% of its neurons during training to curb overfitting. Finally, the last Dense layer leverages the SoftMax activation function to produce probabilistic predictions for each class, ensuring they all add up to 100%. The configuration of 64 units in the LSTM layer and 128 units in the Dense layer is not arbitrarily but meticulously chosen through hyperparameter tuning. These specific values were carefully selected through experiments to strike a balance between model performance and complexity, yielding the most optimal outcome.

## 3. Evaluation Metrics and Hyperparameters

This section is meticulously designed to comprehensively understand the methodology and outcomes associated with the study in question. Initially, the evaluative metrics employed to gauge the efficacy of the models are elucidated. Subsequently, an exposition on selecting hyperparameters for the training phase is proffered, covering a spectrum of parameters and configurations meticulously adjusted to optimize the models' performance during the training regimen. In culmination, a comparative scrutiny of the empirical results is undertaken. The effectiveness of various machine learning methodologies and the model is assessed using criteria such as ROC curves, accuracy, recall, precision, F1-score, True Positive Rate (TPR), and False Positive Rate (FPR) scores.

$$\boldsymbol{Accuracy} = \frac{(\boldsymbol{TP}+\boldsymbol{TN})}{(\boldsymbol{TP}+\boldsymbol{TN}+\boldsymbol{FP}+\boldsymbol{FN})} \tag{2}$$

$$\boldsymbol{Precision} = \frac{\boldsymbol{TP}}{(\boldsymbol{TP}+\boldsymbol{FP})} \tag{3}$$

$$\boldsymbol{Recall} = \frac{\boldsymbol{TP}}{(\boldsymbol{TP}+\boldsymbol{FN})} \tag{4}$$

$$\boldsymbol{F1Score} = \boldsymbol{2}\cdot\frac{(\boldsymbol{Precision}\cdot\boldsymbol{Recall})}{\boldsymbol{Precision}+\boldsymbol{Recall}} \tag{5}$$

$$\text{TPR} = \frac{\boldsymbol{TP}}{\boldsymbol{TP}+\boldsymbol{FN}} \tag{6}$$

$$\text{FPR} = \frac{\boldsymbol{FP}}{\boldsymbol{FP}+\boldsymbol{TN}} \tag{7}$$

In the assessment of the efficacy of classification models, we depend upon four principal metrics: True Positive (TP), True Negative (TN), False Positive (FP), and False Negative (FN). TP denotes the quantity of accurately recognized positive instances, whereas TN pertains to the correct identification of negative cases. In contrast, FP refers to the quantity of positive predictions made in error, and FN represents the true positive cases that were overlooked.

Accuracy is expressed as the quotient of the sum of true positives and true negatives over the total number of cases. Accuracy shines when dealing with balanced data and similar costs for incorrect predictions. However, its utility wanes in the presence of imbalanced class distributions, where it may offer a misleadingly optimistic view of the model's performance.

Precision is the ratio of correctly predicted positive observations to the total predicted positives. Recall is the ratio of correctly predicted positive observations to all observations in the actual class. F1-Score is the harmonic means of Precision and Recall and thus conjoins the properties of both metrics. ROC curve illustrates the relationship between the TPR and the FPR across various classification thresholds. AUC quantifies the total performance of the model by measuring the area beneath the ROC curve [45].

The cross-validation technique constitutes an esteemed metric to gauge the proficiency of a model's generalization capabilities concerning unseen data [46]. It plays a pivotal role in circumventing the predicament of overfitting, where the model demonstrates superior efficacy on the dataset utilized for training [47]. It is a mechanism for adjudicating amongst diverse model candidates, thereby evaluating their capacity for generalization. Various methodologies of cross-validation prevail, including but not limited to k-fold, leave-one-out, and stratified cross-validation, each presenting its unique set of benefits and limitations contingent upon the dataset and the task at hand [25]. Within the ambit of our model, k-fold cross-validation has been predominantly employed. This technique augments the duration of training in comparison to a singular train-test partition, attributing to multiple iterations of training. While it diminishes the propensity for overfitting, it may concurrently engender a modicum of bias contingent upon the selection of folds [48]. It is ubiquitously recognized as a robust method for the selection of models and the fine-tuning of hyperparameters.

The practice of executing k-fold cross-validation repetitively, for instance, tenfold, and calculating the mean of the outcomes, furnishes a more steadfast and dependable gauge of model efficacy [49]. In the case of our model, a criterion of twenty iterations has been adopted. A superior cross-validation indicates a model's enhanced generalization ability [50]. It is imperative, however, to eschew exclusive reliance on cross-validation as the sole criterion for decision-making [51]. Other aspects, such as the model's complexity, interpretability, and other evaluation metrics, should be considered in the final adjudication process.

### 3.1 Hyperparameters for Training

Hyperparameters constitute configurational parameters employed to architect the learning schema, significantly impacting the efficacy of the models [52]. The different approaches have been tested and considered industry best practices. For example, the Adam optimizer has been chosen based on findings in [53], dropout rates have been selected based on findings in [40] and the number of epochs has been selected with the hands-on experiments considering training duration. The scenario of overfitting was considered, and early stopping was employed.

A detailed overview of the hyperparameters used is presented in Table 3, which yielded outstanding outcomes across various ML methodologies.

## 4. Results

This section meticulously analyses the research results and initiates a dialogue on prospective future investigations. It is organized to initially present several graphs that illuminate insights into model performance and evaluation, followed by a discussion on the findings.

Figure 2 compares accuracy, precision, recall, F1-score, and cross-validation score across various models, including CNN, CRNN, LSTM, RF, SVM, GNB, KNN, GRU and DT.

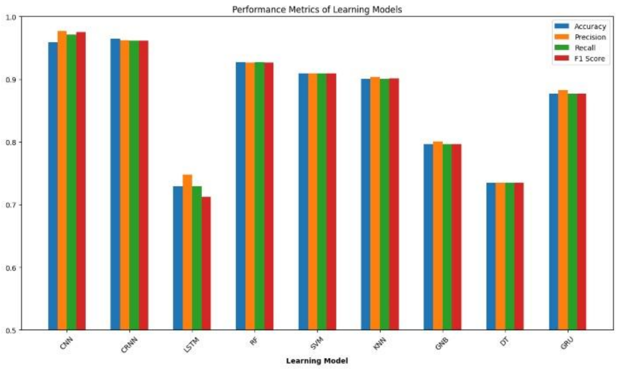

**Figure 2.** Comparative results for CoST task in Turkish.

Figure 3 illustrates the ROC curve for the CRNN model. Furthermore, additional graphs showcase the training and validation loss and accuracy rates over epochs for the models, highlighting their learning trajectory and capability to generalize over time. Subsequently, the discussion focuses on the notable outcomes and their contributions to the existing knowledge, alongside exploring potential avenues for further research.

Figure 4 shows the loss during training (in blue) and validation (in red) across epochs. If the validation loss increases, it could be a sign of overfitting. In the proposed model, the validation loss decreased over time.

**Table 3.** Hyperparameters for training process

| Model Name | Hyperparameters | Model Name | Hyperparameters |
|---|---|---|---|
| **RF** | Number of Estimators: 100<br>Criterion: Gini<br>Max Depth: None<br>Min Samples Split: 2<br>Min Samples Leaf: 1<br>Max Features: Auto<br>Random State: None | **LSTM** | Number of LSTM Units: 64<br>Number of Dense Units: 64<br>Dropout Rate: 0.3<br>Batch Size: 32<br>Optimizer: Adam<br>Loss: Categorical Cross-Entropy<br>Early_Stopping=True |
| **CRNN** | Conv2D Filters: 32, 64<br>Conv2D Kernel Size: (3, 3)<br>Conv2D Activation: ReLU<br>Conv2D Padding: Same<br>MaxPooling Pool Size: (2, 2)<br>MaxPooling Strides: None<br>MaxPooling Padding: Valid<br>LSTM Units: 64<br>First Dense Activation Function: ReLU<br>Last Dense Activation Function: Softmax<br>Number of Dense Units: 128<br>Optimizer: Adam<br>Loss: Categorical Crossentropy<br>Batch Size: 32<br>Early_Stopping=True | **CNN** | Conv2D Filters: 32, 64<br>Conv2D Kernel Size: (3, 3)<br>Conv2D Activation: ReLU<br>MaxPooling Pool Size: (2, 2)<br>Dense Units: 128<br>Dense Activation: ReLU<br>Dropout Rate: 0.25<br>Output Activation: Softmax<br>Loss: Categorical Crossentropy<br>Optimizer: Adam<br>Batch Size: 32<br>Early_Stopping=True |
| **DT** | Criterion: Gini<br>Splitter: Best<br>Max Depth: None<br>Min Samples Split: 2<br>Min Samples Leaf: 1 | **GRU** | Number of GRU and Dense Units: 128<br>Early_Stopping=True<br>Dropout Rate: 0.5<br>Activation of Dense Layer 1: ReLU<br>Activation of Dense Layer 2: Softmax |
| **KNN** | Number of Neighbors: 3<br>Weight: Uniform<br>Algorithm: Auto | **SVM** | C: 1<br>Kernel: RBF<br>Gamma: Scale |

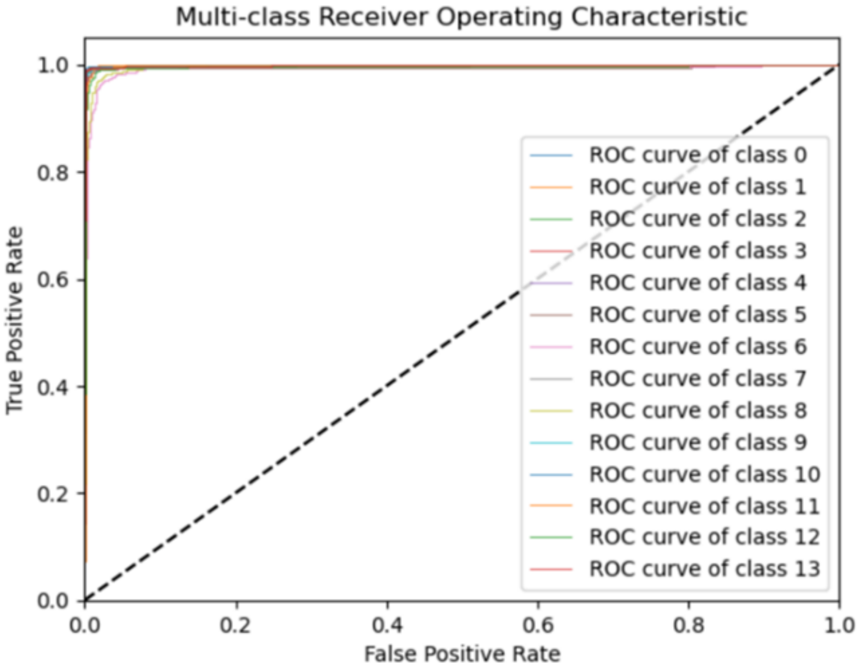

**Figure 3.** The ROC curve plots the performance of the implemented CRNN model.

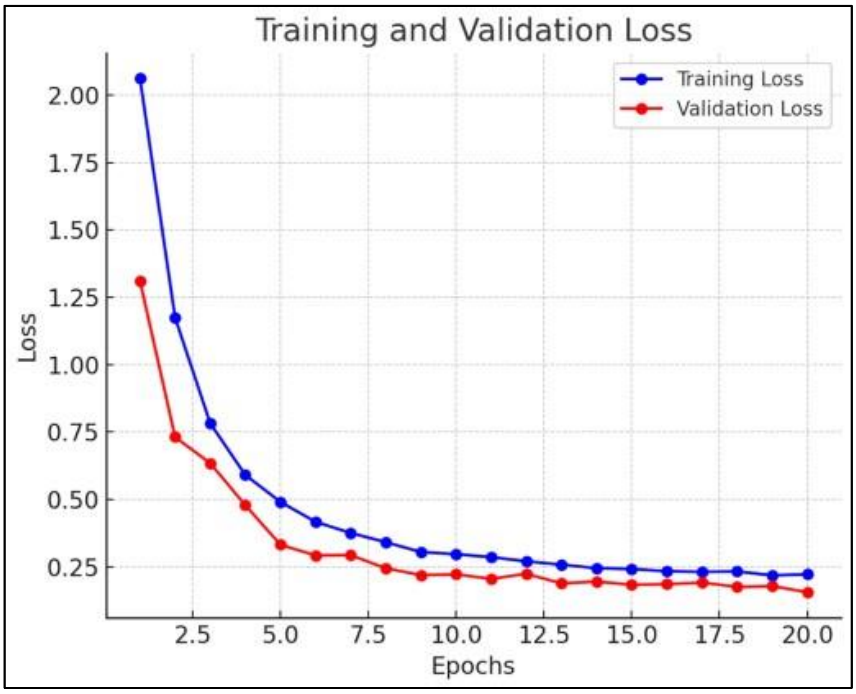

**Figure 4.** Visualizations depicting the training and validation loss progress of the model over time.

Figure 5 displays the accuracy during training (in blue) and validation (in red) across epochs. Increasing accuracy over time is a good sign, showing that the model is effectively learning to classify the data. Consistently higher validation accuracy than training accuracy indicates that the proposed model is generalizing well.

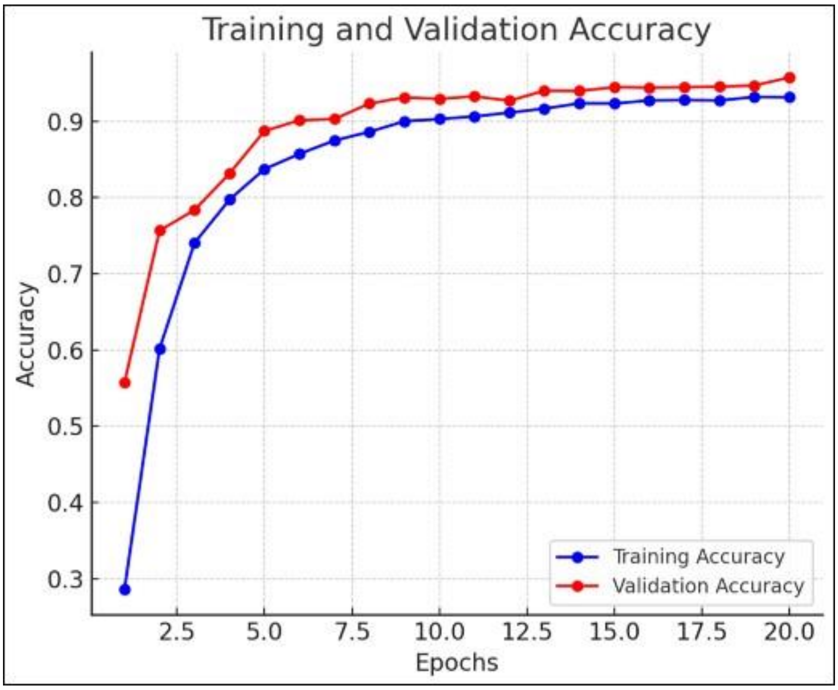

**Figure 5.** Visualizations illustrating the training and validation accuracy progress of the model over time.

Table 4 compares eight different ML models, evaluating their strengths and limitations across five key performance indicators: accuracy, precision, recall, F1 score, and cross-validation score. The CRNN model is pre-eminent, boasting the apex of accuracy (0.96468), while the CNN model eclipses its counterparts in both precision (0.97677) and F1 score (0.97552).

Moreover, the table furnishes statistical insights by summarizing each metric's maximum, minimum, mean, and standard deviation (Std) values. This multifaceted metric evaluation not only identifies the models that excel with the dataset in question but also accentuates the imperative of meticulously aligning ML methodologies with the stipulated performance objectives and the inherent characteristics of the dataset.

**Table 4.** Comparison of results obtained from various ML techniques in a table.

| Proposed Approaches | Learning Model | Accuracy | Precision | Recall | F1-Score |
|---|---|---|---|---|---|
| 1st Approach | CNN | 0.95922 | 0.97677 | 0.97135 | 0.97552 |
| **2nd Approach** | **CRNN** | **0.96468** | **0.96188** | **0.96168** | **0.96164** |
| 3rd Approach | LSTM | 0.72965 | 0.74829 | 0.72921 | 0.71210 |
| 4th Approach | RF | 0.92694 | 0.9268 | 0.92691 | 0.92672 |
| 5th Approach | SVM | 0.90976 | 0.90966 | 0.90985 | 0.90963 |
| 6th Approach | KNN | 0.90070 | 0.9036 | 0.90075 | 0.90143 |
| 7th Approach | GNB | 0.79687 | 0.80101 | 0.79657 | 0.79662 |
| 8th Approach | DT | 0.73532 | 0.73513 | 0.73516 | 0.73486 |
| 9th Approach | GRU | 0.87710 | 0.88287 | 0.87710 | 0.876824 |
| | **Max.:** | 0.96468 | 0.97677 | 0.97135 | 0.97552 |
| | **Min.:** | 0.72965 | 0.73513 | 0.72921 | 0.71210 |
| | **Mean:** | 0.86539 | 0.87039 | 0.86643 | 0.86481 |
| | **Std.:** | 0.09688 | 0.09526 | 0.09837 | 0.10259 |

## 5. Conclusion and Discussion

This section thoroughly reviews the outcomes of our research and initiates a discussion on possible future directions. It begins by exploring the significant findings and their impact on the current state of knowledge. Further areas for research exploration are identified. Different ML models were evaluated, utilizing metrics including accuracy, precision, recall, F1 score, and cross-validation score. Notably, the CNN model exhibited exceptional effectiveness, especially CoST in Turkish, achieving an accuracy rate of 95.34% after 10 epochs, which improved to 95.92% upon reaching 20 epochs.

Moreover, it exhibited high precision, recall, and F1 scores. Surpassing the CNN, the CRNN model showed even higher accuracy, with 96.35% at 10 epochs and 96.46% at 20 epochs, alongside exceptional precision, recall, and F1 scores, indicating superior performance for this specific task. As a side note, the epoch count has been increased to 30 in our methodology. However, due to the activation of the early stopping parameter set to true, the system could identify the optimum number of epochs without succumbing to overfitting or underfitting, thereby ensuring the robustness and efficiency of the training process. On the contrary, the LSTM model could have been more effective, achieving only 73% accuracy, 75% precision, 73% recall, and a 71% F1 score, suggesting it is a less optimal choice for CoST in Turkish. Other models, including Random Forest, SVM, KNN, Gaussian Naive Bayes, GRU and Decision Tree, demonstrated mixed results, with Random Forest achieving the highest accuracy of 93%. There remains potential for improvement in their performance compared to CNN and CRNN. While direct comparison with existing research is challenged by differences in methodologies, datasets, and lack of enough literature about CoST in Turkish, our work distinguishes itself by offering a different solution, achieving outstanding accuracy. Our CRNN model outperforms previous research, achieving outstanding results with accuracy, F1 score, and cross-validation score of 0.96. It exceeds the capabilities of the DNN HM model presented in the article 'Turkish Speech Recognition

Based on Deep Neural Networks' [54], which reports a WER of 14.82 and an accuracy of 0.85. 'A Novel End-to-End Turkish Text-to-Speech (TTS) System via Deep Learning' [55] while prioritizing perceptual quality with 4.49 MOS, our research achieves the highest possible transcription accuracy.

This study marks a significant advancement in speech recognition and NLP within the Turkish language context as we look ahead to future developments. Yet, several areas warrant further investigation. Firstly, expanding the dataset size would be crucial for future studies. A more extensive and diverse dataset would enable a more comprehensive evaluation of the models' generalization capabilities and performance in real-world scenarios. Secondly, the development of model optimization techniques would be beneficial. Investigating strategies such as hyperparameter tuning, diversifying model architectures, and optimizing data pre-processing steps could significantly enhance the effectiveness of CNN, CRNN, and other models. Thirdly, expanding the scope of research to encompass complex tasks like emotion recognition and speech variation analysis is essential. Such advancements allow a more holistic understanding of speech by considering tone, emphasis, and emotional content. Finally, exploring targeted applications and industrial implementations of these models is imperative. Evaluating the performance of CoST techniques in domains like automatic captioning, virtual assistants, and call center speech analysis would provide valuable insights into the usability and effectiveness of these technologies in practical settings. These directions pave the way for future research in Turkish speech recognition and contribute significantly to the broader field of NLP, fostering the development of more sophisticated speech recognition systems.

## Contributions of the authors

This study has significantly profited from the diverse expertise of its authors. Karaoğlan played a crucial role in conceptualization, research design, editing, supervision, project management, critical review, and final approval. Gençyılmaz focused on the literature review, data collection, data analysis, model development, and manuscript writing.

## Conflict of Interest Statement

There is no conflict of interest between the authors.

## Statement of Research and Publication Ethics

The study complies with research and publication ethics.

## References

[1] S. McRoy, *Principles of natural language processing*. Susan McRoy, 2021.

[2] A. Akmajian, A. K. Farmer, L. Bickmore, R. A. Demers, and R. M. Harnish, Linguistics: *An introduction to language and communication.* MIT press, 2017.

[3] M. Gales, S. Young, and Others, “The application of hidden Markov models in speech recognition,” *Foundations and Trends in Signal Processing*, vol. 1, no. 3, pp. 195–304, 2008.

[4] M. L. P. Bueno, A. Hommersom, P. J. F. Lucas, and A. Linard, “Asymmetric hidden Markov models,” *International Journal of Approximate Reasoning*, vol. 88, pp. 169–191, 2017.

[5] M. S. Barakat, M. E. Gadallah, T. Nazmy, and T. El Arif, “Investigating the effect of speech features and the number of HMM mixtures in the quality HMM-based synthesizers,” *in The International Conference on Electrical Engineering*, 2008, vol. 6, pp. 1–12.

[6] T. Hori, S. Watanabe, Y. Zhang, and W. Chan, “Advances in joint CTC-attention based end-to-end speech recognition with a deep CNN encoder and RNN-LM,” arXiv preprint arXiv:1706. 02737, 2017.

[7] H. Sak, A. W. Senior, and F. Beaufays, “Long short-term memory recurrent neural network architectures for large scale acoustic modeling,” 2014.

[8] G. Van Houdt, C. Mosquera, and G. Nápoles, “A review on the long short-term memory model,” *Artificial Intelligence Review*, vol. 53, no. 8, pp. 5929–5955, 2020.

[9] S. Yang, X. Yu, and Y. Zhou, “Lstm and gru neural network performance comparison study: Taking yelp review dataset as an example,” *in 2020 International workshop on electronic communication and artificial intelligence (IWECAI)*, 2020, pp. 98–101.

[10] I. Sutskever, O. Vinyals, and Q. V. Le, “Sequence to sequence learning with neural networks,” Advances in neural information processing systems, vol. 27, 2014.

[11] M. Li et al., “The deep learning compiler: A comprehensive survey,” IEEE Transactions on Parallel and Distributed Systems, vol. 32, no. 3, pp. 708–727, 2020.

[12] K. Mohamad and K. M. Karaoglan, "Enhancing Deep Learning-Based Sentiment Analysis Using Static and Contextual Language Models," *Bitlis Eren Universitesi Fen Bilimleri Dergisi*, vol. 12, no. 3, pp. 712–724, 2023.

[13] A. Mehrish, N. Majumder, R. Bharadwaj, R. Mihalcea, and S. Poria, "A review of deep learning techniques for speech processing," Information Fusion, p. 101869, 2023.

[14] Kurtkaya M, "Turkish Speech Command Dataset," https://www.kaggle.com/, 2021. [Online]. Available: https://www.kaggle.com/datasets/muratkurtkaya/turkish-speech-command-dataset/data. [Accessed: 18-Apr-2024].

[15] M. Tohyama, *Sound and signals*. Springer Science & Business Media, 2011.

[16] F. Riehle, *Frequency standards: basics and applications*. John Wiley & Sons, 2006.

[17] J. O. Smith, "Mathematics of the Discrete Fourier Transform (DFT) with Audio Applications. 2007." W3K Publishing, 2023.

[18] J. L. Flanagan, Speech analysis synthesis and perception, vol. 3. Springer Science & Business Media, 2013.

[19] S. A. Majeed, H. Husain, S. A. Samad, and T. F. Idbeaa, "Mel Frequency Cepstral Coefficients (MFCC) Feature Extraction Enhancement in the Application of Speech Recognition: A Comparison Study," *Journal of Theoretical & Applied Information Technology*, vol. 79, no. 1, 2015.

[20] A. Sithara, A. Thomas, and D. Mathew, "Study of MFCC and IHC feature extraction methods with probabilistic acoustic models for speaker biometric applications," *Procedia computer science*, vol. 143, pp. 267–276, 2018.

[21] P. Zinemanas, M. Rocamora, M. Miron, F. Font, and X. Serra, "An interpretable deep learning model for automatic sound classification," *Electronics*, vol. 10, no. 7, p. 850, 2021.

[22] Y. Jia et al., "Speaker recognition based on characteristic spectrograms and an improved self-organizing feature map neural network," *Complex & Intelligent Systems*, vol. 7, pp. 1749–1757, 2021.

[23] K.-H. N. Bui, H. Oh, and H. Yi, "Traffic density classification using sound datasets: an empirical study on traffic flow at asymmetric roads," *IEEE Access*, vol. 8, pp. 125671–125679, 2020.

[24] J. Salamon and J. P. Bello, "Deep convolutional neural networks and data augmentation for environmental sound classification," *IEEE Signal processing letters*, vol. 24, no. 3, pp. 279–283, 2017.

[25] G. James, D. Witten, T. Hastie, R. Tibshirani, and Others, An introduction to statistical learning, vol. 112. Springer, 2013.

[26] R. Yamashita, M. Nishio, R. K. G. Do, and K. Togashi, "Convolutional neural networks: an overview and application in radiology," *Insights into Imaging*, vol. 9, pp. 611–629, 2018.

[27] K. O'shea and R. Nash, "An introduction to convolutional neural networks," arXiv preprint arXiv:1511. 08458, 2015.

[28] A. Adeel, M. Gogate, and A. Hussain, "Contextual deep learning-based audio-visual switching for speech enhancement in real-world environments," *Information Fusion*, vol. 59, pp. 163–170, 2020.

[29] H. Tian, S.-C. Chen, and M.-L. Shyu, "Evolutionary programming based deep learning feature selection and network construction for visual data classification," *Information Systems Frontiers*, vol. 22, no. 5, pp. 1053–1066, 2020.

[30] T. Young, D. Hazarika, S. Poria, and E. Cambria, "Recent trends in deep learning based natural language processing," *IEEE Computational Intelligence Magazine*, vol. 13, no. 3, pp. 55–75, 2018.

[31] G. Koppe, A. Meyer-Lindenberg, and D. Durstewitz, "Deep learning for small and big data in psychiatry," *Neuropsychopharmacology*, vol. 46, no. 1, pp. 176–190, 2021.

[32] Y. Chen, L. Li, W. Li, Q. Guo, Z. Du, and Z. Xu, "Chapter 6 - Deep learning processors," in AI Computing Systems, Y. Chen, L. Li, W. Li, Q. Guo, Z. Du, and Z. Xu, Eds. Morgan Kaufmann, 2024, pp. 207–245.

[33] M. D. Zeiler and R. Fergus, "Visualizing and understanding convolutional networks," *in Computer Vision--ECCV 2014: 13th European Conference*, Zurich, Switzerland, September 6-12, 2014, Proceedings, Part I 13, 2014, pp. 818–833.

[34] K. Santosh, N. Das, and S. Ghosh, "Deep learning: a review," Deep Learning Models for Medical Imaging, pp. 29–63, 2022.

[35] M. M. Taye, "Theoretical understanding of convolutional neural network: Concepts, architectures, applications, future directions," *Computation*, vol. 11, no. 3, p. 52, 2023.

[36] Y. Wu, H. Mao, and Z. Yi, "Audio classification using attention-augmented convolutional neural network," *Knowledge-Based Systems*, vol. 161, pp. 90–100, 2018.

[37] K. M. Karaoglan and O. Findik, “Enhancing Aspect Category Detection Through Hybridised Contextualised Neural Language Models: A Case Study in Multi-Label Text Classification,” The Computer Journal, p. bxae004, 01 2024.

[38] F. Chollet, *Deep learning with Python*. Simon and Schuster, 2021.

[39] P. Galeone, *Hands-on neural networks with TensorFlow 2.0: understand TensorFlow, from static graph to eager execution, and design neural networks*. Packt Publishing Ltd, 2019.

[40] N. Srivastava, G. Hinton, A. Krizhevsky, I. Sutskever, and R. Salakhutdinov, “Dropout: a simple way to prevent neural networks from overfitting,” *The Journal of Machine Learning Research,* vol. 15, no. 1, pp. 1929–1958, 2014.

[41] J. Jin, A. Dundar, and E. Culurciello, “Flattened convolutional neural networks for feedforward acceleration,” arXiv preprint arXiv:1412. 5474, 2014.

[42] S. Ruder, “Neural transfer learning for natural language processing,” NUI Galway, 2019.

[43] C. Ozdemir, “Avg-topk: A new pooling method for convolutional neural networks,” *Expert Systems with Applications*, vol. 223, p. 119892, 2023.

[44] A. G. Ganie and S. Dadvandipour, “From big data to smart data: a sample gradient descent approach for machine learning,” *Journal of Big Data*, vol. 10, no. 1, p. 162, 2023.

[45] A. P. Bradley, “The use of the area under the ROC curve in the evaluation of machine learning algorithms,” *Pattern recognition*, vol. 30, no. 7, pp. 1145–1159, 1997.

[46] H. Wang and H. Zheng, “Model Cross-Validation,” InEncyclopedia of Systems Biology, 2013.

[47] K. P. Murphy, *Machine learning: a probabilistic perspective*. MIT press, 2012.

[48] G. C. Cawley and N. L. C. Talbot, “On over-fitting in model selection and subsequent selection bias in performance evaluation,” *The Journal of Machine Learning Research*, vol. 11, pp. 2079–2107, 2010.

[49] Y. Jung and J. Hu, “AK-fold averaging cross-validation procedure,” *Journal of nonparametric statistics*, vol. 27, no. 2, pp. 167–179, 2015.

[50] G. Jiang and W. Wang, “Error estimation based on variance analysis of k-fold cross-validation,” *Pattern Recognition*, vol. 69, pp. 94–106, 2017.

[51] R. B. Rao, G. Fung, and R. Rosales, “On the dangers of cross-validation. An experimental evaluation,” *in Proceedings of the 2008 SIAM international conference on data mining*, 2008, pp. 588–596.

[52] E. Bartz, T. Bartz-Beielstein, M. Zaefferer, and O. Mersmann, *Hyperparameter Tuning for Machine and Deep Learning with R: A Practical Guide*. Springer Nature, 2023.

[53] D. P. Kingma and J. Ba, “Adam: A method for stochastic optimization,” arXiv preprint arXiv:1412. 6980, 2014.

[54] U. A. Kimanuka and O. Buyuk, “Turkish speech recognition based on deep neural networks,” *Suleyman Demirel Universitesi Fen Bilimleri Enstitusu Dergisi*, vol. 22, pp. 319–329, 2018.

[55] S. Oyucu, “A Novel End-to-End Turkish Text-to-Speech (TTS) System via Deep Learning,” *Electronics*, vol. 12, no. 8, p. 1900, 2023.

**Bitlis Eren Üniversitesi Fen Bilimleri Dergisi**
BİTLİS EREN UNIVERSITY JOURNAL OF SCIENCE
ISSN: 2147-3129/e-ISSN: 2147-3188
VOLUME: 13 NO: 2 PAGE: 505-511 YEAR: 2024
DOI:10.17798/bitlisfen.1439794

# Investigation of Phenolic, Flavonoid and Total Antioxidant Capacity of Sumac (*Rhus Coriaria* L.) Plant Grown in Different Regions and Subjected to Different Preservation Methods

Haval Ali MUHAMMED[1], Meltem ÇAKMAK[2], Fikret KARATAŞ[3*], Dursun ÖZER[2], Sinan SAYDAM[3]

*[1]1Duhok University, College of Science, Department of Chemistry, Duhok, Iraq*
*[2]Fırat University, Engineering Faculty, Department of Chemical Engineering, 23200 Elazığ, Türkiye*
[3]Fırat University, Faculty Science, Department of Chemistry, 23200 Elazığ, Türkiye
*(ORCID: 0000-0002-2500-9760) (ORCID: 0000-0002-6291-863X) (ORCID: 0000-0002-0884-027X)*
*(ORCID: 0000-0002-7225-8903) (ORCID: 0000-0003-1531-5454)*

**Keywords:** *Rhus coriaria* L, Preservation, Phenolic substance, Total antioxidant capacity

**Abstract**
The total amount of phenolic and flavonoid compounds and the total antioxidant capacity of sumac samples grown in different regions were determined by a spectrophotometer. Freshly ground samples were divided into three parts: the first part was analyzed immediately, the second one was oiled, and the third one was kept as is for six months. The total phenolic and flavonoid compounds were found in between 27.73-51.75 µg GAE $(g\ dw)^{-1}$ and 16.16 -33.50 µg QE $(g\ dw)^{-1}$, respectively, for fresh samples. In the samples that were grounded and kept for six months, the same parameters were observed to be 19.31 - 37.75 µg GAE $(g\ dw)^{-1}$ and 10.76 - 21.82 µg QE $(g\ dw)^{-1}$, respectively. $IC_{50}$ and TEAC values in freshly ground sumac samples were found between 14.79-23.80 µg $mL^{-1}$ and 359.30-665.62 µmol trolox $(g\ dw)^{-1}$, respectively. $IC_{50}$ and TEAC values in the samples oiled were determined to be in between 17.51 - 27.70 µg $mL^{-1}$ and 306.69 - 517.40 µmol trolox $(g\ dw)^{-1}$, respectively. From these findings, it can be said that the higher the amount of total phenolic and flavonoid compounds in the samples, the better the total antioxidant capacity. The decreases in the examined parameters of the samples with oil are lower than those kept without oiling ($p>0.05$). The differences in the examined parameters can be explained by the differences in geographical and ecological conditions.

## 1. Introduction

Sumac (*Rhus coriaria*), which can grow all over the world, especially in subtropical and temperate climates, is a medicinal plant and is also used as a spice [1]. It is reported that in the traditional medicine of the Middle East and Iran, sumac has been used for centuries in the treatment of diseases such as dysentery, diarrhea, hemorrhoids, and gout, as well as for healing wounds and lowering blood sugar, cholesterol, and uric acid levels. It is also stated that sumac contains antibacterial, antifungal, antiviral, antioxidant, anti-inflammatory, hepatoprotective, xanthine oxidase inhibition, hypoglycemia, and cardiovascular protective activities [2]. Studies have reported that it contains many physiologic organic acids, including malic and citric acids, fatty acids, vitamins, flavonoids, and terpenoid derivatives [3], [4]. The proteins, organic acids, minerals, essential oils, vitamins, and phenolics contained in sumac are important for human health. Additionally, sumac is reported to be rich in phenolic chemicals, especially gallic acid and its derivatives, which have a strong antioxidant effect [1], [5]. The fruits and leaves of the sumac plant, which have great economic value, are used in the kitchen, medicine, leather, and dye industries [6]. Antioxidants are chemicals that shield living systems from damage caused by free radical

---

[*] Corresponding author: *fkaratas@firat.edu.tr*

*Received: 19.02.2024, Accepted: 07.06.2024*

oxidation [7]. Oxidative stress can occur when reactive oxygen species (ROS) are not effectively removed from the system. Secondary metabolites such as phytochemicals and especially phenolic compounds are known to have strong antioxidant effects [8].

Phenolic substances are important for human health due to their antimicrobial and antioxidant effects and enzyme inhibition [9]. Flavonoids are generally responsible for colour, the taste, prevention of fat oxidation, and the preservation of vitamins and enzymes in foods [10]. In addition to their properties such as antioxidant, antimutagenic, antiproliferative, antitumor, antiviral and anti-inflammatory, epidemiological studies have shown the importance of flavonoid compounds in reducing the risk of cardiovascular diseases and cancer [11].

Epidemiological studies show that foods have beneficial effects on human health, including their nutritional values. If ROS generated as a result of metabolic activities in living systems exceeds the antioxidant capacity of biological systems, oxidative stress occurs. Intake of antioxidants through food plays an important role in preventing various diseases, such as cancer and cardiovascular diseases, and delaying the aging process [12]. Therefore, it has become important to study the antioxidant capacity of many molecules naturally found in food and biological systems. Foods are sensitive to various environmental factors, such as moisture, light, oxygen, and microorganisms, and these factors can cause spoilage [13]. He et al. [14] report that ginger oil is turned into a film and used to preserve foods such as bread, meat, fish, and fruit. Some biochemical parameters in foods change depending on shelf life. Sumac samples are generally offered for consumption in ground form.

In this study, it was aimed at determining the total phenolic substances, flavonoids, and total antioxidant capacity of sumac grown in different regions. Freshly collected samples were grinded and divided into three parts, first part was analyzed immediately, and the second and third parts were kept for 6 months, with one part being oiled.

## 2. Material and Method

### 2.1. Materials

All sumac samples in Türkiye and Iraq were obtained freshly from public markets. After the samples were dried in an oven at 60 °C for 10 hours, they were ground in a blender and sieved (100 mesh) to separate their seeds and then divided into three parts.

The first group, which is freshly ground, was used immediately for the analysis, the second group was kept as is for 6 months in a plastic bag in the fridge at 4 °C. The third group was oiled by spraying sunflower oil and kept in a plastic bag in the fridge for 6 months at 4 °C. At the end of six months, the necessary analyses were performed similarly to the first group of samples.

### 2.2 Methods

Total phenolic, total flavonoid substances and total antioxidant capacity were determined according to Çakmak et al. [15].

### 2.3 Statistical analysis

All analyses were repeated three times, and the results are given as mean ± deviation. Findings were subjected to One-Way ANOVA using SPSS 26.0 for MS Windows. Differences between group means were analyzed for significance using the Tukey HSD test, and statistical significance was expressed as $p<0.05$. Significant differences in table rows are indicated by different numbers of * while the same numbers of * indicate there is no statistical difference between groups. The same letters in the table column indicate that there is no significant difference ($p>0.05$) between the regions.

## 3. Results and Discussion

Phenolic compounds, which are secondary metabolites in plants, are responsible for antioxidant effects. Flavonoids and other plant polyphenols are important antioxidants with high redox potentials. The antioxidant effects of phenolic compounds are explained by their binding of free radicals, chelating with metals, and inactivation of some enzymes [16]. Total phenolic and flavonoid substance amounts and total antioxidant capacity results, found as a result of different treatments applied to sumac grown in different regions, are given in Table 1-4.

Some biochemical parameters in foods change depending on shelf life. Sumac samples are generally sold for consumption in ground form. Therefore, ground and oiled sumac samples were analyzed after being kept for six months to simulate the average shelf life of the sumac on the market.

**Table 1.** Total phenolic substance in sumac samples (μg GAE (g dw)$^{-1}$).

| Region | First group | Second group | Third group |
|---|---|---|---|
| **Maraş** | $^{b, c, d}$ 38.84 ± 1.11$^{*}$ | $^{c, d}$ 27.56 ± 1.01$^{**}$ | $^{c}$ 30.72 ± 1.08$^{***}$ |
| **Elazığ** | $^{e}$ 44.88 ± 1.49$^{*}$ | $^{e}$ 35.80 ± 1.16$^{**}$ | $^{d}$ 41.72 ± 1.28$^{***}$ |
| **Shelaza** | $^{a}$ 29.42 ± 0.90$^{*}$ | $^{c}$ 25.17 ± 0.78$^{**}$ | $^{a, b}$ 27.54 ± 0.92$^{***}$ |
| **Trawanish** | $^{b, c}$ 36.90 ± 1.09$^{*}$ | $^{c}$ 26.45 ± 0.79$^{**}$ | $^{c}$ 31.43 ± 0.90$^{***}$ |
| **Shahi** | $^{a}$ 28.47 ± 0.98$^{*}$ | $^{b}$ 21.27 ± 0.78$^{**}$ | $^{a}$ 26.50 ± 0.80$^{***}$ |
| **Charput** | $^{a}$ 28.40 ± 0.85$^{*}$ | $^{b}$ 22.59 ± 0.79$^{**}$ | $^{a}$ 25.17 ± 0.91$^{***}$ |
| **Suleymania** | $^{f}$ 51.50 ± 1.46$^{*}$ | $^{e}$ 36.55 ± 1.20$^{**}$ | $^{d}$ 42.37 ± 1.27$^{***}$ |
| **Kadana** | $^{a}$ 27.73 ± 0.92$^{*}$ | $^{a}$ 19.31 ± 0.79$^{**}$ | $^{a}$ 25.98 ± 0.85$^{***}$ |
| **Derişke** | $^{b, c}$ 36.00 ± 1.14$^{*}$ | $^{c}$ 26.19± 0.93$^{**}$ | $^{c}$ 30.78 ± 1.01$^{***}$ |
| **Ranya** | $^{b}$35.67 ± 1.07$^{*}$ | $^{d}$ 28.29 ± 0.91$^{**}$ | $^{c}$ 32.32 ± 1.02$^{***}$ |
| **Shalidize** | $^{f}$51.75 ± 1.48$^{*}$ | $^{e}$ 37.75 ± 1.13$^{**}$ | $^{d}$ 41.35 ± 1.28$^{***}$ |

**Table 2.** Total flavonoids substance in sumac samples (μg QE (g dw)$^{-1}$).

| Regions | First group | Second group | Third group |
|---|---|---|---|
| **Maraş** | $^{d}$ 25.84 ± 1.16$^{*}$ | $^{b}$ 14.62 ± 0.73$^{**}$ | $^{b}$ 18.37 ± 0.86$^{***}$ |
| **Elazığ** | $^{e}$ 30.37 ± 1.76$^{*}$ | $^{d}$ 19.84 ± 1.13$^{**}$ | $^{d}$ 27.75 ± 1.29$^{***}$ |
| **Shelaza** | $^{a}$ 16.16 ± 0.79$^{*}$ | $^{a}$ 10.76 ± 0.68$^{**}$ | $^{a}$ 14.89 ± 0.65$^{***}$ |
| **Trawanish** | $^{c}$ 20.21 ± 1.36$^{*}$ | $^{c}$ 16.23 ± 0.84$^{**}$ | $^{b}$ 18.55 ± 0.87$^{***}$ |
| **Shahi** | $^{c}$ 20.11 ± 1.41$^{*}$ | $^{a}$ 12.54 ± 0.94$^{**}$ | $^{a}$ 14.34 ± 1.10$^{***}$ |
| **Charput** | $^{b}$ 17.88 ± 0.89$^{*}$ | $^{a}$ 12.83 ± 0.61$^{**}$ | $^{a}$ 14.46 ± 0.80$^{***}$ |
| **Suleymania** | $^{e}$ 33.50 ± 1.70$^{*}$ | $^{d}$ 20.37 ± 1.08$^{**}$ | $^{e}$ 30.88 ± 1.28$^{***}$ |
| **Kadana** | $^{b}$ 18.40 ± 0.85$^{*}$ | $^{a}$ 11.57 ± 0.66$^{**}$ | $^{b}$ 16.76 ± 0.87$^{***}$ |
| **Derişke** | $^{d}$25.82 ± 0.76$^{*}$ | $^{d}$ 19.22 ± 0.84$^{**}$ | $^{c, d}$ 23.79 ± 1.36$^{***}$ |
| **Ranya** | $^{c}$22.60 ± 1.16$^{*}$ | $^{b}$14.27 ± 0.80$^{**}$ | $^{b}$ 19.42 ± 1.12$^{***}$ |
| **Shalidize** | $^{d}$ 28.52 ± 1.86$^{*}$ | $^{d, e}$21.82 ± 0.98$^{**}$ | $^{c}$ 25.72 ± 1.13$^{***}$ |

The total amount of phenolic substances in the first group grown in different regions varies between 27.73 ± 0.92 - 51.75 ± 1.48 μg GAE (g dw)$^{-1}$. It can be said that there is no significant difference between Sheladize and Süleymania, Shahi, Charput, Shelaza, and Kadana regions, as well as between Trawanish, Derişke, Ranya, and Maraş regions (Table 1). While the total amount of phenolic substances in the second, group of samples varies between 19.31 ± 0.79 - 37.75 ± 1.13, on the other hand, in the third group of samples, it varied between 25.17 ± 0.91- 42.37 ± 1.27 μg GAE (g dw)$^{-1}$. As seen in the rows of Table 1, the difference between the first, second and third groups is statistically significant ($p < 0.05$). The loss of phenolic substances in the third group is less than in the second group.

According to previous research, the methanol extract of sumac samples contained 151.71 mg GAE (g extract)$^{-1}$, and the ethyl acetate extract contained 65.31 mg GAE (g extract)$^{-1}$ total phenolic substance [17]. In a study conducted by Mazzara et al. [18], total phenolic and flavonoid substances in sumac samples taken from five different regions of Sicilian were between 354.81-473.08 mg GAE (g DE)$^{-1}$, 38.06 – 55.56 mg QE (g DE)$^{-1}$ respectively. Yuksel et al. [19] reported that the total amount of phenolic substances in the methanol extract of sumac samples grown in different regions of Tunceli varied between 797 ± 50 – 1929 ± 63 mg GAE (kg)$^{-1}$.

Flavonoids are generally responsible for color, taste, the prevention of fat oxidation, and the preservation of vitamins and enzymes in foods [20]. The total amounts of flavonoid substances in the sumac samples in the first, second and third groups ranged between 16.16-33.50, 10.76-21.82, 14.34-30.88 μg QE (g dw)$^{-1}$ respectively. Fereidoonfar et al. [21] reported that the amounts of total phenolic and flavonoid substances in the methanol extract of sumacs grown in various regions of Iran were determined to be in between 77.54-389.30 mg GAE (g dw)$^{-1}$ and 2.19-7.54 mg QE (g dw)$^{-1}$, respectively. Özaydin et al. [22] reported that the total phenolic and flavonoid substance in sumacs of the southeastern Anatolia region of Turkey was in the range of 26.3 -

82.2 mg GAE (g sumac)$^{-1}$, 7.4 - 7.55 mg catechin (g sumac)$^{-1}$, respectively.

At the end of the six-month waiting period, the loss in the total amount of phenolic and flavonoid substances in the third group was found to be less than in the second group. This can be explained by the oil film formed on the flakes of sumac samples, which prevents the oxidation of sumac in the air. Çakmak et al. [23] found that the total phenolic and flavonoid substance amounts in wild white hambeles fruits as 37.30 ± 2.10 µg GAE (g dw)$^{-1}$, 22.17 ± 1.15 µg QE (g dw)$^{-1}$, respectively. Adelakun et al. [24] report that essential oils have antimicrobial effects, so they can be applied to food products or incorporated into synthetic packaging films to extend the shelf life of foods. Konfo et al. [25] reported that essential oils, as well as natural antioxidants, are used in the preservation of foodstuffs. Falowo et al. [26] reported that 2% and 4% basil essential oil applied to ground beef increased oxidative stability and preserved color during storage. Karatas et al. [27] reported that vitamin loss was less in oiled samples than in unoiled red pepper flakes for a certain period.

Total antioxidant capacity in sumac samples was determined by the DPPH and TEAC methods. High IC$_{50}$ values calculated in the DPPH method indicate low antioxidant capacity.

Total antioxidant capacity is a measure of the specific amount of free radicals scavenged by a sample. Antioxidant capacity measurements yield the amount of a heterogeneous mixture of antioxidants, which determines the total scavenging ability of the sample [28].

**Table 3.** Total antioxidant capacity (IC$_{50}$) in sumac samples according to the DPPH method (µg mL$^{-1}$).

| Region | First group | Second group | Third group |
|---|---|---|---|
| **Maraş** | $^{c}$ 18.81 ± 0.65 $^{*}$ | $^{c}$ 28.03 ± 0.88 $^{**}$ | $^{c}$ 22.69 ± 0.71 $^{***}$ |
| **Elazığ** | $^{b}$ 16.55 ± 0.61 $^{*}$ | $^{b}$ 22.56 ± 0.69 $^{**}$ | $^{b}$ 19.27 ± 0.64 $^{***}$ |
| **Shelaza** | $^{c, d}$ 20.83 ± 0.61 $^{*}$ | $^{b}$ 24.24 ± 0.71 $^{**}$ | $^{c}$ 22.20 ± 0.69 $^{***}$ |
| **Trawanish** | $^{c}$ 19.12 ±0.61 $^{*}$ | $^{b}$ 23.28 ± 0.67 $^{**}$ | $^{c}$ 21.90 ± 0.66 $^{***}$ |
| **Shahi** | $^{e}$ 22.28 ± 0.57 $^{*}$ | $^{d}$ 32.11 ± 0.90 $^{**}$ | $^{d}$ 25.77 ± 0.80 $^{***}$ |
| **Charput** | $^{e}$ 23.04 ± 0.74 $^{*}$ | $^{d}$ 30.37 ± 1.01 $^{**}$ | $^{e}$ 27.70 ± 0.87 $^{***}$ |
| **Suleymania** | $^{a, b}$ 15.75 ± 0.56 $^{*}$ | $^{a}$ 19.42 ± 0.67 $^{**}$ | $^{a}$ 17.51 ± 0.62 $^{***}$ |
| **Kadana** | $^{e}$ 23.80 ± 0.72 $^{*}$ | $^{c}$ 27.69 ± 0.78 $^{**}$ | $^{d}$ 25.78 ± 0.72 $^{***}$ |
| **Derişke** | $^{c}$ 19.86 ± 0.58 $^{*}$ | $^{b, c}$ 25.44 ± 0.77 $^{**}$ | $^{c}$ 22.09 ± 0.67 $^{***}$ |
| **Ranya** | $^{c, d}$ 20.66 ± 0.65 $^{*}$ | $^{c}$ 28.33 ± 0.76 $^{**}$ | $^{d}$ 24.90 ± 0.70 $^{***}$ |
| **Shalidize** | $^{a}$ 14.79 ± 0.48 $^{*}$ | $^{a}$ 19.37 ± 0.68 $^{**}$ | $^{a}$ 17.81 ± 0.57 $^{***}$ |

**Table 4.** Total antioxidant capacity in sumac samples according to the TEAC method (µmol trolox (g dw)$^{-1}$).

| Region | First group | Second group | Third group |
|---|---|---|---|
| **Maraş** | $^{b, c}$ 544.27 ± 27.30 $^{*}$ | $^{b}$ 332.90 ± 16.40 $^{**}$ | $^{b, c}$ 448.77 ± 20.05 $^{***}$ |
| **Elazığ** | $^{c, d}$ 594.50 ± 26.30 $^{*}$ | $^{b}$ 348.80 ± 17.11 $^{**}$ | $^{c}$ 452.42 ± 18.17 $^{***}$ |
| **Shelaza** | $^{b}$ 515.81 ± 23.48 $^{*}$ | $^{b}$ 326.37 ± 14.48 $^{**}$ | $^{b}$ 433.73 ± 17.24 $^{***}$ |
| **Trawanish** | $^{b}$ 531.37 ± 26.60 $^{*}$ | $^{b, c}$ 364.30 ± 16.82 $^{**}$ | $^{b}$ 437.37 ± 20.14 $^{***}$ |
| **Shahi** | $^{b}$ 502.37 ±25.71 $^{*}$ | $^{b}$ 334.80 ±18.23 $^{**}$ | $^{b}$ 413.83 ± 19.31 $^{***}$ |
| **Charput** | $^{b}$ 488.31 ± 23.13 $^{*}$ | $^{b}$ 324.33 ± 16.93 $^{**}$ | $^{b}$ 414.90 ± 18.93 $^{***}$ |
| **Suleymania** | $^{c, d}$ 636.50 ± 25.00 $^{*}$ | $^{c}$ 407.33 ± 18.03 $^{**}$ | $^{d}$ 517.40 ± 20.17 $^{***}$ |
| **Kadana** | $^{a}$ 359.30 ± 15.82 $^{*}$ | $^{a}$ 259.64 ± 11.83 $^{**}$ | $^{a}$ 306.69 ± 13.13 $^{***}$ |
| **Derişke** | $^{b}$ 527.96 ± 24.61 $^{*}$ | $^{c}$ 389.03 ± 17.06 $^{**}$ | $^{b, c}$ 450.30 ± 17.50 $^{***}$ |
| **Ranya** | $^{b}$ 525.43 ± 24.50 $^{*}$ | $^{b}$ 345.83 ± 14.51 $^{**}$ | $^{b}$ 437.45 ± 16.03 $^{***}$ |
| **Shalidize** | $^{d}$ 665.62 ± 28.12 $^{*}$ | $^{c}$ 389.63 ± 17.82 $^{**}$ | $^{d}$ 510.00 ± 20.45 $^{***}$ |

While the IC$_{50}$ values in the first group samples varied between 14.79 - 23.80, it was determined that they were between 19.37 - 32.11, and 17.51 - 27.70 µg mL$^{-1}$ in the second and third group samples, respectively. Among the findings, the highest antioxidant capacity was observed in

Shalidize region sumac samples, while the lowest was observed in Kadana. According to the $IC_{50}$ values in the third group, the total antioxidant capacity was found to be higher than the second group.

Ereifej et al. [29] reported that the total phenolic substance in the methanol extract of sumac and turmeric samples at 20 °C were reported to be 271.4 and 187.1 mg GAE $(100 \text{ g dw})^{-1}$, respectively. In the same study, they found the $IC_{50}$ values of sumac and turmeric methanol extracts to be 0.15 and 0.16 mg $mL^{-1}$, respectively, according to the DPPH method.

While TEAC values in fresh sumac samples from different regions were found to be in between 359.30 - 665.62 µmole trolox $(\text{g dw})^{-1}$ in the second and third groups, they vary between 259.64 - 407.33 and 306.69 - 517.40 µmole trolox $(\text{g dw})^{-1}$, respectively. The difference between the groups is statistically significant ($p<0.05$), and at the end of the waiting period, the decrease in TEAC values in the second group is greater than in the third group. Isgrò et al. [30] stated that the $IC_{50}$ value of the sumac sample was $0.41 \pm 0.02$ mg $mL^{-1}$ and the TEAC value was $1.76 \pm 0.10$ mmol troloxs E $(\text{g extract})^{-1}$. Cakmak et al. [23] reported that the $IC_{50}$ and TEAC values in wild white hambeles fruits were $39.21 \pm 1.25$ µg $mL^{-1}$ and $295.08 \pm 12.50$ µmol troloxs $(\text{g dw})^{-1}$, respectively. Ayas et al. [31] reported that the TEAC values of Rhus coriaria, Nasturtium officinale and Scolymus hispanicus were $3055.6 \pm 20.4$, $903.0 \pm 17.7$, $539.0 \pm 6.4$ µmole trolox equivalent $(\text{g sample})^{-1}$, respectively. Fereidoonfar et al. [21] reported that the total antioxidant capacity in the methanol extract of Iranian sumac was between 1.55-11.09 AAE $(\text{g dw})^{-1}$.

It was observed that the total phenolic and flavonoid substance and total antioxidant capacity of all sumac samples decreased significantly compared to freshly ground ones. However, the amount of decrease is lower in the oiled samples. The reason why the loss in the parameters examined in oiled samples is less can be explained by the fact that the oil forms a film layer on the sumac surface.

## 4. Conclusion and Suggestions

It was found that the Shalidize, Süleymania, and Elazığ regions were richer than other regions in terms of total phenolic and flavonoid substances. It was concluded that the richest regions in terms of antioxidant capacity were Süleymania and Shalidize, while the poorest regions were Carput and Kadana. In regions where the total amount of phenolic and flavonoid substances is high, antioxidant capacity was also found to be high. The loss of measured values in an oiled sample is less than in the samples kept without oil. Sumac is thought to be a potential source for functional food production due to its high amount of phenolic compounds and antioxidant capacity. Differences in total phenolic, flavonoid, and antioxidant capacity amounts between regions might depend on geographical and ecological conditions.

Based on these results, it can be said that preserving sumac samples by oiling them for long-term consumption is more advantageous in terms of reducing the loss of phenolic substances, flavonoid, and antioxidant capacity.

## Author Contributions

All the authors have contributed equally.

## Conflict of Interest Statement

There is no conflict of interest between the authors.

## References

[1] G. E. S. Batiha, O. M. Ogunyemi, H. M. Shaheen, F. R. Kutu, C. O. Olaiya, J. M. Sabatier and D. M. Waard,“*Rhus coriaria* L. (Sumac), a Versatile and Resourceful Food Spice with Cornucopia of Polyphenols”, *Molecules*, vol. 27, no. 16, pp. 1-21, 5179, August, 2022, https://doi.org/10.3390/molecules27165179.

[2] M. R. Morshedloo, F. Maggi, H. T. Neko and M. S. Aghdam, “Sumac (*Rhus coriaria* L.) fruit: Essential oil variability in Iranian populations”, *Industrial Crops & Products*, vol. 111, pp. 1–7, January, 2018, doi: 10.1016/j.indcrop.2017.10.002.

[3] A. Shabbir, “*Rhus coriaria* Linn, a plant of medicinal, nutritional and industrial importance: A review”, *Journal of Animal and Plant Sciences*, vol. 22, no. 2, pp. 505–512, June, 2012, ISSN: 1018-7081

[4] M. Khalil, S. Hayek, N. Khalil, N. Serale, L. Vergani, M. Calasso, M. D. Angelis and Portincasa, P, “Role of Sumac (*Rhus coriaria* L.) in the management of metabolic syndrome and related disorders:

Focus on NAFLD-atherosclerosis interplay", *Journal of Functional Foods*, vol. 87, pp. 1-17, 104811, December, 2021. https://doi.org/10.1016/j.jff.2021.10481.

[5] A. H. Rad and M. Khaleghi, "Sumac in Food Industry: A Changing Outlook for Consumer and Producer, *Journal of Food Technology & Nutrition sciences,* vol. 2, no. 1, pp. 1–3, May, 2020. doi: 10.47363/jftns/2020(2)104.

[6] I. M. Abu-Reidah, M. S. Ali-Shtayeh, R. M. Jamous, D. Arráez-Román and A. Segura-Carretero, "HPLC-DAD-ESI-MS/MS screening of bioactive components from *Rhus coriaria* L. (Sumac) fruits", Food *Chemistry,* vol. 166, pp. 179–191, January, 2015, doi: 10.1016/j.foodchem.2014.06.011.

[7] A. Galano, "Free Radicals Induced Oxidative Stress at a Molecular Level: The Current Status, Challenges and Perspectives of Computational Chemistry Based Protocols", *Journal of the Mexican Chemical Society,* vol. 59, no. 4, pp. 231-262, October, 2015, ISSN 1870-249X.

[8] H. Alsamri, K. Athamneh, G. Pintus, A. H. Eid and R. Iratni, "Pharmacological and antioxidant activities of *rhus coriaria* l. (sumac)", *Antioxidants,* vol. 10, no. 1, pp. 1–28, January, 2021, doi: 10.3390/antiox10010073.

[9] G. Karabulut and O. Yemiş, "Bound Forms of Phenolic Compounds and their Bioavailability", *Akademik Gıda*, vol. 17, no. 4, pp. 526-537, January, 2019, doi: 10.24323/akademik-gida.667270.

[10] A.N. Panche, A. D. Diwan and S. R. Chandra, "Flavonoids: an overview", *Journal of Nutritional Science*, vol. 5, no. e47, pp. 1-15, December, 2016, doi: 10.1017/jns.2016.41.

[11] A. Roy, A. Ariba Khan, I. Ahmad, S. Alghamdi, B. S. Rajab, A. O. Babalghith, M. Y. Alshahrani, S. Islam and M. R. Islam, "Flavonoids a Bioactive Compound from Medicinal Plants and Its Therapeutic Applications", BioMed *Research International,* 2022, Article ID 544529, pp. 1-9, June, 2022, https://doi.org/10.1155/2022/5445291.

[12] G. Pizzino, N. Irrera, M. Cucinotta, G. Pallio, F. Mannino, V. Arcoraci, F. Squadrito, D. Altavilla and A. Bitto,"Oxidative Stress: Harms and Benefits for Human Health", *Oxidative Medicine and Cellular Longevity*, 2017, 8416763, 13, July, 2017, https://doi.org/10.1155/2017/8416763.

[13] H. N. Redfearn, M. K. Warren and J. M. Goddard, "Reactive Extrusion of Nonmigratory Active and Intelligent Packaging. ACS Applied Materials & Interfaces", *ACS Appl Mater Interfaces*, vol. 15, no. 24, pp. 29511-29524. June, 2023. doi:10.1021/acsami.3c06589.

[14] J. He, Milad M. Hadidi, S. Yang, M. R. Khan, W. Zhang and X. Cong, "Natural food preservation with ginger essential oil: Biological properties and delivery systems", *Food Research International,* vol. 173, 113221, November, 2023, https://doi.org/10.1016/j.foodres.2023.113221

[15] M. Çakmak, B. Bakar, D. Özer, F. Karataş and S. Saydam, "Amino Acid Content and Effect of Different Preservation Methods on Some Biochemical Properties in Black Myrtus communis L. Fruits", *Journal of Agricultural Sciences (Tarim Bilimleri Dergisi),* vol. 29, no. 2, pp. 507-518, March, 2023, doi: 10.15832/ankutbd.941384

[16] S. Çiftçi Yegin, "Farklı Yörelere Ait Sumak (*Rhus Coriaria* L.) Ekşisinin Antioksidan Kapasitesinin Belirlenmesi" *Cumhuriyet Üniv. Sağ. Bil. Enst. Derg*. Vol. 2, no. 2, pp. 35-39, December, 2017.

[17] M. Raodah, A. Al-, Z. H. Alia, H. H. Faleeha, "The Antioxidant and Antimicrobial of Syrian Sumac (*Rhus coriaria*) Fruit Extracts", *Journal of Natural Sciences Research,* www.iiste.org ISSN 2224-3186 (Paper) ISSN 2225-0921 (Online), vol. 4, no. 11, pp. 36–41, January, 2014.

[18] E. Mazzara, A. Caprodossi, A. M. Mustafa, F. Maggi and G. Caprioli, "Phytochemical Investigation of Sumac (*Rhus coriaria* L.) Fruits from Different Sicilian Accessions", *Foods*, vol. 12, no. 23, 4359, December, 2023. https://doi.org/10.3390/foods12234359

[19] E. Yuksel and O. Kaplan Ince, "Physicochemical and Phytochemical Properties of Different Extracts of Sumac Plant (*Rhus coriaria* L.) Grown in Tunceli", Türkiye. *Akademik Gıda, vol.* 21, no. 2, pp. 174-186, May, 2023. doi: 10.24323/akademik-gida.1351175.

[20] S. Kumar and A. K. Pandey, "Chemistry and Biological Activities of Flavonoids: An Overview", *The Scientific World Journal,* Article ID 162750, 16, December, 2013. http://dx.doi.org/10.1155/2013/162750

[21] H. Fereidoonfar, H. Salehi-Arjmand, A. Ali Khadivi, M. Akramian and L. Safdari, "Chemical variation and antioxidant capacity of sumac (*Rhus coriaria* L.)", *Industrial Crops and Products,* vol. 139, 111518, November, 2019. https://doi.org/10.1016/j.indcrop.2019.111518

[22] F. Özaydin and H. Vardin, "Effects of antioxidant and physicochemical properties on antimicrobial activity of sumac (*Rhus coriaria* L.) plant spices which are collected from the southeastern anatolia

region of Turkey", *Harran Tarım ve Gıda Bilimleri Derg., vol.* 26, no. 3, pp. 327-335, September, 2022. doi: 10.29050/harranziraat.1136348

[23] M. Çakmak, B. Bakar, D. Özer, H. Geckil, F. Karatas and S. Saydam, "Investigation of some biochemical parameters of wild and cultured *Myrtus communis* L. fruits subjected to different conservation methods", *Journal of Food Measurement and Characterization*, vol. 15, no. 21, February, 2020. https://doi.org/10.1007/s11694-020-00692-x

[24] O. E. Adelakun, O. J. Oyelade and B. F. Olanipekun, "Use of Essential Oils in Food Preservation. Essential Oils in Food Preservation", *Flavor and Safety, pp.* 71-84, December, 2016. doi:10.1016/b978-0-12-416641-7.00007-9

[25] T. R. C. Konfo, F. M. C. Djouhou, Y. A. Koudoro, E. Dahouenon-Ahoussi, F. Avlessi, C. K. D. Sohounhloue and J. Simal-Gandara, "Essential oils as natural antioxidants for the control of food preservation", *Food Chemistry Advances,* vol. 2, 100312, October, 2023. doi: 10.1016/j.focha.2023.100312.

[26] A. B. Falowo, F. E. Mukumbo, E. M. Idamokoro, A. J. Afolayan and V. Muchenje, "Phytochemical constituents and antioxidant activity of sweet basil (Ocimum basilicum L.) essential oil on ground beef from boran and nguni cattle", *International Journal of Food Science, vol. 2019, January,* 2019. doi:10.1155/2019/2628747.

[27] F. Karatas, A. Baysar and M. Alpaslan, "A comparison of vitamin and folic acid levels of sun and microwave dried *Capsicum annuum* L.", *Journal of Food Processing and Preservation,* vol. 41, e13275, March, 2017. https://doi.org/10.1111/jfpp.13275.

[28] J. Flieger, W. Flieger, J. Baj and R. Maciejewski, "Antioxidants: Classification, Natural Sources, Activity/Capacity Measurements, and Usefulness for the Synthesis of Nanoparticles", *Materials,* vol. 14, no. 15, pp. 1-54, July, 2021. https://doi.org/10.3390/ma14154135

[29] K. I. Ereifej, H. Feng, T. M. Rababah, S. H. Tashtoush, M. H. Al-U'datt, S. Gammoh and G. J. Al-Rabadi, "Effect of Extractant and Temperature on Phenolic Compounds and Antioxidant Activity of Selected Spices", *Food and Nutrition Sciences,* vol. 7, no. 5, pp. 362-370, April, 2016. doi: 10.4236/fns.2016.75038.

[30] C. Isgrò, L. Spagnuolo, E. Pannucci, L. Mondello, L. Santi, L. Dugo and A. M. Sardanelli, "Rhus Coriaria L. Extract: Antioxidant Effect and Modulation of Bioenergetic Capacity in Fibroblasts from Parkinson's Disease Patients and THP-1 Macrophages", *International Journal of Molecular Sciences,* vol. 23, no. 21, 12774, October, 2022. https://doi.org/10.3390/ijms232112774

[31] F. Ayas, F. A. Vuran, K. Yuksel, O. Cinar, S. Tugrul Ay and S. Karabak, "The Antioxidant Capacities and Consumption Per Capita of Edible Wild Species and Local Varieties Collected from Turkey within the GEF-Funded Biodiversity for Food and Nutrition (BFN) Project", *ANADOLU Journal of Aegean Agricultural Research Institute,* vol. 27, no. 2, pp. 46-53, January, 2017. MFAL, ISSN: 1300 - 0225

Bitlis Eren Üniversitesi Fen Bilimleri Dergisi
BİTLİS EREN UNIVERSITY JOURNAL OF SCIENCE
ISSN: 2147-3129/e-ISSN: 2147-3188
VOLUME: 13 NO: 2 PAGE: 512-518 YEAR: 2024
DOI:10.17798/bitlisfen.1469293

# *New Coumarin Ring-Containing Ester Molecule: Facile Synthesis, Characterization, Computational Studies and SwissADME Prediction*

Kamuran SARAÇ[1*]

[1]*Bitlis Eren University, Faculty of Science and Arts, Department of Chemistry, Bitlis, Turkey*

*(ORCID: 0000-0001-6684-8969)*

**Keywords:** 4-Coumarinyl-2-methyl benzoate, Reaction Mechanism, Swissadme, Quantum Chemistry

**Abstract**
The aim of the study was to synthesize 4-Coumarinyl-2-methylbenzoate, elucidate the reaction mechanism, perform quantum chemical calculations, and examine the swiss adme properties of the compound. 4-Coumarinyl-2-methylbenzoate compound was synthesized by nucleophilic substitution reaction. The compound 4-coumarinyl 2-methyl benzoate has been characterized both experimentally and theoretically using quantum chemical calculations and spectral techniques. Nuclear magnetic resonances and infrared spectroscopic values of $^1$H and $^{13}$C in the ground state of the compound were calculated both experimentally and theoretically (density functional theory method was used when making theoretical calculations). It was observed that the calculated infrared and nuclear magnetic resonance values were compatible with the experimental values. The energy difference between the HOMO-LUMO of the 4-Coumarinyl-2-methylbenzoate compound was calculated and it was found that this difference was 1.409 Ev. Finally, swiss adme properties of 4-Coumarinyl-2-methylbenzoate compound such as Molecular Mass (Size), Flexibility (FLEX), Polarity, Saturation (Insatu), Lipophilia, Water Solubility were examined.

## 1. Introduction

Coumarins are the general name given to a group of chemical compounds naturally found in plants and known for their pleasant odors. Coumarins are found especially in cinnamon, blueberries, oak and some other plants [1]. These compounds play a role in the scents of plants and, in some cases, their defense mechanisms. Due to the distinctive odor of coumarins, they are widely used in the perfumery and cosmetics industry. However, it is known that coumarins can be toxic in high doses. For this reason, the use of coumarin-containing products is limited or regulated in some countries [2]. Coumarins are also used in the pharmaceutical industry. For example, coumarin derivatives, which are anticoagulant drugs, significant in the field of medicine [3]. However, the use of coumarin derivatives is carefully monitored because there is a need to control side effects and dosage [4]. Since coumarin derivatives are used in such a wide and diverse field, for the first time in this study, with the aim of using them in at least one of these areas, 4-Coumarinyl-2-methylbenzoate, which is formed by the nucleophilic addition and dissociation reaction of 4-Hydroxycoumarin and 2-methylbenzoyl chloride aroyl compounds, has been investigated. It is aimed at experimental as well as quantum chemical calculation.

## 2. Material and Method

### 2.1. Experimental

**Synthesis of 4-Coumarinyl-2-methylbenzoate (III)**

2-methylbenzoyl chloride (II) (10 mmol) was added dropwise to the solution containing 4-hydroxycoumarin (I) (10 mmol) and pyridine (25 mmol) and mixed for 30-40 minutes at room temperature. The resulting mixture was added to ice water containing dilute hydrochloric acid. After the

---

[*]Corresponding author: ksarac@beu.edu.tr

*Received: 16.04.2024, Accepted: 27.06.2024*

substance was washed with water and filtered, it was placed in 100 mL solution containing 5% sodium bicarbonate and mixed thoroughly. After the product in the beaker was filtered, it was left to dry in the open air. The dried substance was crystallized in ethanol. Yield:(1,9g) 76%, m.p: 135-137° C, $^1$H-NMR: 2.45 (s,3H) $CH_3$; 6,60 (s, 1H) (C-3); 7,20-8,20 (m,8H) phenyl (coumarin and benzoyl). $^{13}$C-NMR: δ 116-135 phenyl (coumarin and benzoyl). FT-IR (KBr, $cm^{-1}$, υ): 1742 $cm^{-1}$ (C=O lactone), 1712 $cm^{-1}$ (C=O ester), 1130 $cm^{-1}$ (C-O)

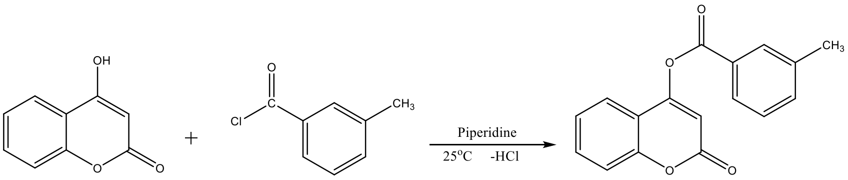

**Figure 1.** Synthesis of title compound.

### 2.2. Computational methods

All theoretical calculations in this work were computed with Gaussian 09 software **[5]**. The 4-Coumarinyl-2-methylbenzoate was optimized by the B3LYP with 6-311G(d,p) basis set. Theoretical $^1$H and $^{13}$C of NMR values were computed within the Gauge Independent Atomic Orbitals (GIAO) approach. The harmonic vibrational frequencies for the optimized structure were assessed and the theoretically obtained frequency values were scaled by 0.958[6].

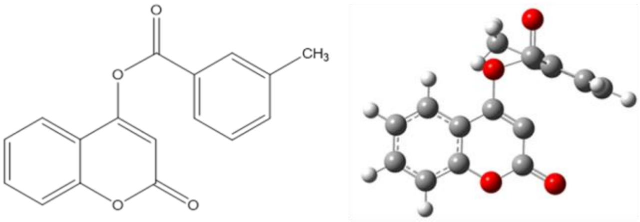

**Figure 2. (**a) Experimental structure of the compound (b) Optimized structure of the compound by B3LYP/6-311G(d,p) method.

## 3. Results and Discussion

### 3.1. Analysis of the synthesized $C_{17}H_{12}O_4$ (III) molecule

The 4-hydroxycoumarin was produced through the nucleophilic addition dissociation reaction of 2-methylbenzoyl chloride and aroyl compounds, and forms 4-Coumarinyl 2-methylbenzoate with a good yield (76%). The reaction formation mechanism of the compound is given in figure 3. As seen in Figure 3 the unshared electron pairs on the oxygen carry out nucleophilic addition to the carbonyl carbon in the acyl structure, the part of which is in the positive state. Then, since the chlorine atom has a high electronegativity, the reaction is completed by separating one mole of hydrochloric acid (-HCl) from the structure.

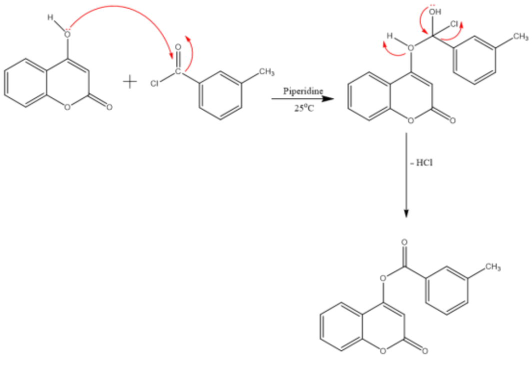

**Figure 2.** Formation mechanism of 4-Coumarinyl 2-methyl benzoate

### 3.2. FT-IR and NMR analysis

While there is a peak of hydroxide (OH) tension in the 3200-3600 $cm^{-1}$ range in the 4-hydroxycoumarin structure, this peak disappears in the compound formed as a result of the reaction and is replaced by carbonyl (C=O), which indicates ester formation, theoretically 1776 $cm^{-1}$, experimentally 1773 $cm^{-1}$) stress peaks appear [7]. On the other hand, asymmetric aliphatic stretching peaks at 2848 $cm^{-1}$ and symmetrical aliphatic stretching peaks at 2780 $cm^{-1}$, coming from the methyl substituent, and $CH_3$ in-plane bending peaks at 1464 $cm^{-1}$ and $CH_3$ out-of-plane bending peaks at 1042 $cm^{-1}$ were observed [8], [9]. Additionally, evaluations of other experimental and theoretical FT-IR spectra of the title compound molecule are given in detail in Table 1.

**Table 1.** Comparison of 4-Coumarinyl-2-methylbenzoate vibration frequencies

| Symbols | Calculated B3LYP/6-311G(d,p) | Experimental FT-IR($cm^{-1}$) |
|---|---|---|
| υ CH, Ar | 2991 | 3010 |
| υ CH, Ar | 2969 | - |
| $\upsilon_{as}$ CH, Ar | 2965 | - |
| υ CH, Prn | 2957 | 2970 |
| $\upsilon_{as}$ CH, Ar | 2948 | - |
| $\upsilon_{as}$ CH, Ar | 2946 | - |
| υ CH, Ar | 2944 | 2958 |
| $\upsilon_{as}$ $CH_3$ | 2848 | - |
| $\upsilon_{as}$ CH,$CH_3$ | 2841 | - |
| $\upsilon_{s}$ $CH_3$ | 2780 | - |
| υ CH, Ar+ υs $CH_3$ | 2774 | - |
| υ C=O+ υC=C | 1776 | 1773 |
| υ C=O, Prn | 1737 | 1712 |
| υ C=C, Ar | 1599 | 1606 |
| δ C-H | 1590 | - |
| υ C=C, Ar | 1578 | 1568 |
| δ C-H | 1475 | 1488 |
| δ $CH_3$ | 1464 | - |
| δ CH | 1446 | 1449 |
| α $CH_3$ | 1399 | 1409 |
| α CH, Ar | 1293 | 1298 |
| υ C-C + α CH, Prn | 1246 | - |
| υ C-O,Prn + α CH, Ar | 1233 | 1208 |
| α CH, Ar | 1123 | 1130 |
| α $CH_3$ | 1042 | 1033 |
| υ C-O Prn + C-C | 971 | 956 |
| α CH, Ar | 845 | 835 |

υ, stress; δ, in-plane bending; α, out-of-plane bending;
Ar, aromatic; prn, pyron; s, symmetric; as, asymmetric;

When the $^{1}H$-NMR chemical shift values of the compound were compared, it was seen that the chemical shift peaks of Hydrogen atoms bonded to electropositive atoms were small. The most characteristic peaks in the synthesized 4-Coumarinyl 2-methylbenzoate compound are the protons of methyl ($CH_3$), which were observed experimentally at 2.45 and theoretically as singlets at 2.52 ppm.

On the other hand, when the $^{13}C$-NMR chemical shift values were examined, it was seen that the carbon atoms of the Phenyl (Benzoyl) ring resonated at high fields due to the increase in electron density on the atoms adjacent to the electropositive atoms, and their chemical shift values were small.

Additionally, evaluations of the experimental and theoretical $^{1}H$-NMR and $^{13}C$-NMR spectra of the compound calculated using the same method are given in Table 2.

**Table 2.** Experimental and calculated NMR spectrum values of 4-Coumarinyl-2-Methyl Benzoate

| Atom | Experimental (ppm)<br>(DMSO-$d_6$) | Calculated (ppm)<br>B3LYP/6-311G(d,p) |
|---|---|---|
| C (Coumarin and Bezoyl) | 115-134 | 108-142 |
| 3H ($CH_3$) | 2.46 | 2.54 |
| 1H (C-9) | 6.63 | 7.85 |
| 8H (Coumarin and benzoyl) | 7.20-8.20 | 7.01-8.18 |

### 3.3. Frontier Molecular Orbitals (FMO) and Electronic Properties

HOMO: This is the highest energy orbital that contains electrons. Electrons in the HOMO are involved in chemical bonding and are more likely to participate in chemical reactions. LUMO: This is the lowest energy orbital that is unoccupied [10]. It's important because it represents an energy level to which electrons can be excited during a chemical reaction. The energy difference between the HOMO and LUMO, often referred to as the HOMO-LUMO gap, is a crucial parameter in understanding various properties of molecules, especially their reactivity and optical properties. Molecules with smaller HOMO-LUMO gaps tend to be more reactive and have different colors compared to those with larger gaps[11], [12].

The molecule was calculated in the DFT/B3LYP/6-311G(d,p) set, and its HOMO and LUMO orbitals are given in Figure 4. As can be seen from the figure, the energy difference between the HOMO and LUMO of the compound is 1.409 eV. This energy gap indicates that the molecule is not in a very stable structure.

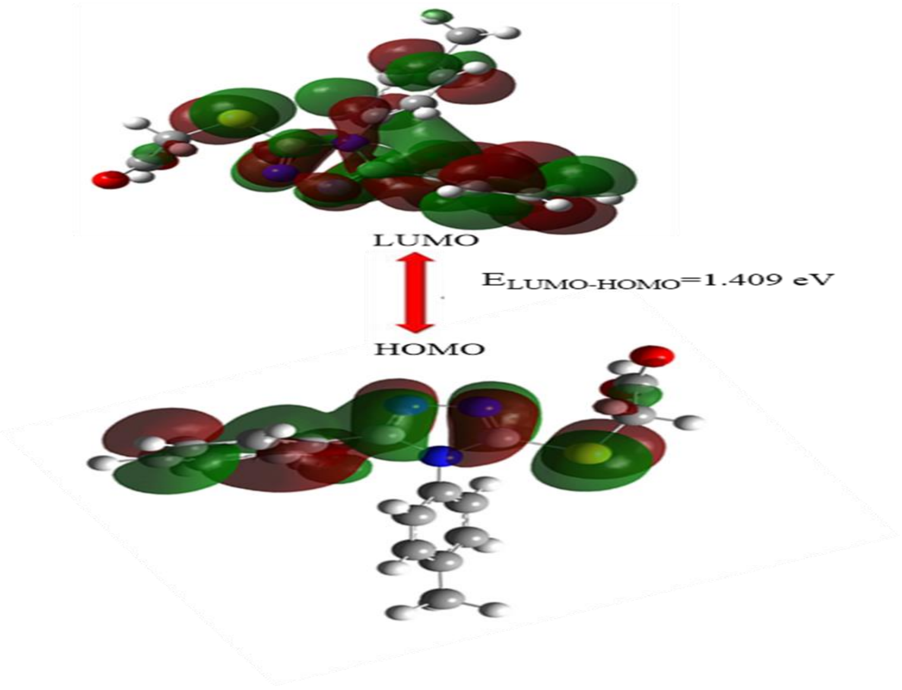

**Figure 4.** By method B3LYP/6-311G(d,p) of the title compound calculated HOMO and LUMO energies.

### 3.4. Swiss Adme Properties

It is one of the widely used tools to estimate the absorption, distribution (Absorption and Distribution of Drugs in the Body), biotransformation and excretion (Metabolism (Biotransformation) Excretion of Drugs in the Body) of drugs in the body in silico and how to estimate some of the pharmacokinetic properties of these parameters and molecules. Traditionally, therapeutics are small molecules that fall under Lipinski's rules. These rules are as follows[13].

1: Molecular Mass (Size): The mole weight of the molecule must be between 150 and 500 g/mol$^{-1}$. Accordingly, the molar weight of the synthesized compound is 280.27 g/mol$^{-1}$.

2: Flexibility (FLEX): A rotatable bond is defined as any single non-ring bond bonded to a non-terminal, non-hydrogen atom (No more than nine rotatable bonds): the title compound number there are 3 types of rotatable bonds.

3: Polarity: The polar surface area (PSA) or topological polar surface area (TPSA) of a molecule is defined as the surface sum of all polar atoms or molecules, especially oxygen and nitrogen, as well as the hydrogen atoms attached to them. (TPSA between 20 and 130 Å ), the title compound TPSA: 56.51 Å²

4:Saturation (Insatu): Saturation, carbon fraction in sp$^3$ hybridization is not less than 0.25; Fraction of the compound Csp$^3$=0.06.

5: Lipophilia or Lipophilism: Lipophilicity refers to the ability of a chemical compound to dissolve in oils, lipids and non-polar solvents such as hexane or toluene. Such nonpolar solvents are lipophilic. LogP is a key component of Lipinski's Rule of five recommendations, which predict the drug-likeness of a new synthetic compound. According to Lipinski's Rule of Five, for good oral and intestinal absorption of an oral drug, the LogP value should be <5, ideally between 1.35-1.8. The LogP value of the compound is: 2.79.

6:Water Solubility: All estimated values are the decimal logarithm of the molar solubility in water (log S). Compounds can be classified according to their solubility values (LogS); Compounds with solubility values of 0 and higher are highly soluble, those in the range of 0 to -2 are soluble, those in the range of -2 to -4 are slightly soluble, and those in the range of -4 are insoluble. LogS value of the compound: -4.09.[14], [15], [16].

According to these data, as seen in Figure-5, the compound largely meets the swissadme properties.

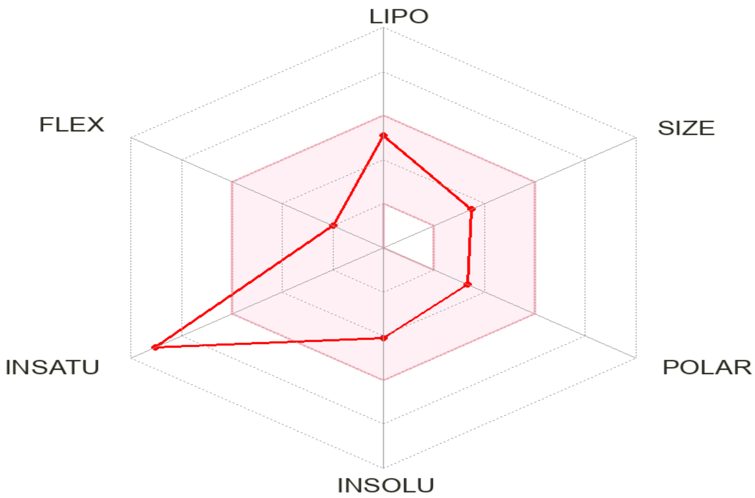

**Figure 5.** Bioavailability radar for title compound within the domain borders of ADME properties, calculated by SwissADME

## 4. Conclusion and Suggestions

In this study, nucleophilic addition-dissociation reaction was carried out with 4-Hydroxycoumarin and 2-methylbenzoyl chloride, and 4-coumarinyl 2-methylbenzoate compound was obtained in good yield. From the experimental values of the obtained compound and the NMR and infrared spectrum results calculated using the DFT/B3LYP/6-311G(d,p) basis set, it was observed that the vibration types of some characteristic peaks were compatible with both the literature values and each other. In addition, the energy difference between the HOMO and LUMO frontier orbitals of the compound was calculated as 1.409 eV, and this large energy gap shows that the molecule is not very stable. Finally, the siwiss adme properties (Molecular Mass, Flexibility, Polarity, Saturation, Lipophilia or Lipophilism, Water Solubility) of the compound were examined and according to the data obtained, it was seen that the compound largely met the siwiss adme properties.

## Acknowledgment

The author is grateful to Bitlis Eren University

## Statement of Research and Publication Ethics

The study is complied with research and publication ethic

## References

[1] H. Kolancilar, “DFT Yöntemi Kullanılarak 1,3-Bis- {(2-Aminobenzoil) Amino} Propanın Teorik Hesaplamaları Ve Bu Değerlerin Literatürdeki Deneysel Değerler İle Karşılaştırılması”, *Düzce Üniversitesi Bilim Ve Teknol. Derg.*, vol. 7, no 3, pp. 1319-1334, Tem. 2019, doi: 10.29130/dubited.463963.

[2] L. Liu and H. Miao, “A Specification-Based Approach to Testing Polymorphic Attributes”,in *Formal Methods and Software Engineering*, vol. 3308, J. Davies, W. Schulte, ve M. Barnett, Ed., ine Lecture Notes in Computer Science, vol. 3308. , Berlin, Heidelberg: Springer Berlin Heidelberg, 2004, pp. 306-319. doi: 10.1007/978-3-540-30482-1_28.

[3] T. Yu, Z. Zhu, Y. Bao, Y. Zhao, X. Liu, and H. Zhang, “Investigation of novel carbazole-functionalized coumarin derivatives as organic luminescent materials”, *Dyes Pigments*, vol. 147, pp. 260-269, Ara. 2017, doi: 10.1016/j.dyepig.2017.08.017.

[4] M. S. A. Abdel-Mottaleb, E. Hamed, M. Saif, and H. S. Hafez, “Binding, and thermodynamics of β-cyclodextrin inclusion complexes with some coumarin laser dyes and coumarin-based enzyme substrates: a simulation study”, *J. Incl. Phenom. Macrocycl. Chem.*, vol. 92, no 3-4, pp. 319-327, Ara. 2018, doi: 10.1007/s10847-018-0850-9.

[5] “Frisch, M. J. E. A. (2009). gaussian 09, Revision d. 01, Gaussian. Inc, Wallingford CT, 201.”.

[6] “T. K. R. Dennington and J. Millam, GaussView, Version 5 (Semichem Inc., Shawnee Mission, KS, 2009).”.

[7] T. J. Gilligan ve G. Schwarz, “The self-association of adenosine-5’-triphosphate studied by circular dichroism at low ionic strengths”, *Biophys. Chem.*, vol. 4, no 1, pp. 55-63, Oca. 1976, doi: 10.1016/0301-4622(76)80007-5.

[8] X. Du *vd.*, “Synthesis and Structure−Activity Relationship Study of Potent Trypanocidal Thio Semicarbazone Inhibitors of the Trypanosomal Cysteine Protease Cruzain”, *J. Med. Chem.*, c. 45, sy 13, ss. 2695-2707, Haz. 2002, doi: 10.1021/jm010459j.

[9] R. A. Omar, P. Koparir, K. Sarac, M. Koparir, and D. A. Safin, “A novel coumarin-triazole-thiophene hybrid: synthesis, characterization, ADMET prediction, molecular docking and molecular dynamics studies with a series of SARS-CoV-2 proteins”, *J. Chem. Sci.*, vol. 135, no 1, p. 6, Oca. 2023, doi: 10.1007/s12039-022-02127-0.

[10] N. M. O’boyle, A. L. Tenderholt, and K. M. Langner, “cclib: A library for package-independent computational chemistry algorithms”, *J. Comput. Chem.*, vol. 29, no 5, pp. 839-845, 2008, doi: 10.1002/jcc.20823.

[11] M. Franco-Pérez ve J. L. Gázquez, “Electronegativities of Pauling and Mulliken in Density Functional Theory”, *J. Phys. Chem. A*, vol. 123, no 46, pp. 10065-10071, Kas. 2019, doi: 10.1021/acs.jpca.9b07468.

[12] J. A. Harrison, J. D. Schall, S. Maskey, P. T. Mikulski, M. T. Knippenberg, ve B. H. Morrow, “Review of force fields and intermolecular potentials used in atomistic computational materials research”, *Appl. Phys. Rev.*, vol. 5, no 3, p. 031104, Ağu. 2018, doi: 10.1063/1.5020808.

[13] E. V. Schmidt *vd.*, “Antiviral Activity of Jodantipyrin – An Anti-Inflammatory Oral Therapeutic with Interferon-Inducing Properties”, *Anti-Inflamm. Anti-Allergy Agents Med. Chem.*, vol. 7, no 2, pp. 106-115.

[14] C. H. Reynolds, B. A. Tounge, and S. D. Bembenek, “Ligand Binding Efficiency: Trends, Physical Basis, and Implications”, *J. Med. Chem.*, vol. 51, no 8, pp. 2432-2438, Nis. 2008, doi: 10.1021/jm701255b.

[15] S. Schultes, C. de Graaf, E. E. J. Haaksma, I. J. P. de Esch, R. Leurs, ve O. Krämer, “Ligand efficiency as a guide in fragment hit selection and optimization”, *Drug Discov. Today Technol.*, vol. 7, no 3, pp. e157-e162, Eyl. 2010, doi: 10.1016/j.ddtec.2010.11.003.

[16] J. Hughes, S. Rees, S. Kalindjian, and K. Philpott, “Principles of early drug discovery”, *Br. J. Pharmacol.*, vol. 162, no 6, pp. 1239-1249, 2011, doi: 10.1111/j.1476-5381.2010.01127.x.